

DOCTORAL THESIS

State Estimation and Control for Small Low-Cost Autonomous Underwater Vehicles

Christian Meurer

TALLINN UNIVERSITY OF TECHNOLOGY
DOCTORAL THESIS
27/2021

State Estimation and Control for Small Low-Cost Autonomous Underwater Vehicles

CHRISTIAN MEURER



TALLINN UNIVERSITY OF TECHNOLOGY
School of Information Technologies
Department of Computer Systems

**The dissertation was accepted for the defence of the degree of Doctor of Philosophy
(Computer and Systems Engineering) on June 4th 2021**

Supervisor: Prof. Maarja Kruusmaa,
Department of Computer Systems, School of Information Technologies,
Tallinn University of Technology
Tallinn, Estonia

Co-supervisor: Prof. Ülle Kotta,
Department of Software Science, School of Information Technologies,
Tallinn University of Technology
Tallinn, Estonia

Opponents: Prof. Yogesh Girdhar,
Woods Hole Oceanographic Institution,
Woods Hole, MA, USA

Prof. Ralf Bachmayer,
University of Bremen,
Bremen, Germany

Defence of the thesis: June 10th 2021, Tallinn

Declaration:

Hereby I declare that this doctoral thesis, my original investigation and achievement, submitted for the doctoral degree at Tallinn University of Technology, has not been submitted for any academic degree elsewhere.

Christian Meurer

signature



European Union
European Regional
Development Fund



Investing
in your future

Copyright: Christian Meurer, 2021
ISSN 2585-6898 (publication)
ISBN 978-9949-83-709-0 (publication)
ISSN 2585-6901 (PDF)
ISBN 978-9949-83-710-6 (PDF)
Printed by Auratrükk

TALLINNA TEHNIKAÜLIKOOL
DOKTORITÖÖ
27/2021

Meetodid olekute hindamiseks ja juhtimiseks soodsa hinnaga autonoomsetele allveerobotitele

CHRISTIAN MEURER



Contents

List of Publications	7
Author's Contributions to the Publications	8
Abbreviations.....	9
Terms	10
Symbols.....	11
Symbols.....	12
1 Introduction	13
1.1 Research questions	16
1.2 Contributions	17
1.3 SNAME notation for marine vessels.....	18
1.4 Thesis outline.....	18
2 Flow based state estimation.....	21
2.1 State-of-the-art.....	22
2.2 Flow sensing with differential pressure	23
2.2.1 Potential flow theory.....	24
2.2.2 Velocity - pressure relationship for a Pitot-like probe	28
2.3 Surge velocity estimation with differential pressure	30
2.3.1 The differential pressure sensor speedometer (DPSS).....	30
2.3.2 DPSS performance characterization	32
2.3.3 Experimental setup for field tests	32
2.3.4 Results and discussion	33
2.4 2D velocity estimation relative to tidal currents.....	35
2.4.1 Prototype design (DPSSv2).....	36
2.4.2 Experimental setup for field tests	38
2.4.3 Results and discussion	39
2.5 Summary and conclusions	41
3 Actuator control for autonomous bio-inspired underwater locomotion.....	43
3.1 Underwater locomotion with compliant actuators.....	44
3.2 Asymmetric actuation for yaw control	45
3.2.1 Control framework	47
3.2.2 Experimental setup.....	49
3.2.3 Results and discussion	50
3.3 Summary and conclusions	52
4 Motion control for AUVs.....	54
4.1 Overview of traditional model-free motion controllers	56
4.1.1 PID control.....	56
4.1.2 RISE control	57
4.2 Overview of model-based motion control	57
4.2.1 AUV dynamics model for 6 DOF	57
4.2.2 Differential flatness.....	59

4.2.3	Disturbance observers	60
4.3	The DFEC framework	62
4.3.1	General DFEC derivation	62
4.3.2	State space equations for underactuated AUV dynamics in horizontal plane	65
4.3.3	Augmented DFEC for underactuated AUV dynamics	65
4.4	Experimental platform - U-CAT	67
4.5	Simulation	69
4.6	Results and discussion	73
4.7	Summary and conclusions	79
5	Conclusions	82
5.1	Summary of thesis contributions	82
5.2	Future directions	83
	List of Figures	89
	List of Tables	90
	References	91
	Acknowledgements	107
	Abstract	108
	Kokkuvõte	110
	Appendix 1	113
	Appendix 2	115
	Appendix 3	117
	Appendix 4	129
	Appendix 5	165
	Appendix 6	175
	Appendix 7	183
	Curriculum Vitae	193
	Elulookirjeldus	195

List of Publications

This Ph.D. thesis is based on the following publications that are referred to in the text by Roman numbers.

- I J. F. Fuentes-Pérez, C. Meurer, J. A. Tuhtan, and M. Kruusmaa, "Differential Pressure Sensors for Underwater Speedometry in Variable Velocity and Acceleration Conditions," IEEE Journal of Oceanic Engineering, vol. 43, no. 2, pp. 418–426, 2018
- II C. Meurer, J. Francisco Fuentes-Perez, N. Palomeras, M. Carreras, and M. Kruusmaa, "Differential Pressure Sensor Speedometer for Autonomous Underwater Vehicle Velocity Estimation," IEEE Journal of Oceanic Engineering, pp. 1–33, 2019
- III C. Meurer, A. Simha, Ü. Kotta, and M. Kruusmaa, "Nonlinear orientation controller for a compliant robotic fish based on asymmetric actuation," in Proceedings - IEEE International Conference on Robotics and Automation (ICRA), vol. 2019-May, pp. 4688–4694, Institute of Electrical and Electronics Engineers Inc., may 2019
- IV A. Kaldmäe, Ü. Kotta, C. Meurer, and A. Simha, "Event-based control for differentially flat systems: Application to autonomous underwater vehicle," in IFAC-PapersOnLine, vol. 52, pp. 180–185, Elsevier B.V., sep 2019
- V C. Meurer, J. F. Fuentes-Perez, K. Schwarzwaldner, M. Ludvigsen, A. J. Sorensen, and M. Kruusmaa, "2D estimation of velocity relative to water and tidal currents based on differential pressure for autonomous underwater vehicles," IEEE Robotics and Automation Letters, vol. 5, pp. 3444–3451, apr 2020

Author's Contributions to the Publications

- I I was a co-author; I helped with the planning of the experiments and conducted them with the first author, I helped in the analysis of the results, and helped in writing the manuscript.
- II I was the main author; I helped define the research problem and conducted simulations. I prepared for and conducted the experiments, analysed the results, prepared the figures, and wrote the manuscript.
- III I was the main author and defined the research problem. I wrote the software framework and implemented the derived controller on the robot. I derived and implemented the algorithm for the asymmetric actuation and planned the experiments. I conducted the experiments and wrote the manuscript.
- IV I was a co-author and contributed to the definition of the control problem and provided the model of the robot. I wrote the modeling section of the paper and contributed to the discussion in the paper.
- V I was the main author and defined the research problem. I planned the experiments and analysed the results. I wrote the manuscript.

Abbreviations

ADCP	Acoustic Doppler Velocity Profiler
AUV	Autonomous Underwater Vehicle
BCF	Body Caudal Fin
BDO	Basic nonlinear Disturbance Observer
CFD	Computational Fluid Dynamics
CAD	Computer Aided Design
COLA	Component Oriented Layer-based Architecture for Au- tonomy
DFEC	Differentially Flat Event-Based Controller
DOBC	Disturbance-Observer-Based Control
DOF	Degree of Freedom
DPSS	Differential Pressure Sensor Speedometer
DPSSv2	Differential Pressure Sensor Speedometer version 2
DVL	Doppler Velocity Log
DVL-BL	Doppler Velocity Log in bottom log mode
DVL-WL	Doppler Velocity Log in water log mode
EKF	Extended Kalman Filter
ESO	Extended State Observer
FILOSE	Fish Locomotion and Sensing
GPS	Global Positioning System
ID	Inverse Dynamics
IMU	Inertial Measurement Unit
INS	Inertial Navigation System
IQR	Interquartile range
KF	Kalman Filter
LAUV	Light Autonomous Underwater Vehicle
MIMO	Multiple-Input Multiple-Output
MPF	Median Paired Fin
NED	North East Down
PID	Proportional Integral Derivative
RISE	Robust Integral of the Sign of the Error
RMSE	Root Mean Squared Error
ROS	Robot Operating System
ROV	Remotely Operated Vehicle
SLAM	Simultaneous Localization and Mapping
SMC	Sliding Mode Control
SNAME	Society of Naval Architects and Marine Engineers
U-CAT	Underwater Curious Archaeology Turtle
VO	Visual Odometry
VIO	Visual Inertial Odometry

Terms (if needed)

surge	linear movement direction along the x-axis of the body coordinate system of a mobile vehicle
sway	linear movement direction along the y-axis of the body coordinate system of a mobile vehicle
heave	linear movement direction along the z-axis of the body coordinate system of a mobile vehicle
roll	direction of angular movement around the x-axis of the body coordinate system of a mobile vehicle
pitch	direction of angular movement around the y-axis of the body coordinate system of a mobile vehicle
yaw	direction of angular movement around the z-axis of the body coordinate system of a mobile vehicle

Symbols

a	Tightness factor
f	Motor oscillation frequency
$f(x, t)$	State transition function
g	Gravitational constant
$g(x, t)$	Control function
$g(\eta)$	Vector of hydrostatic forces and torques
$h(x, t)$	Output function
Δh	Difference in hydrostatic elevation
n	Normal unit normal vector to a bodies surface
p	Angular velocity around the x-axis of a mobile vehicle
p_f	Fluid pressure
Δp	Pressure difference
q	Angular velocity around the y-axis of a mobile vehicle
r	Angular velocity around the z-axis of a mobile vehicle
r_s	Distance from origin in spherical coordinate system
r_b	Centre of buoyancy
$r_m(t)$	Reference trajectory for trajectory tracking
sk	Skew factor
t	Time
u	Linear velocity along the x-axis of a mobile vehicle
v	Linear velocity along the y-axis of a mobile vehicle
v_∞	One dimensional free stream velocity of fluid flow
w	Linear velocity along the z-axis of a mobile vehicle
w	Vector of disturbances on control system
x	Position along the x-axis of a mobile vehicle / vector of states in state space representation
y	Position along the y-axis of a mobile vehicle / vector of outputs in state space representation
y_{mr}	Flat feedforward trajectory
z	Position along the z-axis of a mobile vehicle
A	Motor oscillation amplitude
B	Buoyancy force
C	Matrix of Coriolis and centripetal forces and torques
$C_{RB}(v)$	Matrix of rigid body terms of Coriolis and centripetal forces and torques
$C_A(v)$	Matrix of added mass terms of Coriolis and centripetal forces and torques
$D(v)$	Matrix of hydrodynamic damping forces and torques
$J(\eta)$	6 DOF rotation matrix mapping coordinates in body-fixed frame to earth-fixed frame
K	Torque applied to a mobile vehicle around its x-axis
K_D	Derivative PID control gain
K_I	Integral PID control gain
K_P	Proportional PID control gain
M	Torque applied to a mobile vehicle around its y-axis
M	Inertia matrix
M_{RB}	Rigid Body inertia matrix
M_A	Added mass inertia matrix

Symbols

N	Torque applied to a mobile vehicle around its z-axis
$N_{\dot{r}}$	Added mass coefficient for yaw
N_r	Coefficient for linear hydrodynamic damping in yaw
N_{rr}	Coefficient for quadratic hydrodynamic damping in yaw
$N()$	normal distribution
R^2	Coefficient of determination
T	wave period
W	Weight force
V	Velocity vector of fluid flow
V_∞	Free stream velocity vector of fluid flow
X	Force applied to a mobile vehicle along its x-axis
X_{dotu}	Added mass coefficient for surge
X_u	Coefficient for linear hydrodynamic damping in surge
X_{uu}	Coefficient for linear hydrodynamic damping in surge
Y	Force applied to a mobile vehicle along its y-axis in sway direction
Y_v	Coefficient for linear hydrodynamic damping in sway
Y_{vv}	Coefficient for linear hydrodynamic damping in sway
Y_{dotv}	Added mass coefficient for sway
Z	Force applied to a mobile vehicle along its z-axis in heave direction
η	Robot pose consisting of position and orientation
η_d	Desired robot pose
$\tilde{\eta}$	Tracking error
μ	Mean of a normal distribution / sensor accuracy
μ_D	Doublet strength
v	Vector of linear and angular vehicle velocities
ρ	Fluid density
ϕ	Euler angle around the x-axis of a mobile vehicle
θ	Euler angle around the y-axis of a mobile vehicle
φ	Polar angle in spherical coordinate system
$\varphi()$	Motor actuation function
φ_0	Oscillation offset
ψ	Euler angle around the z-axis of a mobile vehicle
ψ_d	Desired Euler angle around the z-axis of a mobile vehicle
$\dot{\psi}$	Error in Euler angle around the z-axis of a mobile vehicle
σ^2	Variance of a normal distribution
Φ	Velocity potential
Ψ	Azimuth angle in spherical coordinate system
∇	Gradient vector
τ	Vector of control forces and torques

1 Introduction

The world's oceans contain 96 % of the world's water [6], play a critical role in regulating global climate, and serve as a vast, connected ecosystem for flora and fauna. Additionally, around 10 % of the Earth's population (more than 600 Million people) live in coastal areas that are less than 10 m above sea level [7].

Monitoring and collecting data about underwater environments is crucial to improve our understanding of the complex ecosystems that have evolved therein, and would bolster conservation efforts. Notwithstanding its importance, large parts of the underwater environment are still unexplored, mostly due to the difficulty and danger imposed on human observers. The need for artificial air supply and pressure regulation lead to very time limited and high cost operation, no matter if divers, or crewed submersibles, are involved.

Recent decades have seen the development of autonomous systems in many fields. For underwater applications, tethered unmanned vehicles called remotely operated vehicles (ROVs) have enabled operations without placing human workers in danger, while retaining the benefit of extended operational times and increased workspace regarding depth. However, an extensive infrastructure, namely a support vessel and highly specialised operators, are needed to effectively use ROVs. Additionally, the spatial range of the vehicles is limited by the tether connecting it to the support vessel. Long range exploration or the monitoring of confined or highly unstructured spaces can be difficult or impossible with ROVs.

To decrease the dependency on costly external infrastructure and to increase spatial operation range, autonomous underwater vehicles (AUVs) have been introduced. AUVs reduce direct human involvement and can significantly lower operational costs while increasing spatial range. However, the increased autonomy and spatial range come at the cost of decreased temporal range, because the vehicle's energy supply has to be self-sufficient. Additionally, reliable and extensive autonomy is crucial for the successful application of AUVs, because outside intervention is close to impossible in most application scenarios.

Autonomy for robots can be loosely defined as the capability to perceive the environment, make decisions based on those perceptions, and to act on such decisions without the need for external guidance. Those three capabilities can be summarised as sense, think and act [8]. The possible relationships between those elements are defined in robotic paradigms, which describe the nature of a robot's autonomy. The work presented in this thesis was based on the classic hierarchical paradigm [9], where the robot senses the world, forms a goal for the next action and then enacts the required actuation for the given action. For underwater vehicles, most autonomy software architectures mirror this structure by encoding observation, planning and control modules, which can be parallelized and act collaboratively as shown by Palomeras et. al in their COLA2 framework [10]. The vehicles used in the work presented in this thesis will use a similar software architecture. An abstraction of such an autonomy structure is shown in *Figure 1*. To represent a given autonomy framework with higher granularity, the sense element can be further divided into signal acquisition and processing, tightly linked with a respective sensing modality, and into a state estimation component that gathers and fuses sensing data from all available sources to construct a coherent global world model for the robot. State estimation and sensor fusion is typically facilitated by some variant of a Bayesian filter. Those filters are recursive estimators, that try to infer a probability density function based on incoming sensor data and a mathematical process model if available. The most common variants are Kalman and Particle filters [11].

The think element can be divided into a higher level decision making routine, a mid level planning component and a controller that interfaces with the act element to enable the necessary actuations. In the context of underwater robotics the high level decision making component is very often a set of rigid behaviours based on the world model of the robot. The transition from a limited and rigid set of behaviours to more flexible, adaptive and self-dependent decisions is still an open field of research. The planning component for mobile robotics mostly concerns itself with the creation of waypoints in multidimensional space connected by a path or smooth time parametrized functions (i.e. trajectories) that describe a robot's pose and time derivatives (velocity, acceleration, etc.). These are tightly linked to high level objectives identified in the decision making layer. Usually paths or trajectories are created to make the robot cover a specific area or lead the robot to a specific point in space. Additionally, obstacle avoidance, various optimization criteria and platform specific constraints play an important role in shaping the paths or trajectories generated by the planning module.

For traditional AUVs, high level decision making and planning have received an increased focus in recent years, while for sensing, control and actuation solid baseline solutions have already been developed. However, traditional AUVs tend to be large, expensive and require a certain infrastructure for their deployment. While such features tend to play a smaller role for end-users in the military and industrial sector, as well as for big scientific institutions, other potential costumers remain underserved and important use-cases remain unexplored. In recent years attempts have been made to develop small scale low-cost AUVs. Such vehicles have been designed for various applications, such as the inspection of nuclear facilities [12], deployments in swarms [13], or the survey of polar regions where ease of deployment is crucial [14]. Additionally, the usage of more affordable and easy to deploy vehicles could impact the performance for blue growth industries such as algae farms. Lastly, environmental monitoring for marine sciences could be made much more accessible on various government levels and for smaller scientific institutions [15, 16].

On the general AUV market, the segment of archaeology and exploration is projected to have the largest growth over the next years [17]. While this market growth is still mainly attributed to traditional AUVs, specific archaeological sites and exploration targets like shipwrecks or sea caverns are high risk environments in confined spaces, that require agile, small and low-cost alternatives to traditional AUVs.

Traditional AUVs can be usually divided into two groups relative to their motion capabilities. The first and larger group constitutes slender streamlined AUVs that are optimized for speed and efficiency to conduct long range missions. However, they are usually underactuated and thus lack maneuverability. The second group of AUVs is made up out of hover style AUVs that are at least fully actuated and are used for inspection and manipulation missions. However, as a compromise to their agility they lack efficiency, speed and range. Recent focus has been on agile underactuated AUVs that have the potential to bridge the gap between those two types of vehicles [18] and leverage advantages from both sides. Such capabilities would be specifically useful for several applications for the emerging class of small low-cost AUVs. However, the capacity of these vehicles, particularly with respect to state estimation, actuation design, and control, remains in question. The research presented in this thesis focuses on significant improvements to small, low-cost AUVs in each of these critical areas.

With a reduction in size and budget comes a reduction in available sensors for state estimation and navigation, and the available sensors are of lesser quality. While attitude estimation can be maintained with reasonable quality [19], position or velocity estimation

becomes much more difficult, specifically in situations where vision is not a viable option. In addition to that, state-of-the-art positioning or velocity sensors send out high frequency acoustic signals. Recent research suggests that certain high-frequency acoustic signals might have adverse effects on the surrounding fauna [20, 21]. Thus, sensors with novel sensing strategies have the potential to increase navigation performance and to decrease the environmental impact of small low-cost AUVs. This can be specifically important if the vehicles are used in missions in which minimal invasive monitoring is desired.

Inspiration can be taken from aquatic animals, which have co-evolved with their environment for millions of years. They often rely on the sensing of gradients of physical quantities. The perception of those gradients is mostly passive, and has the potential to be a promising role model for developing sensors with less environmental impact and a smaller energy consumption. The work presented in this thesis specifically considers the sensing of pressure gradients in combination with potential flow theory to infer quantities related to fluid flow. Many attempts have been made to develop artificial sensing modalities for such gradients [22, 23, 24, 25, 26, 27, 28, 29, 30, 31]. However, there is a clear lack of testing of the developed sensors in realistic field conditions. Some successful field applications in the context of environmental sensing with static probes have been shown [32, 33, 34], but there is still no proof that such technologies are robust and reliable enough for mobile robotics applications in the field. The research presented in *Chapter 2* addresses this problem.

Additionally, potential research gaps remain in scenarios that require the AUV to be operated in a minimally invasive manner. Motor driven propellers as standard actuators for AUVs produce noise and cavitation with an unaccounted effect on the surrounding flora and fauna. Propellers can additionally affect the surrounding environment in a manner that could be detrimental to the functioning of sensors used in state estimation, like cameras or acoustics. Most aquatic animals utilize some sort of fin or flipper for propulsion. As opposed to the rigid structure of traditional mechanical propulsors, bio-inspired actuators can be soft with a varying degree of compliance. Replacing conventional propellers with bio-inspired actuators can thus create vehicles which are safer to work with in the vicinity of divers or other living organisms, but also could reduce adverse interactions with the environment and living organisms. However, the introduction of soft bio-inspired actuators also adds complex nonlinear dynamics to an already nonlinear nominal system. This increases the difficulty in appropriately controlling such vehicles. A wide variety of control approaches has been proposed for conventional AUVs, with a much smaller coverage for AUVs with bio-inspired propulsion. The research presented in *Chapter 3* tries to leverage the unique character of bio-inspired actuators and the idea of asymmetry in the control action to increase controllability of a sub-class of bio-inspired underwater vehicles.

The potential complexity of actuation, the desired agility and the underactuated nature of many small low-cost AUVs, lead to complex nonlinear motion dynamics. A high level motion control that takes those dynamics into account is therefore desirable. Usually, nonlinear model-based control strategies can be employed to steer such complex systems to desired states [35]. However, such strategies often require high order derivatives of the robot's pose, such as acceleration or jerk, which are usually difficult to measure. This general limitation across all mobile robotic platforms is amplified by the lack of sophisticated sensing modalities for the vehicles that the work presented in this thesis focuses on. The concept of event-based control [36] has the potential to alleviate this problem by removing the requirement for continuous real-time state feedback to the high level controller. Additionally, the underwater environment itself exhibits highly nonlinear dynamics and can cause disturbances to the autonomous operation of AUVs. For successful field appli-

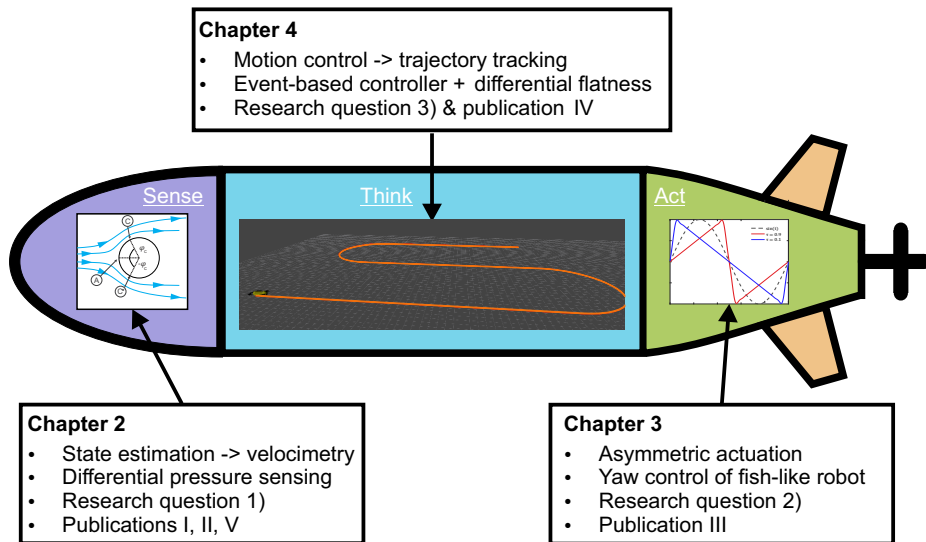


Figure 1 – Research presented in this thesis in the context of robot autonomy. Each of the chapters provides an attempt to answer one of the research questions, and describes contributions to a different layer of the mobile robot autonomy framework. Each box briefly mentions main contributions, which research question is addressed and which publications display the respective research.

cations, high level control approaches that can deal with uncertainty and disturbances are necessary. Another problem for high level control comes with the requirement for agile motion. This requirement necessitates the implementation of efficient and fast trajectory tracking, which is non-trivial for systems with complex dynamics. The exploitation of a property of dynamical systems that is called *differential flatness* [37] can significantly simplify the generation and tracking of viable trajectories. To deal with the above mentioned problems, the work presented in this thesis therefore, proposes a new control strategy that tries to combine ideas from: event-based control, disturbance estimation as well as trajectory generation and tracking based on *differentially flat* motion dynamics. For simplicity, the proposed controller is restricted to movement in the horizontal plane but has potential for extensions into more degrees of freedom (DOFs).

1.1 Research questions

To summarize, the overarching goal of the research presented in this thesis was the improvement of autonomy for AUVs, with a focus on the class of small low cost underwater robots. Improved autonomy was achieved by designing and employing novel methods and/or hardware for state estimation, actuation and control (see Figure 1). The subsequent description of the research questions and related contributions reflect this three-fold division.

- 1) How can state estimation for small low-cost AUVs be improved and made more robust for the application under field conditions?
- 2) Can *asymmetric actuation* increase maneuverability of AUVs using compliant bio-inspired actuators?

- 3) How can model-based nonlinear controllers be augmented, to overcome limitations related to unreliable state feedback and motion constraints of AUVs with complex dynamics?

Quantitative methods in conjunction with clearly defined performance metrics were employed to answer the listed research questions. Where logistically possible, field experiments were conducted to test performances under real world conditions. Otherwise simulations were performed for proofs of concept, taking into account their limited explanatory power for real world applications.

1.2 Contributions

In the context of the above mentioned research questions the research described in this thesis provides the following contributions:

Research question 1)

- The extension and advancement of a sensor system [38] for velocity estimation based on *differential pressure* sensors for the purpose of mobile underwater robotics.
- The mathematical derivation of the relation between velocity and pressure for the design of the given sensor system, by employing standard potential flow theory.
- Testing of the capability of the proposed sensor system for 2D velocity estimation in laboratory and field conditions with a rigorous comparison to state-of-the-art technology.
- The combination of the new sensor system with state-of-the-art technology for mobile environmental sensing, specifically to infer tidal water currents.

Research question 2)

- The design and implementation of a nonlinear orientation control framework for a robotic fish based on *asymmetric actuations* of the fish robot's compliant tail.
- Testing the proposed control framework under field conditions with a comparison to the standard actuation for orientation control of fish-like robots.

Research question 3)

- The design of a nonlinear control framework for the trajectory tracking in the horizontal plane for underactuated AUVs using elements from event based control, *differential flatness* and disturbance estimation. This included the augmentation of the nominal dynamics and a proof of *differential flatness* for the augmented system, as well as the design of a disturbance observer to compensate for the augmentation.
- Testing the efficacy and robustness of the trajectory tracking controller in simulation. The dynamics of an agile underwater vehicle with bio-inspired actuation and a commercial torpedo shaped low cost AUV were simulated. The control framework was validated for scenarios with and without external disturbances and compared to a PID controller serving as a standard baseline. A further comparison was made to a RISE controller [39], which was used as an example for a robust model free control method.

It should be noted that the presented contributions to the three problems of state estimation, actuator control and high level motion control vary in their scope of applicability. The work on actuator control has immediate relevance to bio-inspired actuators only, while the presented sensor system and high level control strategy have a much broader scope. The sensor system is essentially agnostic to the marine vessel on which it is mounted and could be used generically. However, it would have the biggest impact on small resource constraint vehicles, by providing information about states that would be difficult to observe otherwise. Thus, the contextualization of the contribution is made on a specific subset of AUVs. The proposed high level motion controller has theoretically an even bigger scope with a potential applicability to terrestrial or aerial vehicles that exhibit similar motion dynamics as the system the controller was developed for. However, the focus of the work presented in this thesis solely remains on underwater vehicles and the contribution is therefore contextualized in that domain.

Most of the research presented in this thesis has been already published in leading journals and conferences and all publications are attached in Appendices 3 to 7. The only exception is part of the motion control framework presented in *Chapter 4*, which will be the basis for future publications.

1.3 SNAME notation for marine vessels

All methodologies and concepts throughout this thesis are related to the motion of underwater vehicles. Definitions defined by the Society of Naval Architects and Marine Engineers (SNAME) [40] are used to establish a clear framework of notation for various directions of movement, state variables and reference frames for all sensors and vehicles described in this thesis. The SNAME notation for marine vessels concerning the notation of forces, moments, velocities and orientation angles is shown in *Table 1*. Additionally, the motion of AUVs is represented in two distinct reference frames. The first is a reference frame that is fixed to a defined vehicle origin and the second is a static inertial or Earth-fixed reference frame as shown in *Figure 2*. There are various options for the definition of earth fixed reference frames and for the purpose of the work presented in this thesis the earth fixed coordinate frame is represented by a North-East-Down coordinate system also called NED-frame [40], where the North and East directions form a tangent plane on the Earth's surface. In general the NED frame does not represent an Earth-fixed frame, however, for vehicles operating in a local area of approximately constant longitude and latitude the tangent plane on the earth's surface can be seen as static and the NED frame can be defined as an earth fixed and inertial (Newton's laws do apply) frame. It should be noted that throughout the thesis a true NED frame is only being used during field trials. During laboratory tests or simulations an inertial frame with more local meaning for axis directions is used. However, the general downward orientation of the z-axis and the use of a right-handed Cartesian coordinate system remains consistent throughout the research presented in this thesis.

1.4 Thesis outline

Following along with the three research questions, the thesis is organized in three chapters, each describing a contribution to a different part of the introduced autonomy framework, by addressing one of the three research questions (see *Figure 1*). Within each chapter, the context of the given research question is outlined and an overview about relevant state-of-the-art research, as well as theoretical information is provided where required. Then methodologies employed to answer the respective research question are presented.

Table 1 – SNAME notation for marine vessels [40]

Direction	forces and moments	velocities	positions and Euler angles
motion along x-axis (surge)	X	u	x
motion along y-axis (sway)	Y	v	y
motion along z-axis (heave)	Z	w	z
rotation about x-axis (roll)	K	p	ϕ
rotation about y-axis (pitch)	M	q	θ
rotation about z-axis (yaw)	N	r	ψ

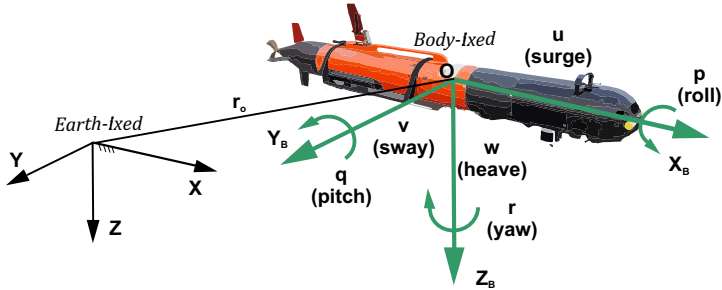


Figure 2 – Body fixed and earth fixed reference frames according to SNAME notation.

This is followed by the validation of the proposed methodologies through an application to a specific use-case and through empirical experimentation. Afterwards, the test results are presented and discussed. Each chapter ends with concluding remarks about the efficacy of the presented solutions to the posed research question. The thesis is thus divided into the following chapters:

- **Chapter 2** describes research on the problem of velocity estimation for small low-cost AUVs and introduces a sensor system that utilizes *differential pressure*. The chapter presents a derivation of first principle relations between velocity and pressure, utilizing standard potential flow theory. Two prototyped iterations of the proposed sensor system are presented and rigorous tests under field conditions are described and discussed.
- **Chapter 3** addresses the second research question and highlights the potential of *asymmetric actuation* for control purposes. First, the use of bio-inspired soft actuators is motivated and *asymmetric actuation* is briefly contextualized in the fields of robotics and biology. Then a nonlinear controller using *asymmetric actuation* is introduced and examined in the application of yaw control for a fish-like robot with a compliant tail.
- **Chapter 4** investigates the effectiveness of a novel model-based nonlinear controller to enable efficient trajectory tracking in the horizontal plane for underactuated AUVs. An overview about the problem of motion control for mobile underwater robots is given, and the problem of trajectory tracking is motivated. The chapter includes a brief presentation of standard model-free controllers that can be used for trajectory tracking. Then, a novel control approach is presented that borrows ideas from event-based control, as well as disturbance estimation and uses the property of *differential flatness*. The efficacy of the proposed control framework is

then tested in simulation, using two small low-cost AUVs. To that end, the derivation of the control framework for the specific dynamics of the vehicles is presented and the simulation setup is described. The chapter closes with the presentation and discussion of the simulation results.

- **Chapter 5** summarizes this thesis and draws conclusions based on the presented results. The chapter also highlights the scientific contributions of the work presented in this thesis. Finally, limitations of the work are explained and an outlook is given on potential future research directions.

2 Flow based state estimation

This chapter addresses the first research question:

"How can state estimation for small low-cost AUVs be improved and made more robust for the application under field conditions?"

The chapter starts with the contextualization of state estimation for underwater vehicles. This is followed by an overview about the present state-of-the-art for a relevant subset of state estimation in AUVs. Then the concept of flow sensing with differential pressure is introduced and motivated. This is followed by a first principle derivation of the relation between flow velocity and pressure by representing the sensor as a simple geometric object within a potential flow. Finally, the design and experimental validation of two prototypes with a measurement principle, based on the derived relation, are described at the end of this chapter. The research presented in this chapter has been published in **publications I, II and V**.

A successful operation and recovery of AUVs requires robust navigation and localization capabilities [41, 42]. Navigation and localization in turn depend on reliable and precise state estimation, where the relevant system states are the physical quantities that describe the vehicle's kinematics and dynamics: pose, velocity and possibly acceleration in 6 DOFs. The quality of the estimation process depends on the employed sensors and algorithms, which are bounded by the size and energy supply of the respective vehicle, as well as monetary budget limitations and operation conditions. Along with the increasing use of low-cost and small underwater vehicles, there is a need for scalable and affordable solutions for state estimation.

Unlike in terrestrial or aerial environments, state estimation underwater is impeded by the rapid high-frequency attenuation of sensor signals, so that the most common state estimation technique using satellite-based global positioning units can not be effectively employed. Another typical state estimation framework in robotics is visual odometry (VO) [43, 44]. Because of its heavy dependency on visual cues VO faces difficulties underwater, where relevant physical conditions, such as turbidity and lighting, are highly dynamic.

An additional complicating factor is the lack of salient and well structured features for the vast majority of the underwater environment. Existing solutions for underwater state estimation can be roughly divided into three main categories, based on the environmental structures used and the type of interaction between the structure and sensor: (1) acoustic state estimation in a local artificial coordinate system, (2) geophysical state estimation and (3) inertial state estimation.

Acoustic state estimation requires additional hardware to be deployed, which creates the artificial local coordinate system. Therefore, this solution is limited to environments where such a hardware deployment is feasible. Geophysical state estimation uses the features near AUVs to track location within an environment, but is not extensible to environments that lack classical salient features such as the open ocean or for highly unstructured or dynamic environments. Inertial state estimation, as the most basic method, uses dead reckoning techniques to estimate the state of a vehicle. Based on introspective measurements, inertial state estimation is independent of and insensitive to environmental characteristics, making it suitable for operations in either featureless or complex environments. Additionally, this method removes the need for costly and complex additional infrastructure, decreasing the expenses for AUV missions. Though contemporary inertial navigation systems (INS) provide increasingly accurate heading and acceleration estimates, the method suffers from unbounded error growth [45].

In best practice, the aforementioned methods are combined through sensor fusion [45, 11] to increase overall robustness and accuracy of the state estimation in the navigation system. Methods for sensor fusion include Kalman Filters (KFs), Particle Filters, and Simultaneous Localization and Mapping (SLAM) [11]. Due to its global applicability, inertial state estimation is the core technique for most navigation solutions. It can be improved by the addition of measurements or estimates of states that can not be directly observed by inertial sensors. A typical and very well studied addition to inertial state estimation is the supplement of pose estimates based on the relative orientation and distance from visual cues located in the local vicinity of a vehicle. The technique of combining visual with inertial information is called visual inertial odometry (VIO) [46]. However, the VIO approach inherits the above mentioned limitations of the VO framework for underwater applications. A standard addition to INS for AUVs is the direct measurement of the vehicle velocity, which usually is less dependent on the environmental conditions. Incorporating velocity information into an INS helps to bound or at least slow its error growth [47]. Measurements of vehicle velocity are usually complicated by naturally occurring water flows relative to the AUV. However, if the water-flow is spatially distributed and sufficiently heterogeneous, it can also be viewed as an information source for navigation and state estimation as shown in various theoretical works and controlled experiments [48, 49]. Furthermore, the estimation of water flows and related natural phenomena can inform environmental research by providing additional opportunities for in situ measurements.

The focus of the sensor related work presented in this thesis was therefore the development and especially the field validation of cost and energy efficient sensor technology that provides velocity estimates and potentially flow related environmental cues for AUVs. To that end, the state-of-the-art for underwater flow estimation is presented in the next chapter, with subsequent chapters describing the rationale behind the choice of how to sense and estimate water flow, as well as prototype designs and their validation under field conditions.

2.1 State-of-the-art

Doppler velocity logs (DVLs) are the most widely applied class of velocity sensors used to aid the INS [50, 51, 47, 52] of AUVs, providing velocity estimation with a sufficiently narrow error margin [45]. DVLs are often used in bottom lock mode (DVL-BL) which relies on a smooth surface where scattering of the hydroacoustic signals can be avoided. In regions with uneven or absent surfaces, DVLs can use a water lock mode (DVL-WL) to estimate velocity. However, DVL-WL has certain limitations as this mode relies on the presence of particles in the water, that can reflect the hydroacoustic signals. Generally, DVL-WL thus cannot provide the same accuracy as the DVL-BL. Recent work suggests the use of acoustic doppler current profilers (ADCP) to solve some of those problems [53, 54]

However, despite recent efforts to reduce their size [55, 56, 57], DVLs and ADCPs are difficult to integrate into small vehicles with a limited payload capacity and a tight budget [58, 59, 60]. Furthermore, as active sensing devices, DVLs have a comparably high energy consumption, which lessens their efficacy on long-term missions [61]. Additionally, low cost vehicles used in applications entailing a high-risk [62], in swarm operations [63] or in consumer robotics [64, 65] could benefit from an inexpensive alternative for velocity estimation.

The state-of-the-art measurement modalities for flow sensing on AUVs almost exclusively rely on active emission of acoustic signals and the subsequent recording and interpretation of resulting reflections. This creates a dependency on available reflective

surfaces and also increases the energy consumption of the devices. In contrast, other engineering fields such as aeronautics have successfully employed passive sensing for the estimation of flow related variables. Commonly, pressure sensors are employed to measure relative speed, angle of attack, yaw rate and altitude of aircrafts [66, 67]. Additionally, pressure sensors are base utilities in other fluid related fields, such as in the control of industrial processes, or in wind and flow tunnels.

Currently, the closest related pressure sensor based systems for the estimation of flow related variables for underwater robots are artificial lateral lines. Those sensor systems are inspired by the lateral line organ that fish employ to navigate their environment by detecting mechanical changes in the surrounding water [68]. Artificial lateral lines have been employed to estimate various flow related parameters such as relative flow speed [25, 26, 27, 33], angle of attack [24, 30, 31], the detection of objects and wake structures [22, 23] or walls [28, 29]. The artificial lateral line systems have been based on various technological approaches, such as micromachined piezoresistive cantilevered beams [69, 70], optical flow sensors [71, 72], or commercially available absolute or gauge pressure sensors [73, 74, 75]. While artificial lateral lines based on micromachined cantilevered beams or optical flow sensors remain highly experimental with usage almost exclusively limited to laboratory conditions, artificial lateral lines based on commercial absolute or gauge pressure sensors have been shown to be robust and accessible enough for environmental measurements in the field at discrete geographically static measurement points [33, 34]. Absolute or gauge pressure sensors measure pressure relative to a fixed reference, which increases the required measurement range and decreases sensitivity proportionally to operation depth. Additionally, absolute and gauge pressure sensors are affected by fluctuations in the height of the water column, which can increase measurement noise for flow features close to the water surface in the presence of wave action. To diminish those problems *differential pressure* sensors can be used instead, showing great potential for improved sensitivity without a significant reduction in robustness [76]. The sensing systems that are presented in this thesis have been designed with such *differential pressure* sensors as a basic component. The following section describes how flow velocity can be estimated by sampling *differential pressure* at several points on the surface of a sensor system.

2.2 Flow sensing with differential pressure

Differential pressure is defined as the difference in pressure between two measurement points. If those measurement points are kept in the same horizontal plane or the relative vertical motion of the two points is detected and filtered out, then the static component of the pressure is mechanically compensated for [28, 38]. It follows, that the necessary pressure range to be measured can be minimized and the measurement sensitivity can be increased. Artificial lateral lines based on *differential pressure* sensors have been shown to successfully estimate hydrodynamic forces for wall detection and vehicle control in [28] and for hydrodynamic force decoupling for motion control in [77] and [78]. To measure flow, velocity several *differential pressure* sensors can be arranged to form a variant of a Pitot-tube, a structure routinely employed in aeronautics and other engineering fields. This concept has been shown to work for the estimation of flow speed in a laboratory setting [38] and for static environmental sensing applications in the field [32].

The relation between the output of several *differential pressure* sensors to flow speed in laminar flow conditions was empirically established for a specific Pitot-tube configuration in [38]. The empirical relation was valid for a limited range of velocities, and the used data was subject to possible wall disturbances caused by a narrow flow tunnel.

The work presented in this thesis provides a simple first principle derivation for the empirical relation found in [38] and expands it for applications in mobile underwater robotics. The tested velocity range is further expanded and field tests are conducted to proof the robustness and applicability of the proposed solution. The following sections outline the theoretical basis for the approach of *differential pressure* based flow sensing. Focus is applied on the estimation of flow velocity based on the pressure distribution over a 3D sphere.

2.2.1 Potential flow theory

To estimate flow velocity it is fundamental to establish a relationship between pressure and velocity on the surface of the sensor in a flow field. The relationships between fundamental quantities of any fluid are generally described by the Navier-Stokes equations, where a solution is not tractable for online applications required in mobile robotics. However, based on several simplifying assumptions first principle relationships can be derived to connect the pressure distribution over a well defined geometrical object to the free stream velocity. The required simplifications are valid if the flow in question can be assumed to be inviscid, irrotational and incompressible. Those assumptions enable the application of potential flow theory, which is very well established for specific geometries. The relationships needed for the estimation of flow velocity based on *differential pressure* are standard in potential flow theory and a lot of exhaustive treatments of this subject exist. However, to provide a sufficient context for the description, application and testing of the prototypes described in later sections, a brief overview about the potential flow over a 3D sphere is provided, by heavily leaning on the treatment of the subject given in [79].

We first start by deriving a relationship between the free stream velocity vector V_∞ and the velocity field on the surface of a measurement probe. For an irrotational flow we can construct a scalar function Φ such that the flow velocity is given by the gradient of that function, while ensuring conservation of mass:

$$\nabla \cdot V = \nabla \cdot (\nabla \Phi) = 0. \quad (1)$$

Equation (1) can be written as:

$$\nabla^2 \Phi = 0. \quad (2)$$

Equation (2) describes the governing relationship for potential flow theory and is called Laplace's equation. It is very well studied and numerous solutions to the equation exist. For flows over a body the solutions to (2) must additionally conform with a boundary condition that describes flow-tangency on the body that is placed in the flow:

$$V \cdot n = 0, \quad (3)$$

with n being a unit vector normal to the bodies surface. For three-dimensional flows, the velocity potential Φ will be a function of three-dimensional space. The choice of a proper coordinate frame to describe the flow is application dependent. For a flow over a spherical body, a natural choice is the use of spherical coordinates $\Phi = \Phi(r, \varphi, \Psi)$. Here r_s presents the distance from the origin of the reference frame defined to coincide with the center of the spherical body, φ describes the polar and Ψ the azimuth angle in the spherical reference frame as can be seen in *Figure 3*.

The flow over a spherical body can be derived based on the superposition of a uniform and a doublet flow (see *Figure 3*), which describes a flow where streamlines emanate from a source point and revolve around that point. The doublet itself is constructed of a pair of source and sink flows which are described in detail in basic potential flow theory

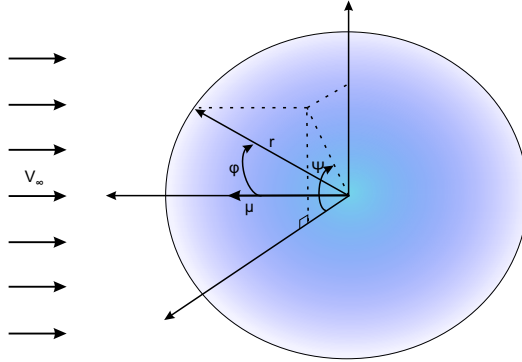


Figure 3 - **Superposition of a uniform flow field and a three dimensional doublet flow.** The uniform flow is characterized by its free stream velocity V_∞ and the doublet is characterized by its strength μ_D . Space is defined by the spherical coordinates r_s , φ , Ψ . adapted from [79]

textbooks such as [79]. The velocity components in spherical coordinates for a uniform velocity field with magnitude V_∞ can be described by:

$$\begin{aligned} V_{r_s} &= -V_\infty \cos \varphi \\ V_\varphi &= V_\infty \sin \varphi \\ V_\Psi &= 0. \end{aligned} \quad (4)$$

The corresponding velocity components for a doublet flow can be described by:

$$\begin{aligned} V_{r_s} &= \frac{\mu_D \cos \varphi}{2\pi r_s^3} \\ V_\varphi &= \frac{\mu_D \sin \varphi}{4\pi r_s^3} \\ V_\Psi &= 0, \end{aligned} \quad (5)$$

with μ_D describing the strength of the doublet. Now the combined flow can be described by the sum of (4) and (5):

$$V_{r_s} = - \left(V_\infty - \frac{\mu_D}{2\pi r_s^3} \right) \cos \varphi \quad (6a)$$

$$V_\varphi = \left(V_\infty + \frac{\mu_D}{4\pi r_s^3} \right) \sin \varphi \quad (6b)$$

$$V_\Psi = 0. \quad (6c)$$

Since the points of the velocity field that are relevant for this derivation are at the surface of the spherical body, the distance from the coordinate system origin can be set to the radius of the spherical body $r_s = R$. Using the stagnation points in the flow where $V_{r_s} = V_\varphi = 0$ and (6a), the relationship between the radius of the spherical body, the strength of the corresponding doublet flow and the free stream velocity can be derived:

$$R = \left(\frac{\mu_D}{2\pi V_\infty} \right)^{\frac{1}{3}}. \quad (7)$$

By reinserting (7) back into (6a) the expression becomes:

$$V_{r_s} = - \left[V_\infty - \frac{\mu_D}{2\pi} \frac{2\pi V_\infty}{\mu} \right] \cos \varphi = 0, \quad (8)$$

leading to $V_{r_s} = 0$ for all values of φ and ψ on the condition of $r_s = R$. This shows that the derived velocity field is compliant with the flow-tangency condition defined in (3).

The relevant velocity for the proposed measurement principle is thus the tangential velocity V_φ and its relationship to the free-stream velocity for $r_s = R$ is given by:

$$V_\varphi = \left(V_\infty + \frac{\mu_D}{4\pi R^3} \right) \sin \varphi. \quad (9)$$

In terms of the proposed measurement principle, the polar angle φ is given by the location of the pressure sensor inlet on the surface of the measurement probe, but the doublet strength is an unknown. By expressing the strength of the doublet flow based on (7):

$$\mu_D = 2\pi R^3 V_\infty \quad (10)$$

and substituting (10) into (9) one can get a direct relationship between φ , V_φ and V_∞ :

$$V_\varphi = \frac{3}{2} V_\infty \sin \varphi. \quad (11)$$

With a relationship for the free stream velocity we can proceed to derive the mapping between velocity distribution over the surface of the measurement probe and the corresponding pressure distribution, specifically considering pressure differences. We first start by stating the momentum equation for a general fluid flow. For simplicity we only consider the x component from a three dimensional flow in Cartesian coordinates. We can state the momentum equation as:

$$\rho \frac{Du}{Dt} = -\frac{\partial p}{\partial x} + \rho f_x + (F_x)_{viscous}. \quad (12)$$

Here ρ denotes the density of the considered fluid element, u is the linear velocity along the x component direction of the fluid element, $\frac{D(*)}{Dt}$ is the substantial derivative, $\frac{\partial p_f}{\partial x}$ the pressure force on a fluid element, ρf_x is the sum of body forces acting on the fluid element (such as gravity) and $(F_x)_{viscous}$ is the viscous shear stress on a fluid element. By assuming an inviscid flow with no body forces (12) becomes:

$$\rho \frac{Du}{Dt} = \rho \frac{\partial u}{\partial t} + \rho u \frac{\partial u}{\partial x} + \rho v \frac{\partial u}{\partial y} + \rho w \frac{\partial u}{\partial z} = -\frac{\partial p_f}{\partial x}, \quad (13)$$

with x, y, z being the principal spatial and t the temporal descriptors of the system, and v, w being the linear velocities along the y and z axes respectively. By adding another simplifying assumption of steady flow $\frac{\partial u}{\partial t} = 0$ equation (13) can be written as:

$$u \frac{\partial u}{\partial x} + v \frac{\partial u}{\partial y} + w \frac{\partial u}{\partial z} = -\frac{1}{\rho} \frac{\partial p_f}{\partial x}. \quad (14)$$

Now considering flow along a streamline in three dimensional space given by the following relationships:

$$\begin{aligned} w \, dy - v \, dz &= 0 \\ u \, dz - w \, dx &= 0 \\ v \, dx - u \, dy &= 0. \end{aligned} \quad (15)$$

By using some calculus we can arrive at the following relationship:

$$u \, du = \frac{1}{2} d(u^2) = -\frac{1}{\rho} \frac{\partial p_f}{\partial x} \, dx. \quad (16)$$

Derivations for the y and z components of the momentum equation are yielding equivalent results:

$$\begin{aligned}\frac{1}{2}d(v^2) &= -\frac{1}{\rho} \frac{\partial p}{\partial y} dy \\ \frac{1}{2}d(w^2) &= -\frac{1}{\rho} \frac{\partial p}{\partial z} dz,\end{aligned}\tag{17}$$

which can be combined into:

$$\frac{1}{2}d(u^2 + v^2 + w^2) = -\frac{1}{\rho} \left(\frac{\partial p_f}{\partial x} dx + \frac{\partial p_f}{\partial y} dy + \frac{\partial p_f}{\partial z} dz \right),\tag{18}$$

given

$$u^2 + v^2 + w^2 = V^2,\tag{19}$$

and

$$\frac{\partial p_f}{\partial x} dx + \frac{\partial p_f}{\partial y} dy + \frac{\partial p_f}{\partial z} dz = dp,\tag{20}$$

we can substitute (19) and (20) into (18) and get:

$$dp_f = -\rho V dV,\tag{21}$$

which is called *Euler's equation* and relates changes in velocity to changes in pressure along a streamline. Now by making the additional simplifying assumption of constant density of the fluid in question (assumption of incompressible flow) equation (21) can be easily integrated between two points a and b along a streamline:

$$\begin{aligned}\int_{p_a}^{p_b} dp &= -\rho \int_{V_a}^{V_b} V dV \\ p_a + \frac{1}{2}\rho V_a^2 &= p_b + \frac{1}{2}\rho V_b^2.\end{aligned}\tag{22}$$

Relationship (22) is valid for rotational and irrotational flows, but is only applicable along streamlines. Assuming irrotational flow instead, allows to generalize (22) between any two points in the flow if all simplifying assumptions are met:

$$p_f + \frac{1}{2}\rho V^2 = \text{const}.\tag{23}$$

We thus have gained a simple first principle relationship between pressure and velocity in a flow field. The simplicity of (23) relies on several assumptions that are explicitly stated again to clarify when (23) can be used: The fluid's viscosity is negligible (**inviscid flow**), gravity is negligible and static pressure is equal for different measurement points (**no body forces**), **steady flow** over a finite time horizon and the flow is assumed to be **irrotational**.

The listed assumptions might seem to be rather restrictive for the use in field applications with dynamic environments. However, flow velocity estimation based on the pressure distribution over an immersed, often spherical, body using equation (23) has been extensively employed in aeronautics. By assuming a steady flow over a spherical body and defining two specific measurement points A and B, lying on the same plane on a sphere's surface, one can infer the one dimensional free stream velocity v_∞ from the pressure measurements at A and B. For a special case shown in *Figure 4.a* point A directly faces the flow and the pressure is measured in a position where the fluid velocity is zero (stagnation point) and point B is situated at an angle φ_{st} where the local velocity equals the free

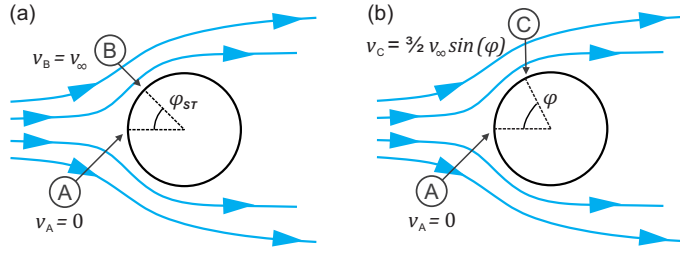


Figure 4 – **Irrotational, inviscid and incompressible flow over a sphere for two measurement points [publication II]**. The stagnation point on the spheres surface is indicated by A. (a) We introduce the static point B, respective velocities v_A , v_B and the enclosing angle φ_{ST} . (b) We introduce an arbitrary surface point C, respective velocities v_A , v_C and the enclosing angle φ . In both cases v_∞ denotes the free stream velocity

stream velocity (static point). In this case equation (23) can be rewritten as the well known Pitot equation:

$$p_A = p_B + \frac{1}{2} \rho v_B^2 \quad (24a)$$

$$v_\infty = v_B = \sqrt{\frac{2(p_A - p_B)}{\rho}} = \sqrt{\frac{2\Delta p}{\rho}}. \quad (24b)$$

2.2.2 Velocity - pressure relationship for a Pitot-like probe

Fuentes-Perez et al. [38] introduced an additional mirrored measurement point C* inspired by the concept described in [80], so that two pressure differences were utilized to increase the robustness of the velocity estimation. This relationship can be expanded for arbitrary mirrored points C and C* as shown in Figure 5.a. A geometric principle derivation of the empirical equation found in [38] is given in the following.

Using equation (11) the relationship between v_∞ and the tangential velocity v_C at an arbitrary measurement point C (see Figure 4.b) can be described as:

$$v_C = \frac{3}{2} v_\infty \sin(\varphi_C), \quad (25)$$

where φ_C is the planar angle between stagnation point A and measurement point C, as shown in Figure 5.a. Now equation (24b) can be rewritten for arbitrary measurement point locations by substituting (25) in (24b):

$$v_\infty = \sqrt{\frac{2}{\rho} \frac{4 \Delta p}{9 \sin^2(\varphi_C)}}, \quad (26)$$

with the pressure difference $\Delta p = p_A - p_C$. Equations (24b) and (26) are only valid if measurement point A coincides with a stagnation point of the flow field, which requires measurement point A to directly face the flow. This can not always be guaranteed during the operation of a mobile underwater robot moving in 3D space. The velocity estimation can be made more robust by introducing a second measurement point C* that is located at the mirrored position from point C as shown in Figure 5.a. Then, equation (26) can be expanded to utilize two pressure differences $\Delta p_1 = p_A - p_C$ and $\Delta p_2 = p_A - p_{C^*}$. First, the quadratic average of both pressure differences is taken to combine the information

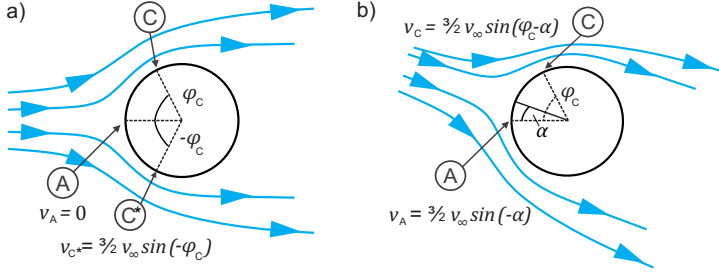


Figure 5 - **Irrotational, inviscid and incompressible flow over a sphere for three measurement points and at angled ambient [publication V].** a) Point A marks the stagnation point on the spheres' surface where the local velocity is zero. Points B and B* describe mirrored and arbitrary positions at the spheres' surface for an angle $0^\circ \leq \varphi_C \leq 90^\circ$. b) Point A is angled towards the flow by α and the local velocity is nonzero. Given the same configuration as in a) both measurement points A and B are shifted by the angle of incoming flow.

from the two measurements. Then, the pressure differences are expressed in terms of free stream velocity by using equations (24a) and (25):

$$\sqrt{\frac{\Delta p_1^2 + \Delta p_2^2}{2}} = \sqrt{\frac{\left(\frac{9}{4}\rho v_\infty^2\right)^2 [\sin^4(\varphi_C) + \sin^4(\varphi_{C*})]}{2}}. \quad (27)$$

By defining $\varphi = \varphi_C = -\varphi_{C*}$ and using the symmetry of the sine function it can be stated that $\sin^4(\varphi_C) + \sin^4(\varphi_{C*}) = 2\sin^4(\varphi)$. Equation (27) can be simplified and solved for v_∞ :

$$v_\infty = \sqrt[4]{\frac{2\alpha(\varphi)}{\rho^2} (\Delta p_1^2 + \Delta p_2^2)}, \quad (28)$$

with

$$\alpha(\varphi) = \left(\frac{4}{9\sin^2(\varphi)}\right)^2. \quad (29)$$

Equation (28) agrees well with the relationship, found by using computational fluid dynamics (CFD), presented in [38]. The relationship presented in equation (28) was further verified under laboratory conditions [publication I], where it showed an accuracy of 0.012 m/s for surge speed estimation. To accurately estimate surge speed in field conditions, self motion effects of the vehicle carrying the sensor have to be taken into account. A hydrostatic correction algorithm can be introduced to account for pitch θ and roll ϕ motions of an AUV [publication II]. Subsequently, we can augment (28) to:

$$v_\infty = \sqrt[4]{\frac{2\alpha(\varphi)}{\rho^2} ((\Delta p_1 - \Delta h_1 \rho g)^2 + (\Delta p_2 - \Delta h_2 \rho g)^2)}, \quad (30)$$

with the vertical height differences between the measurement points as:

$$\begin{aligned} \Delta h_1 &= (x_C - x_A) \cos(\phi) \sin(\theta) - (y_C + y_A) \sin(\phi) \\ \Delta h_2 &= (x_{C*} - x_A) \cos(\phi) \sin(\theta) - (y_{C*} + y_A) \sin(\phi), \end{aligned} \quad (31)$$

where Δp_1 and Δp_2 represent the pressure differences between the stagnation point and the arbitrary mirrored points C / C*. $\varphi = \varphi_C = -\varphi_{C*}$ is the planar angle between the

stagnation point and points C / C*. Additionally, g represents the gravitational constant and $x_{(\cdot)}$ and $y_{(\cdot)}$ are Cartesian coordinates of the respective measurement points relative to the center of the spherical head of the sensor.

The model for sway velocity is based on the assumption, that the location of the stagnation point on the spherical object will change in the presence of a non zero flow in sway direction as depicted in *Figure 4.b*. We furthermore assume that equation (30) is invariant to changes in flow direction of up to 45° [38] and captures the true velocity component in the surge direction. The velocity estimation for a single *differential pressure* sensor for the general case can be written as:

$$\Delta p_1 = p_A - p_C = \frac{1}{2}\rho(v_C^2 - v_A^2 + 2g\Delta h_1). \quad (32)$$

Note that with h_1 the elevation compensation presented in equation (31) is also utilized for the estimation of the velocity component in sway direction. Substituting equation (11) in equation (32) and accounting for a change in the flow direction by the angle α results in the following relationship:

$$\Delta p_1 = \frac{1}{2}\rho \left[\frac{9}{4}v_\infty^2 (\sin^2(\varphi_C - \alpha) - \sin^2(-\alpha)) + 2g\Delta h_1 \right]. \quad (33)$$

Using trigonometric identities and solving for α (see full derivation in Appendix 1) we get:

$$\alpha = \frac{\varphi_B - \arcsin\left(\frac{8(\Delta p_1 - \rho g \Delta h_1)}{9\rho v_\infty^2 \sin(\varphi_C)}\right)}{2}. \quad (34)$$

Based on the assumption that $v_\infty = v_x$ as given by Eq. (30), the sway velocity component can be estimated by:

$$v_y = v_x \tan(\alpha). \quad (35)$$

The following chapters will present prototype designs, which make use of the pressure-velocity relationships derived above.

2.3 Surge velocity estimation with differential pressure

To validate the theoretical relation (30) and to test the hardware design presented in [38] under realistic conditions, field tests with an AUV where necessary. To that end, a new sensor prototype, defined as differential pressure sensor speedometer (DPSS), was build. The DPSS was then integrated into the commercial AUV SPARUS II (Iqua Robotics) and tested in the harbor of St. Feliu de Guixols, Spain. Those tests are described in detail in **publication II** and are briefly presented in subsections 2.3.1 to 2.3.4.

2.3.1 The differential pressure sensor speedometer (DPSS)

In accordance with the derived concepts in *section 2.2*, the two differential pressure sensors build the core of the DPSS. They are connected to three flush holes, subsequently called pressure taps, which are normal to the surface of the DPSS housing. *Figure 6.b* illustrates the location of the pressure taps at an azimuth angle of 0° (stagnation point) and $\pm 35^\circ$. A 6DOF IMU provides input to the correction algorithm (31) and the vehicle's surge velocity is calculated using a microcontroller that computes (30). The total power consumption of the full electronics setup is 243.5 mW and everything is integrated into a 3D printed water-tight housing (see *Figure 6.a*). To reduce size and budget, but mostly

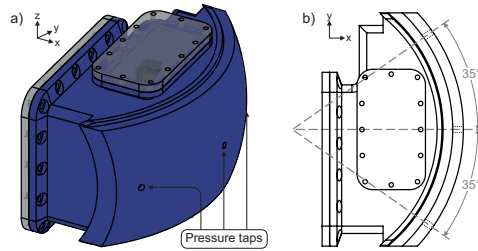


Figure 6 – **DPSS housing and pressure tab location [publication II]**. a) Isometric view of a CAD model of the 3D printed DPSS housing indicating the location of the pressure tabs that directly connect to the differential pressure sensors. b) Top view of a schematic drawing of the DPSS with indications at which planar angle (relative to the local x-axis starting at the center of the spherical outermost section of the housing) the pressure taps are located.

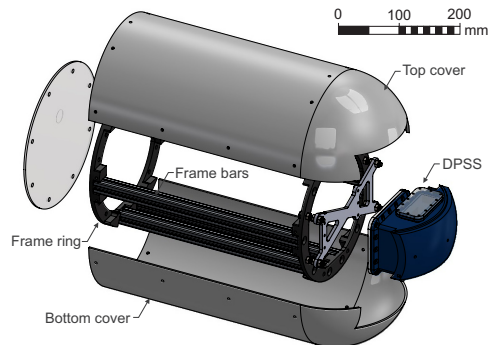
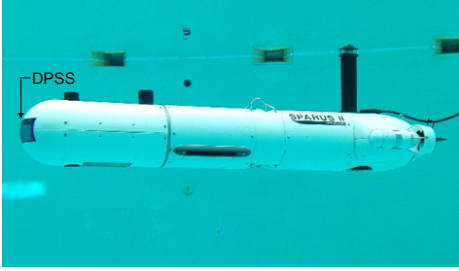


Figure 7 – **Exploded view of DPSS CAD Assembly [publication II]**. The DPSS is shown together with a custom made frame and covers that reproduce the payload section of the SPARUS II AUV. A new frame and new covers are used to ensure a spherical geometry at the head of the AUV during trials with the DPSS, so that the derived potential flow model can be directly applied.

to increase sensitivity, the DPSS uses differential pressure sensors not directly rated for water. To ensure that do not come into contact with water, but still measure the pressure at the pressure tabs, a tubing system is designed that forms a permanent layer of air between the sensor and it's surrounding medium when the DPSS is submerged. A more detailed description of the prototype can be found in [publication I] and [publication II].

The housing of the DPSS was specifically designed to be integrated with a SPARUS II AUV (IQUA Robotics), which has an interchangeable head section [81]. This head section is replicated and slightly modified for the purpose of seamless integration of the DPSS into SPARUS II. Figure 7 shows the computer aided design (CAD) drawing of the DPSS and auxiliary components that recreated the head section of SPARUS II. Those components are comprised of a mounting frame and 3D printed covers that have a modified geometry as compared to the standard SPARUS II covers. When assembled, the covers and the outer surface of the DPSS form a hemisphere, which allows the use of the relations derived in section 2.2.1.



General specifications:

Length: 1.60 m
 Hull diameter: 0.23 m
 Max. width: 0.46 m
 Weight in air: 52 kg
 Max. depth: 200 m
 Li-Ion batteries: 1.4 kWh
 Endurance: 8-10 h
 Max. surge velocity: 1.5-2.0 m/s

Installed sensors:

IMU: Analog Devices ADIS
 DVL: Teledyne RDI Explorer 600
 GPS: OEM Fastrax IT 500
 Pressure sensor: Keller

Figure 8 – SPARUS II AUV [publication II]. On left SPARUS II is shown with integrated DPSS in an indoor pool at the Underwater ROBotics Research Centre (CIRS, University of Girona, Girona, Spain). Relevant specifications of SPARUS II can be seen on the right (adapted from [81])

2.3.2 DPSS performance characterization

For a successful assessment of the DPSS's performance under field conditions, a performance characterization under controlled laboratory conditions was required first. The baseline performance of the DPSS for surge velocity estimation was characterized by tow tank experiments, which are described in [publication I]. Given a sampling rate of 100 Hz of the raw pressure data, the effect of the number of pressure samples that are used for the computation of surge velocity at a given time-step was investigated. The results presented in [publication I] show that a stable optimum accuracy can be obtained for estimation rates between 5 Hz to 13 Hz. One possibility to establish an error model for the DPSS, would be the propagation of the nominal error attributed to the commercial pressure sensors through (30). However, the error estimates provided by the manufacturer are conservative, which makes it difficult to establish an accurate error model. Instead, the error model was developed based on empirical data from the tow tank experiments. All error sources were lumped together into a probabilistic error term “*err*” assuming a normal distribution where the mean μ represents the sensor accuracy:

$$v_{\infty} = \sqrt[4]{\frac{2\alpha(\varphi)}{\rho^2}((\Delta p_1 - \Delta h_1 \rho g)^2 + (\Delta p_2 - \Delta h_2 \rho g)^2) + err} \quad err \sim N(\mu, \sigma^2). \quad (36)$$

The obtained accuracy of $\mu = 0.012 \text{ m/s} \pm 0.01 \text{ m/s}$ [publication I] was then used as a baseline for the evaluation of the DPSS's performance in the field tests, which are presented in the following subsection.

2.3.3 Experimental setup for field tests

For field testing the DPSS prototype the SPARUS II AUV was used. SPARUS II is a lightweight surveillance AUV for long term missions with a classical torpedo shaped hull. The vehicle can be actuated in surge, heave, pitch and yaw and the DPSS was integrated into the front part of the hull as can be seen in Figure 8. The basic sensor suite of SPARUS II consisted of a pressure sensor, IMU, DVL and GPS (see Figure 8) and all information was forwarded to an EKF for state estimation [82]. The DVL was used as the reference for surge velocity estimation. More specifically information from the DVL-BL was favored by the EKF over information from the DVL-WL.

Field trials were conducted in the harbor area of Sant Feliu de Guixols, Catalonia, Spain (see Figure 9). The DPSS was tested for different reference paths (linear, loop, lawn mower) and at a variety of reference velocities ranging from 0.2 m/s to 2 m/s at a con-



Figure 9 – **Geographic location of the test site [publication II]**. Harbor area of Sant Feliu de Guíxols (Catalonia, Spain). WGS84 (km) — 41.7775° N, 3.0325° E

stant target depth of either 3 m or 4 m. Additionally, different test sites within the harbor provided variable environmental conditions. SPARUS II was following the reference paths using the EKF state estimation based on the sensor suite described above and in Figure 8. The DPSS was recording data independently, but was not used online in the control framework of the robot. In postprocessing the surge velocity estimates of the DPSS were calculated based on relation (30) and after filtering the raw pressure signals. It is important to note, that all the postprocessing steps done for the DPSS, can be done online during vehicle operation. Based on the described experiments, a comparable performance between DPSS and DVL surge velocity estimations was expected. Additionally, a degradation of the accuracy, if compared to the nominal values from the DVL datasheet and from [publication I], of both sensors was anticipated as a consequence environmental disturbances. For this reason the most degradation was expected in scenario C which was less sheltered from wave and other ocean dynamics.

Based on the assumption of equal performance of the surge velocity estimation for DVL-BL and DPSS a fit was defined and the coefficient of determination R^2 was used for evaluation. Additionally, the root mean squared error (RMSE) was used to compare both velocity estimations. Given the field character of the experiments the RMSE is here to be considered as a measure for a difference in estimation between two sensors rather than an absolute error between sensor and the true reference. To reduce environmental disturbances all estimates are filtered through the EKF of SPARUS II [82].

2.3.4 Results and discussion

Figure 10 shows a logarithmic density plot of the correlation between DPSS and DVL-BL surge velocity estimations with associated R^2 values for different environmental settings A to C. Here A describes the most sheltered setting with least environmental disturbances and C the most open setting with higher environmental disturbances. It can be seen that R^2 is smallest for the most open setting C as expected. However, for all settings R^2 is bigger than 0.9, with $R^2 = 0.95$ for the set of all surge velocity estimation pairs. This indicates that DPSS and DVL-BL had a comparable average performance for surge velocity estimation. Additionally, a higher variability in all plots can be seen for smaller target velocities. This can be explained on the one hand by the decreased ratio between vehicle velocity and environmental disturbances and on the other hand by the quadratic relationship between

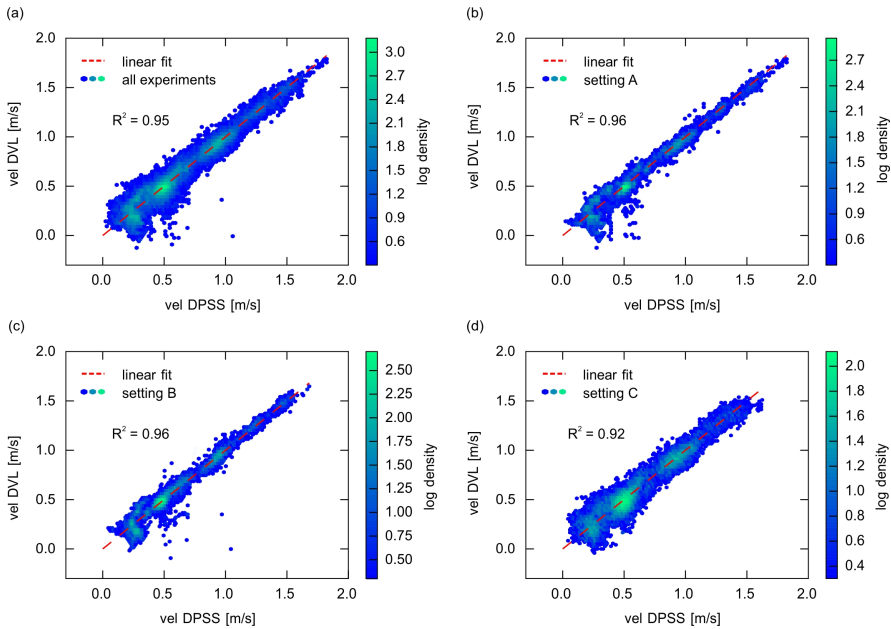


Figure 10 – **Logarithmic density plot for the correlation between DVL-BL and DPSS surge velocity estimates [publication II]**. a) Correlation plot for experiments across all scenarios, b) - d) plots for environmental settings A-C. For all plots an assumed perfect fit $v_x^{DVL} = v_x^{DPSS}$ is shown as red dotted line and the R^2 value, computed based on the assumed perfect fit, is shown as a quantitative measure of the correlation.

pressure and velocity for the DPSS, which makes the velocity estimation more susceptible to pressure noise at lower velocities.

Figure 11.a shows the RMSE between DPSS and DVL-BL velocity estimation for different settings and repetitions. Again it can be seen that for the more open setting C variability between the sensors is higher and that the difference between the sensors decreases with increasing velocity. The differences even approach the accuracy boundaries established by the manufacturer (DVL) and previous calibration experiments (DPSS) for setting A. In contrast, the differences between DVL-BL and DVL-WL, shown in Figure 11.b seem to significantly increase with increasing target velocity. RMSEs for loop and lawn mower paths are consistent with the results presented in Figure 11. The better performance of the DPSS compared to the DVL-WL for higher target velocities is specifically important, because both measure the same velocity, namely the velocity relative to the surrounding medium, as opposed to velocity over ground measured by the DVL-BL. Therefore, these results indicate that the DPSS could be not just a replacement for a DVL for vehicles with budget and payload constraints, but also a good complement to a standard AUV sensor suite that already includes a DVL. This is further supported by the raw velocity estimates shown in Figure 12 where SPARUS II was moving over a rough terrain close to the harbor wall, causing continuous outtakes from the DVL while the DPSS is unaffected. In this context the addition of the DPSS to the regular sensor suite can improve navigation in conditions where the DVL-BL fails to provide reliable velocity estimates such as mid water column travels or movement over rough and unstructured terrain.

To the best of the author’s knowledge, the described field trials marked the first successful implementation of pressure based speedometry for AUVs in field conditions. The

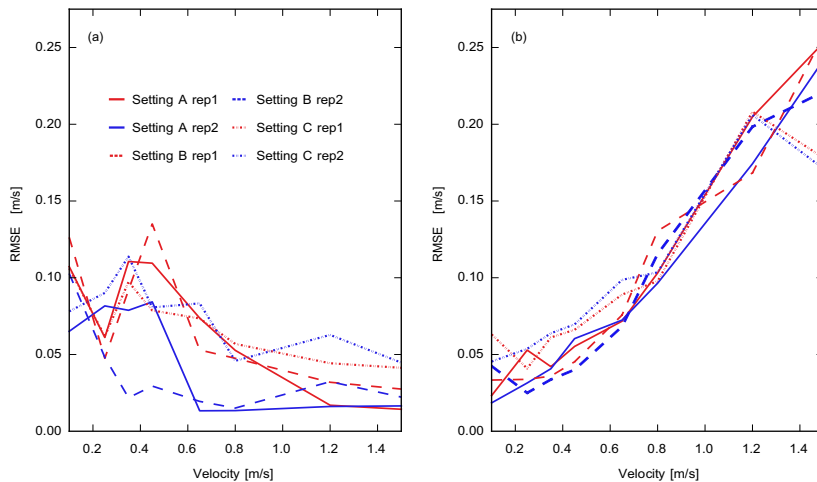


Figure 11 – RMSE between various surge velocity estimations at different target velocities [publication II]. a) DPSS vs DVL-BL and b) DVL-WL vs DVL-BL. Repetitions of the same experimental configuration are distinguished by color and the three different environmental settings are differentiated by line type.

results were a successful proof of concept for the differential pressure based surge velocity estimation and confirmed that the proposed algorithms and hardware work under field conditions. However, there is remaining potential for reducing the size of the sensor and expanding measurement capabilities for more degrees of freedom. The following iteration of the DPSS prototype addressed those remaining potentials and is described in the next section.

2.4 2D velocity estimation relative to tidal currents

The first iteration of the DPSS was specifically designed and tailored for the integration into the SPARUS II AUV. For the next iteration (DPSSv2) the hardware design was changed so that the resulting sensor was platform agnostic and self sustained. Additionally, the size of the sensor was significantly reduced and the velocity estimation was expanded to 2D still relying upon potential flow theory and using geometric principles as described by equations (26) - (35).

All DPSS prototypes measure velocity relative to water and not relative to a static reference. Previous experiments were carried out in a sheltered environment in relatively calm conditions. Therefore, the frame of reference for the measurement did not play a big role. In fact it was possible to directly compare the DPSS performance to the DVL-BL performance. However, in generic open water applications, conditions are most likely more dynamic with a including reference frame for the DPSS velocity estimation. Therefore, it was necessary to conduct experiments in conditions with a relatively controlled natural flow. Additionally, the combination of the DPSS relative velocity estimates with a source for velocity estimates relative to a static reference frame can enable the estimation of hydraulic influences on a robot such as water currents. An estimation of such currents could be then used to inform controllers for dynamic positioning or trajectory tracking. Estimates of water currents can also help to update and improve oceanographic models [83] or can inform the decision making for adaptive sampling [84]. If estimates of vehicle velocity relative to a static reference and a source of vehicle velocity relative to the sur-

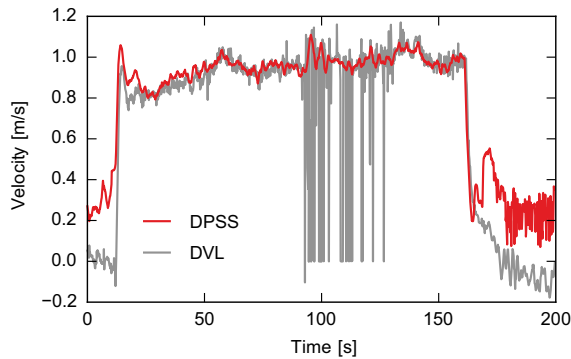


Figure 12 – Example of raw velocity readings for DPSS and DVL-BL for lawn mower trajectory [publication II]. At around 90 s SPARUS II got close to the harbor wall, where the ground is unstructured and rough. This disadvantageous environmental conditions is clearly reflected in the sensor output. It can be clearly seen that the DPSS was not affected. Differences at the beginning and the end of the plot are due to vertical movement of the robot which was not compensated for in the DPSS.

rounding water are simultaneously available, the water current velocity can be inferred as the difference of the former two quantities.

Different approaches to estimate water currents have been presented in the literature. A completely computational approach makes use of the concept of observers from control theory. Given an observable model describing the movement of a vehicle, a second model can be developed based on inputs and weighted outputs of the real system. Several types of observers such as Luenberger type observers [85, 86, 87, 88, 89] and high gain observers [90, 91] have been shown to work in simulation and have been partially verified on real physical systems. However, they all rely on accurate position feedback which is not readily available for AUVs. Some methods, developed for ocean gliders, are making use of sparse GPS fixes [92, 93] and predictive ocean models [94, 95, 96]. However, even sparse GPS fixes might be unavailable for AUVs, especially during long term missions. Several solutions for water current estimation that do not rely on measurements of the global position of the vehicle have been proposed as well. Medagoda et al. use an ADCP to estimate currents during midwater column travel [54]. While this would be an approach where ocean currents could be directly measured, the use of an ADCP demands amounts of energy, space, as well as monetary and computational costs that are usually only fulfilled by heavyweight high budget vehicles.

Hegreneaes et al. showed that an INS, aided either by a dynamics model of the vehicle [97] or by a DVL-WL [52] both in combination with a DVL-BL, can provide the necessary information to estimate water currents. The DPSS prototypes can be seen in the same light as an alternative source of in situ measurements of velocity relative to water and thus act as a replacement or a complement for the DVL-WL or dynamics model used by Hegreneaes et al, but also for the other approaches previously mentioned.

2.4.1 Prototype design (DPSSv2)

The hardware design of the new DPSSv2 resulted in a volume reduction of 28 % and a weight reduction of 39 % while integrating the same electronic components as the original DPSS. Table 2 compares the DPSSv2 with three small-scale DVLs regarding size, weight, and energy consumption. The DPSSv2 has a comparable size to the smallest DVL available at the moment. The DPSSv2 is also about an order of magnitude more energy efficient in

Table 2 – Comparison of DPSSv2 with three small DVLs for size, weight and power consumption / adapted from [2]

Sensor	Size L x W x H [cm]	Weight (air / water) [kg]	Power Consumption [W]
Teledyne Wayfinder [55]	10 x 10 x 7	0.85 / 0.51	3
Nortek DVL1000 [57]	15.8 x \varnothing 11.4	1.3 / 0.15	1.3
NavQuest 600 Micro [56]	17.4 x \varnothing 12.6	2.9 / 1.2	2 - 5
DPSSv2	14.1 x \varnothing 5	0.27 / 0.17	0.244

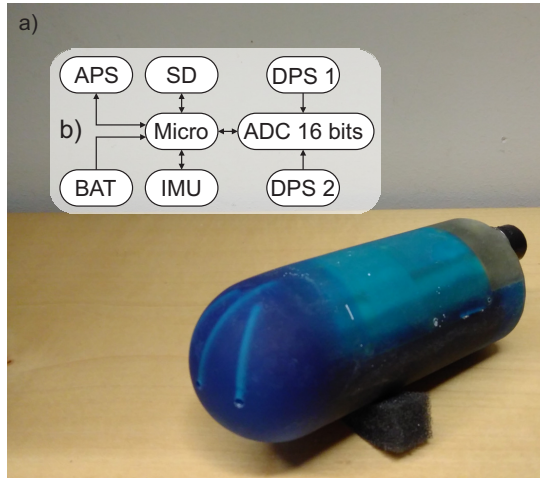


Figure 13 – The new DPSSv2 prototype. a) fully assembled prototype with 3D printed housing. b) Electronic component architecture of the DPSSv2 with the following notation: APS - absolute pressure sensor, SD - SD card, Micro - Microcontroller, BAT - Battery pack, IMU - Inertial Measurement Unit, ADC - Analog to Digital Converter, DPS - differential pressure sensor.

comparison to all the three DVLs. Cost is another important metric to evaluate the DPSSv2 against state of the art technology. However, a direct comparison is very complicated, because the listed DVLs are fully developed products, whereas the DPSSv2 is still in the prototyping stage. Nevertheless, based on a rough projection the price range for DPSSv2 could probably at least be around one order of magnitude lower.

Additionally, the DPSSv2 is now equipped with a battery so that it can be used as a standalone measurement device in addition to a possible integration into an AUV sensor suite. Figure 13 shows the new prototype with a schematic of its electronic components (Figure 13 b).

The performance of the DPSSv2 was verified with tow tank experiments equivalent to the ones described in [publication I]. Based on the results, an accuracy of $\mu = 0.01 \text{ m/s} \pm 0.046 \text{ m/s}$ was determined. The standard deviation is larger, when compared to the original DPSS. This was expected to some extent, because the noise sensitivity of the velocity estimation seems to scale with the distance between the pressure taps. A slightly reduced performance is thus to some extent a sacrifice for volume and weight reduction of the sensor. However, a slightly increased noise sensitivity should not have a major influence on the estimation performance for typical target velocities of AUVs and is a worthwhile compromise to make the sensors usable for a wider class of vehicles and other applications. It is also clear that the combination of the DPSS velocity estimation with a Bayesian

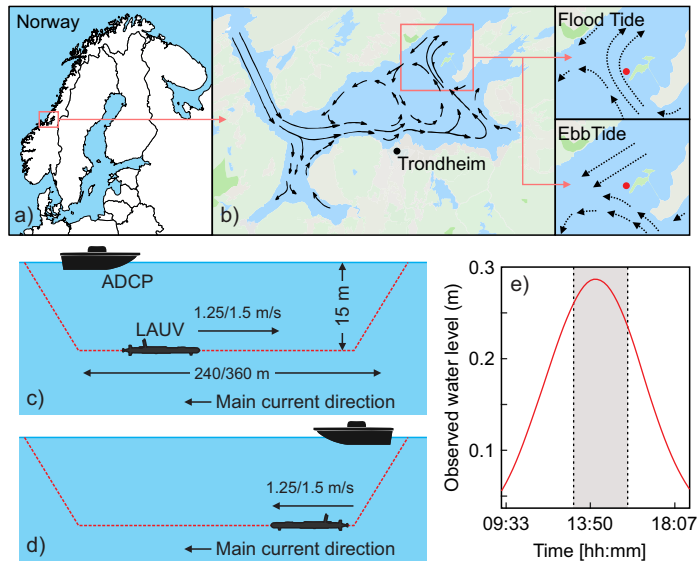


Figure 14 – **Test site and experimental setup [publication V]**. a) and b) Indication of the test site near the Island of Tautra in the Trondheim Fjord, Norway. The right site of b) shows the exact location of the experiments as a red dot. Tidal currents patterns for the upper fluid layer are shown as black arrows (reproduced from [98]). c) and d) Experimental setup to test the capability of the DPSSv2 for 2D velocity estimation in the presence of ambient flows. The main direction was assumed to be as shown in b) and the LAUV was operated alternately driven in-line and against this predicted tidal current main direction. A surface vehicle with an ADCP was employed to provide an additional resource for water flow estimation. e) Tidal cycle for the day of the experiments (2019/05/20). The gray area in the tidal graph represents the time slot of the experiments.

filter or other applicable signal processing techniques can compensate for a slightly decreased signal to noise ratio. The reported accuracy is with 0.01 m/s equal to the reported accuracy for the original DPSS, which is a very positive result.

2.4.2 Experimental setup for field tests

To test the DPSS under significant environmental forcing, a test site with strong enough but still relatively controlled water currents was required. A suitable test site was found in the Trondheim Fjord, close to the island of Tautra, Norway (see Figure 14.a and b). The fjord experiences a semi-diurnal tide, leading to noticeable tidal currents which reverse their direction between ebb and flood tide conditions three times a day [98]. The experiments were conducted during one day before and after the maximum tide was reached as shown in Fig. 14.e. Therefore, the tidal current estimates were expected to reflect a change in flow direction between flood and ebb flow.

As shown in Figure 15, the DPSSv2 was mounted on a light AUV (LAUV) [15], which was equipped with an IMU, and a DVL providing DVL-WL and DVL-BL estimates simultaneously. Additionally, an ADCP mounted on a surface vehicle was used to acquire global water current measurements for comparison. To predict the tidal currents the DVL-BL estimates were combined with the DPSSv2 estimates or with the DVL-WL estimates respectively. In total 14 trials were conducted at a constant target depth. The robot was following a straight line path with half of the trials running at the minimum sustainable velocity for the vehicle (around 1.25 m/s) and the other half of the trials running with the target velocity of 1.5 m/s.



Figure 15 – LAUV Fridtjof with attached DPSSv2 [publication V]. The AUV used DVL, GPS and INS for navigation and the DPSSv2 was sampling independently.

Aside from different velocities, half of the trials were conducted in opposite direction of what was predicted to be the main tidal current direction as shown in Figure 14.c and half of the trials were running along the assumed main direction of the tidal currents, see Figure 14.d.

The tidal currents were calculated by subtracting the DPSSv2 and DVL-WL velocity estimates from the velocity estimates of the DVL-BL. The resulting planar water current velocity vector was then rotated into a global reference frame based the attitude and heading reference system of the LAUV.

2.4.3 Results and discussion

Figure 16 presents the tidal current estimates in the form of median (IQR) magnitude of the current velocity and the heading of the tidal current relative to True North. Considering Figure 16.a, in most cases the ADCP provides estimates for the tidal current velocities that are larger and have a higher variance than the DPSSv2 and DVL-WL estimates. Both higher median magnitude and variability led to the exclusion of the ADCP data in the further analysis. The ADCP employed on a surface vehicle is usually used for the estimation of river flow velocities, where several transects across the river are made to determine a bulk flow velocity. However, in our application only instantaneous velocities could be recorded in conditions of higher waves and varying salinity. Those factors indicate that the ADCP was not operating in optimal conditions and could thus not provide the best tidal current estimates.

Figure 16.b and c depict the tidal current magnitude and orientation relative to True North as 2D vectors. Results for cases when the AUV moved against the tidal currents are shown in Figure 16.b, and Figure 16.c displays results for cases where the vehicle moves along the tidal currents. According to data provided by the Norwegian Meteorological Institute a reversal in flow direction shortly before high tide was to be expected and that reversal can be seen in the estimates of both sensors. Additionally, the DPSSv2 and DVL-WL estimates have relatively good agreement for trials against the predicted tidal current, but significant differences in trials that were running along the predicted tidal current. The greater difference for the later scenario is to be expected, as the potential flow assumption that is required for the derivation of (30) breaks down if there is a flow component that is moving in the same direction than the DPSSv2.

This inherent limitation of the current DPSSv2 design could be resolved in various ways. One could design trajectories or paths, which guarantee changes in the direction of move-

ment such as lawn mower paths. Some works have shown that a few changes in heading can make water relative velocities and water currents observable [99, 100]. Furthermore, a combination with almost all of the solutions provided at the beginning of section 2.4 like observers, GPS fixes or ocean models could improve the performance. Current limitations notwithstanding, the analysis of the summary statistics (provided in detail in publication V) suggests that for the more favourable conditions when the LAUV was moving against the tidal flow, the tidal current estimation based on DPSSv2 measurements was close to the DVL-WL measurements with a median absolute (IQR) difference in magnitude of 0.03 m/s and in heading of 8.13° (11.0°). Specifically for the tidal current magnitude are those differences close to the accuracy bound of the DPSS in field conditions [publication II] and at the same scale as estimation errors reported by other approaches [91, 101].

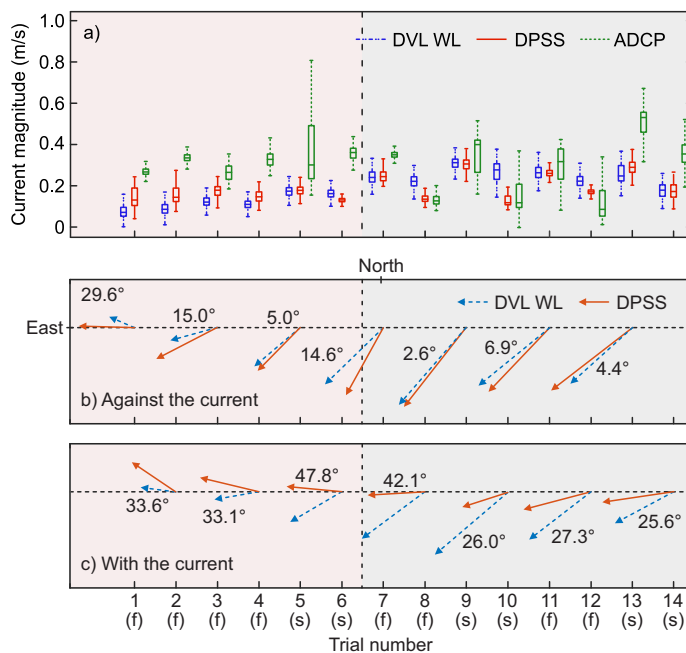


Figure 16 – Estimation of tidal current velocity vector for DVL, DPSSv2 and ADCP [publication V]. Tidal current estimates for the DVL and DPSSv2 are both augmented by DVL-BL readings. a) Magnitude estimates of the tidal current in the global reference frame represented by median, IQR and extreme values for each trial. b) and c) Median magnitude and heading estimates of the tidal current relative to true north for DVL and DPSSv2 (ADCP estimates are not used in the performance comparison and thus omitted to improve the readability of the figure). The difference between the two median heading estimates in degrees is annotated for each trial. Instances where the LAUV was moving with the tidal currents, shown in c), are distinguished from instances where the LAUV was moving against the tidal currents, shown in d). The trial numbers are further augmented with either (s) for trials with the slower target velocity of 1.25 m/s or (f) for the faster target velocity of 1.5 m/s. The light beige patch (trials 1–6) represents slack water conditions close to high tide, where the currents are less strong, more turbulent and change direction eventually. The light grey patch (trials 7 to 14) shows the tidal conditions for ebb flow, which occurs after the maximum tidal water level has been reached.

2.5 Summary and conclusions

This chapter introduced the problem of pressure based velocity estimation for AUVs. A potential flow model is given that generalizes an empirical model defined in an earlier work [38]. Additionally, a new prototype, the DPSS, was presented to test the efficacy of the proposed approach for speedometry under field conditions. Compared to previous work [38], this new prototype had added capabilities, which were tailored to its application on mobile platforms. The efficacy of the proposed approach was tested through laboratory tests and most importantly, through the integration of the DPSS into a commercial AUV and rigorous testing in various scenarios in the field. The obtained test results confirmed that, under the constraint of near constant depth, the derived first principle relations hold under dynamic field conditions and that speedometry based on differential pressure can provide information of equivalent quality compared to state of the art sensors.

In a subsequent iterative procedure, a next generation prototype, the DPSSv2 was designed with equivalent capabilities to the DPSS but a significantly smaller size and weight. Additionally, theoretical relations were expanded to enable 2D velocimetry in the horizontal plane instead of 1D speedometry. The new design and relations were tested under laboratory and field conditions. A special focus was placed on the performance of the DPSSv2 in the presence of ambient flow fields, which had been absent for previous field tests with the DPSS. Furthermore, the capabilities of the DPSSv2, in conjunction with additional sensing modalities, for estimating those flow fields were tested. For test scenarios where the potential flow assumption was fully valid, results showed again, that under the constraint of near constant depth the DPSSv2 could provide 2D velocimetry of equivalent quality compared state of the art sensors. Additionally, it could be shown that tidal currents could be observed by the DPSSv2 when used together with complementary sensor technologies.

In regards to the research question that was posed at the beginning of the chapter: *"How can state estimation for small low-cost AUVs be improved and made more robust for the application under field conditions?"*, the work presented in this chapter shows that differential pressure can be used to provide robust estimates of vehicle velocity. Additionally, there is a large range of possible extensions for the sensor system to enable the estimation of more complex environmental features such as mixing zones (presently work in progress), hydrodynamic imprints of other vehicles [102] or animals and hydrodynamic forces [77].

Additionally, its small size and low energy consumption make the DPSSv2 a valid candidate to make direct estimates of velocity more broadly available for low-cost and / or small AUVs. Additionally, the DPSS prototypes could be established as complementary sensing modalities for higher grade vehicles to add redundancy or for vehicles with very strict energy efficiency requirements during long term missions. Results in both field tests showed that for certain scenarios the DPSS estimates can outperform state of the art velocity sensors and a fusion of the information of both sensor system would provide better state estimation capabilities.

However, the field experiments with the DPSS and DPSSv2 also clearly indicated limitations and problems that still need to be solved and provide guidance for future research. One of the main limitations for the DPSS prototypes is the occurrence of a seemingly depth dependent offset on the pressure measurements. This could be caused either by a change of volume in the air boundary in the pressure tubing or by overpressure on the sensors themselves where the total pressure on the full sensor is out of the linear range for the devices. Both hypotheses are currently investigated but both problems would essentially require basic engineering solutions. Another limitation that was expected but

also became apparent during tests with the DPSSv2, is the dependence on the sensor on conditions that approximate potential flow. An extension of the theoretical framework in which the pressure-velocity relations were derived could alleviate this problem. Another option is the addition of either more sensing modalities or mathematical constructs such as ocean current observers in conjunction with coarse ocean models to provide an estimate of local ambient flow that can be used to compensate for some adverse effects on the DPSS measurements. Such a combination could also have the potential to lead to estimates for vehicle velocity over ground which would enable the DPSS to provide a full navigation solution. Another limitation that is subject to future work is the restriction of measurements in two dimensions. By adding two more sensors on the vertical axis of the DPSSv2 sensor head, the system is enabled to estimate flow in all three dimensions including a 3D angle of attack. Numerous similar solutions already exist in the field of airflow measurements [103, 104, 105].

In addition to a good and robust state estimation for salient world models, a mobile robot needs a sophisticated control framework to achieve increased autonomy. The two following chapters in this thesis describe contributions to control related problems on two different levels of abstraction. Chapter 3 describes contributions to problems of control directly affecting the actuator layer, while chapter 4 introduces a novel trajectory tracking controller operating on the layer of robot motion control.

3 Actuator control for autonomous bio-inspired underwater locomotion

This chapter addresses the second research question:

"Can asymmetric actuation increase maneuverability of AUVs using compliant bio-inspired actuators?"

The chapter starts by contextualizing actuator control in the bigger framework of control for autonomous robots. Afterwards an overview about compliant actuators for underwater locomotion is given and then the idea of asymmetric action is introduced and investigated using the example of attitude control for a fish-like robot with a motor-driven compliant tail. The research presented in this chapter has been published in **publication III**.

The knowledge base for controlling general robotic systems is vast and growing for decades. A lot of early development was dedicated to static robotic manipulators for industrial manufacturing, with a focus on high speed and accuracy for repetitive movements. Beginning in the 1990s control problems for autonomous mobile robots came into sharper focus, as this class of robots does not share the inherent location restraints of static manipulators. Mobile robots therefore, are more versatile and flexible.

However, unsupervised mobility comes with its own challenges, specifically in highly dynamic environments. The first challenge is locomotion itself. How can a mobile robot affect its environment to trigger reactions that cause movement in a desired manner? The choice of specific actuators, the hardware components that enable locomotion, and their control is thus the first fundamental problem that needs to be solved. However, the capability to change locations in a controlled manner is not enough for an unsupervised mobile robot to achieve autonomy.

Additionally, the mobile robot needs to estimate its configuration (pose, velocity and acceleration in most cases) in relation to the environment through state estimation. Based on the estimated present configuration, an autonomous mobile robot is required to decide which actions its actuators need to conduct to move towards a desired configuration that satisfies a higher level goal.

This high level goal can be either provided by an additional abstraction layer of the robot autonomy framework or by an external user. It becomes obvious that problems and solutions to autonomous mobility are layered and dependent on each other. Therefore, also control problems in mobile robotics are layered and interdependent.

At least two control layers can be identified. The first layer constitutes the movement of the robot as a whole. Motion demands are generated to minimize the error between a desired configuration of the robot and the robot's present configuration. The desired configuration is designed to achieve a higher level goal that is either given as an input by a user or comes from an even higher abstraction layer in the autonomy framework of the mobile robot. This robot control layer depends on an accurate estimation of the robot's configuration, which connects the robot control layer to the sensing and state estimation utilities of the robot. The second, lower, control layer constitutes the actuator control, which is necessary to achieve the effects that satisfy the demands of the robot control layer.

In the field of marine robotics most of the research on control architectures is concerned with the robot control layer. Reliable and robust control of underwater vehicles is still an open problem due to complex interactions of the robots with their environment. This is specifically true for small resource constraint and unconventional AUVs. On

the actuator control layer instead, well developed standard control structures are used in conjunction with standard actuators and propulsors. However, bio-inspired underwater vehicles rely on non-standard actuators and propulsors that have unique advantages, but do also present challenges regarding the actuator control. To increase the autonomous capabilities of agile, small and low-cost AUVs, improvements in both control layers are still necessary, which is reflected in the contributions of the research presented in this thesis.

The contribution on the actuator control layer is focused on improvements for bio-inspired compliant actuators. The contribution on the robot control layer is more broadly defined and applicable to a much more general class of AUVs, namely agile underactuated vehicles. However, the development and application of the control framework will be on an AUV with bio-inspired locomotion.

Thus, the presentation of theoretical frameworks, prototypes, experiments and results in the following two chapters will be two-part, with the first part presenting contributions to the actuator control layer and the second part presenting contributions to the robot control layer for small bio-inspired underwater robots.

3.1 Underwater locomotion with compliant actuators

Locomotion for underwater vehicles is classically facilitated by a set of propellers. Depending on the number and arrangement of those propellers an underwater vehicle can move holonomically in all degrees of freedom and is additionally capable of hovering, or a vehicle's active motion space is limited to reduced number of degrees of freedom due to underactuation and nonholonomic motion constraints. While at first glance it seems sensible to equip a vehicle with sufficiently many actuators to enable holonomic motion, in practice it is often more prudent to reduce the number of actuators in favor of vehicle cost, energy efficiency, payload capacity or a reduced mechanical complexity of the vehicle. One of the most prominent configurations for AUVs is a torpedo shaped body with one or two propellers at the aft combined with several control surfaces [106, 107, 108]. Occasionally a vertical thruster is added [81].

Propellers as the actuators of choice for underwater vehicles have been in use in the maritime industry for centuries, they have reached a state of high optimization and sophistication. However, in recent years more focus has been centered around bio-inspired actuation for underwater locomotion. Aquatic animals, honed by millions of years of evolution are very well adapted to movement in their habitat. Fish, for instance, have been shown to exhibit superior maneuverability and efficiency compared to engineered systems [109]. In addition, bio inspired locomotion promises actuation that should create less turbulence, which enables minimally invasive observations of marine life or archaeological sites. This has led to the development of an increasing number of aquatic robots with bio-inspired locomotion including fish-like robots [110, 111, 112, 113, 114, 115] and robots relying on a multitude of flippers [116, 117, 118, 119, 120, 121, 122, 123]. Reflecting the wide range of aquatic niches, each requiring a specific locomotion profile, a wide variety of propulsion mechanisms have been studied and developed. Excluding inspirations from the locomotion amphibious animals, which exhibit trade-offs in swimming performance for land or air locomotion, most aquatic locomotion solutions have been based on propulsion with one or several hydrofoil-like appendages called fins.

The subsequent presentation of locomotion types is further restricted to fish, as locomotion principles based on several independently appendages will be discussed later in chapter 4. Depending on the location of the fins that are used for propulsion, several locomotion types can be distinguished. Fish that are mainly using their body or caudal fin to produce thrust are defined as BCF swimmers, while fish that are using their median or

paired fins to propel themselves are known as MPF swimmers. Both groups are further distinguished into subgroups based on the actual fin type that is used [124]. Another grouping for both BCF and MPF swimmers is their association with undulatory or oscillatory swimming. In undulatory swimming a significant part of the body is involved in the generation of wave traveling from head to tail which propels the fish forward, while in oscillatory swimming the periodic movement of the respective appendage(s) creates the thrust. For robotic applications, that go beyond the study of the biomechanics or fluid dynamics of the actual animal, inspiration from oscillatory locomotion types is usually preferable, because the thrust generation is fully restricted to the appendages and the main body can be completely used for the transport of the power electronics and additional payload. The BCF oscillatory locomotion type is arguably the most studied and implement propulsion type in the robotics community [110, 111, 112, 113, 114, 115, 125]. Based on their inspiring counterparts, the major expected benefit for this locomotion type was the efficient generation of thrust for fast cruising, while MPF swimmers are usually thought to excel at maneuverability and to be more efficient at low speeds.

Fish and other aquatic animals often rely on rhythmic motions of compliant bodies. To take inspiration from their locomotion, requires a fundamentally different engineering approach compared to ordinary marine technology. The advent of soft robotics has provided the necessary tools to facilitate the integration of novel propulsion and subsequently locomotion methods for underwater vehicles. There are two distinct approaches to emulate a soft actuation. The first approach uses multiple rigid components and actuators, potentially connected by softer or compliant parts, and a soft actuator like behavior emerges from the interaction of the rigid elements [126, 114, 127, 128]. This approach provides a high degree of controllability over the actuator and relative ease of mathematical modeling at the expense of an increased mechanical complexity. The second approach is based on soft, often elastomeric materials that mimic the properties of the soft biological counterpart, while actuation can be realized mechanically, hydraulically or pneumatically [129, 130, 125]. The material properties of the elastomeric material can be designed to passively assist the realization of the desired actuator kinematics, and potentially dynamics, without the need for an increased active actuation effort. This comes at the expense of a higher control complexity. However, a truly soft actuator has the additional benefit that it is much safer to interact with, which is specifically important for applications that require minimal invasive observation or missions where the robot is supposed to collaborate with a diver.

Based on the state-of-the-art for bio-inspired underwater propulsors, it can be stated that the goal of more efficient and maneuverable locomotion has not been achieved yet and will be a task with a large future horizon. However, the other benefits of specifically soft bio-inspired actuators such as minimal invasive monitoring and safe interaction can be leveraged upon more readily and are therefore the main motivation in this thesis to investigate the actuator control of bio-inspired underwater locomotion.

3.2 Asymmetric actuation for yaw control

A new control approach that leverages the unique features of compliant propulsors, but also tackles new constraints imposed by such actuators, is tested on a fish like robot that was developed in the European project Fish Locomotion and Sensing (FILOSE). The robot can be seen in *Figure 17* and was designed to demonstrate solution driven bio-inspired design for flow sensitive sensor systems and compliant propulsors [131]. State estimation is achieved in part by flow sensing and in part by inertial measurements. The improvements in state estimation based on differential pressure shown in 2 could be transferred and ex-

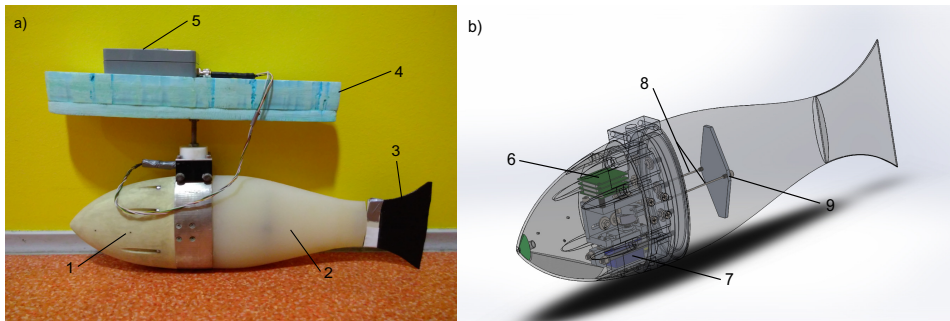


Figure 17 – Specifics of the FILOSE robot [publication III]. a) Side view: 1 - rigid head of the robot; 2 - compliant silicon tail; 3 - rigid fin; 4 - Styrofoam float; 5 - splash proof box containing battery pack and Bluetooth module. b) CAD drawing of electronics and actuation mechanism: 6 - microcontroller and orientation sensor; 7 - servomotor; 8 - steel cables; 9 - actuation plate

tended to the artificial lateral line that the FILOSE robot has so far used. However, the focus of this chapter is on control and to test the new control approach only attitude estimation was necessary, which can be achieved by inertial measurements using a standard IMU.

The FILOSE robot consist of a rigid head connected to a compliant silicon tail with a rigid fin. Tail and fin were designed to emulate the morphology and compliance of a rainbow trout (*Oncorhynchus mykiss*) [132]. The tail is actuated by a single motor, located in the rigid head, that is connected to the tail via cables attached to an embedded plate. Additionally, the rigid head contains all on-board electronics, including a microcontroller and an IMU for orientation feedback. Additionally, the robot is connected to a float which carries a battery pack and a Bluetooth module for wireless communication. *Figure 17.a* shows the robot with the attached float, while *Figure 17.b* describes the internal structure of the robot.

The FILOSE robot has been mostly used to develop and test flow relative control strategies [133, 134, 75] utilizing an artificial lateral line, based on absolute pressure sensors, to augment state estimation. Linear motion of the robot is facilitated by a sinusoidal excitation of the compliant tail with a static frequency and a variable amplitude. The robot is enabled to turn, by adding an offset to the sinusoidal excitation. The offset causes the centre of oscillation of the compliant tail to be out of line with the centre line of the robot, which creates a turning moment. This strategy has been proven to be effective in conditions where external flow is present, but seems to be ineffective in calm environmental conditions. However, orientation control is crucial for the autonomy of the robot and should be effective independent of the environmental conditions. To overcome this problem new control strategies are necessary.

The main focus of both, biologists and roboticists, has been on rapid turning maneuvers for fish or fish-like robots that utilize large tail bending angles [135, 126, 136, 137, 138, 115]. However, for fish-like robots with simple and robust actuation mechanisms optimized for cruising such a solution is not feasible. Additionally, steady turns that could play an important role during inspection and observation tasks have been given little attention so far. Hu et al. [139] and Tan et al. [140] present results for steady turns where an offset to the tail beat is added, which is identical to the strategy employed for the FILOSE robot when external flow is present. However, the mechanical structure of the robot used in [140] allows for much larger tail beat offsets compared to the FILOSE robot. Since the off-

set approach does not seem to be fruitful for the actuation setup of the FILOSE robot, a different solution was necessary. The necessity for a turning moment around the robots centre mass makes the problem of attitude control for the FILOSE robot a good example to test the new control approach based on *asymmetric actuation*, which should provide such a turning moment.

Utilization of asymmetry for underwater locomotion has been shown in rowing-like motions of appendages. The asymmetry is produced by a fast power stroke and a slow recovery stroke of the appendages, that is used for thrust production [141]. Those rowing motions have been mimicked by robotic prototypes either focusing on fins following a specific kinematic profile [142, 143], or by adapting the morphology of moving appendages as shown in [144] and [145]. However, in all cases the purpose of the *asymmetric actuation* was the generation of drag-based thrust in a low Reynolds number regime.

More complex *asymmetric actuation* patterns have been shown in [146] and [147], again with a focus on thrust generation. A different type of asymmetry related to underwater locomotion can be observed in the caudal fins of fish as shown in [148]. Here either the basic morphology of the caudal fins is already asymmetric or a symmetric caudal fin is differentially actuated to create asymmetries during motion. The latter has been investigated using an artificial caudal fin actuated by independent fin rays [149]. Similar to previously cited works, the main focus was on in-plane thrust generation, however results presented in both [148] and [149] indicate to the existence of out of plane forces that are modulated by the asymmetries of the caudal fin. The generation of an out of plane force is also utilized by the work presented here. However, the asymmetric motion is generated by a compliant tail of a robotic fish using only one actuator instead of a caudal fin equipped with many actuators. Additionally, the application of *asymmetric actuation* in the presented work aims for the extension of maneuverability of an underwater robot, as opposed to the focus on increased thrust production shown in the previously cited works. A novel skewed waveform is defined and implemented as actuator input, which produces asymmetric tail motions that in turn create significant torques that the FILOSE robot can use in turning manoeuvres. The following sections describe the control framework that is built to drive the *asymmetric actuation*, show results from field trails to validate the proposed framework. The results are subsequently analysed and discussed and the chapter ends with a summar and conclusion of the research on actuation control presented in the thesis.

3.2.1 Control framework

In it's basic form the motor actuates the compliant tail based on a sinusoidal input φ of the following form:

$$\varphi(t, f, A, \varphi_0) = A * \sin(2\pi ft) + \varphi_0, \quad (37)$$

where A is the amplitude of the motor's oscillation, f is the oscillation frequency, t is time and φ_0 is the oscillation offset.

To implement a novel *asymmetric actuation* framework the sinusoidal input is replaced by an asymmetric periodic waveform defined as a piecewise continuous function $\varphi(t, f, A, sk)$ with a skew parameter $sk \in \mathbb{R}$, $0.1 \leq \tau \leq 0.9$:

$$\varphi(t, f, A, sk) = \begin{cases} 0 & t = 0 \\ \frac{2Af\Phi(t)}{sk} & 0 \leq \Phi(t) < \frac{sk}{2}T \\ \frac{A(1-2f\Phi(t))}{1-sk} & \frac{sk}{2}T \leq \Phi(t) < (1 - \frac{sk}{2})T \\ \frac{A(2f\Phi(t)-2)}{sk} & (1 - \frac{sk}{2})T \leq \Phi(t) \leq T, \end{cases} \quad (38)$$

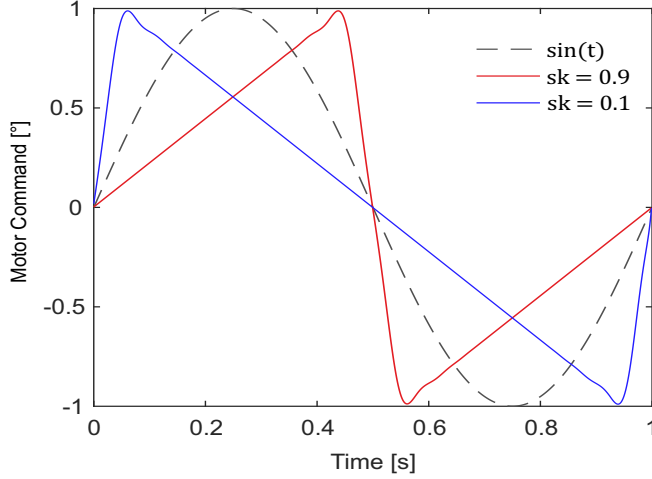


Figure 18 – **Asymmetric Periodic Waveform [publication III]**. All functions are normalized and have a wave period $T = 1$ s. The skewed triangle waves are represented by the limit cases $sk = 0.9$ and $sk = 0.1$, all other waveforms lie between these two cases. The standard sine wave commonly used for actuation is shown as reference

where $T = f^{-1}$ is the wave period of the function and we define $\Phi(t) = t \bmod T$ as modulo operator for time. For a sk of 0.5 a triangle wave is generated without skew, which should induce no turning action. The upper and lower limits of sk also define the limits of the corresponding turning rate and the resulting waveform of the two limit cases is shown in Figure 18. Two 8-th order Savitzky-Golay filters are used to smoothen the output signal.

Now a feedback control law can be designed for the skew factor based on an empirically validated relation between skew factor sk and torque N in the following form:

$$sk = 0.5 + \alpha N, \quad (39)$$

where α is an experimentally determined constant. The control law is based on the nonlinear proportional-derivative control strategy as described in [150]. However, it is assumed that the hydrodynamic damping of the water will act similar to a derivative control term, so that the resulting control law is in the form of a proportional controller. Inspired by [151] a control law for N can then be designed as:

$$N = -\frac{1}{\alpha} \frac{\sin(a\hat{\psi})}{\sqrt{2(1 + \cos(a\hat{\psi}))}}, \quad (40)$$

where $\hat{\psi} = \psi - \psi_d$ is the orientation error comprised of the measured yaw angle ψ_m and the desired yaw angle ψ_d . Additionally, a is a factor that determines the *tightness* of the error. The effect of that tightness factor on the skew factor can be seen in Figure 19. A full derivation of this control law and a stability analysis can be found in [3].

Finally substituting (40) in (39) the final feedback control law for sk , taking into account saturation effects $(sk_{max}, sk_{min}) = (0.9, 0.1)$, can be synthesized as:

$$sk = \begin{cases} 0.4 * \text{sign}(\hat{\psi}) + 0.5 & |a\hat{\psi}| \geq \pi/4 \\ 0.5 - \frac{\sin(a\hat{\psi})}{\sqrt{2(1 + \cos(a\hat{\psi}))}} & |a\hat{\psi}| < \pi/4. \end{cases} \quad (41)$$

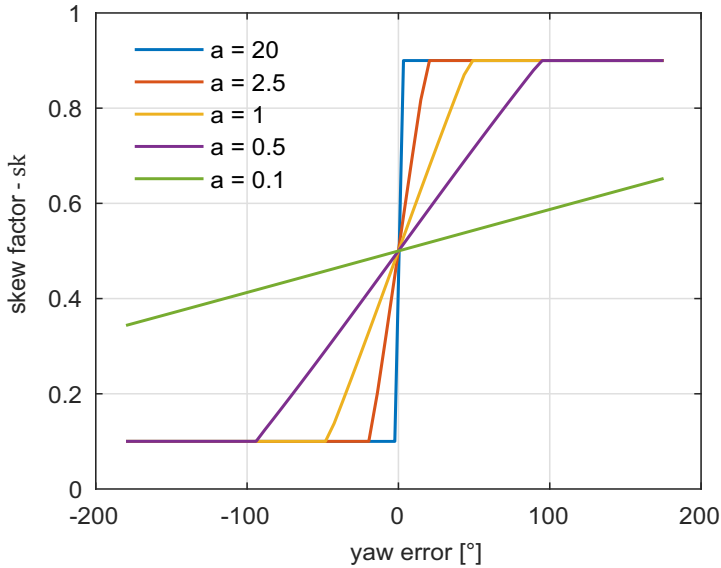


Figure 19 – **Skew factor τ vs. heading error [publication III]**. The choice of the tightness factor a determines the error bandwidth for which the derived controller operates between the two maximum skew factors of 0.9 and 0.1. A bigger tightness factor leads to an increased tracking rate, but also to a higher risk of overshoot. For very high tightness factors the controller approximates a bang bang control.

Note that the above nonlinear proportional control law differs from the standard one considered in [151], in order to avoid sluggish tracking when $a\hat{\psi}$ is close to $\pm\pi$. Increasing the tightness factor a increases the tracking rate (Fig. 19), at the cost of an overshoot after reaching the desired orientation. Figure 20 shows the complete orientation control scheme, which highlights that the yaw angle is measured by the IMU of the robot and that amplitude A and frequency f for the waveform generation are defined by a higher level layer that can either be a user or a higher level control layer.

3.2.2 Experimental setup

After initial tests in a small laboratory tank, the effectiveness of the proposed control scheme was evaluated under field conditions in a lake. The initial orientation of the robot was set 110° away from the desired yaw angle and trials were conducted for different

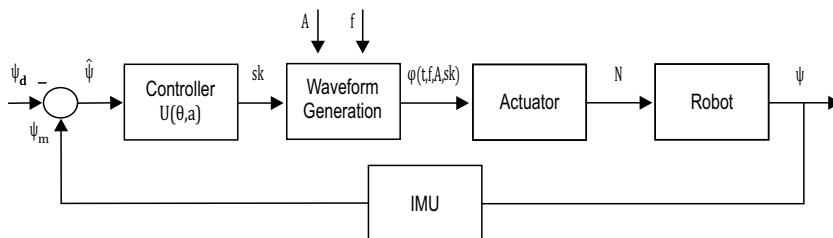


Figure 20 – **The proposed control scheme [publication III]**: The shown parameters are: ψ - yaw, ψ_m - measured yaw, ψ_d - desired yaw, $\hat{\psi}$ - heading error ($\psi_m - \psi_d$), sk - skew factor, $\varphi(*)$ - motor input, N - body torque, A - actuation amplitude and f - actuation frequency

tightness parameters a . The trials were stopped when the orientation error had settled within the 2% bound or the robot ran out of space for movement. The frequency of the tail actuation was held constant at 2 Hz and the actuation amplitude was set to $A = 30^\circ$. This experimental setup allowed to study the effectiveness of the controller and to determine its step response for different tightness factors. Standard metrics such as rise time (10%), overshoot and settling time (2%) were used to quantify the controller performance in contrast to the turning performance of the robot with a sinusoidal actuation of the form described in equation (37) and a maximum attainable phase offset φ_0 of 10°

3.2.3 Results and discussion

The results for the offset based turning and the novel *asymmetric actuation* based turning for tightness factors $a = 20, 5, 0.1$ is shown in *Figure 21*. A distinct oscillation is superimposed on the general trend of the yaw signal in all trials. This oscillation is caused by the recoil of the anterior part of the robot due to the tail motion. The yaw is subsequently time averaged (blue lines in *Figure 21.a-d*) over one tail beat cycle to smooth the output signal.

The default orientation control, based on an offset to the center of oscillation, fails to approach the desired yaw setpoint in a reasonable amount of time (*Figure 21.a*) and the trial had to be aborted. This result strengthens the claim that the offset based orientation control is not effective for the FILOSE robot in the absence of external flow. In contrast to that, with the proposed control scheme, the robot could reach the setpoint in all tested configurations (*Figure 21.b-d*). However, the results clearly show that the controller performance depends on the tightness factor. For a tightness factor $a = 20$ the controller approaches a bang-bang control which is reflected in the overshoot seen in *Figure 21.b*.

With a smaller tightness factor the approach towards the setpoint was expected to be less steep, projecting less overshoot. *Figure 21.c* shows the yaw control for $a = 5$ and it can be seen that the approach to the setpoint is indeed smoother. However, this achieved at the expense of a larger settling time, because for $a = 5$ the skew factor and subsequently the turning rate are small when the heading is close to the setpoint.

A further decrease of the tightness factor causes the controller to deviate earlier from the maximum skew which results in a slower turning motion. *Figure 21.d* shows an extreme case for a skew factor of 0.1. Here the bandwidth for the *asymmetric actuation* is significantly narrowed with an admissible range for the skew factor between 0.6 and 0.5. This causes slows down the turning motion significantly, which is reflected by a much higher rise time and the absence of any stabilization of the yaw around the setpoint. Furthermore, the controller was more susceptible to disturbances because the heading error increases again after 24 s, possibly due to local currents in the pond or wind induced disturbances acting on the float. However, the robot was able to recover and continued to turn towards the setpoint. Environmental influences also seem to be reflected in the controller performances for larger gain factors (see *Figure 21.b* and *c*), because the turning rates are varying for constant skew factors. The results suggest that the controller is robust against such influences. Another limiting factor for the turning rate was the attachment of the FILOSE robot to a float. Its hydrofoil profile reduces drag in surge direction, but produces a large drag in lateral direction which opposes the turning motion. It can be thus expected that the control performance would be improved on a free swimming robot.

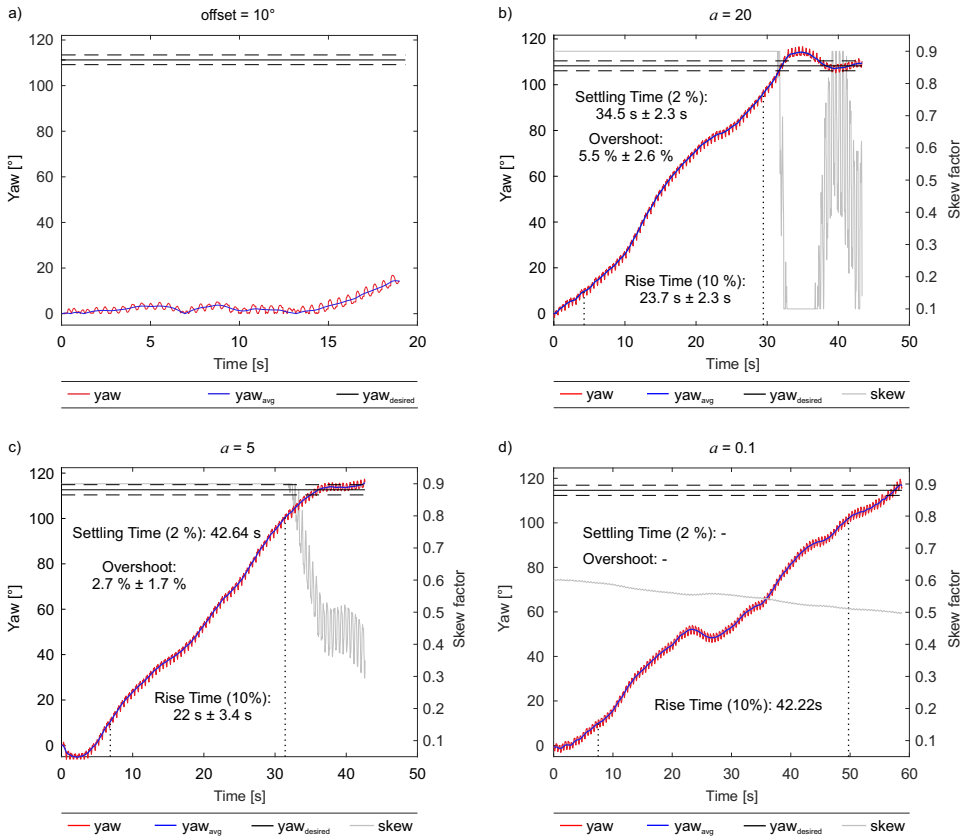


Figure 21 - Results of the field trials [publication III]. Shown are the time series of instantaneous (red) and averaged over one tail beat cycle (blue), yaw angle during field tests for different parameter settings. For figures b) - d) the time series of the skew factor (grey) is shown to visualize the control action. In a) the default orientation control with an oscillation offset of $\varphi_0 = 10^\circ$ was used. In b) - d) the novel orientation control was applied with tightness factors of $a = 20, 5, 0.1$ respectively. The controller performance is characterized by the rise time from 10% to 90% of the desired yaw, the overshoot in % of the desired yaw and the settling time where the actual yaw stays within a 2% error band of the desired yaw.

3.3 Summary and conclusions

This chapter introduced a novel nonlinear control framework for the orientation control of a fish-like robot with compliant tail. The control strategy is based on controlling an asymmetric waveform that is used as a reference input for the motor that actuates the tail of the robotic fish.

With the presented new control approach the FILOSE robot was enabled to conduct reliable and steady turns in conditions without flow. A comparison to the standard tail-beat offset based turning of such fish-like robots showed the efficacy of the proposed method. In the absence of flow, the standard approach does not produce enough torque to enable the robot to control its orientation, while the proposed method based on the *asymmetric actuation* successfully enables turning maneuvers. The tests with different tightness factors show that this parameter controls the aggressiveness of the controller when approaching a given setpoint. It seems that for a given environmental condition and for specific actuator properties an optimal tightness factor exists. A rigorous tuning procedure for the tightness factor and for the proportional gain of the controller have the potential to improve the performance further. Investigations into the complex fluid body interactions between compliant actuator and the surrounding fluid would provide useful insights for such an optimization procedure.

To refer back to the second research question of the thesis "*Can asymmetric actuation increase maneuverability of AUVs using compliant bio-inspired actuators?*", it can be concluded that the *asymmetric actuation* in combination with the nonlinear controller was indeed capable of improving the attitude control of the FILOSE robot.

One limitation of the asymmetric control approach, is the increasing speed at which the motor has to actuate the tail in the direction of the fast tail beat. The slope of the skewed triangular wave cannot be increased indefinitely due to physical constraints of the actuator. The achieved turning rate is significantly lower than for other orientation control frameworks shown in the literature [152, 26]. However, this difference is mainly caused by the different mechanical design of the actuator, specifically the difference in maximum tail bending angles. A significantly increased bending capability usually comes with increases in the mechanical and / or control complexity.

The experimental setup that was used to test the efficacy of the proposed control scheme presents another limitation of the research presented in this chapter. The predictive strength of the results shown above is limited by the damping effect of the float that is attached to the robot. The dynamics of a free swimming robot might be significantly different and turning should become easier. However, at the moment necessary equipment is carried by the float and a redesign of the mechatronic system for the fish robot would be necessary to get rid of the float. A possible compromise could be the use of a spherical geometry for the float that does experience equivalent drag in all directions of movement. Nevertheless, the effect of those changes would be impacting both tested actuation approaches in the same way and should not have an effect on their relative performance. Finally, orientation control by itself is not sufficient for mobile robots and a path following or trajectory tracking scheme should be layered on top of the existing orientation controller.

Although, the control method developed in this thesis was designed for fish-like robots that do not have the capability of large tail-bend angles, the control scheme is generic and can be applied to any fish-like robot using BCF locomotion mechanism. Beyond applications for fish-like robots the *asymmetric actuation* scheme can also provide additional versatility for the actuation of a broader class of AUVs propelled by bio-inspired appendages. The presented *asymmetric actuation* control can be best viewed as an additional tool to

leverage the unique capabilities of bio-inspired actuators and should be used in conjunction with other state of the art solutions.

Given improvements for state estimation and locomotion control the next chapter in this thesis presents contributions on the higher abstraction layer of motion control for a general class of underactuated AUVs. This class includes the two commercial AUVs used to test the DPSS prototypes in *Chapter 2* as well as the FILOSE robot introduced in this chapter.

4 Motion control for AUVs

This chapter addresses the third research question:

"How can model-based nonlinear controllers be augmented, to overcome limitations related to unreliable state feedback and motion constraints of AUVs with complex dynamics?"

The chapter first introduces the general problem of motion control for underwater vehicles and provides an overview of common control methodologies. A novel model-based control approach, which combines event-based control, a *differentially flat* dynamics model and disturbance estimation, is then presented. Validation and experimentation through simulation is discussed. While several core concepts of the novel control approach are published in **publication IV**, *chapter 4* also represents, at the time of this thesis, some unpublished work."

Motion control of AUVs can be classified into two key categories: dynamic positioning and path following. Dynamic positioning concerns the problem of stabilizing a vehicle at a given set point, which is essential for applications such as monitoring of underwater structures, underwater manipulation or object identification. In contrast, path following entails the goal to reach a set of given configurations potentially in multidimensional space. The capability for path following is relevant for survey operations and for traveling to, from or between mission sites / areas. An extension of path following is the problem of trajectory tracking where a time instance is assigned to every configuration of the path. The trajectory tracking control problem is particularly relevant for applications that require energy and / or time efficiency as well as for applications where obstacle avoidance and agility play a major role. The focus of the work presented in this chapter was on trajectory tracking control.

Another classification can be made based on the degrees of freedom (DOFs) in which a vehicle is actively moving. While surface vehicles are mostly restricted to 2D planar motion, AUVs, in general, move in 3D space and thus exhibit 6 DOFs with potentially significant coupling between DOFs, which increases the control complexity. However, depending on the respective vehicle and it's application various DOFs can be decoupled or neglected. Then, only a subset of motion directions are considered in the control problem, which reduces the complexity. The center of gravity and centre of buoyancy for most AUVs are configured so that the vehicle experiences a passive restoring force, which counters roll motions. Thus, the control of the roll DOF can be often neglected. A vast amount of work has been focused on motion restricted to some plane in 3D space, either horizontal motion only considering movements in surge, sway and yaw [153, 154, 155], or vertical motion only considering surge, heave and pitch DOFs [156]. For 3D motion those two planes can be combined to control motion in surge, sway, heave, pitch and yaw [157, 158].

An additional factor that increases control complexity is the underactuated nature of most standard AUVs. Due to resource, budget or efficiency constraints it is often not sensible to design AUVs that can be independently actuated for all DOFs that are relevant for a certain mission. The lack of actuation increases the control complexity, because the reachable configuration space of the vehicle is reduced and the actuation and control in the remaining degrees of freedom need to be utilized to compensate for the loss of control action in a specific direction. Further complicating factors for AUV control are the nonlinear dynamics, which significantly restrict common linear control approaches to distinct operating points.

The control performance of linear control approaches can be sufficient in applications in which vehicles are operating in a close neighbourhood of a linearizing point or for AUVs that are operating in stationary and deterministic environments. However, most environments that AUVs are deployed in violate these assumptions: they are dynamic, characterized by sharp nonlinearities or non-stationary processes, and may be non-deterministic.

Complex fluid body interactions are the main contributor to the nonlinear dynamics and can only be approximated in the vehicle dynamics model, making the accurate representation of AUV dynamics difficult. The nonlinear character of the AUV dynamics together with the difficulty to identify an accurate parametric model for those dynamics pose an interesting dichotomy from the control point of view. On the one hand the highly nonlinear and potentially coupled dynamics of AUVs suggest the use of nonlinear model based control approaches to either cancel out the nonlinear dynamics or to utilize the "useful" nonlinear parts of the dynamics. On the other hand, the inherent uncertainty in AUV modeling poses a significant challenge for nonlinear model based control and seems to favor robust model free control approaches that need to concede some of their control performance for robustness. The most favourable control architecture is therefore dependent on the respective underwater vehicle, the application and measures of implementation effort such as computational complexity and complexity of the tuning process for hyperparameters. In recent years machine learning approaches, specifically neural networks and reinforcement learning type architectures have found widespread interest and application in the mobile robotics community [159, 160, 161, 162]. However, machine learning approaches are highly dependent on access to datasets which are expensive or impossible to collect and which typically fail to generalize well to real-world scenarios. Thus, this thesis specifically focuses on non-learning based techniques.

The research presented throughout this thesis pays specific attention to the control of AUVs with bio-inspired actuation. For this chapter the focus will be especially on multi-fin underwater vehicles. While a variety of such vehicles exist [116, 117, 118, 119, 120, 121, 122, 123] their motion control has not been studied extensively. In most work only open loop or manual control is presented [116, 119, 163, 164, 165] with a specific focus on gait generation using central pattern generators [163, 165, 164]. Some studies have focused on 1 DOF motion control during surge motions. Geder et al. show a model-free control framework for either heading or depth control [122], while Siegenthaler et al. use model-free control of the angular rate to stabilize forward swimming [123]. Attitude control for different turning maneuvers is presented by Licht et al [120]. However, those control frameworks only were concerned with controlling single DOFs at a time, using simple model-free control frameworks. Additionally, control was mostly employed for set point regulation, while more advanced control tasks remained unstudied. An exception is the motion control of the Aqua AUV [118], which has been extensively studied in recent years. In [166] and [167] modeling and model-based control of the vehicle are presented, but again only for single DOFs at a time. Multi DOF control for attitude and heave, using model-free PID and PI control is presented by Giguere et al. [168]. Problems regarding the control range and coupling were avoided using gain scheduling, which resulted in adequate trajectory following. However, the gain scheduling technique necessitated the tuning of an array of 45 control parameters, resulting in extensive and complex development of the control framework.

Some research on control has also been published on the Underwater Curious Archaeology Turtle (U-CAT), which will be the main experimental platform (see *section 4.4*) to validate the research presented in this chapter. Chemori et al. [169] presented a depth controller for U-CAT comparing two model-free control approaches, RISE and PID. The

authors conclude that the RISE controller has a better tracking performance compared to the standard PID controller. In [170] Salumäe et al. show a control framework enabling the robot to move in several degrees of freedom (surge, yaw, heave) simultaneously, while only yaw and heave were actively controlled. The authors used a model-based approach, termed inverse dynamics (ID), which was utilizing feedback linearization with acceleration feedforward [35]. This ID controller was compared with the standard model-free PID controller in various scenarios that included disturbances. The results show that the ID controller outperforms the PID controller, specifically in the presence of disturbances.

The work presented in [169] and [170] showed the autonomous capabilities of U-CAT for motions in the vertical plane. However, surge and pitch were not actively controlled and surge was effectively decoupled from heave through DOF prioritization so that active trajectory tracking in the vertical plane was not shown. However, for fully autonomous and reactive exploration of confined spaces U-CAT should be able to effectively track trajectories in 3D space that are produced by navigation and obstacle avoidance nodes such as presented in [171]. General problems for the extension of tracking in more DOFs are reliable state estimation and the potentially underactuated nature of U-CAT specifically but also of many commonly used AUVs in general. This motivates the development of a model-based controller that extends trajectory tracking capabilities and addresses these issues specifically, but not exclusively for U-CAT.

In the following sections commonly used model-free control architectures for AUVs are briefly introduced, followed by the novel model-based control framework that represents the research contribution to answer the third research question. For all subsequently presented controllers we consider as underlying dynamics a control affine nonlinear Multiple-Input Multiple-Output (MIMO) system of the following classical form:

$$\begin{aligned}\dot{x} &= f(x,t) + g(x,t)\tau \\ y &= h(x,t),\end{aligned}\tag{42}$$

where x represents the system states, τ the control inputs, t time and y system outputs. $f(\cdot), g(\cdot), h(\cdot)$ are the nonlinear mappings for system states, control inputs and system outputs respectively. Additionally, the tracking error $\tilde{\eta}$ is defined as the difference between a desired reference configuration η_d and the actual robot configuration:

$$\tilde{\eta} = \eta - \eta_d.\tag{43}$$

4.1 Overview of traditional model-free motion controllers

For brevity only two model-free motion controllers, the PID controller and the RISE controller, will be presented. These controllers will subsequently be used as baselines to which the novel model-based control approach will be compared.

4.1.1 PID control

The most widely applied control architecture in engineering in general, but also in mobile robotics, is arguably the PID controller. The control law can be expressed as follows:

$$\tau = K_P \tilde{\eta} + K_I \int_0^t \tilde{\eta} dt + K_D \dot{\tilde{\eta}}.\tag{44}$$

K_P, K_I, K_D are positive definite matrices representing the feedback gains for the proportional, integral and derivative terms for the controller. The popularity of PID control is mostly attributed to its simplicity and ease of implementation.

4.1.2 RISE control

Much focus for model free controllers has been applied on increasing their robustness, i.e. their capability to handle uncertainties including exogenous disturbances and nonlinearities. A popular and widespread nonlinear robust approach is sliding mode control (SMC) [172]. The control design for SMC is a two part process, where the first part is concerned with the design of a specific surface in the state space, defined as sliding surface, onto which the system states need to be driven. During this design steps the sliding surface can be tailored to influence the dynamic behavior of the controlled system. In the second design step a control law is synthesized that ascertains that the system states remain in the neighborhood of the sliding surface. A problem of SMC control is that it is discontinuous, which makes it prone to chatter and it theoretically requires infinite bandwidth [173]. The problem of chatter can be addressed by the introduction of higher order state derivative inputs to the controller. However, higher order state derivatives like acceleration or jerk are generally hard to obtain or estimate in a reliable manner for constant feedback.

In contrast, robust integral of the sign of the error (RISE) control is structurally similar, but continuous and so does not suffer as much from the aforementioned problems [39]. To synthesise the RISE feedback controller we first define an auxiliary tracking error of the following form:

$$\tilde{\eta}_2 = \dot{\tilde{\eta}} + \alpha_1 \tilde{\eta}, \quad (45)$$

where $\tilde{\eta}$ is defined as in (43). Note that the preceding error synthesis is done for the special case of a second order MIMO system, to which the general AUV dynamics belong to. The subsequent feedback structure for a RISE controller then takes the following form:

$$\tau(t) = (k_s + 1)\tilde{\eta}_2(t) - (k_s + 1)\tilde{\eta}_2(t_0) + \int_{t_0}^t [(k_s + 1)\alpha_2 \tilde{\eta}_2(\sigma) + \beta \text{sgn}(\tilde{\eta}_2(\sigma))] d\sigma, \quad (46)$$

where $\alpha_1, \alpha_2, \beta, k_s \in \mathbb{R}$ are a positive constant control gains and $\text{sgn}(\cdot)$ is the standard signum function. Stability analysis and experimental results in the context of the control of AUVs is provided in [173]. With the two model-free baseline controllers being defined, the next section will provide the necessary mathematical background to understand the novel model-based motion controller that is introduced in this thesis.

4.2 Overview of model-based motion control

This section will give an overview about the standard AUV dynamics model that, in some form, almost always is used as the basis for any kind of model-based control algorithm for AUVs. Additionally, the property of *differential flatness* is introduced and the structure of a novel event-based controller for fully actuated vehicles, first presented in **publication IV**, is derived. This general controller will later be adapted for underactuated vehicles moving in the 2D horizontal plane, which constitutes the major contribution of the unpublished part of the work presented in this chapter (shown in *section 4.3.3*). This adaptation requires the use of disturbance observers to estimate motion in unmodeled DOFs. Therefore, the theory of disturbance observers is shortly introduced at the end of the current section.

4.2.1 AUV dynamics model for 6 DOF

The full 6 DOF rigid-body equations of motion for an AUV can be described by the following vectorial representation [40]:

$$\begin{aligned} M\dot{v} + C(v)v + D(v) + g(\eta) &= \tau \\ \dot{\eta} &= J(\eta)v, \end{aligned} \quad (47)$$

where the first equation describes the dynamics and the second equation the kinematics of the system. In both cases $\eta = [x, y, z, \varphi, \vartheta, \psi]^T$ is the pose vector of the robot in a Cartesian earth-fixed frame with orientation represented by the Euler-angles $[\varphi, \vartheta, \psi]^T$. Furthermore, $v = [u, v, w, p, q, r]^T$ represents the linear and angular velocities in body-fixed frame. $J(\eta) \in \mathbb{R}^{6 \times 6}$ maps the body-fixed frame to the earth fixed frame [40].

M is the inertial matrix of the vehicle, while C and D represent Coriolis-centripetal and damping effects respectively and $g(\eta)$ is the vector hydrostatic forces and moments. Finally, $\tau = [X, Y, Z, K, M, N]$ is the vector of control inputs. The matrices M and C can be further subdivided into:

$$\begin{aligned} M &= M_{RB} + M_A \\ C(v) &= C_{RB}(v) + C_A(v), \end{aligned} \quad (48)$$

where the subscript "RB" indicates that the parameters in the respective matrix describe rigid body effects. The subscript A instead indicates a matrix summarizing parameters describing the hydrodynamic effect of added mass [174]. By using the simplifying assumptions that the centre of gravity of the robot coincides with the origin of the body-fixed coordinate frame, that the robot is symmetric along all body axes and that the vehicle is moving at reasonably low speed [40] the inertia matrix M can be described by:

$$M = \begin{bmatrix} mI_{3 \times 3} & 0_{3 \times 3} \\ 0_{3 \times 3} & I_c \end{bmatrix} - \text{diag}\{X_{\dot{u}}, Y_{\dot{v}}, Z_{\dot{w}}, K_{\dot{p}}, M_{\dot{q}}, N_{\dot{r}}\}, \quad (49)$$

with m being the mass of the vehicle, I being the identity matrix and $I_c = \text{diag}\{I_{xx}, I_{yy}, I_{zz}\}$ describing the moments of inertia around the principle axis of the vehicle. The diagonal terms of the second element in (49) are added mass coefficients that are tied to the kinetic energy of the fluid that is moved aside by the motion of the vehicle [174].

With the same assumptions, the Coriolis-centripetal matrix C can be defined as:

$$C(v) = \begin{bmatrix} 0_{3 \times 3} & -mS(v_1) \\ -mS(v_1) & -S(I_c v_2) \end{bmatrix} + \begin{bmatrix} 0_{3 \times 3} & S([X_{\dot{u}}u, Y_{\dot{v}}v, Z_{\dot{w}}w]^T) \\ S([X_{\dot{u}}u, Y_{\dot{v}}v, Z_{\dot{w}}w]^T) & S([K_{\dot{p}}p, M_{\dot{q}}q, N_{\dot{r}}r]^T) \end{bmatrix}, \quad (50)$$

where $v_1 = [u, v, w]^T$, $v_2 = [p, q, r]^T$ and $S(\cdot)$ denotes the skew symmetric matrix of the following form:

$$S(\lambda) = \begin{bmatrix} 0 & -\lambda_3 & \lambda_2 \\ \lambda_3 & 0 & -\lambda_1 \\ -\lambda_2 & \lambda_1 & 0 \end{bmatrix}. \quad (51)$$

The damping matrix D can be approximated as a combination of linear and quadratic damping effects on the vehicle and takes the following form:

$$\begin{aligned} D(v) &= -\text{diag}\{X_u, Y_v, Z_w, K_p, M_q, N_r\} \\ &\quad - \text{diag}\{X_{|u|u}|u|, Y_{|v|v}|v|, Z_{|w|w}|w|, K_{|p|p}|p|, M_{|q|q}|q|, N_{|r|r}|r|\}. \end{aligned} \quad (52)$$

Finally, assuming the centre of buoyancy of the vehicle $r_b = [x_b, y_b, z_b]^T$ coincides with the centre of gravity along the x-axis and y-axis of the body coordinate frame, the vector of hydrostatic forces and moments $g(\eta)$ can be described by:

$$g(\eta) = \begin{bmatrix} (W - B) \sin(\theta) \\ -(W - B) \cos(\theta) \sin(\phi) \\ -(W - B) \cos(\theta) \cos(\phi) \\ -z_b B \cos(\theta) \sin(\phi) \\ -z_b B \sin(\theta) \\ 0 \end{bmatrix}. \quad (53)$$

A commonly used nonlinear control strategy for marine systems of the form (47) is called state feedback linearization. The basic idea behind state feedback linearization is to define a control input and a state transformation that transform the nonlinear system dynamics into a linear system [175]. An underlying assumption for the control with state feedback linearization is that the system is fully actuated or overactuated.

However, many AUVs are underactuated systems where some entries in the vector of control forces τ are zero. It has been shown that one can still linearize the actuated degrees of freedom by feedback of some form [176], which is called partial feedback linearization. However, the dynamics of the remaining degrees of freedom are not directly accessible and remain as nonlinear internal dynamics. For certain underactuated systems it was shown that the dynamics of the system without actuation can be also linearized [177].

If one wishes to employ control strategies for trajectory tracking feasible trajectories for the system to follow need to be found. This can be a non-trivial problem for complex dynamics system and is layered on top of the actual control problem that one might want to address with state feedback linearization. A different framework that is closely related to state feedback linearization makes use of a property of control systems that is called *differential flatness* [178, 37], which is introduced in the next section.

4.2.2 Differential flatness

Differential flatness is a property of control systems, which characterize the possibility of parameterizing all possible system trajectories by the so-called flat output. A system of form (42) is said to be *differentially flat* if there exists an output function $y \in \mathbb{R}^n$:

$$y = h(\eta, \tau, \dots, \tau^{(l)}) \quad l \geq 0, \quad (54)$$

called flat output, such that all states $\eta \in \mathbb{R}^n$ and inputs $\tau \in \mathbb{R}^m$ can be determined from these outputs without integration:

$$\eta = \varphi_\eta(y, \dots, y^{(k)}) \quad (55)$$

$$\tau = \varphi_\tau(y, \dots, y^{(k)}), \quad (56)$$

with analytic functions $\varphi_\eta, \varphi_\tau$ and $k \in \mathbb{N}$.

Flat outputs are not unique; in fact for a given flat system there are infinitely many. While finding flat outputs for an arbitrary systems can be non-trivial [179, 180], it has been shown that physically meaningful quantities, such as the pose of a robot, are valid flat outputs for robot control problems. The property of *differential flatness* is closely related to the possibility of state feedback linearization. In fact, any flat system can be feedback-linearized using dynamic feedback. Additionally, *differential flatness* has important implications for automated trajectory generation and tracking, because trajectories can be defined in the flat output space, where they are by definition consistent with the system's dynamics.

Thus, *differential flatness* is a very convenient framework for trajectory tracking, as it is very natural and straight forward to construct a feedforward controller for *differentially flat* systems. In fact, feedforward trajectories can be generated automatically, because any smooth trajectory with properly bounded derivatives in the flat output space can be followed by the respective system. In most cases a feedforward controller, constructed based on the flat system, is combined with other control constructs, like PID or pole placement to ensure stability or tracking [181, 182, 183]. Flatness based control strategies have

been successfully applied in the mobile robotics domain for terrestrial robots [184] and for drones [185]. For underwater robots the framework presented in [185] has been used, but only for attitude control [186].

As soon as a controller needs to be deployed in a real world scenario in dynamic environmental conditions, certain unmodeled external influences on the controlled system dynamics arise. Additionally, the first principle derivations for the dynamics models of physical systems are always based on simplifying assumptions and, sometimes, empirically determined parts, to make them conceptually and computationally tractable. This means that dynamics models are only able to predict the system behavior up to a certain level of accuracy. Disturbance observers can be used to compensate for unmodeled external and internal influences on the vehicle dynamics and are therefore introduced in the next section.

4.2.3 Disturbance observers

Both, unmodeled external influences and internal inaccuracies of the vehicle dynamics are usually combined into a lumped parameter, which is called disturbance. Disturbances are often unknown and not measurable and, therefore, cause difficulties in the control design. In the context of AUV control, irrotational ocean currents are often defined as the main external disturbance, but eddies and wave induced changes in the environment can be also encountered by an AUV. Inaccuracies of the hydrodynamic coefficients of the dynamics model (47) represent the biggest internal source of error for AUVs and are also often modeled as disturbance.

One solution to deal with both internal and external disturbances is the use of robust controllers, which are able to achieve a satisfactory performances even under the influence of disturbances. The integral component in a PID controller adds robustness toward disturbances to a limited degree. The RISE controller defined in 4.1.2 is part of a family of robust controllers together with SMC, H_∞ control or high-gain feedback control, that have all been shown to accomplish their goal under disturbances. However, those controllers trade part of their performance for their increased robustness.

Model based approaches generally have a better control performance compared to robust model free controllers. Yet, they are very reliant on an accurate dynamics model. This prerequisite is violated under conditions with significant disturbances. To fully leverage the control performance of model based controllers when disturbances are present, disturbance observers can be used. These structures are designed to estimate disturbances and, possibly, a certain number of their time derivatives. Those disturbance estimates can then be directly integrated into the chosen controller design to create a disturbance-observer-based control (DOBC). Running a disturbance observer in the inner loop of a DOBC does not degrade the control performance of the outer loop controller, so that no sacrifice is necessary for increased robustness [187]. This makes DOBC also attractive for robust control methods in applications where their base performance is not satisfactory.

Many types of disturbance observers have been proposed in the literature, however, the two main types of nonlinear observers that have received the most attention are basic nonlinear disturbance observers (BDO)[188, 189] and extended state observers (ESO) [190, 191, 192]. The efficacy of the proposed disturbance observers relies on various assumptions about the character of the disturbances to be estimated. In many cases disturbance dynamics are assumed to be known [188, 193, 190, 194], which is generally not the case in real world scenarios. Other approaches rely on the assumption that the first or a higher order time derivative of the disturbance is bounded [195, 191, 192]. For both assumptions, known disturbances or zero time derivatives, the resulting observer will im-

prove the overall performance of the DOBC, but does not necessarily provide the capability to reject the disturbance. However, a seemingly restrictive assumption that the first time derivative of the disturbance is zero might still provide a sufficiently performing DOBC if the disturbance is constant or slowly time varying [187]. Knowledge about the expected application conditions is thus of high importance for the controller design. The following section will describe a version of the BDO, introduced in [187], with less restrictive assumptions on the system dynamics and disturbance dynamics compared to BDOs presented in [195, 196, 197]. We first extend the description of our system to be controlled (42) with the notion of disturbance $w \in \mathbb{R}^p$:

$$\dot{x} = f(x, t) + g_1(x, t)\tau + g_2(x, t)w. \quad (57)$$

Based on the assumption of $w^{(k)} = 0$ we can define the observer as [187]:

$$\begin{aligned} \dot{z}_0 &= -L_0(x)[f(x) + g_1(x)\tau + g_2(x)(z_0 + p_0(x))] + z_1 + p_1(x) \\ \dot{z}_1 &= -L_1(x)[f(x) + g_1(x)\tau + g_2(x)(z_0 + p_0(x))] + z_2 + p_2(x) \\ &\vdots \\ \dot{z}_{k-2} &= -L_{k-2}(x)[f(x) + g_1(x)\tau + g_2(x)(z_0 + p_0(x))] + z_{k-1} + p_{k-1}(x) \\ \dot{z}_{k-1} &= -L_{k-1}(x)[f(x) + g_1(x)\tau + g_2(x)(z_0 + p_0(x))] \\ \hat{w} &= z_0 + p_0(x) \\ \hat{w}^{(1)} &= z_1 + p_1(x) \\ &\vdots \\ \hat{w}^{(k-1)} &= z_{k-1} + p_{k-1}(x), \end{aligned} \quad (58)$$

with $z_i(t) \in \mathbb{R}^p$, $i = 0, \dots, k-1$ being the observer state, $\hat{w}^{(i)}$ the estimation of $w^{(i)}$ and $p_i(x)$, $L_i(x)$ observer gains chosen to be satisfying:

$$L_i(x) = \frac{\partial p_i(x)}{\partial x}. \quad (59)$$

If we now assume that the k th time derivative of w is approximately zero, $w^{(k)} \approx 0$, and define the estimation error as $e_i := w^{(i)} - \hat{w}^{(i)}$, $i = 0, \dots, k-1$, one can write the error dynamics as:

$$\begin{aligned} \dot{e}_0 &= e_1 - L_0(x)g_2(x)e_0 \\ \dot{e}_1 &= e_2 - L_1(x)g_2(x)e_0 \\ &\vdots \\ \dot{e}_{k-2} &= e_{k-1} - L_{k-2}(x)g_2(x)e_0 \\ \dot{e}_{k-1} &= -L_{k-1}(x)g_2(x)e_0 \end{aligned} \quad (60)$$

To stabilize e_i , $i = 0, \dots, k-1$ to zero one can choose $L_i(x)$, $i = 0, \dots, k-1$, such that (60) is stable for all x . Subsequently, $p_i(x)$ can be calculated from (59).

Now that the theoretical foundations for relevant control related concepts have been introduced, the next section will describe the research contributions to the research question of this chapter. First a general *differentially flat* feedforward controller with event-based feedback (DFEC) is derived for fully actuated AUVs. This constitutes the research

contribution published in **publication IV**. Afterwards, the presented controller is augmented to apply it to underactuated AUVs moving in the 2D horizontal plane. To that end a state space representation of the AUV dynamics model is reduced and the previously described concept of DOBC is leveraged to compensate for that reduction and robustify the resulting controller.

4.3 The DFEC framework

For model based control as presented in section 4.2, an accurate feedback of higher order derivatives of the robot's pose, such as acceleration, is necessary. Those quantities are either very difficult or impossible to accurately measure or estimate for continuous feedback, which has been a general problem for many model based control strategies that are using state feedback. A possible solution to this problem can be the use of tools from event-based control [36], which can be used to reduce the number of instances that state feedback is required. With a reduced number of state feedback instances measurements can be processed and filtered without a real-time requirement which should improve the state estimation performance for higher order derivatives of the robot's state.

Event-based control [36] is a technique that only makes use of feedback if a chosen metric indicates that a correction of the feedforward control is necessary. In the case of a feedforward controller based on flat trajectories an event can be triggered by an increase of the difference between output trajectory and desired trajectory over some predefined threshold. The event based control framework consists of three main parts: an event generator, the controller and a control input generator. The event generator checks a predefined metric continuously and generates events if it registers a deviation of the metric from a predefined range. The controller defines the control input when an event occurs and the control input generator, usually defined as a zero-order hold, takes control input values received from the controller and generates a continuous time input for the system in question.

In a novel control framework described in **publication IV** that fuses flatness based feedforward control with event-based control, the flatness based feedforward controller acts as the controller and the control input generator in the event-based control framework. An event generator tracks the output of the feedforward controller and compares it with the desired output. If the difference reaches a predefined threshold an event is triggered and at the time instance of the event the feedforward controller parameters are recalculated based on measurements and estimates of the system outputs and their derivatives.

4.3.1 General DFEC derivation

For system (47) the flat outputs could be defined as the robot's pose η as well as, τ from (56) a tracking controller can be derived following [**publication IV**]. First, a trajectory $y_{mr}(t)$ is defined, which converges to a given reference trajectory $r_m(t)$ of y_m , $m = 1, 2, \dots, n$. Additionally, a discrete time constant t_{event} is defined that is equal to the last time instance that corresponds to an event. Let:

$$y_{mr}(t, t_{event}) = p_m(t - t_{event})e^{-K_m(t - t_{event})} + r_m(t), \quad (61)$$

where $K_m > 0$ is a constant parameter and $p_m(t - t_{event}) \in \mathbb{R}[t]$ is a time dependent polynomial, which is chosen so that the initial state and input satisfy the relations (55) - (56), where y is replaced by y_m from (61). This means that the coefficients of $p_m(t)$ depend on the initial conditions of the system states and inputs. In addition, the degree ρ_m of $p_m(t)$ is equal to the highest time-derivative in (55) - (56). The flat feedforward trajectories y_{mr}

are then substituted in (56) to define a feedforward controller, which also means that the reference trajectories have to be k times differentiable.

In contrast to the usual choice $y_{mr} = r_m(t)$ the definition in (61) simplifies the definition of the event-based control strategy by avoiding the necessity to solve the trajectory planning problem at each event [**publication V**]. The polynomial $p_m(t - t_{event})$ in (61) can be calculated in the following way:

$$p_m(t - t_{event}) = \sum_{\lambda=0}^{\rho_m} p_{m,\lambda} (t - t_{event})^\lambda, \quad (62)$$

where the coefficients of p_m are calculated by solving the system of the following algebraic equations:

$$\begin{aligned} p_{m,0} &= e_m(0) \\ p_{m,j} &= \frac{e_m^{(j)}(0)}{j!} - \sum_{\mu=1}^j \binom{j}{\mu} (-K_m)^\mu \frac{(j-\mu)!}{j!} p_{m,j-\mu}, \quad j > 0, \end{aligned} \quad (63)$$

with $e_m(0) = y_m(0) - r_m(0)$. Then to complete the feedforward controller the time derivatives of y_{mr} are computed as:

$$y_{mr}^{(j)}(t, t_{event}) = \sum_{\mu=0}^j \binom{j}{\mu} (-K_m)^\mu p_m^{(j-\mu)}(t - t_{event}) e^{-K_m(t-t_{event})} + r_i^{(j)}(t). \quad (64)$$

Finally, by substituting (61) and (64) in (56) the following feedforward controller can be constructed:

$$\tau = \varphi_\tau(y_{mr}, \dots, y_{mr}^{(k+1)}). \quad (65)$$

The efficacy of the constructed feedforward controller heavily relies on the assumption that model (67) accurately captures the real dynamics of the vehicle. Specifically for underwater vehicles the presented models can only be an approximation of the real dynamics and the environment is usually non-stationary as well. This means that (65) will not yield the desired trajectories y_{mr} and a compensation becomes necessary. To this end a feedback loop is introduced leveraging the concept of event-based control. Figure 22 shows the control algorithm of the feedforward controller combined with a feedback loop. At all times the difference between the flat output $y_m(t)$ and the computed desired flat output $y_{mr}(t)$ is monitored. In case this difference exceeds the predefined threshold ε an event is triggered and the error and feedforward controller are essentially reset and the desired flat trajectory is recomputed based on state and input feedback. This requires that the full set of states and inputs are provided at the moment an event is triggered, whereas only the flat outputs need to be monitored between events.

In **publication IV** the novel control approach presented in this thesis was applied to a general model for fully actuated AUVs of the form (47) that was restricted to the horizontal plane. In the case of underactuated vehicles, the resulting dynamics model is not *differentially flat* and the proposed control approach can not be directly used. This has been somewhat addressed in **publication IV** under the problem of fault tolerant control. However, the assumptions that have been made to derive underactuated dynamics that are *differentially flat* would be difficult to justify from a physics point of view.

To that end, the development of a control framework extended from **publication IV** and inspired by work of Ryu et al. [184] is presented in the following subsections, which present, as of the time of writing, unpublished work. The presented augmented DFEC will

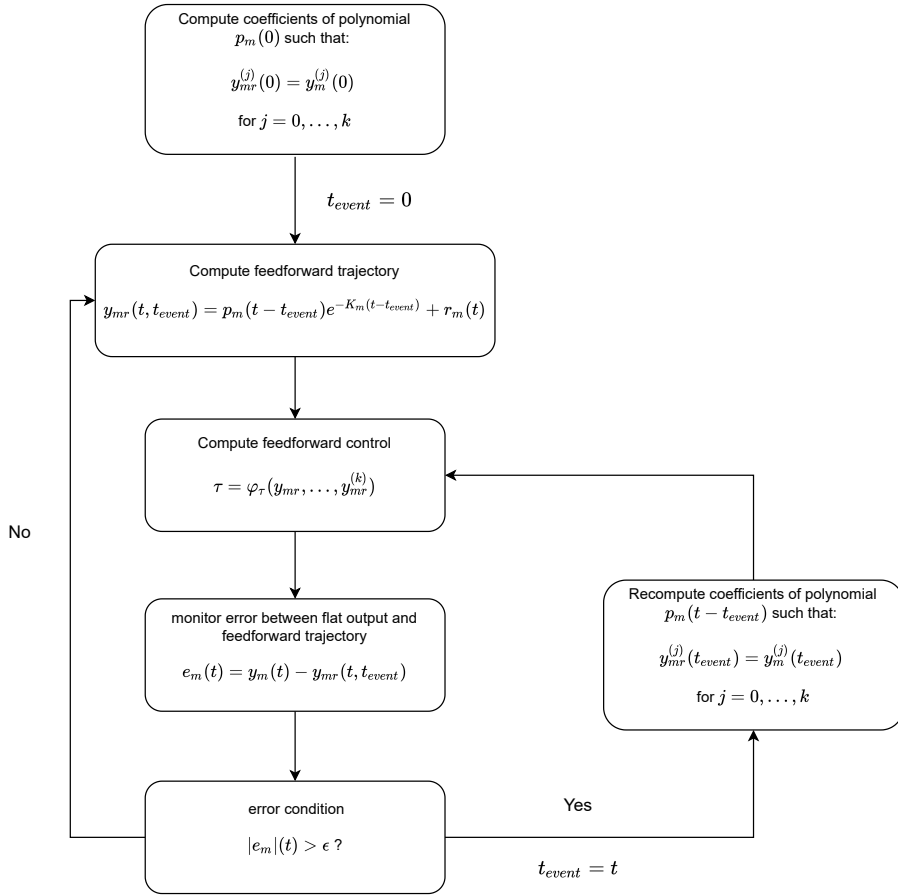


Figure 22 - Flow chart for the DFEC algorithm based on work presented in publication IV. The algorithm starts with the initialization of the polynomial p_m so that the feedforward trajectory coincides with the flat output of the dynamics, which are state space variables of the robot. The time t_{event} represents the last time an event has occurred and therefore resets the timing of the controller for each event so that a fresh feedforward trajectory can be generated starting from known "initial" conditions that are provided by the event based feedback.

be restricted to 2D AUV motions in the horizontal plane for a prove of concept with simpler derivations. However, the presented approach should be generalizable to 3D motions under certain restrictions for the degree of underactuation.

4.3.2 State space equations for underactuated AUV dynamics in horizontal plane

For motion in the horizontal plane, the state space of the dynamics model (47) can be reduced to $q = [x, y, \psi, u, v, r]^T = [x_1, x_2, x_3, x_4, x_5, x_6]^T$. Additionally, a classical underaction in sway direction is considered. Therefore, the control space gets reduced by one input $\tau = [X, 0, N]^T = [u_1, 0, u_2]$. The state space equations can then be formulated as:

$$\begin{aligned}
 \dot{x}_1 &= x_4 \cos(x_3) - x_5 \sin(x_3) \\
 \dot{x}_2 &= x_4 \sin(x_3) + x_5 \cos(x_3) \\
 \dot{x}_3 &= x_6 \\
 \dot{x}_4 &= -\frac{1}{m_{11}} [(Y_{\dot{v}} - m)x_5 x_6 + X_u x_4 + X_{uu} x_4 |x_4| - u_1] \\
 \dot{x}_5 &= -\frac{1}{m_{22}} [(m - X_{\dot{u}})x_4 x_6 + Y_v x_5 + Y_{vv} x_5 |x_5|] \\
 \dot{x}_6 &= -\frac{1}{m_{66}} [(X_{\dot{u}} - Y_{\dot{v}})x_4 x_5 + N_r x_6 + N_{rr} x_6 |x_6| - u_2],
 \end{aligned} \tag{66}$$

with m_{11} , m_{22} , m_{66} , X_u , X_{uu} , Y_v , Y_{vv} , N_r , N_{rr} being constants that define inertial and hydrodynamic attributes of the vehicle dynamics respectively. Additionally, $X_{\dot{u}}$ and $Y_{\dot{v}}$ are constant that define the influence of the Coriolis and centripetal forces on the system. Whenever the robot turns, i.e. $x_4 \neq 0$ and $x_6 \neq 0$, a force arises in lateral (sway) direction due to the centripetal and Coriolis terms that is reduced by the drag in sway (because $\text{sgn}(x_4) = -\text{sgn}(x_6)$) but can not be actively countered, due to the underactuated nature of the robot. The robot thus experiences an undesired sideslip motion. This can significantly decrease the tracking performance for curved paths or trajectories, depending on the amount of environmental damping and the velocities in the actuated DOFs. The underactuated nature of the system also prohibits the use of classical state feedback linearization [177] and the state space model is not *differentially flat*.

Nevertheless, the model can be augmented by excluding the sway velocity x_5 , which reduces the state space by one. Thus, all terms in (66) that are related to x_5 vanish. However, the cross-dimensional coupling effects of the sway velocity can be expected to be nonzero. Therefore, the terms associated with the sway velocity are re-introduced into the state space model in the form of additive disturbances, which are estimated by a disturbance observer. The resulting model is *differentially flat*, which is shown in the next subsection where a DFEC, as described in 4.3.1, is constructed based on the flat properties of the reduced state space model.

4.3.3 Augmented DFEC for underactuated AUV dynamics

For each state the sway velocity related effects are lumped together with other unmodelled phenomena in an additive disturbance term and the sway velocity is reduced from

the system states. Model (66) then becomes:

$$\begin{aligned}
\dot{x}_1 &= x_4 \cos x_3 + d_1 \\
\dot{x}_2 &= x_4 \sin x_3 + d_2 \\
\dot{x}_3 &= x_5 \\
\dot{x}_4 &= -\frac{1}{m_{11}}(X_u x_4 + X_{uu} x_4 |x_4| - u_1) + d_3 \\
\dot{x}_5 &= -\frac{1}{m_{66}}(N_r x_5 + N_{rr} x_5 |x_5| - u_2) + d_4,
\end{aligned} \tag{67}$$

with $d = [d_1, d_2, 0, d_3, d_4]^T$ as the disturbances on different degrees of freedom.

Now a DOBC can be derived based on *differential flatness* and by including the disturbances. Following (55) - (56) the states and inputs can be defined in terms of the flat outputs $F = [x_1, x_2] = [y_1, y_2]$ and the disturbances d :

$$x_4 = \sqrt{(\dot{y}_1 - d_1)^2 + (\dot{y}_2 - d_2)^2}, \tag{68}$$

$$\dot{x}_4 = \frac{(\dot{y}_1 - d_1)(\ddot{y}_1 - \dot{d}_1) + (\dot{y}_2 - d_2)(\ddot{y}_2 - \dot{d}_2)}{\sqrt{(\dot{y}_1 - d_1)^2 + (\dot{y}_2 - d_2)^2}}, \tag{69}$$

$$x_3 = \arctan\left(\frac{\dot{y}_2 - d_2}{\dot{y}_1 - d_1}\right), \tag{70}$$

$$x_5 = \dot{x}_3 = \frac{(\dot{y}_1 - d_1)(\ddot{y}_2 - \dot{d}_2) - (\dot{y}_2 - d_2)(\ddot{y}_1 - \dot{d}_1)}{(\dot{y}_1 - d_1)^2 + (\dot{y}_2 - d_2)^2}, \tag{71}$$

$$\begin{aligned}
\dot{x}_5 = \ddot{x}_3 &= \frac{(\dot{y}_2 - d_2)(\ddot{y}_1 - \dot{d}_1) - (\dot{y}_1 - d_1)(\ddot{y}_2 - \dot{d}_2)}{(\dot{y}_1 - d_1)^2 + (\dot{y}_2 - d_2)^2} \\
&\quad - \frac{[(\dot{y}_2 - d_2)(\ddot{y}_1 - \dot{d}_1) - (\dot{y}_1 - d_1)(\ddot{y}_2 - \dot{d}_2)] [2(\dot{y}_1 - d_1)(\ddot{y}_1 - \dot{d}_1) + 2(\dot{y}_2 - d_2)(\ddot{y}_2 - \dot{d}_2)]}{[(\dot{y}_1 - d_1)^2 + (\dot{y}_2 - d_2)^2]^2},
\end{aligned} \tag{72}$$

$$\begin{aligned}
u_1 &= m_{11} \left[\frac{(\dot{y}_1 - d_1)(\ddot{y}_1 - \dot{d}_1) + (\dot{y}_2 - d_2)(\ddot{y}_2 - \dot{d}_2)}{\sqrt{(\dot{y}_1 - d_1)^2 + (\dot{y}_2 - d_2)^2}} - d_3 \right] \\
&\quad + X_u \sqrt{(\dot{y}_1 - d_1)^2 + (\dot{y}_2 - d_2)^2} + X_{uu} [(\dot{y}_1 - d_1)^2 + (\dot{y}_2 - d_2)^2],
\end{aligned} \tag{73}$$

$$\begin{aligned}
u_2 &= m_{66} \left[\frac{(\dot{y}_2 - d_2)(\ddot{y}_1 - \dot{d}_1) - (\dot{y}_1 - d_1)(\ddot{y}_2 - \dot{d}_2)}{(\dot{y}_1 - d_1)^2 + (\dot{y}_2 - d_2)^2} \right. \\
&\quad \left. - \frac{[(\dot{y}_2 - d_2)(\ddot{y}_1 - \dot{d}_1) - (\dot{y}_1 - d_1)(\ddot{y}_2 - \dot{d}_2)] [2(\dot{y}_1 - d_1)(\ddot{y}_1 - \dot{d}_1) + 2(\dot{y}_2 - d_2)(\ddot{y}_2 - \dot{d}_2)]}{[(\dot{y}_1 - d_1)^2 + (\dot{y}_2 - d_2)^2]^2} - d_4 \right] \\
&\quad + N_r \frac{(\dot{y}_2 - d_2)(\ddot{y}_1 - \dot{d}_1) - (\dot{y}_1 - d_1)(\ddot{y}_2 - \dot{d}_2)}{(\dot{y}_1 - d_1)^2 + (\dot{y}_2 - d_2)^2} \\
&\quad + N_{rr} \left[\frac{(\dot{y}_2 - d_2)(\ddot{y}_1 - \dot{d}_1) - (\dot{y}_1 - d_1)(\ddot{y}_2 - \dot{d}_2)}{(\dot{y}_1 - d_1)^2 + (\dot{y}_2 - d_2)^2} \right]^2.
\end{aligned} \tag{74}$$

Now a BDO for the disturbance vector d can be derived following the theory presented in section 4.2.3. For brevity only the resulting conditions for choosing gains that guarantee stability of the BDO are presented. The full derivation can be found in Appendix 2. The BDO gains should be computed according to the following inequalities:

$$\begin{aligned} l_{0,n} &> 0 \\ l_{1,n} &= \frac{l_{0,n}^2}{3} \\ \frac{l_{0,n}^3}{27} &\leq l_{2,n} \leq \frac{l_{0,n}^3}{9}, \end{aligned} \tag{75}$$

with $n = 1, 2, 3, 4$.

Following the statement in [publication IV] that the error threshold ε should not be much smaller than the noise in the disturbance, an adaptive law is defined for the error threshold if disturbances are present:

$$\varepsilon_{ad} = \max(\varepsilon, \max(d) + k_\varepsilon \max(d)), \tag{76}$$

with $0 \leq k_\varepsilon < 1$ being a positive constant parameter. The final feedforward controller is then defined as:

$$\tau = \begin{pmatrix} u_1 \\ u_2 \end{pmatrix} = \begin{pmatrix} \varphi_{\tau 1}(y, y^{(1)}, y^{(2)}, d, d^{(1)}) \\ \varphi_{\tau 2}(y, y^{(1)}, y^{(2)}, y^{(3)}, d, d^{(1)}, d^{(2)}) \end{pmatrix}, \tag{77}$$

with u_1 and u_2 defined by equations (73) and (74). ε_{ad} and τ are then inserted into the event based control framework presented Figure 22.

To test the efficacy of the proposed controller, U-CAT was used as an experimental platform and first proof of concept tests were carried out with a simulated version of the vehicle. U-CAT itself and the simulation framework are presented in the next sections.

4.4 Experimental platform - U-CAT

U-CAT is a small size, low cost vehicle designed for shipwreck penetration [58]. The vehicle was designed to support archaeologists during inspection and survey operations in potentially dangerous environments by autonomously navigating in confined spaces and creating visual maps [170]. To enable highly maneuverable actions and minimize disturbance of its environment, U-CAT's movements are facilitated by a bio-inspired locomotion mechanism, which is comprised of four flexible fins (see Figure 23). The four fins are mounted at an angle, which in theory enables fully holonomic motion of the vehicle with possible actuation in 6 DOFs. Each fin can be actuated independently in any direction around the motors axis. To propel the robot forward the fins are usually oscillating with a sinusoidal motion profile with a fixed frequency and a varying amplitude.

The robot can be operated in two motion modes, denoted by SLOW and FAST, which differ in their fin configuration and subsequent motion capabilities of the robot. In SLOW mode the neutral position of all fins is facing inwards as shown in Figure 24.a. This should provide higher maneuverability and stability as the fin's mass distribution is symmetric and forces can be produced in all directions. However, this comes at the cost of maximum achievable thrust in surge direction, as only two fins can contribute in that direction. Additionally, the pitching torque caused by periodic oscillations of the front fins cannot be completely countered by oscillating the back fins, which leads to periodic pitching motions of



Figure 23 – **Rendering of bio-inspired AUV U-CAT with 4-fin propulsion.** The vehicle is shown in FAST mode configuration where all flippers point towards the back of the robot when not actuated. This is the configuration that will be used throughout the subsequent controller development.

the vehicle. In this configuration, the robot can essentially turn in place in yaw direction which makes it highly maneuverable in confined spaces, however, this comes at the cost of the ability to effectively surge and yaw at the same time, as the torque generation for yawing would be detrimental to the thrust generation for surging. Instead in "FAST" mode (see Figure 24.b) the fin configuration allows for simultaneous surging and yawing at the expense of the capability to move in sway direction. The inability to produce forces in sway direction essentially makes the robot underactuated and nonholonomic in FAST mode. To prevent continuous oscillations in roll and pitch direction in FAST mode, diagonal fins are actuated synchronously while fins at the opposite diagonal are actuated with a 180° Motion in heave direction is possible in both modes by shifting the centre of oscillation of the fins out of the horizontal plane. Rolling motions are also achievable in both modes, while FAST mode is more conducive to pitching motions, especially in combination with surging. While the SLOW mode is the mode of choice for station keeping tasks and slow motion in very confined spaces, the FAST mode is the most promising for more general trajectory tracking tasks. Since the motion control work presented in this thesis is concerned about planar trajectory tracking for U-CAT, the robot will be always assumed to be configured in FAST mode.

The vehicle has a length of 0.56 m and a mass of 19 kg and battery power for continuous operation of up to 6 hr. The main computation unit of the robot is a Nvidia Jetson TX2. U-CAT uses a monocular camera (Grey Chameleon digital color camera CMLN-13S2C-CS.), ultrasonic rangefinders (in-house manufactured based on [198]), an IMU (Invensense MPU-6050) and a analog output pressure sensor (GEMS 3101) for state estimation. The work presented in this thesis mainly relies on camera, pressure and IMU information. In regards to software architecture an autonomy framework has been developed using the robot operating system (ROS). In this framework various software nodes were designed for state estimation, to model vehicle dynamics, establish trajectories and control actuators and the robot's motion. Additionally, software layers for higher level behavior definitions were added for autonomous confined space mapping [199].

The full autonomy framework of U-CAT is described by Salumäe et al. in [200] is shown in Figure 25. Here the dynamics node is essentially a representation of the nominal dynamics model of the robot as defined in equation (47). The odometry node gathers all sensor information and estimates all relevant states of the robot, while the automatic control

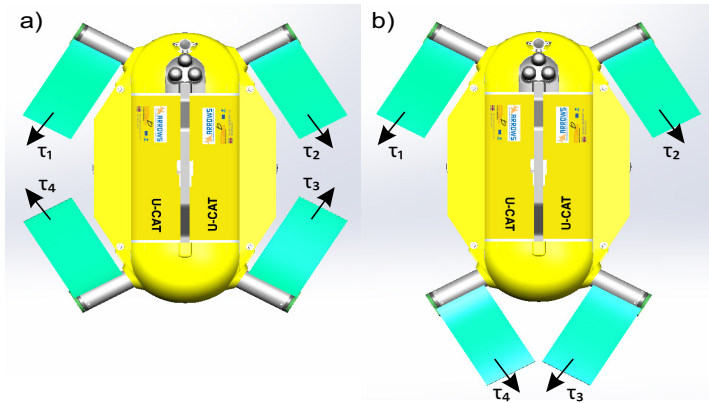


Figure 24 – Top view of U-CAT with indications for the direction of mean forces τ that are produced by oscillations of each flipper around an axis in the horizontal plane [publication IV]. a) Fin configuration for SLOW mode. In this configuration the robot can be theoretically actuated in all degrees of freedom simultaneously. However, the control allocation problem that arises is still subject to investigation and it is unclear how efficient the resulting motions will be. U-CAT also only uses half of its available fins for surging which leads to constant pitch oscillations and a lower maximum achievable speed. b) fin configuration for FAST mode. Here all fins can be utilized for actuation in surge direction. However, the sway direction becomes uncontrollable making the vehicle in this configuration underactuated (at least for maneuvers that include the simultaneous control of several DOFs).

node is essentially the motion controller of the robot that produces desired control forces based on the state input from the odometry node and desired trajectories from the trajectory manager. The trajectory manager in its present form uses predefined timed setpoints interpolated by hyperbolic tangent functions to produce smooth trajectories through the given set-points. Important to ensure safe operation of the robot's fins are the rate limiter and saturation functionalities contained within the automatic control node, which pose an additional restriction to any controller that is employed for motion control. To deal with the complex problem of motion coupling Salumäe et al. [200] proposed a DOF prioritization that essentially weighs the importance of control in a certain DOF based on the required control action for each DOF. Finally, the Wrenchdriver translates the required control forces for the robot's body into separate kinematic profiles for each fin, also serving as a control allocation node. The desired kinematic fin profiles in turn are produced by low level control on each fin's motor.

The following section will describe the simulation setup to test the efficacy of the control framework proposed in section 4.3.3 applied to the motion dynamics of U-CAT. Additionally, components of U-CAT's autonomy framework that are necessary to enable trajectory tracking control are presented as well.

4.5 Simulation

To enable trajectory tracking for U-CAT in the horizontal plane, several modifications and additions to the existing autonomy framework presented in Figure 25 were necessary. The new autonomy framework is described in Figure 26. Firstly, the previous trajectory manager, which was taking user defined set points, was replaced by a dual structure made out of a planner and a new trajectory manager. The planner takes a user defined rectangular area that is to be covered in a lawn mower pattern by the robot. The planner then com-

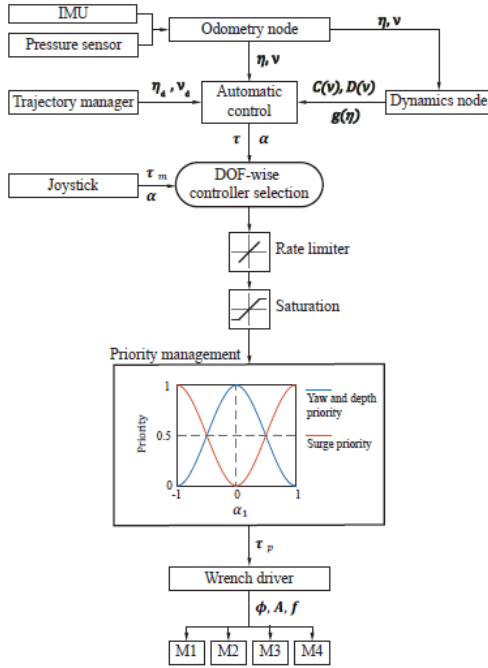


Figure 25 – Present autonomy framework of U-CAT as shown in [200].

puts a lawn mower type path, by taking into account the motion limitations due to the nonholonomic nature of U-CAT in FAST mode. This is achieved by computing the shortest path between several seed points based on a Dubin’s car model [201] using algorithms developed in [202] and [203]. Figure 27 shows an example for a path created by the planner. The Dubin’s model only allows forward motion with a defined minimum turning radius. While U-CAT can theoretically move backwards in FAST mode, it would need to reverse it’s fin orientation by 180°. This would result in a prolonged transition period, where efficient trajectory tracking would be not possible. Additionally, any efficient trajectory tracking for the sway direction necessitates a non-zero motion in surge due to the underactuation of the robot. Therefore, the Dubin’s car model was a natural choice for the path generation.

Once the path is generated, it is sent to the trajectory manager where the path points are timed and interpolated. B-splines are used to generate smooth multiple times differentiable trajectories. The trajectories are then sent to the pilot node, which is the equivalent of the automatic control node in the old framework. This node defines the tracking errors, decides which controller type to use, runs the controller and provides desired control forces to the Wrenchdriver, which is unchanged compared to the old framework. A new addition to the framework is the navigator node, which is essentially an extension of the old odometry node. The navigator takes available sensor information and fuses it with an EKF that is structurally equivalent to the filter described by Palomerias et al. in [10]. Since trajectory tracking in the horizontal plane requires position and velocity feedback, a camera is used to track fiducial markers, thereby providing position and velocity estimates used by the EKF of the navigator.

The model based control approach requires higher order derivatives (acceleration and jerk) of the robot’s pose. While a noisy and potentially unreliable measurement of acceleration can be gained by an IMU, the jerk can not be directly measured. The problem

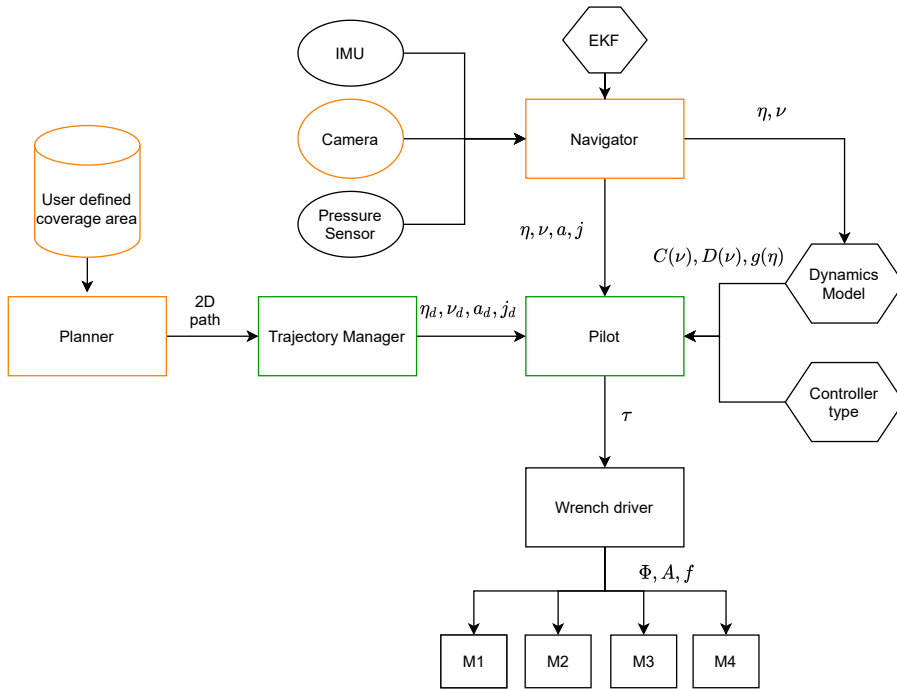


Figure 26 – **Updated autonomy framework for the U-CAT AUV.** An orange border indicates novel functionalities, compared to the framework in Figure 25, and green borders indicate existing functionalities that have been extended or improved

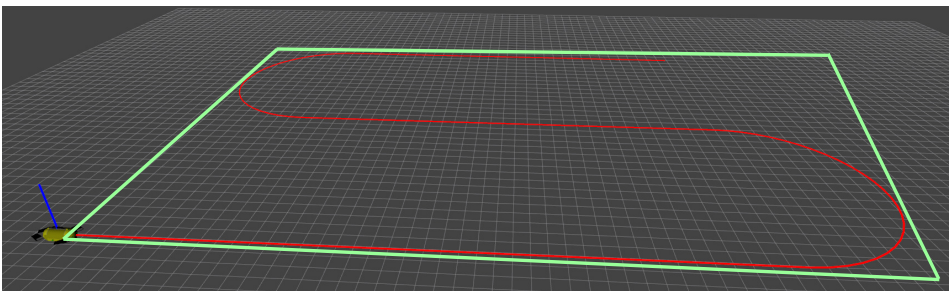


Figure 27 – **Example of a lawn mower path.** The lawn mower type path generated by the planner node of the new autonomy framework is shown in red. The user defined area that is the input to the path planner providing the seed points for the Dubins model based path generation is shown in green

Table 3 – Model parameters used to simulate U-CAT’s dynamics

Parameter	Value	Parameter	Value
m	19	I_{zz}	0.512
$X_{\dot{u}}$	-40	$Y_{\dot{v}}$	-21
$N_{\dot{r}}$	-2.306	$m_{11} = m - X_{\dot{u}}$	59
$m_{22} = m - Y_{\dot{v}}$	40	$m_{66} = I_{zz} - N_{\dot{r}}$	2.818
X_{uu}	3.342	X_{uu}	18.98
Y_v	31.7	Y_{vv}	184.3
N_r	2.013	N_{rr}	3.312

of obtaining and using higher order state derivatives in real applications of the controller is informing the controller structure and will be addressed in the discussion of the results of the controller comparison. During simulations, the accelerations can be directly gained from the dynamics model that forms the basis of the simulator. A simple time differentiation then yields the jerk. Given the desired state trajectories the three different controllers can now be constructed. In the following sections the event-based controller using a feedforward term based on flat trajectories will be derived and the error definition for the model free controllers will be provided as well.

Simulations are conducted using the same ROS based autonomy framework as described in Figure 26, including a slightly modified dynamics model of U-CAT that includes water current disturbances and by using the UWSim virtual environment [204] to simulate sensor input. The dynamics of the bio-inspired actuators of U-CAT are simulated based on a simple hydrodynamics model presented in [205]. The lift and drag coefficients of this model were determined based on empirical data of the amplitude-frequency-force relationship of U-CAT’s fins. The parameters used to simulate the dynamics of U-CAT in the horizontal plane are shown in Table 3.

To include water current disturbances, a planar irrotational water flow with magnitude V_c is introduced. A 1st-order Gauss-Markov process is used to simulate the flow [40]:

$$w = \dot{V}_c + \mu_c V_c, \quad (78)$$

where w is Gaussian white noise with $N(0, var_c)$ and $\mu_c \geq 0$ is a constant. The water current V_c is defined in the inertial frame and can be transformed into flow velocities v_c in the robot’s reference frame via:

$$v_c = \begin{pmatrix} u_c \\ v_c \\ 0 \end{pmatrix} = J_{0x3}(\eta) R^{rot}(\alpha_{flow}) \begin{pmatrix} V_c \\ 0 \\ 0 \end{pmatrix}, \quad (79)$$

with J_{0x3} the upper half of the Jacobian in (47), $R^{rot}(\cdot)$ being the standard 2D rotation matrix and α_{flow} the incidence angle of the water flow disturbance in the inertial frame. Given v_c we can now define the relative velocity $v_r = v - v_c$ and by assuming the water current vector to be slowly varying $\dot{v}_c \approx 0$ the nominal dynamics model (47) becomes:

$$M\dot{v} + C_{RB}(v)v + g(\eta) + C_A(v_r)v_r + D(v_r)v_r = \tau. \quad (80)$$

To test the three controllers on U-CAT two scenarios are simulated, one scenario is without any water flow disturbance and one with water flow disturbance. In both scenarios a lawn mower trajectory to cover an area of 15 m x 10 m (width x height) was generated with a constant target velocity of 0.3 m/s. In the second scenario a constant water flow

Table 4 – Parameters for different simulation scenarios. l_m - lawn mower, α_{flow} - angle at which water flow disturbance acts in the inertial frame

Scenario	l_m – width[m]	l_m – height[m]	u_{target} [m/s]	V_c [m/s]	α_{flow} [deg]
1	15	10	0.3	0.15	45
2	15	10	0.3	0.15	45
3	100	60	1.5	0.5	45

Table 5 – PID controller gains for different simulation scenarios

Scenario	K_p	K_i	K_d
1	[9.0, 3.0]	[5.0, 1.0]	[0.5, 3.0]
2	[9.0, 3.0]	[5.0, 1.0]	[0.5, 3.0]
3	[8.0, 6.0]	[8.2, 5.0]	[1.0, 20.0]

of magnitude of 0.15 m/s + N(0, 0.01) and incidence angle of 45° is introduced. A comparison between both scenarios indicates that the difference in operation conditions are not very high, which is owed to the slow movement of the vehicle in the horizontal plane due to actuator limitations. However, the robot is capable of fast attitude changes which would change the operational range significantly. Since a full 3D motion control was beyond the scope of this thesis a third scenario with a surrogate AUV model was introduced to simulate faster operational ranges. The dynamics model of the LAUV [15] was chosen as an example of a more traditional torpedo shaped underactuated nonholonomic AUV operating at higher velocities. The dynamics of the LAUV are described in [206]. In this third scenario the area covered by the lawn mower was significantly larger (100 m x 60 m) as was the constant target velocity 1.5 m/s and the water current disturbance 0.5 m/s + N(0, 0.1). The parameters for each scenario are presented in Table 4.

The gains for all three controllers were hand tuned based on a testing scenario without disturbances within approximately the same maximum time. The gains remained the same for scenarios 1 and 2 but were adjusted for scenario 3. The numeric values of the gains for the respective controllers can be found in Table 5 to 7. Additionally, the BDO gains are provided in Table 8.

To evaluate the performance of the various controllers the RMSE between reference trajectory and actual trajectory of the vehicle was computed. Additionally, the time derivative of the control output was used as a measure of control action that can give an indication about the energy efficiency of the controller in relation to the actuator.

4.6 Results and discussion

Figure 28 shows the trajectory tracking performance of U-Cat using the Flat-event based controller for the scenario without any disturbances. The position trajectories shown in Figure 28.a and c indicate that the reference trajectory was very closely tracked by the

Table 6 – RISE controller gains for different scenarios

Scenario	α_1	α_2	β	k_s
1	[0.02, 0.05]	[0.5, 0.05]	[0.04, 0.01]	[0.85, 0.5]
2	[0.02, 0.05]	[0.5, 0.05]	[0.04, 0.01]	[0.85, 0.5]
3	[0.05, 0.01]	[0.3, 0.05]	[0.3, 0.25]	[0.5, 12.1]

Table 7 - Flat-event controller gains for different scenarios

Scenario	K	ε	k_ε
1	[1.0, 1.0]	0.05	0.05
2	[1.0, 1.0]	0.05	0.05
3	[0.47, 0.47]	0.15	0.2

Table 8 - BDO gains calculated based on (75)

$l_{0,1} = l_{0,2}$	$l_{0,3} = l_{0,4}$	$l_{1,1} = l_{1,2}$	$l_{1,3} = l_{1,4}$	$l_{2,1} = l_{2,2}$	$l_{2,3} = l_{2,4}$
80	20	2133.3	133.3	28444	444.4

controller. In *Figure 28.b* and *d* the velocity trajectories are closely tracked as well but some oscillations can be observed at the end of turns, which indicates the difficulty to counter the forces in sway direction without any actuation for that DOF, although the drag based dampening decreases this cross coupling effect already. Moreover, the control signals shown in *Figure 28.e* and *f* are very smooth without many instances of large control action. Only a very small number of events was triggered as can be seen in *Figure 28.g*. Given the accurate state measurements and no differences between the dynamic models of the controller and the simulation it was expected that the feedforward part of the controller would be sufficient.

Figure 29 displays the results of the same controller under unknown disturbances. It can be seen that the positions are still tracked very closely (see *Figure 29.a* and *c*), but that there are deviations specifically in global y direction visible. This becomes more obvious when looking at the velocity tracking (see *Figure 29.b* and *d*). A lot of oscillations are present in the global y -direction, which indicates the constant struggle of the controller to counter the disturbance and to deal with sudden directional changes of the disturbance as the robot changes heading. The control signals are qualitatively comparable to the ones in *Figure 29*, but the control commands are less smooth, with increased control action indicating again the attempts of the controller to counter the disturbances. The number of events has gone up as well, but only slightly (8 vs 14). This seems to indicate that the BDO was working well and that it enabled the feedforward part of the controller to effectively deal with the disturbances most of the time. The low number of events is specifically promising, because it reduces the number of required full state measurements. One of the major limitations of model-based nonlinear controls for underwater vehicles in real applications is the requirement for continuous observation of the full state and its derivatives, including accelerations and possibly even higher order derivatives. Acceleration measurements or estimates are usually very noisy unless expensive and bulky hardware is deployed. Since the events for the DFEC are all at least several seconds apart, the close to real-time restriction for filters is somewhat lifted and advanced signal processing algorithms such as the Rauch-Tung-Striebel filter [207] could be used to filter acceleration measurements. With increased estimation accuracy, full state estimates could become available for robots employing lower budget hardware in real world scenarios as well. This possibility poses one of the main differences to the controller proposed in [184] where continuous full state feedback was necessary, which seems to have prohibited tests for the dynamics based controller on the real vehicle.

The efficacy of the BDO is further highlighted by the results shown in *Figure 30*. The kinematic disturbances are tracked very well as shown in *Figure 30.a* and *b*. The disturbances on the dynamics level are also very well tracked and the white noise of the water

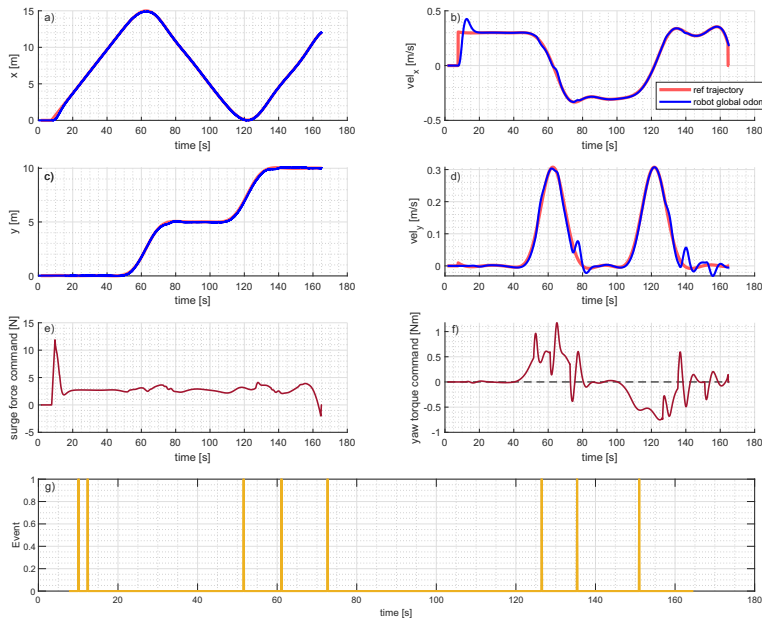


Figure 28 – Trajectory tracking performance for the flat event controller when disturbances were absent. a) and c) Description of the position tracking performance for global x and y position. b) and d) Velocity tracking performance along the global x and y axes. e) - f) Control force in surge and control torque in yaw. g) Occurrence of events denoted in a binary graph, where 0 means no event and 1 means event.

flow disturbance is filtered to some extent, as indicated by Figure 30.c and d. Figure 31 shows the position tracking performance of all three tested controllers for scenario 1 (without disturbances) and for scenario 2 (with disturbances). All controllers show a very good position tracking in scenario 1 as seen in Figure 31.a. For the two model-free controllers it can be seen that the robot exhibits slight oscillations during the first and last straight part in x-direction, which would increase the energy consumption of the vehicle. However, the oscillations are on a rather small scale around 0.1 m.

In the scenario with disturbances, shown in Figure 31.b, the tracking performances degrades for all controllers, which is to be expected. Yet, all controllers are still able to track the trajectory within a reasonable error margin. Surprisingly, the robust RISE controller seems to be outperformed by the standard PID controller in this scenario. In fact the PID controller seems to be even performing as well as the DFEC. However, as indicated by the actual RMSE metrics shown in Figure 32 the DFEC outperforms both model free controllers. It becomes clear that the PID controller indeed performs better than the RISE controller in scenario 2 and performs better in y-direction compared to the x-direction. For the tracking in x-direction there is a constant error as the PID controller and the RISE controller could not fully steer the vehicle trajectory on the reference trajectory. This was different for the DFEC, which partially explains the better performance in x-direction. It becomes also evident that a 2D position plot does not reflect the tracking performance in x-direction well and can be slightly misleading for trajectory tracking problems. This stresses the importance of evaluation metrics such as the RMSE.

The second evaluation metric defined for this simulation was the control effort defined as first time derivative of the control signal shown in Figure 33. Here it becomes

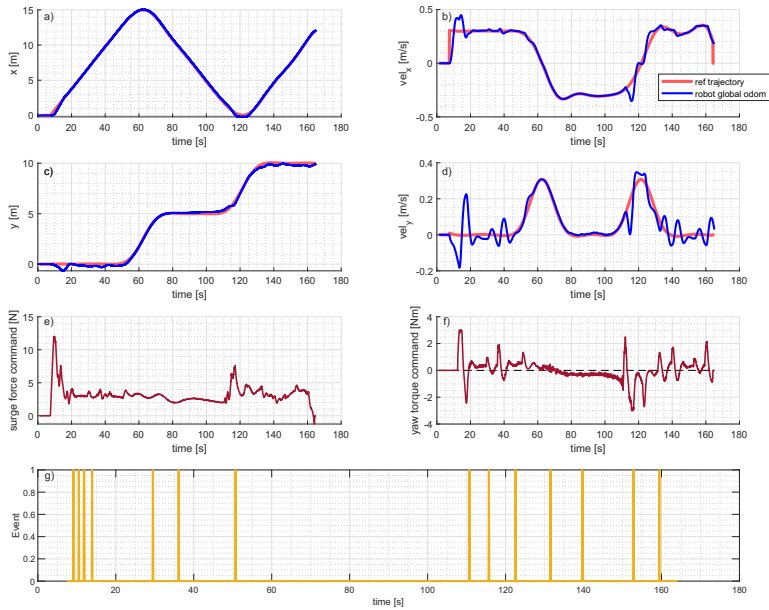


Figure 29 – **Trajectory tracking performance for the flat event controller when disturbances are present.** Disturbances were modeled as modeled as a constant irrotational fluid flow with an incidence angle of 45° and a magnitude of 0.5 m/s. a) and c) Position tracking performance for global x and y position. b) and d) Velocity tracking performance along the global x and y axes. e) - f) Control force in surge and control torque in yaw. g) Occurrence of events denoted in a binary graph, where 0 means no event and 1 means event.

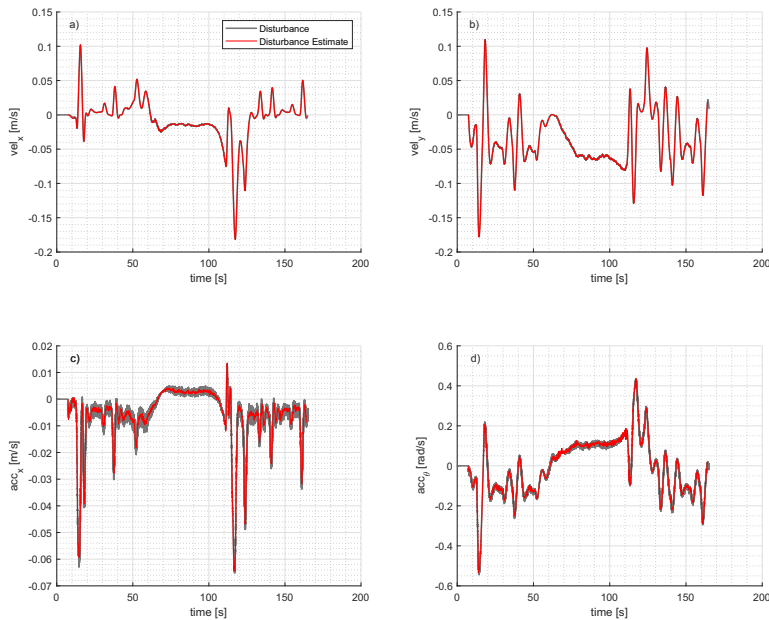


Figure 30 – **Disturbance estimates for the DFEC.** a) - b) Kinematic disturbances in global x and y directions. c) - d) Dynamic disturbances in global x and y directions

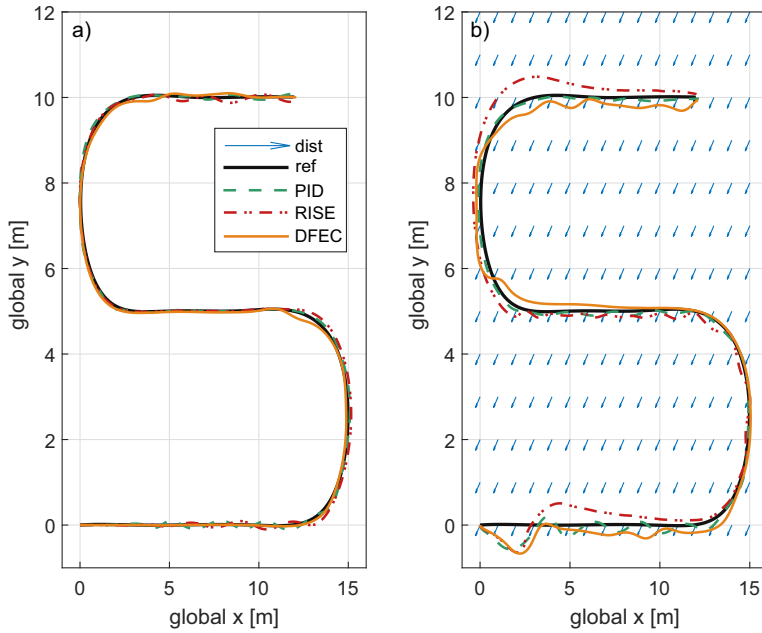


Figure 31 – Visualization of planar tracking for the three tested controllers. a) Without disturbances and b) With disturbances illustrated as blue arrows. The arrows show the correct incidence angle but the arrow length is a scaled representation of the magnitude. The flow was modeled as a constant irrotational fluid flow with an incidence angle of 45° and a magnitude of 0.5 m/s.

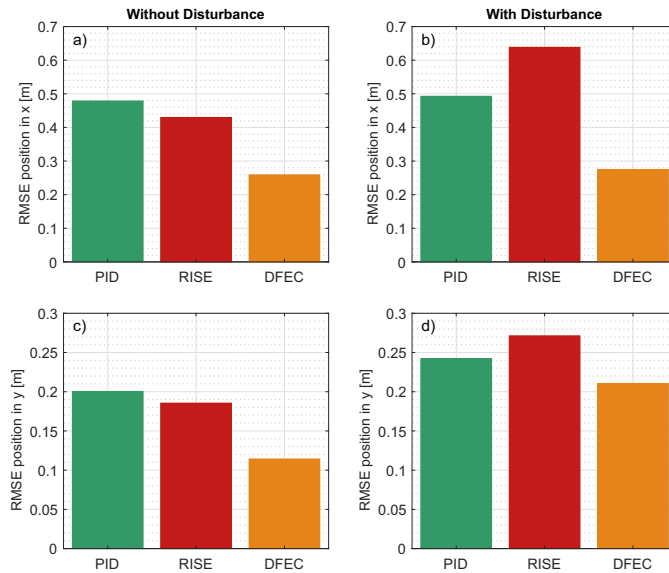


Figure 32 – RMSE for the three tested controllers with and without disturbances. a) and c) Tracking performance of the three tested controllers for global x and y directions when disturbances were absent. b) and d) Tracking performance of the three tested controllers for global x and y directions when disturbances were present. The disturbance was modeled as a constant irrotational fluid flow with an incidence angle of 45° and a magnitude of 0.5 m/s.

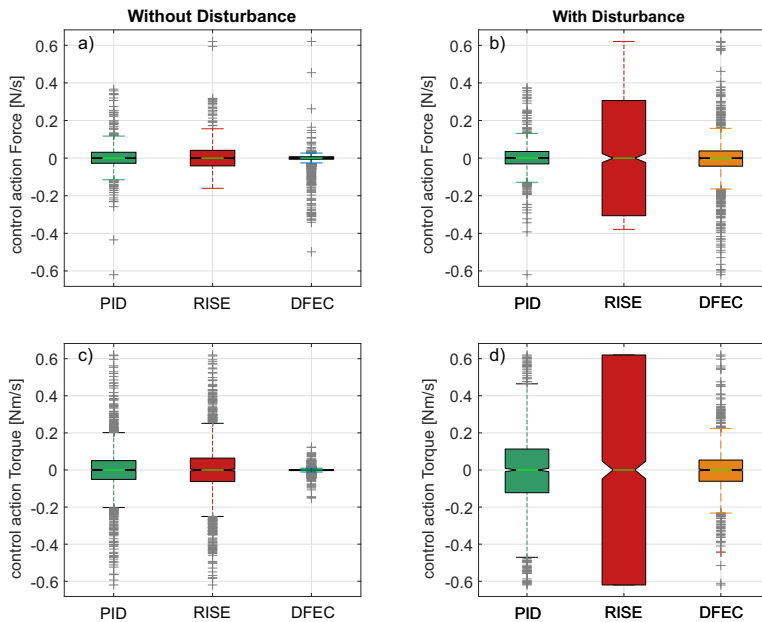


Figure 33 – Control action for the three tested controllers. Control action is quantified by the first time derivative of the time series of control commands, which the controllers have issued during a simulation run. The control action for one run is then characterized using the median and IQR, which are shown in the figure. Additionally, "outliers" expressing large changes in subsequent control signals, are represented in red.

apparent that the DFEC produces smoother and less varying control signals, which leads to less control effort for the actuators. The wide spread of outliers in the control action in the DFEC could be explained with the re-initialisation of the whole controller structure at each event, which can cause steps in the control signal. As expected the control effort is increasing between scenario 1 and scenario 2 as more force and torque is needed to counter the water flow disturbance. The increase in control action is specifically apparent for the RISE controller, but to a lesser extent also for the PID controller. The increase in control action is smallest for the DFEC. The results so far would indicate the PID controller would be a preferable choice over the RISE controller for a model-free controller for trajectory tracking with U-CAT. A possible explanation for this could be the manual tuning process. Given that the RISE controller has one gain more to tune with a less intuitive behavior of the different gains, the resulting gains for this simulation might be further away from the optimal values for the RISE controller as compared to the PID controller. For a more rigorous performance comparison it would be necessary to find globally optimal gains for all controllers, which could be done via a Bayesian optimization framework as presented in [208]. However, in a real world scenario it is unlikely that a computationally heavy optimization framework is always available and usually time for tuning is restricted. Therefore, the employed method of manually tuning the gains for a similar set amount of time can be seen as a valid approach. The control performances after manual tuning might also inherently reflect the complexity in the tuning process of a given controller, which would be another important metric for controller evaluation. Though tuning complexity remains hard to quantify, specifically in real world applications with time and computational restraints.

Another explanation for the good performance of the PID controller could be that the disturbances have not been big enough to place the operation conditions outside of the permissible range of the PID controller with the given gains. To test this further, *scenario 3* was used exhibiting larger disturbances, a much larger absolute range between the disturbance free and the disturbance cases, as well as generally faster dynamics. *Figure 34* shows a summary of the controller performances for *scenario 3*. It can be seen here, that in the presence of disturbances the PID controller cannot adequately track the trajectories anymore. The robot control became unstable in the second straight segment in x-direction as can be seen in *Figure 34* and the trial was aborted after oscillations and rotations got too extensive. On the contrary the RISE controller showed a convincing performance, even outperforming the DFEC on the RMSE metric. Again, the manual gain tuning could introduce artificial differences, although the tuning procedure and available time was similar across all scenarios.

While the RISE and DFECs show a similar performance regarding the trajectory tracking itself, significant differences can be seen in the control action metric. Here the DFEC is far more economical with its control actions, which should lead to more efficient movements. Beyond its application to general torpedo shaped AUVs with similar dynamics to the LAUV, this scenario is also of relevance for future tracking scenarios for U-CAT. While linear motions will remain rather slow in the 3D tracking case as well, orientation changes can happen on a much faster time-scale with a higher relative importance of the rotation dynamics on the overall system. In that scenario the benefits of the model based controller should become apparent similarly to *scenario 3* presented here. One could argue that trajectory tracking in the horizontal plane is not the best use-case for the proposed controller, however, given U-CAT's available capabilities in locomotion and state estimation it is the most accessible problem to be tested on the real vehicle. The results shown for this sub-optimal case are still a sufficient for a proof of concept for the controller that highlight the benefits compared to standard model free controllers.

A very important detail to contextualize the control performance of the model based controller, is the accuracy of the dynamics model of the vehicles and the accuracy of the state estimation. In simulations, as employed here, dynamics models are assumed to be fully accurate which biases results towards model-based control strategies. The hydrodynamic coefficients only represent rough approximations of the true fluid body interactions between the vehicles and its surrounding water. Additionally, some assumptions about symmetries of the vehicles geometry do not fully hold introducing cross coupling effects. Finally, the actuator dynamics are only roughly approximated, and are more complex in reality, which is specifically true for U-CAT's actuator dynamics. However, the proposed control framework has already proven a good robustness to modeling uncertainties using the BDO. Additional model identification and adaptation can be employed to improved the used dynamics model [209, 210, 211, 212]. Of course, real world tests with U-CAT are the next necessary step to validate the controller performance and its potential to solve the problem of reliable full state feedback for higher order pose derivatives. Additionally, such experiments would show if there is a benefit of using discontinuous full state feedback instead of a model free feedback loop as used for example in [185]. Such experiments are currently under preparation and will be conducted in the near future.

4.7 Summary and conclusions

This chapter introduced the problem of trajectory tracking in the horizontal plane for underactuated AUVs subject to motion constraints. A new control framework was derived taking ideas from event-based control and using the property of differential flatness. The

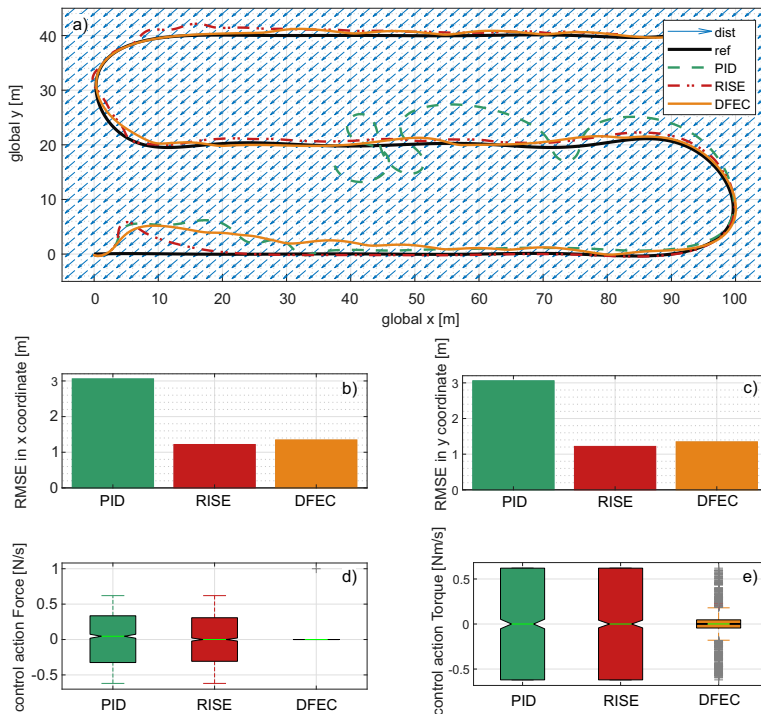


Figure 34 – Controller performances for simulated LAUV dynamics. a) Global x and y coordinates for trajectory tracking using PID, RISE and flat event controller. A lawn mower trajectory was computed for an area of 100 m x 45 m and the target velocity was set to 1.5 m/s. A disturbance was introduced as constant irrotational water flow (blue arrows / not to scale) at an incidence angle of 45° and a magnitude of 0.5 m/s corrupted by zero-centered white Gaussian noise with a variance of 0.01. b) RMSE for x-coordinate tracking for the three tested controllers. c) RMSE for y-coordinate tracking for the three tested controllers. d) - e) Distribution of control action for force / torque, defined as first derivative of the control force / torque, for the three tested controllers. The distribution of control action is shown as a box plot and represented by the median and IQR. Outliers are shown in red.

property of differential flatness was used to construct a controller that can guarantee efficient tracking of trajectories, while the ideas for event-based control were employed to deal with the problem of required state feedback of high order derivative that are hard to measure.

The resulting DFEC was derived for the dynamics of the bio-inspired AUV U-CAT. While the nominal AUV dynamics in the horizontal plane are *differentially flat* [publication IV], the dynamics of underactuated AUVs, such as U-CAT in its FAST motion mode, do not have that property. The state space model of U-CAT was then augmented by reducing the state space by one state (sway velocity), so that the resulting dynamics were *differentially flat*. Afterwards, a BDO was designed, to estimate the influences of the unmodeled state on the system dynamics. The estimated disturbances were then integrated into the proposed event-based controller following the DOBC concept. As additional benefit, the integration of the disturbance estimates increased the robustness of the controller against external disturbances. The proposed control scheme was tested in simulation in a disturbance free scenario and a scenario with disturbances modeled after irrotational constant water currents. The controller was then compared to a standard PID and a robust RISE controller using the metrics of RMSE and control action. The results showed that the proposed controller outperformed both standard controllers for both scenarios. Additionally, a third scenario was used to test the controller for disturbances and dynamics at a larger scale. To this end a more conventional torpedo shaped low-cost AUV, the LAUV, was simulated instead of U-CAT. Here the PID failed to track the trajectory successfully and the DFEC showed a similar performance in terms of RMSE to the RISE controller. However, the DFEC outperformed the RISE controller on the metric of control action.

In regards to the research question posed at the beginning of the chapter: "*How can model-based nonlinear controllers be augmented, to overcome limitations related to unreliable state feedback and motion constraints of AUVs with complex dynamics?*", it can be concluded that the simulation results provided a proof of concept that the combination of a feedforward controller based on the property of differential flatness for an augmented state space model, an event-based state feedback and a BDO can overcome the limitations stated in the research question. The simulation results also indicated potential benefits of the DFEC over standard model free controllers.

The main limitation for the presented trajectory tracking control scheme is the lack of real world tests. This limitation is currently addressed and the logistics are set up to test the controller on the real U-CAT vehicle. As far as the simulation is concerned, a more expansive simulation environment with a comparison to more advanced controllers such as [157], [185] or [158] and various extensions for the presented baseline controllers would be interesting and useful. Additionally, the robustness of various controllers should be tested for a wider variety of trajectories and disturbances. The work presented in this chapter should thus be seen as an initial step to establish the proposed control framework as a viable option for model-based trajectory tracking control for marine vehicles.

5 Conclusions

Here I provide an overview about the contributions that were presented in this thesis. This is followed by a discussion about the limitations of the presented work and possible future directions are mentioned.

5.1 Summary of thesis contributions

Small, agile, and low-cost AUVs have the potential to significantly expand the use of autonomous vehicles as tools for environmental monitoring and exploration. However, the reduction in size and cost comes with a trade-off in capabilities in the areas of state estimation, actuation and motion control. To extend the autonomous capabilities of small, agile, and low-cost AUVs, the work presented in this thesis was aimed at addressing one problem in each of the three areas, by asking the following research questions:

- 1) How can state estimation under field conditions for AUVs, with a specific focus on small resource constraint autonomous underwater vehicles, be improved based on ubiquitous environmental information?
- 2) Can asymmetric actuation increase maneuverability of AUVs using compliant bio-inspired actuators?
- 3) Can a model-based nonlinear controller combining ideas from event based control, differential flatness and disturbances estimation, be used to improve the trajectory tracking performance of AUVs with complex dynamics and motion constraints?

In line with the three research questions, the contributions of the work described in this thesis fall into the same three research areas, state estimation, actuator control and motion control, which are all embedded within the framework of mobile vehicle autonomy.

The main contribution in the first area, state estimation, is the extension and advancement of a differential pressure sensor based system for the estimation of velocity for AUVs. The main advantages of the proposed sensor system, compared to state of the art technology, are its small size, low energy consumption and the lack of potentially adverse effects on the environment during operation. The developed technology is based on the sensing of differential pressure and potential flow theory. To that end a simple potential flow model was derived from first principles to extend an empirical model previously build using an early laboratory prototype [38]. The efficacy of various prototypes was tested in laboratory conditions and most importantly under field conditions. Pressure based sensors for environmental sampling have been successfully tested in the field beforehand [32, 33, 34], however the field tests with the developed prototypes constituted to the best of my knowledge the first application of differential pressure based sensing on AUVs. By combining the new sensor system with state of the art technology providing complementary information it was possible to gather in-situ information about tidal currents.

With respect to actuator control, the main contribution of this thesis is the development of an asymmetric actuation scheme for the orientation control of the FILOSE robot, a fish-like robot with a compliant motor-actuated tail. The application of asymmetric actuation to support orientation control provides a novel tool in the control framework for robots with bio-inspired propulsors. The efficacy of the proposed solution was tested under field conditions where it outperformed the standard approach for turning in fish-like robots due to the motion restrictions of the specific robot in question. The control and actuation framework also showed a certain robustness to environmental disturbances.

However, orientation control alone will not provide sufficient autonomy for the FILOSE robot, so that methods for path following or trajectory tracking would be required. This necessitates robust and precise capabilities in navigation, that are hard to achieve on robots of this type. The FILOSE robot employs an array of absolute pressure sensors to aid in navigation and the research presented in *Chapter 2* could be used to improve this sensing modality, linking the contributions of this thesis in the fields of state estimation and actuation. From an autonomy perspective orientation control by itself is not sufficient and methods to ensure path following or trajectory tracking capabilities are required. The FILOSE robot is underactuated and motions in different DOFs are coupled which makes it difficult to apply some traditional motion control techniques. This provides a link to the contributions of this thesis in the area of motion control that will be summarized below.

To answer the third research question which concerns motion control, a novel control framework for trajectory tracking in the horizontal plane was developed. The controller is based on ideas from event-based control and makes use of the property of differential flatness. To enable trajectory tracking for a class of underactuated vehicles that is very common among AUVs, the system dynamics were augmented and a disturbance observer was designed to estimate any adverse affects of this augmentation on the vehicle dynamics. The estimated disturbances were integrated into the control scheme, which increased the robustness of the resulting controller. The proposed control framework was tested in simulation on a small low-cost AUV with bio-inspired actuation (U-CAT) and a commercial low-cost torpedo shaped AUV (LAUV). The controller performance was assessed for scenarios with and without external disturbances and compared to standard model free controllers. The results indicate that the proposed control scheme is a viable alternative for trajectory tracking problems for AUVs.

U-CAT is another good example to highlight the connections between the different research contributions of this thesis. The design of the new motion controller assumed that the problems of actuation control and state estimation have been sufficiently solved. However, U-CAT is too small and has a too low budget to employ state of the art velocity sensing technologies, so that adequate state estimation for velocity and position is entirely dependent on VO or VIO. Salient features for vision based state estimation are not always present. Even given that the most likely application scenarios for the robot are confined spaces with sufficient environmental markers, it U-CAT has to reach the target location first. A velocity aiding as could be provided by the DPSS prototypes would thus be very valuable. Additionally, the versatility of U-CAT's four flipper based propulsion system has not been fully explored. Initial tests show that the rotation of the fins can create large torques that could be leveraged for orientation control. Here the asymmetric control approach developed in this thesis could be a helpful starting point. Even a direct implementation of the skewed waveform could be useful for applications were a reorientation of U-CAT's fins would be detrimental.

5.2 Future directions

In this section some broader research questions are discussed that go beyond the limitations and future work discussed in the conclusion sections of the respective chapters.

The present versions of the DPSS prototypes were mainly designed for velocity estimation, however, such designs do not use the full potential of pressure based measurements. Ongoing work investigates the capability of the existing prototypes to detect environmental features that affect ambient pressure, while simultaneously providing velocity information for an AUV. Adding more differential pressure sensors to the prototypes can extend to include an artificial lateral line type sensor array, can enable the detection of various

flow features [213, 214, 215, 216]. Extensions of the DPSS prototypes could therefore enable other researchers to bridge the gap between simulations or controlled laboratory environments and applications in the field. Additionally, the presented research provides potential platforms for testing or implementing findings related to biology such as stated in [217].

Reversely, the research about asymmetric actuation presented in *Chapter 3* could inspire more investigations into how asymmetric forces are used in fish beyond thrust modification. A better investigation of the fluid-body interactions between compliant actuators and surrounding fluid during asymmetric actuation would benefit the related controller design. From a more practical point of view, it seems very promising to test the concept of asymmetric actuation for robots that are using several flippers such as U-CAT [58] or Aqua [218] to increase maneuverability.

Regarding the proposed trajectory tracking controller proposed in *Chapter 4*, the reduction of the tracking problem to the horizontal plane, made sense for a proof of concept but is not the final goal. Work is ongoing to implement and test a 3D trajectory tracking scheme. The ability to efficiently track trajectories in three dimensions would be specifically useful in combination with more sophisticated trajectory generation frameworks as shown for example in [185] or in [171].

A limitation of model based controllers in general, is their dependency on a very accurate dynamics model. The complex actuator dynamics of U-CAT might necessitate additional, potentially online, identification procedures to bring the dynamics model to an acceptable level of accuracy. Such a dynamics model augmentations could be done with Gaussian processes as shown in a different context by McKinnon et al. [219].

Generally, the possible range of application of the proposed control framework reaches beyond marine robotics, such that this controller could be potentially useful for terrestrial robots that experience significant slip as shown in [184] or for aerial vehicles where underactuation in sway direction would lead to substantially more sideslip due to the lag of environmental damping.

As a whole, a guiding principle for future research will be the maturation of the proposed solutions, so that they can reliably improve the navigation and motion capabilities of small low-cost AUVs, which in turn will enable a much bigger variety of researchers to investigate the underwater environment.

List of Figures

1	Research presented in this thesis in the context of robot autonomy. Each of the chapters provides an attempt to answer one of the research questions, and describes contributions to a different layer of the mobile robot autonomy framework. Each box briefly mentions main contributions, which research question is addressed and which publications display the respective research.	16
2	Body fixed and earth fixed reference frames according to SNAME notation.	19
3	Superposition of a uniform flow field and a three dimensional doublet flow. The uniform flow is characterized by its free stream velocity V_∞ and the doublet is characterized by its strength μ_D . Space is defined by the spherical coordinates r_S, φ, Ψ . adapted from [79]	25
4	Irrrotational, inviscid and incompressible flow over a sphere for two measurement points [publication II]. The stagnation point on the spheres surface is indicated by A. (a) We introduce the static point B, respective velocities v_A, v_B and the enclosing angle φ_{ST} . (b) We introduce an arbitrary surface point C, respective velocities v_A, v_C and the enclosing angle φ . In both cases v_∞ denotes the free stream velocity	28
5	Irrrotational, inviscid and incompressible flow over a sphere for three measurement points and at angled ambient [publication V]. a) Point A marks the stagnation point on the spheres' surface where the local velocity is zero. Points B and B* describe mirrored and arbitrary positions at the spheres' surface for an angle $0^\circ \leq \varphi_C \leq 90^\circ$. b) Point A is angled towards the flow by α and the local velocity is nonzero. Given the same configuration as in a) both measurement points A and B are shifted by the angle of incoming flow.	29
6	DPSS housing and pressure tab location [publication II]. a) Isometric view of a CAD model of the 3D printed DPSS housing indicating the location of the pressure tabs that directly connect to the differential pressure sensors. b) Top view of a schematic drawing of the DPSS with indications at which planar angle (relative to the local x-axis starting at the center of the spherical outermost section of the housing) the pressure taps are located.	31
7	Exploded view of DPSS CAD Assembly [publication II]. The DPSS is shown together with a custom made frame and covers that reproduce the payload section of the SPARUS II AUV. A new frame and new covers are used to ensure a spherical geometry at the head of the AUV during trials with the DPSS, so that the derived potential flow model can be directly applied.	31
8	SPARUS II AUV [publication II]. On left SPARUS II is shown with integrated DPSS in an indoor pool at the Underwater Robotics Research Centre (CIRS, University of Girona, Girona, Spain. Relevant specifications of SPARUS II can be seen on the right (adapted from [81])	32
9	Geographic location of the test site [publication II]. Harbor area of Sant Feliu de Guíxols (Catalonia, Spain). WGS84 (km) — 41.7775° N, 3.0325° E	33

10	Logarithmic density plot for the correlation between DVL-BL and DPSS surge velocity estimates [publication II]. a) Correlation plot for experiments across all scenarios, b) - d) plots for environmental settings A-C. For all plots an assumed perfect fit $v_x^{DVL} = v_x^{DPSS}$ is shown as red dotted line and the R^2 value, computed based on the assumed perfect fit, is shown as a quantitative measure of the correlation.	34
11	RMSE between various surge velocity estimations at different target velocities [publication II]. a) DPSS vs DVL-BL and b) DVL-WL vs DVL-BL. Repeitions of the same experimental configuration are distinguished by color and the three different environmental settings are differentiated by line type.	35
12	Example of raw velocity readings for DPSS and DVL-BL for lawn mower trajectory [publication II]. At around 90 s SPARUS II got close to the harbor wall, where the ground is unstructured and rough. This disadvantageous environmental conditions is clearly reflected in the sensor output. It can be clearly seen that the DPSS was not affected. Differences at the beginning and the end of the plot are due to vertical movement of the robot which was not compensated for in the DPSS.	36
13	The new DPSSv2 prototype. a) fully assembled prototype with 3D printed housing. b) Electronic component architecture of the DPSSv2 with the following notation: APS - absolute pressure sensor, SD - SD card, Micro - Microcontroller, BAT - Battery pack, IMU - Inertial Measurement Unit, ADC - Analog to Digital Converter, DPS - <i>differential pressure</i> sensor.	37
14	Test site and experimental setup [publication V]. a) and b) Indication of the test site near the Island of Tautra in the Trondheim Fjord, Norway. The right site of b) shows the exact location of the experiments as a red dot. Tidal currents patterns for the upper fluid layer are shown as black arrows (reproduced from [98]). c) and d) Experimental setup to test the capability of the DPSSv2 for 2D velocity estimation in the presence of ambient flows. The main direction was assumed to be as shown in b) and the LAUV was operated alternately driven in-line and against this predicted tidal current main direction. A surface vehicle with an ADCP was employed to provide an additional resource for water flow estimation. e) Tidal cycle for the day of the experiments (2019/05/20). The gray area in the tidal graph represents the time slot of the experiments.	38
15	LAUV Fridtjof with attached DPSSv2 [publication V]. The AUV used DVL, GPS and INS for navigation and the DPSSv2 was sampling independently. ...	39

16	<p>Estimation of tidal current velocity vector for DVL, DPSSv2 and ADCP [publication V]. Tidal current estimates for the DVL and DPSSv2 are both augmented by DVL-BL readings. a) Magnitude estimates of the tidal current in the global reference frame represented by median, IQR and extreme values for each trial. b) and c) Median magnitude and heading estimates of the tidal current relative to true north for DVL and DPSSv2 (ADCP estimates are not used in the performance comparison and thus omitted to improve the readability of the figure). The difference between the two median heading estimates in degrees is annotated for each trial. Instances where the LAUV was moving with the tidal currents, shown in c), are distinguished from instances where the LAUV was moving against the tidal currents, shown in d). The trial numbers are further augmented with either (s) for trials with the slower target velocity of 1.25 m/s or (f) for the faster target velocity of 1.5 m/s. The light beige patch (trials 1-6) represents slack water conditions close to high tide, where the currents are less strong, more turbulent and change direction eventually. The light grey patch (trials 7 to 14) shows the tidal conditions for ebb flow, which occurs after the maximum tidal water level has been reached.</p>	40
17	<p>Specifics of the FILOSE robot [publication III]. a) Side view: 1 - rigid head of the robot; 2 - compliant silicon tail; 3 - rigid fin; 4 - Styrofoam float; 5 - splash proof box containing battery pack and Bluetooth module. b) CAD drawing of electronics and actuation mechanism: 6 - microcontroller and orientation sensor; 7 - servomotor; 8 - steel cables; 9 - actuation plate</p>	46
18	<p>Asymmetric Periodic Waveform [publication III]. All functions are normalized and have a wave period $T = 1$ s. The skewed triangle waves are represented by the limit cases $sk = 0.9$ and $sk = 0.1$, all other waveforms lie between these two cases. The standard sine wave commonly used for actuation is shown as reference</p>	48
19	<p>Skew factor τ vs. heading error [publication III]. The choice of the tightness factor a determines the error bandwidth for which the derived controller operates between the two maximum skew factors of 0.9 and 0.1. A bigger tightness factor leads to an increased tracking rate, but also to a higher risk of overshoot. For very high tightness factors the controller approximates a bang bang control.</p>	49
20	<p>The proposed control scheme [publication III]: The shown parameters are: ψ - yaw, ψ_m - measured yaw, ψ_d - desired yaw, $\hat{\psi}$ - heading error ($\psi_m - \psi_d$), sk - skew factor, $\varphi^{(*)}$ - motor input, N - body torque, A - actuation amplitude and f - actuation frequency</p>	49
21	<p>Results of the field trials [publication III]. Shown are the time series of instantaneous (red) and averaged over one tail beat cycle (blue), yaw angle during field tests for different parameter settings. For figures b) - d) the time series of the skew factor (grey) is shown to visualize the control action. In a) the default orientation control with an oscillation offset of $\varphi_0 = 10^\circ$ was used. In b) - d) the novel orientation control was applied with tightness factors of $a = 20, 5, 0.1$ respectively. The controller performance is characterized by the rise time from 10 % to 90 % of the desired yaw, the overshoot in % of the desired yaw and the settling time where the actual yaw stays within a 2 % error band of the desired yaw.</p>	51

22	Flow chart for the DFEC algorithm based on work presented in publication IV. The algorithm starts with the initialization of the polynomial p_m so that the feedforward trajectory coincides with the flat output of the dynamics, which are state space variables of the robot. The time t_{event} represents the last time an event has occurred and therefore resets the timing of the controller for each event so that a fresh feedforward trajectory can be generated starting from known "initial" conditions that are provided by the event based feedback.	64
23	Rendering of bio-inspired AUV U-CAT with 4-fin propulsion. The vehicle is shown in FAST mode configuration where all flippers point towards the back of the robot when not actuated. This is the configuration that will be used throughout the subsequent controller development.	68
24	Top view of U-CAT with indications for the direction of mean forces τ that are produced by oscillations of each flipper around an axis in the horizontal plane [publication IV]. a) Fin configuration for SLOW mode. In this configuration the robot can be theoretically actuated in all degrees of freedom simultaneously. However, the control allocation problem that arises is still subject to investigation and it is unclear how efficient the resulting motions will be. U-CAT also only uses half of its available fins for surging which leads to constant pitch oscillations and a lower maximum achievable speed. b) fin configuration for FAST mode. Here all fins can be utilized for actuation in surge direction. However, the sway direction becomes uncontrollable making the vehicle in this configuration underactuated (at least for maneuvers that include the simultaneous control of several DOFs.	69
25	Present autonomy framework of U-CAT as shown in [200].	70
26	Updated autonomy framework for the U-CAT AUV. An orange border indicates novel functionalities, compared to the framework in <i>Figure 25</i> , and green borders indicate existing functionalities that have been extended or improved	71
27	Example of a lawn mower path. The lawn mower type path generated by the planner node of the new autonomy framework is shown in red. The user defined area that is the input to the path planner providing the seed points for the Dubins model based path generation is shown in green	71
28	Trajectory tracking performance for the flat event controller when disturbances were absent. a) and c) Description of the position tracking performance for global x and y position. b) and d) Velocity tracking performance along the global x and y axes. e) - f) Control force in surge and control torque in yaw. g) Occurrence of events denoted in a binary graph, where 0 means no event and 1 means event.	75
29	Trajectory tracking performance for the flat event controller when disturbances were present. Disturbances were modeled as modeled as a constant irrotational fluid flow with an incidence angle of 45° and a magnitude of 0.5 m/s. a) and c) Position tracking performance for global x and y position. b) and d) Velocity tracking performance along the global x and y axes. e) - f) Control force in surge and control torque in yaw. g) Occurrence of events denoted in a binary graph, where 0 means no event and 1 means event.	76

30	Disturbance estimates for the DFEC. a) - b) Kinematic disturbances in global x and y directions. c) - d) Dynamic disturbances in global x and y directions	76
31	Visualization of planar tracking for the three tested controllers. a) Without disturbances and b) With disturbances illustrated as blue arrows. The arrows show the correct incidence angle but the arrow length is a scaled representation of the magnitude. The flow was modeled as a constant irrotational fluid flow with an incidence angle of 45° and a magnitude of 0.5 m/s.....	77
32	RMSE for the three tested controllers with and without disturbances. a) and c) Tracking performance of the three tested controllers for global x and y directions when disturbances were absent. b) and d) Tracking performance of the three tested controllers for global x and y directions when disturbances were present. The disturbance was modeled as a constant irrotational fluid flow with an incidence angle of 45° and a magnitude of 0.5 m/s.....	77
33	Control action for the three tested controllers controllers. Control action is quantified by the first time derivative of the time series of control commands, which the controllers have issued during a simulation run. The control action for one run is then characterized using the median and IQR, which are shown in the figure. Additionally, "outliers" expressing large changes in subsequent control signals, are represented in red.	78
34	Controller performances for simulated LAUV dynamics. a) Global x and y coordinates for trajectory tracking using PID, RISE and flat event controller. A lawn mower trajectory was computed for an area of 100 m x 45 m and the target velocity was set to 1.5 m/s. A disturbance was introduced as constant irrotational water flow (blue arrows / not to scale) at an incidence angle of 45° and a magnitude of 0.5 m/s corrupted by zero-centered white Gaussian noise with a variance of 0.01. b) RMSE for x-coordinate tracking for the three tested controllers. c) RMSE for x-coordinate tracking for the three tested controllers. d) - e) Distribution of control action for force / torque, defined as first derivative of the control force / torque, for the three tested controllers. The distribution of control action is shown as a box plot and represented by the median and IQR. Outliers are shown in red. 80	80

List of Tables

1	SNAME notation for marine vessels [40]	19
2	Comparison of DPSSv2 with three small DVLs for size, weight and power consumption / adapted from [2]	37
3	Model parameters used to simulate U-CAT's dynamics	72
4	Parameters for different simulation scenarios. Im - lawn mower, α_{flow} - angle at which water flow disturbance acts in the inertial frame.....	73
5	PID controller gains for different simulation scenarios	73
6	RISE controller gains for different scenarios	73
7	Flat-event controller gains for different scenarios	74
8	BDO gains calculated based on (75)	74

References

- [1] J. F. Fuentes-Pérez, C. Meurer, J. A. Tuhtan, and M. Kruusmaa, "Differential Pressure Sensors for Underwater Speedometry in Variable Velocity and Acceleration Conditions," IEEE Journal of Oceanic Engineering, vol. 43, no. 2, pp. 418–426, 2018.
- [2] C. Meurer, J. Francisco Fuentes-Perez, N. Palomeras, M. Carreras, and M. Kruusmaa, "Differential Pressure Sensor Speedometer for Autonomous Underwater Vehicle Velocity Estimation," IEEE Journal of Oceanic Engineering, pp. 1–33, 2019.
- [3] C. Meurer, A. Simha, Ü. Kotta, and M. Kruusmaa, "Nonlinear orientation controller for a compliant robotic fish based on asymmetric actuation," in Proceedings - IEEE International Conference on Robotics and Automation (ICRA), vol. 2019-May, pp. 4688–4694, Institute of Electrical and Electronics Engineers Inc., may 2019.
- [4] A. Kaldmäe, Ü. Kotta, C. Meurer, and A. Simha, "Event-based control for differentially flat systems: Application to autonomous underwater vehicle," in IFAC-PapersOnLine, vol. 52, pp. 180–185, Elsevier B.V., sep 2019.
- [5] C. Meurer, J. F. Fuentes-Perez, K. Schwarzwald, M. Ludvigsen, A. J. Sorensen, and M. Kruusmaa, "2D estimation of velocity relative to water and tidal currents based on differential pressure for autonomous underwater vehicles," IEEE Robotics and Automation Letters, vol. 5, pp. 3444–3451, apr 2020.
- [6] I. A. Shiklomanov, "World fresh water resources," in Water in Crisis: A Guide to the Worlds Fresh Water Resources (P. H. Gleick, ed.), ch. 2, pp. 13–24, New York: Oxford University Press, 1993.
- [7] U. Nations, "Factsheet: People and oceans," in 2017 UN Ocean Conference, United Nations, 2017.
- [8] N. J. Nilsson, Principles of artificial intelligence. Morgan Kaufmann, 2014.
- [9] H. P. Moravec, "The stanford cart and the cmu rover," Proceedings of the IEEE, vol. 71, no. 7, pp. 872–884, 1983.
- [10] N. Palomeras, A. El-Fakdi, M. Carreras, and P. Ridao, "COLA2: A control architecture for AUVs," IEEE Journal of Oceanic Engineering, vol. 37, no. 4, pp. 695–716, 2012.
- [11] L. Stutters, H. Liu, C. Tiltman, and D. J. Brown, "Navigation technologies for autonomous underwater vehicles," IEEE Transactions on Systems, Man and Cybernetics Part C: Applications and Reviews, vol. 38, no. 4, pp. 581–589, 2008.
- [12] A. Griffiths, A. Dikarev, P. R. Green, B. Lennox, X. Poteau, and S. Watson, "Avexis—aqua vehicle explorer for in-situ sensing," IEEE Robotics and Automation Letters, vol. 1, no. 1, pp. 282–287, 2016.
- [13] S. Mintchev, E. Donati, S. Marrazza, and C. Stefanini, "Mechatronic design of a miniature underwater robot for swarm operations," in 2014 IEEE International Conference on Robotics and Automation (ICRA), pp. 2938–2943, IEEE, 2014.
- [14] H. Singh, T. Maksym, J. Wilkinson, and G. Williams, "Inexpensive, small auvs for studying ice-covered polar environments," Science Robotics, vol. 2, no. 7, pp. 1–2, 2017.

- [15] A. Sousa, L. Madureira, J. Coelho, J. Pinto, J. Pereira, J. Borges Sousa, and P. Dias, "LAUV: The Man-Portable Autonomous Underwater Vehicle," IFAC Proceedings Volumes, vol. 45, pp. 268–274, jan 2012.
- [16] C. Edge, S. S. Enan, M. Fulton, J. Hong, J. Mo, K. Barthelemy, H. Bashaw, B. Kallevig, C. Knutson, K. Orpen, et al., "Design and experiments with loco auv: A low cost open-source autonomous underwater vehicle," arXiv preprint arXiv:2003.09041, 2020.
- [17] M. R. P. Ltd., "Autonomous underwater vehicle (auv) market by type (shallow auvs, medium auvs, large auvs), application (military & defense, oil & gas), shape, technology (navigation, imaging), payload type (cameras, sensors), region – global forecast to 2025," 2021.
- [18] S. Bhat and I. Stenius, "Hydrobotics: A review of trends, challenges and opportunities for efficient and agile underactuated auvs," in 2018 IEEE/OES Autonomous Underwater Vehicle Workshop (AUV), pp. 1–8, IEEE, 2018.
- [19] J. Weston and D. Titterton, "Modern inertial navigation technology and its application," Electronics & Communication Engineering Journal, vol. 12, no. 2, pp. 49–64, 2000.
- [20] R. Gisiner, S. Harper, E. Livingston, and J. Simmen, "Effects of sound on the marine environment (esme): An underwater noise risk model," IEEE Journal of Oceanic Engineering, vol. 31, no. 1, pp. 4–7, 2006.
- [21] S. Isojunno, P. J. Wensveen, F.-P. A. Lam, P. H. Kvadsheim, A. M. von Benda-Beckmann, L. M. M. López, L. Kleivane, E. M. Siegal, and P. J. Miller, "When the noise goes on: received sound energy predicts sperm whale responses to both intermittent and continuous navy sonar," Journal of Experimental Biology, vol. 223, no. 7, 2020.
- [22] Y. Yang, N. Nguyen, N. Chen, M. Lockwood, C. Tucker, H. Hu, H. Bleckmann, C. Liu, and D. L. Jones, "Artificial lateral line with biomimetic neuromasts to emulate fish sensing," Bioinspiration and Biomimetics, vol. 5, pp. 16001–16010, jan 2010.
- [23] V. I. Fernandez, A. Maertens, F. M. Yaul, J. Dahl, J. H. Lang, and M. S. Triantafyllou, "Lateral-line-inspired sensor arrays for navigation and object identification," Marine Technology Society Journal, vol. 45, pp. 130–146, jul 2011.
- [24] A. Gao and M. Triantafyllou, "Bio-inspired pressure sensing for active yaw control of underwater vehicles," in OCEANS 2012 MTS/IEEE, pp. 1–7, IEEE, oct 2012.
- [25] C. Wang, W. Wang, and G. Xie, "Speed estimation for robotic fish using onboard artificial lateral line and inertial measurement unit," in 2015 IEEE International Conference on Robotics and Biomimetics (ROBIO), (Zhuhai), pp. 285–290, IEEE, 2015.
- [26] F. Zhang, F. D. Lagor, D. Yeo, P. Washington, and D. A. Paley, "Distributed flow sensing for closed-loop speed control of a flexible fish robot," Bioinspiration & Biomimetics, vol. 10, no. 6, p. 65001, 2015.
- [27] N. Strokina, J. K. Kamarainen, J. A. Tuhtan, J. F. Fuentes-Perez, and M. Kruusmaa, "Joint Estimation of Bulk Flow Velocity and Angle Using a Lateral Line Probe," IEEE Transactions on Instrumentation and Measurement, vol. 65, pp. 601–613, mar 2016.

- [28] Y. Xu and K. Mohseni, "A Pressure Sensory System Inspired by the Fish Lateral Line: Hydrodynamic Force Estimation and Wall Detection," IEEE Journal of Oceanic Engineering, vol. 42, pp. 532–543, jul 2017.
- [29] W. K. Yen, D. M. Sierra, and J. Guo, "Controlling a Robotic Fish to Swim Along a Wall Using Hydrodynamic Pressure Feedback," IEEE Journal of Oceanic Engineering, vol. 43, pp. 369–380, apr 2018.
- [30] M. Li, Z. Shang, R. Wang, and T. Li, "Attitude determination of autonomous underwater vehicles based on hydromechanics," in Proceedings of the World Congress on Intelligent Control and Automation (WCICA), vol. 2016-September, pp. 292–296, Institute of Electrical and Electronics Engineers Inc., sep 2016.
- [31] J. Zheng, X. Zheng, T. Zhang, M. Xiong, and G. Xie, "Dual-sensor fusion based attitude holding of a fin-Actuated robotic fish," Bioinspiration and Biomimetics, vol. 15, p. 046003, jul 2020.
- [32] J. N. Moum, "Ocean speed and turbulence measurements using pitot-static tubes on moorings," Journal of Atmospheric and Oceanic Technology, vol. 32, no. 7, pp. 1400–1413, 2015.
- [33] J. A. Tuhtan, J. F. Fuentes-Perez, G. Toming, and M. Kruusmaa, "Flow velocity estimation using a fish-shaped lateral line probe with product-moment correlation features and a neural network," Flow Measurement and Instrumentation, vol. 54, pp. 1–8, apr 2017.
- [34] J. A. Tuhtan, J. F. Fuentes-Perez, G. Toming, M. Schneider, R. Schwarzenberger, M. Schletterer, and M. Kruusmaa, "Man-made flows from a fish's perspective: Autonomous classification of turbulent fishway flows with field data collected using an artificial lateral line," Bioinspiration and Biomimetics, vol. 13, p. 046006, may 2018.
- [35] T. I. Fossen, Handbook of marine craft hydrodynamics and motion control. John Wiley & Sons, 2011.
- [36] J. Lunze and M. Miskowicz, "Event-based control: introduction and survey," Event-based control and signal processing, pp. 3–20, 2016.
- [37] J. Levine, Analysis and control of nonlinear systems: A flatness-based approach. Springer Science & Business Media, 2009.
- [38] J. F. Fuentes-Pérez, K. Kalev, J. A. Tuhtan, and M. Kruusmaa, "Underwater vehicle speedometry using differential pressure sensors: Preliminary results," in 2016 IEEE/OES Autonomous Underwater Vehicles (AUV), pp. 156–160, 2016.
- [39] B. Xian, D. M. Dawson, M. S. de Queiroz, and J. Chen, "A continuous asymptotic tracking control strategy for uncertain nonlinear systems," IEEE Transactions on Automatic Control, vol. 49, no. 7, pp. 1206–1211, 2004.
- [40] T. I. Fossen, "Marine control systems—guidance, navigation, and control of ships, rigs and underwater vehicles," Marine Cybernetics, Trondheim, Norway, Org. Number NO 985 195 005 MVA, ISBN: 82 92356 00 2, 2002.
- [41] P. E. Hagen, O. Midtgaard, and O. Hasvold, "Making AUVs truly autonomous," in OCEANS 2007, IEEE, 2007.

- [42] L. Paull, S. Saeedi, M. Seto, and H. Li, "AUV navigation and localization: A review," IEEE Journal of Oceanic Engineering, vol. 39, no. 1, pp. 131-149, 2014.
- [43] M. Dunbabin, P. Corke, and G. Buskey, "Low-cost vision-based AUV guidance system for reef navigation," in Proceedings - IEEE International Conference on Robotics and Automation, vol. 2004, pp. 7-12, Institute of Electrical and Electronics Engineers Inc., 2004.
- [44] S. Wirth, P. L. N. Carrasco, and G. O. Codina, "Visual odometry for autonomous underwater vehicles," in OCEANS 2013 MTS/IEEE Bergen: The Challenges of the Northern Dimension, 2013.
- [45] J. C. Kinsey, R. M. Eustice, and L. L. Whitcomb, "A Survey of Underwater Vehicle Navigation: Recent Advances and New Challenges," IFAC Conference on Maneuvering and Control of Marine Craft, vol. 88, no. April 2016, pp. 1-12, 2006.
- [46] M. Hildebrandt and F. Kirchner, "IMU-aided stereo visual odometry for ground-tracking AUV applications," in OCEANS'10 IEEE Sydney, OCEANSSYD 2010, 2010.
- [47] B. Jalving, K. Gade, K. Svartveit, A. Willumsen, and R. Sørhagen, "DVL velocity aiding in the HUGIN 1000 integrated inertial navigation system," Modeling, Identification and Control, vol. 25, no. 4, pp. 223-235, 2004.
- [48] Z. Song and K. Mohseni, "Long-Term Inertial Navigation Aided by Dynamics of Flow Field Features," IEEE Journal of Oceanic Engineering, vol. 43, pp. 940-954, oct 2018.
- [49] N. Muhammad, J. F. Fuentes-Perez, J. A. Tuhtan, G. Toming, M. Musall, and M. Kruusmaa, "Map-based localization and loop-closure detection from a moving underwater platform using flow features," Autonomous Robots, vol. 43, pp. 1419-1434, aug 2019.
- [50] L. Whitcomb, D. Yoerger, H. Singh, and D. Mindell, "Towards Precision Robotic Maneuvering , Survey , and Manipulation in Unstructured Undersea Environments-1 Introduction," Robotics Research - The Eighth International Symposium, vol. 8, pp. 45-54, 1998.
- [51] G. Grenon, P. E. An, S. M. Smith, and A. J. Healey, "Enhancement of the inertial navigation system for the Morpheus autonomous underwater vehicles," IEEE Journal of Oceanic Engineering, vol. 26, no. 4, pp. 548-560, 2001.
- [52] O. Hegrenæs, E. Berglund, Ø. Hegrenæs, and E. Berglund, "Doppler water-track aided inertial navigation for autonomous underwater vehicle," in OCEANS 2009-EUROPE, (Bremen), pp. 1-10, IEEE, may 2009.
- [53] M. J. Stanway, "Water profile navigation with an Acoustic Doppler Current Profiler," OCEANS'10 IEEE Sydney, OCEANSSYD 2010, no. Dvl, 2010.
- [54] L. Medagoda, J. C. Kinsey, and M. Eilders, "Autonomous Underwater Vehicle localization in a spatiotemporally varying water current field," in 2015 IEEE International Conference on Robotics and Automation (ICRA), no. June, IEEE, may 2015.
- [55] Teledyne Marine, Teledyne RDI Wayfinder DVL Brochure, 4 2021.
- [56] LinkQuest inc, NavQuest 600 Micro DVL Data Sheet, 4 2021.

- [57] Nortek, DVL1000 - 300 m technical specification, 4 2021.
- [58] T. Salumäe, R. Raag, J. Rebane, A. Ernits, G. Toming, M. Ratas, and M. Kruusmaa, "Design principle of a biomimetic underwater robot U-CAT," in 2014 Oceans - St. John's, (St. John's, NL), pp. 1-5, IEEE, 2014.
- [59] A. Underwood and C. Murphy, "Design of a micro-auv for autonomy development and multi-vehicle systems," in OCEANS 2017-Aberdeen, pp. 1-6, IEEE, 2017.
- [60] D. A. Duecker, N. Bauschmann, T. Hansen, E. Kreuzer, and R. Seifried, "Hippocampus-a hydrobatic open-source micro auv for confined environments," in 2020 IEEE/OES Autonomous Underwater Vehicles Symposium (AUV)(50043), pp. 1-6, IEEE, 2020.
- [61] D. L. Rudnick, R. E. Davis, C. C. Eriksen, D. M. Fratantoni, and M. J. Perry, "Underwater Gliders for Ocean Research," Marine Technology Society Journal, vol. 38, no. 2, pp. 73-84, 2004.
- [62] B. Allotta, R. Costanzi, A. Ridolfi, C. Colombo, F. Bellavia, M. Fanfani, F. Pazzaglia, O. Salvetti, D. Moroni, M. A. Pascali, M. Reggiannini, M. Kruusmaa, T. Salumae, G. Frost, N. Tsiogkas, D. M. Lane, M. Cocco, L. Gualdesi, D. Roig, H. T. Gündogdu, E. I. Tekdemir, M. I. C. Dede, S. Baines, F. Agneto, P. Selvaggio, S. Tusa, S. Zangara, U. Dresen, P. Latti, T. Saar, and W. Daviddi, "The ARROWS project: Adapting and developing robotics technologies for underwater archaeology," IFAC-PapersOnLine, vol. 48, no. 2, pp. 194-199, 2015.
- [63] C. Osterloh, T. Pionteck, and E. Maehle, "MONSUN II: A small and inexpensive AUV for underwater swarms," in 2012 7th German Conference on Robotics, pp. 1-6, [VDE Verlag], 2012.
- [64] blueye, blueye underwater drones, <https://www.blueyerobotics.com/> 2021-04.
- [65] ThorRobotics, ThorRobotics ROV dragonfish, <https://thorrobotics-shop.com/collections/dragonfish-200h-rov-max-depth-300m/products/thorrobotics-new-rov-underwater-drone-camera-dragonfish-200h-with-manipulator-arm> 2021-04.
- [66] K. H. Beij, "Aircraft Speed Instruments," tech. rep., NACA Rep. No. 42, 1933.
- [67] E. Ower and R. C. Pankhurst, The measurement of air flow. Elsevier, 2014.
- [68] H. Bleckmann and R. Zelick, "Lateral line system of fish.," mar 2009.
- [69] M. Asadnia, A. G. P. Kottapalli, R. Haghghi, A. Cloitre, P. V. Y. Alvarado, J. Miao, and M. Triantafyllou, "MEMS sensors for assessing flow-related control of an underwater biomimetic robotic stingray," Bioinspiration & Biomimetics, vol. 10, no. 3, pp. 1-15, 2015.
- [70] C. Abels, A. Quattieri, M. De Vittorio, W. M. Megill, and F. Rizzi, "A bio-inspired real-time capable artificial lateral line system for freestream flow measurements," Bioinspiration & Biomimetics, vol. 11, no. 3, p. 035006, 2016.
- [71] A. Klein and H. Bleckmann, "Determination of object position, vortex shedding frequency and flow velocity using artificial lateral line canals," Beilstein Journal of Nanotechnology, vol. 2, no. 1, pp. 276-283, 2011.

- [72] B. J. Wolf, J. A. Morton, W. N. Macpherson, and S. M. Van Netten, "Bio-inspired all-optical artificial neuromast for 2D flow sensing," Bioinspiration and Biomimetics, vol. 13, no. 2, 2018.
- [73] V. I. Fernandez, Performance analysis for lateral-line-inspired sensor arrays. PhD thesis, Massachusetts Institute of Technology, 2011.
- [74] R. Venturelli, O. Akanyeti, F. Visentin, J. Ježov, L. D. Chambers, G. Toming, J. Brown, M. Kruusmaa, W. M. Megill, and P. Fiorini, "Hydrodynamic pressure sensing with an artificial lateral line in steady and unsteady flows," Bioinspiration & biomimetics, vol. 7, no. 3, p. 36004, 2012.
- [75] T. Salumäe and M. Kruusmaa, "Flow-relative control of an underwater robot," Proceedings of the Royal Society A: Mathematical, Physical and Engineering Science, vol. 469, no. 2153, p. 20120671, 2013.
- [76] J. F. Fuentes-Pérez, Flow sensing with pressure sensor-based artificial lateral lines: From the laboratory to the field. PhD thesis, Ph. D. dissertation, Tallinn Univ. Technol., Tallinn, Estonia, 2019.
- [77] M. Krieg, K. Nelson, and K. Mohseni, "Distributed sensing for fluid disturbance compensation and motion control of intelligent robots," Nature machine intelligence, vol. 1, no. 5, pp. 216–224, 2019.
- [78] K. Nelson and K. Mohseni, "Hydrodynamic force decoupling using a distributed sensory system," IEEE Robotics and Automation Letters, vol. 5, no. 2, pp. 3235–3242, 2020.
- [79] J. Anderson Jr, Fundamentals of Aerodynamics, vol. Third Edit. Tata McGraw-Hill Education, 1985.
- [80] C. J. Fechheimer, "Measuring Device," 1931.
- [81] M. Carreras, C. Candela, D. Ribas, A. Mallios, L. L. Magí, E. Vidal, N. Palomeras, and P. Ridao, "Sparus II, design of a lightweight hovering AUV," Proceedings of the 5th international workshop on marine technology. Martech'13, pp. 152–155, 2013.
- [82] N. Palomeras, S. Nagappa, D. Ribas, N. Gracias, and M. Carreras, "Vision-based localization and mapping system for AUV intervention," in OCEANS-Bergen, 2013 MTS/IEEE, pp. 1–7, 2013.
- [83] E. Kalnay, Atmospheric modeling, data assimilation and predictability. Cambridge University Press, 2003.
- [84] T. O. Fossum, J. Eidsvik, I. Ellingsen, M. O. Alver, G. M. Fragoso, G. Johnsen, R. Mendes, M. Ludvigsen, and K. Rajan, "Information-driven robotic sampling in the coastal ocean," Journal of Field Robotics, vol. 35, pp. 1101–1121, oct 2018.
- [85] P. Encarnação, A. Pascoal, and M. Arcak, "Path Following for Marine Vehicles in the Presence of Unknown Currents," IFAC Proceedings Volumes, vol. 33, pp. 507–512, sep 2000.
- [86] A. P. Aguiar and A. M. Pascoal, "Dynamic positioning and way-point tracking of underactuated AUVs in the presence of ocean currents," in Proceedings of the 41st IEEE Conference on Decision and Control, 2002, vol. 2, IEEE, 2002.

- [87] J. E. Refsnes, K. Y. Pettersen, and A. J. Sørensen, "Control of slender body under-actuated AUVs with current estimation," in Proceedings of the IEEE Conference on Decision and Control, pp. 43–50, IEEE, 2006.
- [88] S. Moe, W. Caharija, K. Y. Pettersen, and I. Schjølberg, "Path following of under-actuated marine surface vessels in the presence of unknown ocean currents," in Proceedings of the American Control Conference, pp. 3856–3861, IEEE, jun 2014.
- [89] C. Paliotta and K. Y. Pettersen, "Geometric path following with ocean current estimation for ASVs and AUVs," in Proceedings of the American Control Conference, pp. 7261–7268, IEEE, jul 2016.
- [90] S. Fan, W. Xu, Z. Chen, and F. Zhang, "Nonlinear observer design for current estimation based on underwater vehicle dynamic model," in OCEANS 2016 - Shanghai, pp. 1–5, IEEE, apr 2016.
- [91] E. Kim, S. Fan, and N. Bose, "Autonomous Underwater Vehicle Model-Based High-Gain Observer for Ocean Current Estimation," in AUV 2018 - IEEE/OES Autonomous Underwater Vehicle Workshop, Proceedings, pp. 1–6, IEEE, nov 2018.
- [92] L. M. Merckelbach, R. D. Briggs, D. A. Smeed, and G. Griffiths, "Current measurements from autonomous underwater gliders," in Proceedings of the IEEE Working Conference on Current Measurement Technology, pp. 61–67, IEEE, 2008.
- [93] D. Chang, W. Wu, C. R. Edwards, and F. Zhang, "Motion tomography: Mapping flow fields using autonomous underwater vehicles," International Journal of Robotics Research, vol. 36, pp. 320–336, mar 2017.
- [94] R. N. Smith, J. Kelly, Y. Chao, B. H. Jones, and G. S. Sukhatme, "Towards the Improvement of Autonomous Glider Navigational Accuracy through the use of Regional Ocean Models," in ASME 2010 29th International Conference on Ocean, Offshore and Arctic Engineering, pp. 597–606, 2010.
- [95] D. Chang, F. Zhang, and C. R. Edwards, "Real-time guidance of underwater gliders assisted by predictive ocean models," Journal of Atmospheric and Oceanic Technology, vol. 32, pp. 562–578, mar 2015.
- [96] K. M. B. Lee, C. Yoo, B. Hollings, S. Anstee, S. Huang, and R. Fitch, "Online Estimation of Ocean Current from Sparse GPS Data for Underwater Vehicles," in IEEE 2019 International Conference on Robotics and Automation (ICRA), (Montreal), IEEE, 2019.
- [97] Ø. Hegrenæs and O. Hallingstad, "Model-aided INS with sea current estimation for robust underwater navigation," IEEE Journal of Oceanic Engineering, vol. 36, pp. 316–337, apr 2011.
- [98] P. Jacobson, "Physical Oceanography of the Trondheimsfjord," Geophysical & Astrophysical Fluid Dynamics, vol. 26, pp. 3–26, oct 1983.
- [99] Ø. Hegrenæs, O. Hallingstad, and B. Jalving, "A framework for obtaining steady-state maneuvering characteristics of underwater vehicles using sea-trial data," in 2007 Mediterranean Conference on Control and Automation, MED, pp. 1–6, IEEE, jun 2007.

- [100] Ø. Hegrehaes, O. Hallingstad, and B. Jalving, "Comparison of mathematical models for the HUGIN 4500 AUV based on experimental data," in International Symposium on Underwater Technology, UT 2007 - International Workshop on Scientific Use of Submarine Cables and Related Technologies 2007, pp. 558–567, IEEE, apr 2007.
- [101] D. Chang, C. R. Edwards, F. Zhang, and J. Sun, "A data assimilation framework for data-driven flow models enabled by motion tomography," International Journal of Intelligent Robotics and Applications, vol. 3, pp. 158–177, jun 2019.
- [102] A. A. R. Gao, Sensing and control for fishlike propulsion in unsteady environments. PhD thesis, Massachusetts Institute of Technology, 2018.
- [103] C. Nowack, "Improved calibration method for a five-hole spherical pitot probe," Journal of Physics E: Scientific Instruments, vol. 3, no. 1, p. 21, 1970.
- [104] E. N. Brown, C. Friehe, and D. Lenschow, "The use of pressure fluctuations on the nose of an aircraft for measuring air motion," Journal of Applied Meteorology and Climatology, vol. 22, no. 1, pp. 171–180, 1983.
- [105] S. Shaw-Ward, A. Titchmarsh, and D. M. Birch, "Calibration and use of n-hole velocity probes," AIAA Journal, vol. 53, no. 2, pp. 336–346, 2015.
- [106] B. Allen, R. Stokey, T. Austin, N. Forrester, R. Goldsborough, M. Purcell, and C. von Alt, "Remus: a small, low cost auv; system description, field trials and performance results," in Oceans' 97. MTS/IEEE Conference Proceedings, vol. 2, pp. 994–1000, IEEE, 1997.
- [107] R. Marthiniussen, K. Vestgard, R. A. Klepaker, and N. Storkersen, "Hugin-auv concept and operational experiences to date," in Oceans' 04 MTS/IEEE Techno-Ocean'04 (IEEE Cat. No. 04CH37600), vol. 2, pp. 846–850, IEEE, 2004.
- [108] General Dynamics - Mission Systems, Bluefin-21 Data sheet, 5 2021.
- [109] D. Scaradozzi, G. Palmieri, D. Costa, and A. Pinelli, "Bcf swimming locomotion for autonomous underwater robots: a review and a novel solution to improve control and efficiency," Ocean Engineering, vol. 130, pp. 437–453, 2017.
- [110] M. S. Triantafyllou and G. S. Triantafyllou, "An efficient swimming machine," Scientific american, vol. 272, no. 3, pp. 64–70, 1995.
- [111] R. Mason and J. Burdick, "Construction and modelling of a carangiform robotic fish," in Experimental Robotics VI, pp. 235–242, Springer, 2000.
- [112] X. Tan, D. Kim, N. Usher, D. Laboy, J. Jackson, A. Kapetanovic, J. Rapai, B. Sabadus, and X. Zhou, "An autonomous robotic fish for mobile sensing," in 2006 IEEE/RSJ International Conference on Intelligent Robots and Systems, pp. 5424–5429, IEEE, 2006.
- [113] V. Kopman and M. Porfiri, "Design, modeling, and characterization of a miniature robotic fish for research and education in biomimetics and bioinspiration," IEEE/ASME Transactions on mechatronics, vol. 18, no. 2, pp. 471–483, 2012.
- [114] R. J. Clapham and H. Hu, "isplash-i: High performance swimming motion of a carangiform robotic fish with full-body coordination," in 2014 IEEE International Conference on Robotics and Automation (ICRA), pp. 322–327, IEEE, 2014.

- [115] J. Yu, C. Zhang, and L. Liu, "Design and control of a single-motor-actuated robotic fish capable of fast swimming and maneuverability," IEEE/ASME Transactions on Mechatronics, vol. 21, no. 3, pp. 1711–1719, 2016.
- [116] A. Konno, T. Furuya, A. Mizuno, K. Hishinuma, K. Hirata, and M. Kawada, "Development of turtle-like submergence vehicle," in Proceedings of the 7th International Symposium on Marine Engineering, 2005.
- [117] J. H. Long, J. Schumacher, N. Livingston, and M. Kemp, "Four flippers or two? tetrapodal swimming with an aquatic robot," Bioinspiration & Biomimetics, vol. 1, no. 1, p. 20, 2006.
- [118] G. Dudek, P. Giguere, C. Prahacs, S. Saunderson, J. Sattar, L.-A. Torres-Mendez, M. Jenkin, A. German, A. Hogue, A. Ripsman, et al., "Aqua: An amphibious autonomous robot," Computer, vol. 40, no. 1, pp. 46–53, 2007.
- [119] K.-H. Low, C. Zhou, T. Ong, and J. Yu, "Modular design and initial gait study of an amphibian robotic turtle," in 2007 IEEE International Conference on Robotics and Biomimetics (ROBIO), pp. 535–540, IEEE, 2007.
- [120] S. C. Licht, "Biomimetic oscillating foil propulsion to enhance underwater vehicle agility and maneuverability," tech. rep., WOODS HOLE OCEANOGRAPHIC INSTITUTION MA, 2008.
- [121] S. Licht and N. Durham, "Biomimetic robots for environmental monitoring in the surf zone & in very shallow water," in IEEE/RSJ International Conference on Intelligent Robots and Systems, 2012.
- [122] J. D. Geder, R. Ramamurti, M. Pruessner, and J. Palmisano, "Maneuvering performance of a four-fin bio-inspired uuv," in 2013 OCEANS-San Diego, pp. 1–7, IEEE, 2013.
- [123] C. Siegenthaler, C. Pradalier, F. Günther, G. Hitz, and R. Siegwart, "System integration and fin trajectory design for a robotic sea-turtle," in 2013 IEEE/RSJ International Conference on Intelligent Robots and Systems, pp. 3790–3795, IEEE, 2013.
- [124] M. Sfakiotakis, D. M. Lane, and J. B. C. Davies, "Review of fish swimming modes for aquatic locomotion," IEEE Journal of oceanic engineering, vol. 24, no. 2, pp. 237–252, 1999.
- [125] R. K. Katzschmann, A. D. Marchese, and D. Rus, "Hydraulic autonomous soft robotic fish for 3d swimming," in Experimental Robotics, pp. 405–420, Springer, 2016.
- [126] J. M. Anderson and N. K. Chhabra, "Maneuvering and stability performance of a robotic tuna," Integrative and comparative biology, vol. 42, no. 1, pp. 118–126, 2002.
- [127] B. Chen and H. Jiang, "Swimming performance of a tensegrity robotic fish," Soft robotics, vol. 6, no. 4, pp. 520–531, 2019.
- [128] J. Shintake, D. Zappetti, T. Peter, Y. Ikemoto, and D. Floreano, "Bio-inspired tensegrity fish robot," in 2020 IEEE International Conference on Robotics and Automation (ICRA), pp. 2887–2892, IEEE, 2020.
- [129] P. P. A. Valdivia y Alvarado, Design of biomimetic compliant devices for locomotion in liquid environments. PhD thesis, Massachusetts Institute of Technology, 2007.

- [130] C. Fiazza, T. Salumäe, M. Listak, G. Kulikovskis, R. Templeton, O. Akanyeti, W. Megill, P. Fiorini, and M. Kruusmaa, "Biomimetic mechanical design for soft-bodied underwater vehicles," in OCEANS'10 IEEE SYDNEY, pp. 1–7, IEEE, 2010.
- [131] M. Kruusmaa, P. Fiorini, W. Megill, M. De Vittorio, O. Akanyeti, F. Visentin, L. Chambers, H. El Daou, M. C. Fiazza, J. Jezov, M. Listak, L. Rossi, T. Salumae, G. Toming, R. Venturelli, D. S. Jung, J. Brown, F. Rizzi, A. Qaltieri, J. L. Maud, and A. Liszewski, "FILOSE for svenning: A flow sensing bioinspired robot," IEEE Robotics and Automation Magazine, vol. 21, no. 3, pp. 51–62, 2014.
- [132] T. Salumäe, Flow-sensitive Robotic Fish: From Concept to Experiments. TUT Press, 2015.
- [133] T. Salumäe, I. Ranó, O. Akanyeti, and M. Kruusmaa, "Against the flow: A braitenberg controller for a fish robot," in 2012 IEEE International Conference on Robotics and Automation, pp. 4210–4215, IEEE, 2012.
- [134] D. S. Jung, P. P. Pott, T. Salumäe, and M. Kruusmaa, "Flow-aided path following of an underwater robot," in 2013 IEEE International Conference on Robotics and Automation, pp. 4602–4607, IEEE, 2013.
- [135] D. Weihs, "A hydrodynamical analysis of fish turning manoeuvres," Proceedings of the Royal Society of London. Series B. Biological Sciences, vol. 182, no. 1066, pp. 59–72, 1972.
- [136] G. Wu, Y. Yang, and L. Zeng, "Routine turning maneuvers of koi carp cyprinus carpio koi: effects of turning rate on kinematics and hydrodynamics," Journal of Experimental Biology, vol. 210, no. 24, pp. 4379–4389, 2007.
- [137] C. Rossi, W. Coral, J. Colorado, and A. Barrientos, "A motor-less and gear-less biomimetic robotic fish design," in 2011 IEEE International Conference on Robotics and Automation, pp. 3646–3651, IEEE, 2011.
- [138] A. D. Marchese, C. D. Onal, and D. Rus, "Autonomous soft robotic fish capable of escape maneuvers using fluidic elastomer actuators," Soft robotics, vol. 1, no. 1, pp. 75–87, 2014.
- [139] Q. Hu, D. R. Hedgepeth, L. Xu, and X. Tan, "A framework for modeling steady turning of robotic fish," in 2009 IEEE International Conference on Robotics and Automation, pp. 2669–2674, IEEE, 2009.
- [140] X. Tan, M. Carpenter, J. Thon, and F. Alequin-Ramos, "Analytical modeling and experimental studies of robotic fish turning," in 2010 IEEE International Conference on Robotics and Automation, pp. 102–108, IEEE, 2010.
- [141] R. M. Alexander, Principles of animal locomotion. Princeton university press, 2013.
- [142] N. Kato, "Application of study on aqua bio-mechanisms to ocean engineering," in Proc of 16th Ocean Engineering Symposium, 2001, pp. 131–138, 2001.
- [143] P. Kodati, J. Hinkle, A. Winn, and X. Deng, "Microautonomous robotic ostraciiform (marco): Hydrodynamics, design, and fabrication," IEEE Transactions on Robotics, vol. 24, no. 1, pp. 105–117, 2008.

- [144] B. Kwak and J. Bae, "Design of hair-like appendages and comparative analysis on their coordination toward steady and efficient swimming," Bioinspiration & biomimetics, vol. 12, no. 3, p. 036014, 2017.
- [145] A. Simha, R. Gkliva, Ü. Kotta, and M. Kruusmaa, "A flapped paddle-fin for improving underwater propulsive efficiency of oscillatory actuation," IEEE Robotics and Automation Letters, vol. 5, no. 2, pp. 3176–3181, 2020.
- [146] S. C. Licht, M. Wibawa, F. S. Hover, and M. S. Triantafyllou, "Towards amphibious robots: Asymmetric flapping foil motion underwater produces large thrust efficiently," tech. rep., Massachusetts Institute of Technology. Sea Grant College Program, 2009.
- [147] S.-H. Song, M.-S. Kim, H. Rodrigue, J.-Y. Lee, J.-E. Shim, M.-C. Kim, W.-S. Chu, and S.-H. Ahn, "Turtle mimetic soft robot with two swimming gaits," Bioinspiration & biomimetics, vol. 11, no. 3, p. 036010, 2016.
- [148] G. V. Lauder, "Function of the caudal fin during locomotion in fishes: kinematics, flow visualization, and evolutionary patterns," American Zoologist, vol. 40, no. 1, pp. 101–122, 2000.
- [149] C. J. Esposito, J. L. Tangorra, B. E. Flammang, and G. V. Lauder, "A robotic fish caudal fin: effects of stiffness and motor program on locomotor performance," Journal of Experimental Biology, vol. 215, no. 1, pp. 56–67, 2012.
- [150] F. Bullo and A. D. Lewis, Geometric control of mechanical systems: modeling, analysis, and design for simple mechanical control systems, vol. 49. Springer, 2019.
- [151] A. Simha, S. Vadgama, and S. Raha, "Almost-global exponential tracking of a variable pitch quadrotor on se (3)," IFAC-PapersOnLine, vol. 50, no. 1, pp. 10268–10273, 2017.
- [152] Z. Su, J. Yu, M. Tan, and J. Zhang, "Implementing flexible and fast turning maneuvers of a multijoint robotic fish," IEEE/ASME Transactions on Mechatronics, vol. 19, no. 1, pp. 329–338, 2013.
- [153] F. Repoulias and E. Papadopoulos, "Planar trajectory planning and tracking control design for underactuated auvs," Ocean engineering, vol. 34, no. 11-12, pp. 1650–1667, 2007.
- [154] T. Elmokadem, M. Zribi, and K. Youcef-Toumi, "Terminal sliding mode control for the trajectory tracking of underactuated autonomous underwater vehicles," Ocean Engineering, vol. 129, pp. 613–625, 2017.
- [155] C. Paliotta, E. Lefeber, K. Y. Pettersen, J. Pinto, M. Costa, et al., "Trajectory tracking and path following for underactuated marine vehicles," IEEE Transactions on Control Systems Technology, vol. 27, no. 4, pp. 1423–1437, 2018.
- [156] C. Yu, X. Xiang, Q. Zhang, and G. Xu, "Adaptive fuzzy trajectory tracking control of an under-actuated autonomous underwater vehicle subject to actuator saturation," International Journal of Fuzzy Systems, vol. 20, no. 1, pp. 269–279, 2018.
- [157] C. P. Bechlioulis, G. C. Karras, S. Heshmati-Alamdari, and K. J. Kyriakopoulos, "Trajectory tracking with prescribed performance for underactuated underwater vehicles under model uncertainties and external disturbances," IEEE Transactions on Control Systems Technology, vol. 25, no. 2, pp. 429–440, 2016.

- [158] H. C. Henninger, K. D. von Ellenrieder, and J. D. Biggs, "Trajectory generation and tracking on se (3) for an underactuated auv with disturbances," IFAC-PapersOnLine, vol. 52, no. 21, pp. 242–247, 2019.
- [159] M. De Paula and G. G. Acosta, "Trajectory tracking algorithm for autonomous vehicles using adaptive reinforcement learning," in OCEANS 2015-MTS/IEEE Washington, pp. 1–8, IEEE, 2015.
- [160] M. Bojarski, D. Del Testa, D. Dworakowski, B. Firner, B. Flepp, P. Goyal, L. D. Jackel, M. Monfort, U. Muller, J. Zhang, et al., "End to end learning for self-driving cars," arXiv preprint arXiv:1604.07316, 2016.
- [161] I. Carlucho, M. De Paula, S. Wang, B. V. Menna, Y. R. Petillot, and G. G. Acosta, "Auv position tracking control using end-to-end deep reinforcement learning," in OCEANS 2018 MTS/IEEE Charleston, pp. 1–8, IEEE, 2018.
- [162] E. Kaufmann, A. Loquercio, R. Ranftl, M. Müller, V. Koltun, and D. Scaramuzza, "Deep drone acrobatics," arXiv preprint arXiv:2006.05768, 2020.
- [163] W. Zhao, Y. Hu, L. Wang, and Y. Jia, "Development of a flipper propelled turtle-like underwater robot and its cpg-based control algorithm," in 2008 47th IEEE Conference on Decision and Control, pp. 5226–5231, IEEE, 2008.
- [164] G. Yao, J. Liang, T. Wang, X. Yang, Q. Shen, Y. Zhang, H. Wu, and W. Tian, "Development of a turtle-like underwater vehicle using central pattern generator," in 2013 IEEE International Conference on Robotics and Biomimetics (ROBIO), pp. 44–49, IEEE, 2013.
- [165] C. Wang, G. Xie, X. Yin, L. Li, and L. Wang, "Cpg-based locomotion control of a quadruped amphibious robot," in 2012 IEEE/ASME International Conference on Advanced Intelligent Mechatronics (AIM), pp. 1–6, IEEE, 2012.
- [166] N. Plamondon and M. Nahon, "A trajectory tracking controller for an underwater hexapod vehicle," Bioinspiration & biomimetics, vol. 4, no. 3, p. 036005, 2009.
- [167] N. Plamondon, Modeling and control of a biomimetic underwater vehicle, vol. 72, 2010.
- [168] P. Giguere, Y. Girdhar, and G. Dudek, "Wide-speed autopilot system for a swimming hexapod robot," in 2013 International Conference on Computer and Robot Vision, pp. 9–15, IEEE, 2013.
- [169] A. Chemori, K. Kuusmik, T. Salumäe, and M. Kruusmaa, "Depth control of the biomimetic u-cat turtle-like auv with experiments in real operating conditions," in 2016 IEEE International Conference on Robotics and Automation (ICRA), pp. 4750–4755, IEEE, 2016.
- [170] T. Salumäe, A. Chemori, and M. Kruusmaa, "Motion control of a hovering biomimetic four-fin underwater robot," IEEE Journal of Oceanic Engineering, vol. 44, no. 1, pp. 54–71, 2017.
- [171] M. Xanthidis, N. Karapetyan, H. Damron, S. Rahman, J. Johnson, A. O'Connell, J. M. O'Kane, and I. Rekleitis, "Navigation in the presence of obstacles for an agile autonomous underwater vehicle," in 2020 IEEE International Conference on Robotics and Automation (ICRA), pp. 892–899, IEEE, 2020.

- [172] C. Edwards and S. Spurgeon, Sliding mode control: theory and applications. Crc Press, 1998.
- [173] N. Fischer, D. Hughes, P. Walters, E. M. Schwartz, and W. E. Dixon, "Nonlinear rise-based control of an autonomous underwater vehicle," IEEE Transactions on Robotics, vol. 30, no. 4, pp. 845–852, 2014.
- [174] H. Lamb, Hydrodynamics. Cambridge university press, 1993.
- [175] E. Freund, "Decoupling and pole assignment in nonlinear systems," Electronics Letters, vol. 9, no. 16, pp. 373–374, 1973.
- [176] Y.-L. Gu and Y. Xu, "A normal form augmentation approach to adaptive control of space robot systems," Dynamics and Control, vol. 5, no. 3, pp. 275–294, 1995.
- [177] M. W. Spong, "Partial feedback linearization of underactuated mechanical systems," in Proceedings of IEEE/RSJ International Conference on Intelligent Robots and Systems (IROS'94), vol. 1, pp. 314–321, IEEE, 1994.
- [178] M. Fliess, J. Lévine, P. Martin, and P. Rouchon, "Flatness and defect of non-linear systems: introductory theory and examples," International journal of control, vol. 61, no. 6, pp. 1327–1361, 1995.
- [179] K. Schlacher and M. Schöberl, "A jet space approach to check pfaffian systems for flatness," in 52nd IEEE Conference on Decision and Control, pp. 2576–2581, IEEE, 2013.
- [180] M. Schöberl and K. Schlacher, "On an implicit triangular decomposition of nonlinear control systems that are 1-flat—a constructive approach," Automatica, vol. 50, no. 6, pp. 1649–1655, 2014.
- [181] S. K. Chung, C. R. Koch, and A. F. Lynch, "Flatness-based feedback control of an automotive solenoid valve," IEEE Transactions on Control Systems Technology, vol. 15, no. 2, pp. 394–401, 2007.
- [182] L. Menhour, B. d'Andréa Novel, M. Fliess, and H. Mounier, "Coupled nonlinear vehicle control: Flatness-based setting with algebraic estimation techniques," Control Engineering Practice, vol. 22, pp. 135–146, 2014.
- [183] M. Bröcker and L. Herrmann, "Flatness based control and tracking control based on nonlinearity measures," IFAC-PapersOnLine, vol. 50, no. 1, pp. 8250–8255, 2017.
- [184] J.-C. Ryu and S. K. Agrawal, "Differential flatness-based robust control of mobile robots in the presence of slip," The International Journal of Robotics Research, vol. 30, no. 4, pp. 463–475, 2011.
- [185] D. Mellinger and V. Kumar, "Minimum snap trajectory generation and control for quadrotors," in 2011 IEEE international conference on robotics and automation, pp. 2520–2525, IEEE, 2011.
- [186] D. A. Duecker, N. Bauschmann, T. Hansen, E. Kreuzer, and R. Seifried, "Towards micro robot hydrobatics: Vision-based guidance, navigation, and control for agile underwater vehicles in confined environments," in Proceedings of the IEEE/RSJ International Conference on Intelligent Robots and Systems (IROS), Las Vegas, NV, USA, pp. 25–29, 2020.

- [187] A. Kaldmäe and Ü. Kotta, "A brief tutorial overview of disturbance observers for nonlinear systems: application to flatness-based control," Proceedings of the Estonian Academy of Sciences, vol. 69, no. 1, pp. 57–73, 2020.
- [188] W.-H. Chen, D. J. Ballance, P. J. Gawthrop, and J. O'Reilly, "A nonlinear disturbance observer for robotic manipulators," IEEE Transactions on Industrial Electronics, vol. 47, no. 4, pp. 932–938, 2000.
- [189] W.-H. Chen, "Disturbance observer based control for nonlinear systems," IEEE/ASME transactions on mechatronics, vol. 9, no. 4, pp. 706–710, 2004.
- [190] S. Li, J. Yang, W.-H. Chen, and X. Chen, "Generalized extended state observer based control for systems with mismatched uncertainties," IEEE Transactions on Industrial Electronics, vol. 59, no. 12, pp. 4792–4802, 2011.
- [191] M. Ran, Q. Wang, and C. Dong, "Active disturbance rejection control for uncertain nonaffine-in-control nonlinear systems," IEEE Transactions on Automatic Control, vol. 62, no. 11, pp. 5830–5836, 2016.
- [192] A. Castillo, P. García, R. Sanz, and P. Albertos, "Enhanced extended state observer-based control for systems with mismatched uncertainties and disturbances," ISA transactions, vol. 73, pp. 1–10, 2018.
- [193] X. Wei and L. Guo, "Composite disturbance-observer-based control and terminal sliding mode control for non-linear systems with disturbances," International Journal of Control, vol. 82, no. 6, pp. 1082–1098, 2009.
- [194] T. D. Do and H. T. Nguyen, "A generalized observer for estimating fast-varying disturbances," IEEE Access, vol. 6, pp. 28054–28063, 2018.
- [195] D. Ginoya, P. Shendge, and S. Phadke, "Sliding mode control for mismatched uncertain systems using an extended disturbance observer," IEEE Transactions on Industrial Electronics, vol. 61, no. 4, pp. 1983–1992, 2013.
- [196] L. Tan, G. Jin, C. Sun, and Z. Xiong, "High-order disturbance observer for nonlinear systems using sliding-mode technology," in 2018 Chinese Control And Decision Conference (CCDC), pp. 1382–1386, IEEE, 2018.
- [197] K. Zhan, Y. Wang, and L. Liu, "Improved sliding-mode disturbance observer for non-linear system," in 2018 10th International Conference on Modelling, Identification and Control (ICMIC), pp. 1–5, IEEE, 2018.
- [198] S. Nolan and D. Toal, "A low directivity ultrasonic sensor for collision avoidance and station keeping on inspection-class auvs," Journal of Marine Engineering & Technology, vol. 7, no. 1, pp. 1–11, 2008.
- [199] V. Preston, T. Salumäe, and M. Kruusmaa, "Underwater confined space mapping by resource-constrained autonomous vehicle," Journal of Field Robotics, vol. 35, no. 7, pp. 1122–1148, 2018.
- [200] T. Salumäe, A. Chemori, and M. Kruusmaa, "Motion control architecture of a 4-fin u-cat auv using dof prioritization," in 2016 IEEE/RSJ International Conference on Intelligent Robots and Systems (IROS), pp. 1321–1327, IEEE, 2016.

- [201] L. E. Dubins, "On curves of minimal length with a constraint on average curvature, and with prescribed initial and terminal positions and tangents," American Journal of mathematics, vol. 79, no. 3, pp. 497–516, 1957.
- [202] R. R. Smart, Evolutionary Control of Autonomous Underwater Vehicles. PhD thesis, MIT University, 2008.
- [203] A. Walker et al., "Hard real-time motion planning for autonomous vehicles," Walker, A.—"Hard Real-Time Motion Planning for Autonomous Vehicles PhD thesis, Swinburne University, 2011.
- [204] M. Prats, J. Perez, J. J. Fernandez, and P. J. Sanz, "An open source tool for simulation and supervision of underwater intervention missions," in 2012 IEEE/RSJ international conference on Intelligent Robots and Systems, pp. 2577–2582, IEEE, 2012.
- [205] C. Georgiades, "Simulation and control of an underwater hexapod robot.," 2005.
- [206] J. E. da Silva, B. Terra, R. Martins, and J. B. de Sousa, "Modeling and simulation of the lauv autonomous underwater vehicle," in 13th IEEE IFAC international conference on methods and models in automation and robotics, vol. 1, Szczecin, Poland Szczecin, Poland, 2007.
- [207] H. E. Rauch, F. Tung, and C. T. Striebel, "Maximum likelihood estimates of linear dynamic systems," AIAA journal, vol. 3, no. 8, pp. 1445–1450, 1965.
- [208] F. Berkenkamp, A. P. Schoellig, and A. Krause, "Safe controller optimization for quadrotors with gaussian processes," in 2016 IEEE International Conference on Robotics and Automation (ICRA), pp. 491–496, IEEE, 2016.
- [209] G. Fagogenis, D. Flynn, and D. M. Lane, "Improving underwater vehicle navigation state estimation using locally weighted projection regression," in 2014 IEEE international conference on robotics and automation (ICRA), pp. 6549–6554, IEEE, 2014.
- [210] Y. H. Eng, K. M. Teo, M. Chitre, and K. M. Ng, "Online system identification of an autonomous underwater vehicle via in-field experiments," IEEE Journal of Oceanic Engineering, vol. 41, no. 1, pp. 5–17, 2015.
- [211] G. C. Karras, P. Marantos, C. P. Bechlioulis, and K. J. Kyriakopoulos, "Unsupervised online system identification for underwater robotic vehicles," IEEE Journal of Oceanic Engineering, vol. 44, no. 3, pp. 642–663, 2018.
- [212] B. Wehbe, M. Hildebrandt, and F. Kirchner, "A framework for on-line learning of underwater vehicles dynamic models," in 2019 International Conference on Robotics and Automation (ICRA), pp. 7969–7975, IEEE, 2019.
- [213] L. DeVries, F. D. Lagor, H. Lei, X. Tan, and D. A. Paley, "Distributed flow estimation and closed-loop control of an underwater vehicle with a multi-modal artificial lateral line," Bioinspiration & biomimetics, vol. 10, no. 2, p. 025002, 2015.
- [214] B. Colvert, K. Chen, and E. Kansa, "Local flow characterization using bioinspired sensory information," Journal of Fluid Mechanics, vol. 818, p. 366, 2017.

- [215] M. Alsalman, B. Colvert, and E. Kanso, "Training bioinspired sensors to classify flows," Bioinspiration & biomimetics, vol. 14, no. 1, p. 016009, 2018.
- [216] F. Dang and F. Zhang, "Distributed flow estimation for autonomous underwater robots using pod-based model reduction," in 2018 IEEE Conference on Decision and Control (CDC), pp. 4453–4458, IEEE, 2018.
- [217] P. Oteiza, I. Odstrcil, G. Lauder, R. Portugues, and F. Engert, "A novel mechanism for mechanosensory-based rheotaxis in larval zebrafish," Nature, vol. 547, no. 7664, pp. 445–448, 2017.
- [218] C. Georgiades, A. German, A. Hogue, H. Liu, C. Prahacs, A. Ripsman, R. Sim, L.-A. Torres, P. Zhang, M. Buehler, et al., "Aqua: an aquatic walking robot," in 2004 IEEE/RSJ International Conference on Intelligent Robots and Systems (IROS)(IEEE Cat. No. 04CH37566), vol. 4, pp. 3525–3531, IEEE, 2004.
- [219] C. D. McKinnon and A. P. Schoellig, "Learning multimodal models for robot dynamics online with a mixture of gaussian process experts," in 2017 IEEE International Conference on Robotics and Automation (ICRA), pp. 322–328, IEEE, 2017.

Acknowledgements

The last five years have been a great adventure and an incredible journey. First and foremost I would like to thank my supervisors Prof. Dr. Maarja Kruusmaa and Prof. Dr. Ülle Kotta for guiding and supporting me through the good and the difficult times, for sharing your incredible expertise, but also for giving me the freedom to explore ideas and to chart my own path through the research landscape. You have taught me many valuable things during the last years and I look forward to continued collaborations. I was also very lucky to share the lab with very talented and creative people that have become dear friends over the years. I want to thank Juan-Fran for being a great mentor at the beginning of my journey and for all the fun and fruitful teamwork that we had throughout the years. Thank you for sharing your experience and your knowledge, and for all the fun moments that we had outside of research. I also want to thank Roza and Walid, for all the inspiring hours spend together in the lab, for great collaborations on research projects and for making teaching such a fun and engaging experience. You too have become good friends and I have greatly enjoyed exploring Estonia together with you. A big thanks goes to Andres and Jaan, no one in the lab could do their work properly without you two. You always took time to help me out with hardware or software problems and you always solved them, thank you very much for that. A special thanks goes to Mihkel for doing his work so well, that I felt I could fully concentrate on my research with almost no administrative overhead, and of course for many engaging late night discussions. Thank you to Arvo and Ashu for fruitful collaborations and for helping to get interesting ideas to work. Moreover, I want to thank all of my colleagues from the Centre for Biorobotics for being such a fun and inspiring bunch. The work atmosphere is truly special and stimulating. I am very grateful for the opportunity to be part of this community. I also want to express gratitude towards my international colleagues from the Underwater Robotics lab at the University of Girona and from the AUR-lab at NTNU, Norway. You have warmly welcomed me at your institutions and fully supported me during field trials. You were thus crucial for the success of the research presented in this thesis.

I would also like to take the opportunity to thank the funding sources that made my research possible, namely:

- the Estonian Centre of Excellence in ICT Research, project EXCITE (TAR16013)
- the IUT (IUT33-9) institutional research funding of the Estonian Ministry of Education and Research.
- the Dora+ short term mobility scholarship program

A special thanks goes to Victoria for valuable feedback on the thesis manuscript and for being an inspiration to me professionally and privately. I want to thank the rest of my friends for their continued support and for their encouragement throughout the last years. And last but certainly not least I want to thank my family, especially my grandparents and parents: Ohne euch wäre ich nie so weit gekommen. Ihr seid immer für mich da, besonders in den schweren Zeiten. Ihr habt mich immer bedingungslos und mit Liebe unterstützt, egal welchen Weg ich genommen habe. Dafür bin ich euch unglaublich dankbar!

Abstract

State Estimation and Control for Small Low-Cost Autonomous Underwater Vehicles

Autonomous underwater vehicles (AUVs) have extended human capabilities for monitoring and exploration of the underwater environment. However, commercial AUVs are almost exclusively used by entities with large monetary budgets, due to the high capital investment that is required to acquire, maintain and develop such vehicles. This has restricted the use of AUVs to sectors of oil and gas industry, military, and well-funded big research institutions. Thus, the potential of AUVs as tools to provide important and meaningful knowledge about the underwater environment has been only marginally explored.

In recent years there have been attempts to develop small, low-cost AUVs to increase accessibility of such technology for smaller research institutions and government agencies. Additionally, small low-cost vehicles have broadened the application area of AUVs towards swarm implementations, high risk missions in confined environments, and consumer robotics. However, the reduction in cost and size comes with trade-offs in terms of the navigation and motion capabilities of such vehicles, which essentially reduces their achievable autonomy. Standard state of the art solutions for state estimation and control rely on sophisticated and expensive hardware that may not be available to small low-cost vehicles. Additionally, propellers as conventional tools used to maneuver AUVs, might be unsatisfactory in applications that require minimal invasive monitoring or close proximity to wildlife or humans. This points to open questions in several key parts of AUV autonomy, namely state estimation, actuation and motion control. The work presented in this thesis tries to address one specific research question in each field and therefore thematically assumes a tripartite structure.

Work presented in *Chapter 2* investigates the question of state estimation, and tests the hypothesis that the passive mechanism of sensing instantaneous *pressure differences* across a body in fluid flow can be used to robustly estimate the motion velocity of AUVs in field conditions. To that end, early prototypes, that had been tested under stationary laboratory conditions, were extended and tailored to the use on autonomous mobile vehicles. This was done by utilizing fundamental relations from potential flow theory and by employing additional sensing modalities to compensate for self-motion effects. Several advanced prototypes were developed, characterized under laboratory conditions, and then rigorously tested in field conditions. Quantitative comparisons were made to state of the art sensors. The obtained results indicate that for the tested scenarios, velocity estimation with a comparable performance to state of the art technology was achieved. Additionally, the presented prototypes have a smaller size, an energy consumption that is one order of magnitude lower and a lower projected price compared to the state of the art sensors. The presented work provides an important step towards the establishment of the tested technology as a complement or alternative to the state of the art, specifically for small low cost vehicles.

Given the improvements in state estimation as presented in *Chapter 2*, the research in *Chapter 3* is aimed at the problem of robot mobility using bio-inspired soft actuators. Compliant actuators are safer to interact with and potentially less harmful to their environment than propellers, which is specifically important when minimally invasive observation is the goal of the underwater robot. However, those benefits usually come with higher control complexity. Usually, soft bio-inspired actuators are driven by a symmetrical periodic motion similar to their biological counterparts. In contrast, the research presented in *Chapter 3* investigates the use of *asymmetric actuation* to increase the maneuverabil-

ity of robots with bio-inspired soft actuators. The role of asymmetric movements in the generation of thrust has been investigated in various animals and robotic platforms. The main contribution of the research presented in *Chapter 3* is the utilization of *asymmetric actuation* for turning control instead of focusing on thrust generation. A nonlinear proportional controller was developed and used to control the actuation asymmetry for a robotic fish driven by a compliant tail. The efficacy of the proposed control approach was tested under field conditions. The proposed controller outperformed the standard approach to turning control for the given type of robot. While the direct application of the controller might be only immediately useful for a very narrow set of robots, the idea of *asymmetric actuation* for orientation control can be applied to a much wider set of vehicles and adds another tool to utilize the unique features of soft bio-inspired actuators.

Finally, *Chapter 4* addresses a core problem in motion control. Many underwater vehicles are not fully and independently actuated in all degrees of freedom, something which is specifically true for small low-cost vehicles. Furthermore, certain applications, like the monitoring of confined spaces or the motion within a group of vehicles, require agile motion and efficient trajectory tracking capabilities. Nonlinear model based controllers have been shown to be able to enable efficient trajectory tracking for agile motions, but often require permanent feedback of higher order time derivatives of the vehicle's pose, such as acceleration. Those quantities can not be measured effectively in real time with sensors available on small low-cost AUVs.

A major contribution of the research presented in chapter *Chapter 4* is the introduction of an *event-based* controller that could alleviate the requirement of permanent state feedback. The controller is combined with a feedforward part that relies on the *differential flatness* property of the vehicle's state space model to efficiently generate and track feasible trajectories. A base implementation of the controller is then extended to under-actuated systems subject to nonholonomic constraints, which are usually not *differentially flat*. The efficacy of the proposed approach is then tested in simulation for planar trajectory tracking for a small low-cost AUV with bio-inspired actuation and a small torpedo shaped AUV. The controller is compared to standard model free approaches and shows an equal or better tracking performance with more economical control actions both in the absence and presence of external disturbances.

As a whole the research presented in this thesis provides contributions to three core aspects of the autonomy framework, state estimation, actuation and motion control, for small low-cost AUVs. A combination of all three contributions has the potential to enable small low-cost vehicles to move more efficiently, with more agility and with increased navigation capacities. However, each research contribution by itself provides a starting point for future improvement and investigation of related research problems. There is significant potential in the utilization of *differential pressure* for measurements of environmental states beyond fluid relative velocity and the true strengths of *asymmetric actuation* and the presented model based controller are expected to emerge for fast agile motions in three dimensions.

Kokkuvõte

Meetodid olekute hindamiseks ja juhtimiseks soodsa hinnaga autonoomsetele allveerobotitele

Autonoomsete allveesõidukite (AUV-de) kasutuselevõtt on laiendanud veealuste keskkondade uurimise ja seirevõimalusi. Kommertsallveesõidukeid kasutavad aga peaaegu eranditult suure eelarvega ettevõtted, sest selliste sõidukite soetamine, hooldamine ja arendamine nõuab suuri investeeringuid. See piirab AUV-de rakendamist valdavalt nafta- ja gaasitööstuses, sõjaväes ning hästi rahastatud suurtes teadusasutustes. AUV-de potentsiaali veealuse keskkonna kohta oluliste ja sisukate teadmiste saamiseks on kasutatud vaid vähesel määral.

Viimastel aastatel on hakatud arendama väikeseid ja odavaid AUV-sid, et võimaldada ka väiksemate teadusasutuste ja riiklike institutsioonide ligipääsetavust tehnoloogiale. Lisaks on väikesed ning odavad lahendused laiendanud AUV-de rakendusvaldkondi sülemite (swarm) rakendustesse, kõrge riskiga missioonide jaoks tõkestatud keskkondades ja leidnud tee isegi kodurobootikasse. Hinna ja suuruse vähenemisega kaasnevad paraku kompromissid sõidukite navigeerimis- ja liikumisvõimekuse osas, mis kahjuks vähendavad nende poolt saavutatavat autonoomiat. Standardsed nüüdisaegsed lahendused allveesõidukite olekute hindamiseks ja juhtimiseks põhinevad keerukal ja kallil riistvaral, mis ei pruugi väikeste odavate sõidukite jaoks saadaval olla. Samuti võivad propellerid (olles tavapäraselt kasutatavad vahendid AUV-de manööverdamisel) muutuda mitesobivaks rakendustes, mis vajavad minimaalset invasiivset seiret või liikumist eluslooduse ning inimese läheduses. See osundab lahendust ootavatele ülesannetele AUV-de autonoomsusega seonduvates võtmekohtades, nimelt olekute hindamises, täiturmehhanismide rakendamises ja liikumise juhtimises. Antud dissertatsioonis käsitletakse üht konkreetset uurimisprobleemi igas eelpool nimetatud valdkonnas, mis tingib uurimistöö kolmeks jaotuva struktuuri.

Töö teine peatükk käsitleb süsteemi olekute hindamise küsimust ja testib hüpoteesi, et AUV-de liikumiskiiruse robustne hindamine välitingimustes on võimalik nõ passiivset lähenemist kasutavate sensorite abil, mis mõõdvad vedeliku rõhu diferentsi kahe mõõtepunkti vahel antud ajahetkel. Sel eesmärgil arendati edasi prototüüpe, mida oli varasemalt katsetatud laboritingimustes, kohandamaks neid edaspidiseks kasutamiseks autonoomsetes liikurites. Voolukiiruse hindamisel kasutati potentsiaalse voolamise põhialused ja rakendati täiendavaid tajumismooduseid, et kompenseerida omaliikumise mõjusid. Töötati välja ja mitu edasiarendatud prototüüpi, mille tööd uuriti laboritingimustes ja katsetati seejärel põhjalikult välitingimustes, võrreldes prototüüpe ühtlasi tipp tehnoloogiste sensorite kvantitatiivsete näitajatega. Saadud tulemused näitavad, et testitud stsenaariumite puhul saavutati kiiruse hindamisel tipp tehnoloogiliste lahendustega võrreldav kvaliteet. Lisaks on edasiarendatud prototüüpidel väiksem suurus, suurusjärgu võrra madalam energiatarbimine ja odavam prognoositav hind võrreldes kõrg tehnoloogiliste sensoritega. Antud töö astus olulise sammu testitud tehnoloogia kasutuselevõtu suunas kui täiendus või alternatiiv olemasolevatele tipp tehnoloogilistele lahendustele, seda eriti väikeste ning odavate AUV-de korral.

Tuginedes teises peatükis kirjeldatud arendustele olekute hindamisel, keskendub kolmas peatükk bioloogiast inspireeritud pehmete täiturmehhanismidega varustatud robotite mobiilsusprobleemidele. Painduvad täiturmehhanismid on ohutumad ning potentsiaalselt ka keskkonda vähem mõjutavad kui propellerid, mis on eriti oluline, kui eesmärgiks on minimaalse invasiivsusega vaatlustegevus. Ent mainitud eelistega kaasneb keerulisem juhtimisloogika. Pehmete bioloogiast inspireeritud täiturmehhanismide käitamisel kasutatakse tavaliselt (sarnaselt nende bioloogilistele vastetele) sümmeetrilist perioodilist lii-

kumist. Vastupidiselt tavapärasele uuritakse 3. peatükis asümmeetrilise liikumise rakendamist eesmärgiga parandada selliste robotite manööverdusvõimet. Asümmeetriliste liigutuste rolli tõukejõu tekitamisel on uuritud erinevatel loomadel ja robotplatvormidel. Kolmanda peatüki peamiseks panuseks on asümmeetriliste liigutuste rakendamine tõukejõu tekitamise asemel robotkala orientatsiooni juhtimisel. Painduva sabaga robotkala asümmeetriliseks käitamiseks arendati välja mittelineaarne proportsionaalne kontrolleri. Antud juhtimismeetodi tõhusust katsetati välikatsetel ning eelpool mainitud roboti tüübi orientatsiooni juhtimise puhul töötas väljapakutud juhtimismeetod paremini standardsetest juhtimislahendustest. Kuigi kontrolleri vahetu rakendamine võib olla kasulik ainult väga kitsa rühma robotite jaoks, on idee asümmeetrilisest käitamisest orientatsiooni juhtimisel rakendatav palju enamatele sõidukitele ja annab meie käsutusse veel ühe tööriista kasutamaks pehmete bioloogiast inspireeritud täiturite ainulaadseid omadusi.

Viimane, neljas peatükk käsitleb liikumise juhtimise tuumprobleemi. Paljud allveesõidukid ei ole täielikult ega sõltumatult juhitud kõikides vabastastmetes. Eriti peab see paika väikeste odavate sõidukite puhul. Lisaks on mõningates rakendustes nagu näiteks kitsaste ruumide seire või rühmas liikumine vajalik hea manööverdus- ja efektiivne trajektoori järgimise võimekus. Varasemalt on näidatud, et mittelineaarsed mudelipõhised kontrollid võimaldavad keerukate liikumiste korral efektiivset trajektoori järgimist, kuigi vajavad selleks sageli pidevat tagasisidet sõiduki asendi ja orientatsiooni kõrgema astme tuletiste, näiteks kiirenduste näol. Antud muutujate efektiivne mõõtmine reaajas pole aga väikestel odavatel AUV-del kasutatavate sensoritega võimalik.

Neljandas peatükis esitatud uurimistöö peamine panus on sündmuspõhise kontrolleri kasutuselevõtt, mis võimaldab pideva tagasiside vajadust leevendada. Controller kasutab juhtimisalgoritmi, mis põhineb roboti diferentsiaalse lameduse omadusel, et genereerida ja järgida efektiivselt võimalikke trajektoore. Seejärel laiendatakse baaskontrollerit alajuhitud süsteemidele, millele rakenduvad mitte-holonoomsed piirangud. Sellised süsteemid ei ole tüüpiliselt diferentsiaalselt lamedad. Kavandatud lähenemisviisi tõhusust testiti simulaatoris tasapinnaliste trajektooride järgimiseks väikesel odaval AUV-l, millel on bioloogiliselt inspireeritud täiturmehhanismid ning väikesel torpeedokujulisel AUV-l. Väljapakutud kontrolleri võrreldi standardsete mudelivabade juhtimismeetoditega ning uus meetod andis võrdse või parema järgimistulemuse ökonoomsemate vahenditega nii väliste häiringute puudumisel kui ka nende olemasolul.

Tervikuna annab dissertatsioonis esitatud uurimus oma panuse autonoomia raamistiku kolmele põhiaspektile: olekute hindamisele, täiturmehhanismide rakendamisele ja liikumise juhtimisele väikeste odavate AUV-de jaoks. Kolme panuse kombinatsioon võimaldab väikestel odavatel sõidukitel liikuda tõhusamalt, kiiremini ja parema navigeerimisvõimega. Aga iga uurimistulemus iseenesest annab lähtepunkti edasisteks täiendusteks ja teemaga seotud teadusküsimustega tegelemiseks. Vedeliku rõhu diferentside mõõtmisel baseeruvale olekute hindamisele on märkimisväärne potentsiaal keskkonna olekute hindamisel lisaks suhtelise vedelikukiiruse hindamisele ning asümmeetriliste täiturmehhanismide ja mudelipõhise juhtimise tõelised väärtused tõusevad eeldatavalt esile eriti just kiirete kõrge manööverdusvõimega kolmedimensionaalsetel liikumistel.

Appendix 1 - DPSS flow-angle derivation

We begin with equation (33) in section 2.2.2:

$$\Delta p_1 = \frac{1}{2}\rho \left[\frac{9}{4}v_\infty^2 (\sin^2(\varphi_B - \alpha) - \sin^2(-\alpha)) + 2g\Delta h_1 \right]. \quad (81)$$

We then start solving for α :

$$\sin^2(\varphi_B - \alpha) - \sin^2(-\alpha) = \frac{8\Delta p_1 - \rho g\Delta h_1}{9\rho v_\infty^2}. \quad (82)$$

By using the power reduction formula:

$$\sin^2(\theta) = \frac{1 - \cos(2\theta)}{2} \quad (83)$$

we and get:

$$\frac{1}{2} - \frac{\cos(2(\varphi_B - \alpha))}{2} - \left(\frac{1}{2} - \frac{\cos(-2\alpha)}{2} \right) = \frac{8\Delta p_1 - \rho g\Delta h_1}{9\rho v_\infty^2} \quad (84)$$

$$\cos(-2\alpha) - \cos(2(\varphi_B - \alpha)) = 2 \left(\frac{8\Delta p_1 - \rho g\Delta h_1}{9\rho v_\infty^2} \right). \quad (85)$$

Now we use the sum to product relation:

$$\cos(\theta) + \cos(\varphi) = -2\sin\left(\frac{\theta + \varphi}{2}\right)\sin\left(\frac{\theta - \varphi}{2}\right). \quad (86)$$

and get from 84:

$$-2\sin(\varphi_B - 2\alpha)\sin(-\varphi_B) = 2 \left(\frac{8\Delta p_1 - \rho g\Delta h_1}{9\rho v_\infty^2} \right) \quad (87)$$

Now we can solve for α :

$$\sin(\varphi_B - 2\alpha) = -\frac{8\Delta p_1 - \rho g\Delta h_1}{\sin(-\varphi_B)9\rho v_\infty^2} = \frac{8\Delta p_1 - \rho g\Delta h_1}{\sin(\varphi_B)9\rho v_\infty^2} \quad (88)$$

$$\alpha = \frac{\varphi_B - \arcsin\left(\frac{8\Delta p_1 - \rho g\Delta h_1}{9\rho v_\infty^2 \sin(\varphi_B)}\right)}{2}, \quad (89)$$

and get equation (34) in section 2.2.2

Appendix 2 - BDO derivation for augmented DFEC

Summarizing (67) from section 4.3.3 we can write:

$$\dot{x} = f(x) + g_1(x)u + g_2(x)d, \quad (90)$$

with $\dot{x} = [\dot{x}_1, \dot{x}_2, \dot{x}_3, \dot{x}_4, \dot{x}_5]^T$, $u = [u_1, u_2]^T$, $d = [d_1, d_2, 0, d_3, d_4]$, and

$$f(x) = \begin{pmatrix} x_4 \cos(x_3) \\ x_4 \sin(x_3) \\ x_5 \\ -\frac{1}{m_{11}}(X_{uu}x_4 + X_{uu}x_4|x_4|) \\ -\frac{1}{m_{66}}(N_{rr}x_5 + N_{rr}x_5|x_5|) \end{pmatrix}, \quad (91)$$

$$g_1(x) = \begin{pmatrix} 0 & 0 \\ 0 & 0 \\ 0 & 0 \\ \frac{1}{m_{11}} & 0 \\ 0 & \frac{1}{m_{66}} \end{pmatrix}, \quad (92)$$

$$g_2(x) = \begin{pmatrix} 1 & 0 & 0 & 0 \\ 0 & 1 & 0 & 0 \\ 0 & 0 & 0 & 0 \\ 0 & 0 & 1 & 0 \\ 0 & 0 & 0 & 1 \end{pmatrix}, \quad (93)$$

Given that (73) and (74) depend on d and its first and second time derivatives the assumption is made of $\ddot{d} \approx 0$, which means $k = 3$ and the following disturbance observer can be defined:

$$\begin{aligned} \dot{z}_0 &= -L_0(x)[f(x) + g_1(x)u + g_2(x)(z_0 + p_0(x))] + z_1 + p_1(x) \\ \dot{z}_1 &= -L_1(x)[f(x) + g_1(x)u + g_2(x)(z_0 + p_0(x))] + z_2 + p_2(x) \\ \dot{z}_2 &= -L_2(x)[f(x) + g_1(x)u + g_2(x)(z_0 + p_0(x))] \\ \hat{d} &= z_0 + p_0(x) \\ \hat{d}^{(1)} &= z_1 + p_1(x) \\ \hat{d}^{(2)} &= z_2 + p_2(x), \end{aligned} \quad (94)$$

with $z_i(t) \in \mathbb{R}^p$, $i = 0, 1, 2$ being the observer state, $\hat{d}^{(i)}$ the estimation of $d^{(i)}$ and $p_i(x)$, $L_i(x)$ observer gains chosen to satisfy:

$$L_i(x) = \frac{\partial p_i(x)}{\partial x}. \quad (95)$$

We further can define the following error dynamics for the estimation error $e_i := d^{(i)} - \hat{d}^{(i)}$ as:

$$\begin{aligned} \dot{e}_0 &= e_1 - L_0(x)g_2(x)e_0 \\ \dot{e}_1 &= e_2 - L_1(x)g_2(x)e_0 \\ \dot{e}_2 &= -L_2(x)g_2(x)e_0. \end{aligned} \quad (96)$$

Given $g_2(x) \in \mathbb{R}^{5 \times 4}$ we choose $L_i(x) \in \mathbb{R}^{4 \times 5}$ and get:

$$L_i = \begin{pmatrix} l_{i,1} & 0 & 0 & 0 & 0 \\ 0 & l_{i,2} & 0 & 0 & 0 \\ 0 & 0 & 0 & l_{i,3} & 0 \\ 0 & 0 & 0 & 0 & l_{i,4} \end{pmatrix}, \quad (97)$$

with (97) in (96) we get the linear autonomous system:

$$\begin{aligned} \dot{e} &= Ae \\ &= \begin{pmatrix} -L_0 g_2(x) & I_{4 \times 4} \\ -L_1 g_2(x) & I_{4 \times 4} \\ -L_2 g_2(x) & 0_{4 \times 4} \end{pmatrix} e. \end{aligned} \quad (98)$$

Now we determine the characteristic polynomial, which results in four independent systems with three roots each:

$$\begin{aligned} \det(A - sI) &= (-s^3 - s^2 l_{0,1} - s l_{1,1} - l_{2,1})(-s^3 - s^2 l_{0,2} - s l_{1,2} - l_{2,2}) \\ &\quad (-s^3 - s^2 l_{0,4} - s l_{1,4} - l_{2,4})(-s^5 - s^2 l_{0,5} - s l_{1,5} - l_{2,5}) \end{aligned} \quad (99)$$

Restricting the roots of the polynomial to be on the left side of the complex plane we can compute the conditions of (75) in section 4.3.3.

Appendix 3 - Publication 1

I

J. F. Fuentes-Pérez, C. Meurer, J. A. Tuhtan, and M. Kruusmaa, "Differential Pressure Sensors for Underwater Speedometry in Variable Velocity and Acceleration Conditions," IEEE Journal of Oceanic Engineering, vol. 43, no. 2, pp. 418–426, 2018

Differential Pressure Sensors for Underwater Speedometry in Variable Velocity and Acceleration Conditions

Juan Francisco Fuentes-Pérez , Christian Meurer, Jeffrey Andrew Tuhtan, and Maarja Kruusmaa

Abstract—Autonomous underwater vehicles require estimation of their velocity relative to the surrounding flow to perform essential navigation tasks. Available technologies for speed estimation rely on Doppler velocity logs or acoustic Doppler current profilers and are not suitable for application in small low cost or energy consumption vehicles. Encouraged by the successful results of our previous lab-scale investigations using pressure-based speedometry, we developed differential pressure sensor speedometry as an alternative to conventional technologies. We built a full-scale physical prototype, compared analog and digital differential pressure sensors and evaluated the performance in variable velocity (0–2 m/s) and acceleration (0–2 m²/s) conditions in a marine tow tank. A simple equation based on the conservation of energy accurately estimated the velocity, with estimated mean absolute errors of 0.0087 m/s for analog and 0.0107 m/s and digital configurations. This equation is shown to hold under variable velocity and acceleration conditions. We conclude that differential pressure sensor speedometry is a valid solution to perform underwater speedometry and we confirm that the system can provide instantaneous and stable velocity estimates with a sampling rate higher than 10 Hz.

Index Terms—Bernoulli, differential pressure sensor, pitot, speedometry, underwater vehicles.

NOMENCLATURE

a	Acceleration (m/s ²).
C_c	Correlation coefficient (dimensionless).
C_p	Pressure coefficient (dimensionless).
p	Pressure (Pa or indicated).
R^2	Determination coefficient.
Re	Reynolds number (dimensionless).
T	Temperature (°C).
v	Velocity (m/s).
α	Coefficient in a (dimensionless).
Δp	Pressure drop (Pa).
β	Coefficient in (4).

Manuscript received February 28, 2017; accepted October 23, 2017. Date of publication January 31, 2018; date of current version April 12, 2018. This work was supported in part by the European Union FP7 Project ROBOCADEMY (608096) and in part by the Estonian Centre of Excellence in ICT Research project EXCITE (TAR16013). The work of J. A. Tuhtan was supported by the Estonian base financing Grant B53, Octavo and PUT Grant 1690, Bioinspired flow sensing. (Corresponding author: Juan Francisco Fuentes-Pérez)

Guest Editor: W. Kirkwood.

The authors are with the Centre for Biorobotics, Tallinn University of Technology, Tallinn 12616, Estonia (e-mail: Juan.fuentes@ttu.ee; christian.meurer@ttu.ee; jeffrey.tuhtan@ttu.ee; maarja.kruusmaa@ttu.ee).

Digital Object Identifier 10.1109/JOE.2017.2767786

Θ	Angle (°).
ρ	Density (kg/m ³).

I. INTRODUCTION

OBTAINING vehicle speed information using onboard sensing is essential to perform navigation in autonomous underwater vehicles (AUVs) [1]. However, underwater vehicles do not enjoy the benefit of global positioning, and must instead rely on local sensing. One of the oldest and most common navigation techniques is dead reckoning [2]. In the most frequent configuration, inertial sensor data are used to estimate the vehicle's location from a known position using integrated speed or acceleration measurements. Unfortunately, sensor drift leads to unbounded errors [1], requiring the fusion of multiple sensors with different error characteristics [3], [4].

To overcome these problems, the basic navigation suite of most AUVs consists of an inertial navigation system aided by a Doppler velocity log (DVL) [5]–[7] or an acoustic Doppler current profiler (ADCP) [8] for additional velocity information. Both technologies make use of hydroacoustic measurements based on the Doppler shift [9]: An acoustic signal is transmitted and reflected back to the sensor via a solid reference surface as in DVL or by ambient particles in the water as in ADCP. Afterward, the relative velocity is computed from the Doppler shift of the reflected signal.

However, both DVL and ADCP suffer from certain limitations. The devices are expensive, typically have a large form factor and high energy consumption. Therefore, they are not suitable for small vehicles [10] or for prolonged missions with low energy consumption requirements [11]. Moreover, these technologies are too expensive for low-cost vehicles, which are useful in high risk applications, swarm operations, or in confined environments such as rivers and lakes [10], [12], [13]. Additionally, low-cost vehicles represent a developing market in consumer robotics [14].

Engineering fields such as aeronautics have successfully solved the problem of speed estimation by using pressure-based sensors [15], [16]. For instance, pressure sensors are commonly used to measure the relative speed, angle of attack, yaw rate, or altitude of aircrafts [17]–[20]. Moreover, they are standard applications in fluid related fields, e.g., to control industrial processes, for physical modeling, or for wind and flow tunnels. In view of their widespread and successful use in many fields,

exploring the potential of pressure sensors for underwater robotics is a logical step.

The most closely related pressure-based systems for underwater applications use artificial lateral lines that have been proposed for flow and speed measurements in underwater applications [21]–[24]. They are inspired by the passive sensing modalities present in fish, which are used to detect mechanical changes in the surrounding water [25], and they have shown the potential to overcome the following limitations of hydroacoustic methods.

- 1) They can be considered as a low-cost solution.
- 2) They have a lower energy consumption.
- 3) They can measure flows around the vehicles [26]. Likewise, they can be useful to perform complementary tasks such as for force estimation and wall detection [27].

In [26], we demonstrated the potential of differential pressure sensor based speedometry for underwater velocity estimation. We overcame some of the limitations of artificial lateral lines by substituting common absolute pressure sensors by differential pressure sensors, which a) increased the measuring range as well as the sensitivity and b) introduced a mechanical filtering for the static pressure components. Furthermore, we demonstrated that combining the output from two differential pressure sensors allowed speed estimations even under yaw angle deviations. Our previous study was made using a static small-scale laboratory platform. The obtained conclusions were thus limited and did not completely confirm the viability of the system for AUVs.

In this paper, we overcome the aforementioned limitations to validate differential pressure sensor speedometry as a viable full-scale technology for AUVs. To achieve this, following steps were performed.

- 1) A full-scale physical model based on differential pressure sensors is developed.
- 2) Two different types of sensors, digital and analog, are tested to obtain a more robust and faster platform.
- 3) A marine tow tank with a velocity range of 0–2 m/s is used.
- 4) The velocity time series under variable acceleration (0–2 m/s²) are analyzed.

With this, we conclude that differential pressure sensor speedometry is a valid solution to perform underwater speedometry and we confirm that the system can provide instantaneous and stable velocity estimates with a sampling rate higher than 10 Hz.

II. MATERIALS AND METHODS

A. Derivation of the Velocity–Pressure Relation

Invoking the conservation of energy within a fixed fluid volume, the fundamental relation [see (1)] between the pressure p and velocity v for an inviscid, incompressible flow is described by Bernoulli's law as follows:

$$p + \frac{1}{2}\rho v^2 = \text{const} \quad (1)$$

where p is pressure (Pa), ρ is the density (kg/m³), and v is the velocity (m/s). The equation states that between two points along the same streamline, the relation between v and p is a constant.

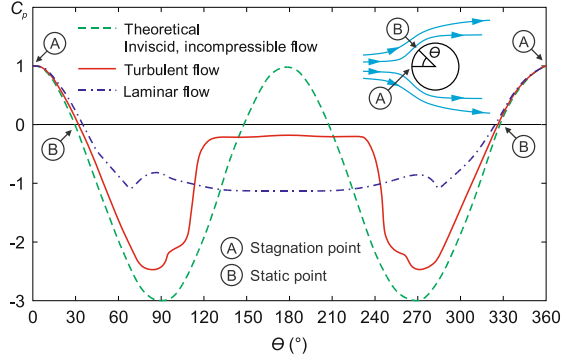


Fig. 1. Pressure coefficient $[C_p = (p - p_{\text{max}})/0.5 \cdot \rho \cdot v_{\text{max}}^2 = 1 - (v/v_{\text{max}})^2]$ distribution over a circular cylinder under laminar and turbulent air-flows according to the angle (Θ) from stagnation point (modified from [16]).

A common application of Bernoulli's law is the estimation of flow velocity using the effect of a rigid body in the flow [15]. The presence of such a body distorts the flow passing over it, and the undisturbed freestream velocity can be estimated utilizing the pressure difference across two or more points on surfaces encompassing a wide variety of geometries [28]. Our probe relies on the known empirical relation across two points on a spherical or circular body (see Fig. 1). At these points, the device is equipped with flush holes (pressure taps), which are normal to the surface. At the upstream most point, stagnation point A, the velocity is equal to zero ($v_A = 0$ m/s). At the second location, static point B, the pressure is equal to the static pressure of the undisturbed freestream flow (pressure coefficient, C_p , is equal to 0). The general equation for flow speed estimation is then derived based on the two measurement locations A and B as follows:

$$p_B + \frac{1}{2}\rho v_B^2 = p_A + \frac{1}{2}\rho v_A^2 = p_A \quad (2)$$

$$v_B = \sqrt{\frac{2(p_A - p_B)}{\rho}} = \sqrt{\frac{2\Delta p}{\rho}} \quad (3)$$

Equation (3) is well known as a basic principle in fluid mechanics, and widely applied for velocity estimation in air [15], [17] and water [21], [22]. The simplicity of the underlying physics has allowed others to successfully use alternative pressure tap placements [21].

In our previous work with a static small-scale laboratory prototype, we were able to demonstrate that the equations for the left and right differential inputs could be combined into a single formulation [26] as follows:

$$v = \sqrt[4]{\beta(\Delta p_1^2 + \Delta p_2^2)} \quad (4)$$

where $\beta = 2\alpha/\rho^2$ and Δp_1 and Δp_2 are the pressure drops at each side of the circular shape from the stagnation point to another point downstream and α is a coefficient that depends on the position of the points downstream ($\alpha \geq 1$ if $-35^\circ \leq \Theta \leq 35^\circ$). Note that when the circular shape is facing the flow

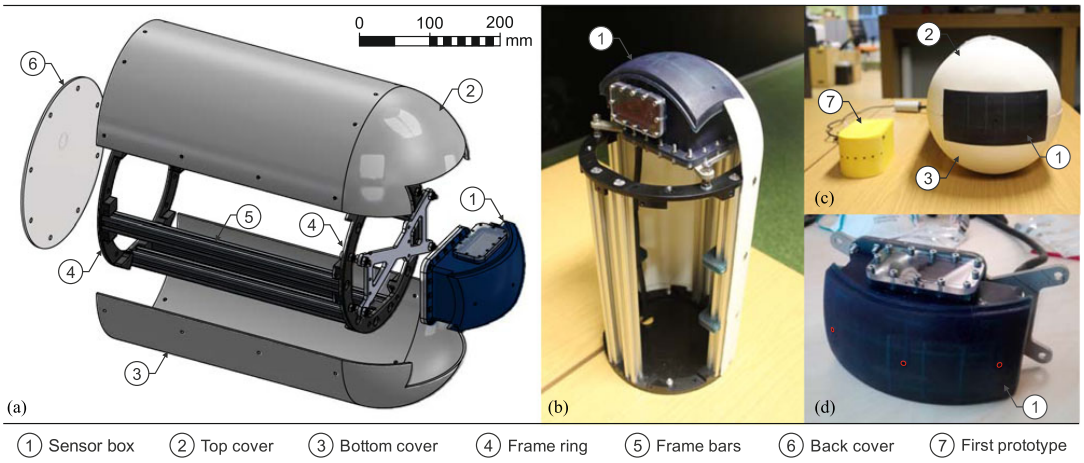


Fig. 2. Physical platform used in the experiments. (a) CAD design of the prototype. (b) Side view of the real prototype. (c) Comparison of the current platform against the static lab platform used for the preliminary results [26]. (d) Sensor box with pressure holes in red.

($\Delta p_1 = \Delta p_2$), (4) is equal to (3) if $\alpha = 1$. This equation was found to provide satisfactory performance even under yaw deviations of up to 45° [26]. It is valid for static or forward-moving bodies to provide estimates of one-dimensional speedometry, which can be expanded into two and three dimensions using multihole probes [15], [19].

The decision to work with circular and spherical geometries was not only based on their simplicity. Additionally, radially symmetric shapes benefit from a near-analytical pressure distribution up to $\pm 35^\circ$, which is nearly independent of the Reynolds number (Re) [29]. As shown in Fig. 1, the distribution of pressure and the flow over a circular cylinder are dependent on the orientation angle and present flow conditions, which are described by their respective Re . Neglecting the effects of vorticity or large-scale gradients in the static pressure field (e.g., the sensor body is impacted by waves), the fundamental physics underlying our design should allow it to perform under a large variety of real-world conditions.

B. Experimental Platform

The prototype was designed to be used in torpedo-shaped AUVs with interchangeable heads (e.g., [30]). However, as can be seen from Fig. 2(c), due to the small size of the pressure sensors, the design and dimensions can be easily adapted to cover an expanded range of vehicle sizes and sensor head geometries.

Drawing from our previous laboratory work based on a small-scale half cylinder [see Fig. 2(c)] [26], the experimental platform for these trials is a full-size hemisphere (see Fig. 2). It is worth noting that differential pressure speedometry with a hemispherical sensing head has also been applied successfully in aeronautics [17]–[19], [31]. The design consists of a frame of aluminum bars [5 in Fig. 2(a)] and polyoxymethylene rings [4 in Fig. 2(a)], where two three-dimensional (3-D) printed covers (printed using fused deposition modeling out of polylactic acid with epoxy reinforcement) [2 and 3 in Fig. 2(a)] and a

TABLE I
DIFFERENT ELECTRONICS TESTED IN THE PHYSICAL PLATFORM

Component	Analog	Digital
Microcontroller board	Arduino Micro	
Pressure sensors	MPXV7002	SSCDRRN005ND2A5
Number of pressure sensors	2	
Range	± 2000 Pa	± 1244 Pa
Maximum pressure ($p_A > p_B$)	75 000 Pa	4903.325 Pa
Temperature sensor	ADT7301 (13 bits)	On-board
Multiplexer	—	TCA9548A
Analog to digital converter	16 bits—LTC1867	14 bits—on-board
Resolution	0.0695 Pa	0.03 Pa
Tested sampling frequency	200 Hz	100 Hz
Maximum sampling frequency	>400 Hz	200 Hz

sensor box [1 in Fig. 2(a)] are attached. The sensor box is the most essential part of the system, as it houses all the electronics and provides the connection of the sensors with the environment. The box was 3-D printed using stereolithography.

Digital and analog sensors were tested and their comparison can be found in Table I. The digital sensors used the setup from our previous small-scale lab experiments [26]. In both cases, each pressure sensor measures one of the side pressure drop across the sensor box, from the stagnation point ($\theta = 0^\circ$) to the static point ($\theta = 35^\circ$) [see Fig. 2(d)].

Analog sensor conversion into standard pressure units requires a two-step calibration process (see Fig. 3): 1) subtraction of the constant temperature offset and 2) the transformation to real units. After calibration, a performance similar to the self-calibrating digital sensors was achieved.

C. Experimental Setup

Experiments were performed in a 59.4 m long and 5 m wide marine tow tank at the Small Craft Competence Centre in Kuressaare (Saaremaa, Estonia) (see Fig. 4). The prototype was

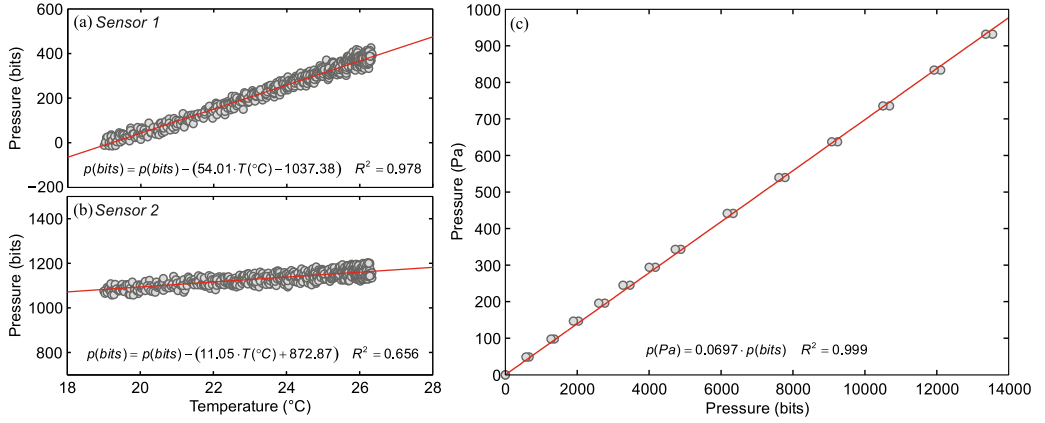


Fig. 3. Calibration of the analog sensor. (a) and (b) Subtraction of the offset due to temperature. (c) Fit to transform digital values to pressure in SI units.

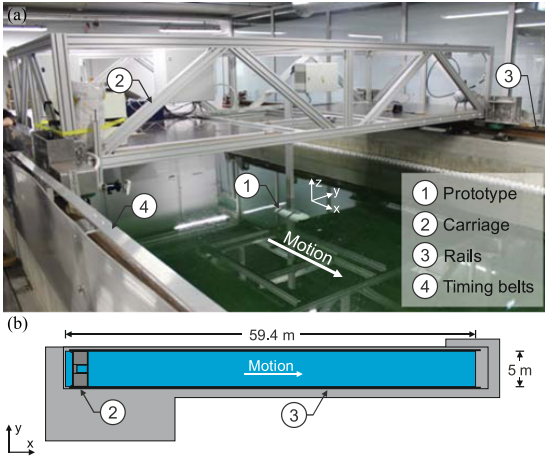


Fig. 4. Experimental setup. (a) Image of the tow tank carriage. (b) Top view of the tow tank.

attached to a tow tank carriage at a water depth of 0.5 m facing the motion direction parallel to the tank walls [see Fig. 4(a)]. The carriage belt drive is capable of covering a velocity range from 0.01 to 5.5 m/s and an acceleration a range from 0.01 to 3 m/s², in steps of 0.01 m/s and 0.01 m/s², respectively. At the lowest velocity ranges (<0.05 m/s), it was found that the carriage could not provide completely smooth motion and exhibited stepping, presumably caused by the belt drive. This was detected by the speedometry system, and its potential influence is discussed in Section III-B.

All velocity and acceleration tests were repeated using both analog and digital sensors (see Table II). Before each of the two replicates, a measurement in still water with a sampling time of 60 s was done. During velocity tests, the carriage was driven with a constant velocity, and data were gathered for 60 s in low velocities (≤ 0.5 m/s). Due to the fixed length of the tank, the sample duration was shorter for higher velocities. A similar procedure was used for acceleration, where the maximum

constant acceleration time was recorded taking into account the observed pressure sensor velocity limitations (2.4 m/s for analog and 2.0 m/s for digital).

D. Data Processing and Validation

The still water measurements were used as a reference point in each of the conducted replicates. All the proposed fits were evaluated using the coefficient of determination R^2 as well as graphically. In addition, the observed data were compared to the predicted data and the mean absolute error was used as the measure of achieved accuracy.

In the time series analysis, the relation between the estimated velocity and the carriage velocity data was evaluated graphically, as well as using the cross correlation C_c between signals. Likewise, the time series were estimated from (4). However, this formulation does not allow the use of negative values [note that Δp in (4) is squared] leading to a poor performance in low velocities. For low velocities, negative values of Δp occurred, either due to the influence of other pressure sources in the water or, in the case of these experiments, because of the stepping of the carriage. To solve this, a short correction algorithm was implemented as follows:

$$v = \begin{cases} 0, & \text{if } \Delta p_1, \Delta p_2 < 0 \\ \sqrt[4]{\beta |(\Delta p_1 |\Delta p_1| + \Delta p_2 |\Delta p_2|)|}, & \text{if } \Delta p_1 + \Delta p_2 > 0 \\ -\sqrt[4]{\beta |(\Delta p_1 |\Delta p_1| + \Delta p_2 |\Delta p_2|)|}, & \text{if } \Delta p_1 + \Delta p_2 < 0. \end{cases} \quad (5)$$

The performance of this correction algorithm will be discussed in Section III-C.

III. RESULT AND DISCUSSIONS

A. General Equation

Fig. 5 summarizes the pressure distribution and the expected results for long-term velocity estimations using the designed prototype with both sensor types. In Fig. 5(a) and (b), the pressure distribution of each sensor for each velocity test replicate

TABLE II
CONDUCTED EXPERIMENTS

Variables	Replicates	Configurations	Tow tank carriage settings	Total number of experiments
v (m/s)	2	2	[0.01, 0.05] every 0.01 m/s [0.10, 0.50] every 0.10 m/s [0.75, 1.00] every 0.25 m/s	64
a (m/s ²)	2	2	[0.01, 0.05] every 0.01 m/s ² [0.075] [0.10, 0.50] every 0.10 m/s ² [0.75, 1.00] every 0.25 m/s ²	68

In each test, the target variable was held constant.

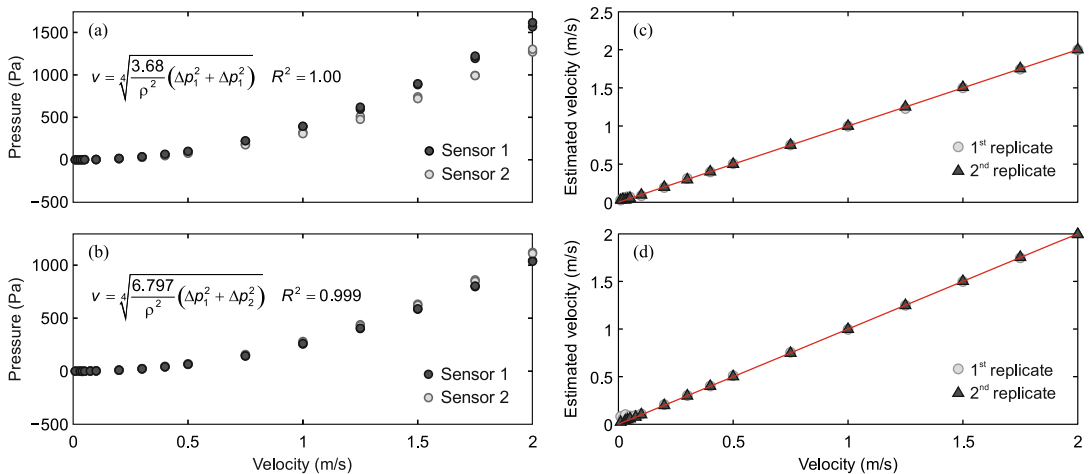


Fig. 5. Pressure distribution and fits for the two studied sensor types. (a) Pressure distribution in analog sensors. (b) Pressure distribution in digital sensors. (c) Estimated against observed results for analog sensors. (d) Estimated against observed results for digital sensors.

can be observed. When comparing the analog and digital results, a slight deviation between the sensors is present, which is produced by a small misalignment of the prototype with the motion vector of the carriage. The deviation is more distinct for analog sensors, because the misalignment of the prototype was corrected prior to the experiments with digital sensors. Despite this small deviation, the results provide a good example to demonstrate the potential of (4), which can correct these deviations with a small error margin ($R^2 = 1.00$ for analog and $R^2 = 0.99$ for digital) [see Fig. 5(c) and (d)]. After fitting, the estimated mean absolute errors were 0.0087 m/s for analog and 0.0107 m/s for digital sensors. The obtained mean errors of both analog and digital sensor configurations were lower than those obtained in our previous small-scale tests in [26] (0.024 m/s).

Fig. 5 further shows the importance of sensitivity when measuring low velocities. Based on the fitted equations for a velocity of 0.01 m/s, the pressure difference is 0.037 Pa for analog and 0.027 Pa for digital configurations. These quantities are outside the sensitivity range of the pressure sensors and could be easily corrupted by other pressure sources, especially turbulence. To estimate lower velocities, a large number of data samples are required.

In the same way, when the prototype was placed in the water, a still water measurement was recorded as reference. Although this is not always necessary, placing the robot into the water may generate a small constant offset due to the different quantity of water in the pressure tap internal tubing. Precise knowledge of this difference could be used to improve the estimation of low-range velocities.

B. Effective Sampling Frequency and Sensor Comparison

Fig. 6 shows the expected behavior of the mean velocity error with respect to the sampling time. For both electronic configurations, errors are higher for low velocities (darker lines, Fig. 6) and a stable value is achieved later. It is worth mentioning that the observed stepping in the carriage could also have contributed to increase this error.

As argued in Section III-A, due to the quadratic relation between v and p , the sensitivity requirements to estimate different velocities are also different. This leads to the need of an increased sample size to estimate low velocities. A similar behavior is expected for the error, it will be higher for low velocities due to the sensitivity requirements and a higher influence of external pressure noise sources.

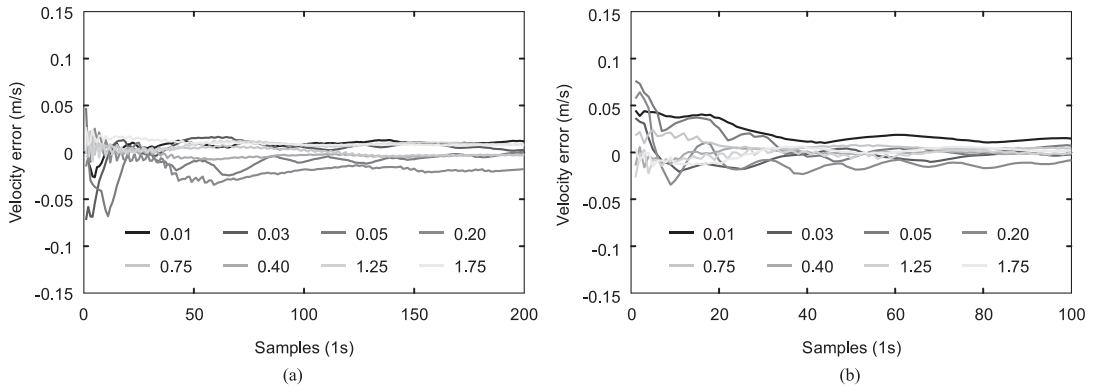


Fig. 6. Average error evolution over time. (a) Evolution of analog sensor mean value in 1 s (200 Hz) for different velocities. (b) Evolution of digital sensor mean value in 1 s (100 Hz) for different velocities.

Considering the evolution of the mean absolute velocity error, an error lower than 0.01 m/s is achieved using 15 analog and 29 digital samples. Taking this and the sampling rate of analog sensors 200 Hz into account, an effective sampling rate of 13 Hz is obtained. In the case of digital sensors due to the lower measurement rate 100 Hz, an effective sampling rate of 3 Hz is achieved. In view of this, we presume that by exploiting the highest possible measurement rate in the sensors we could increase the effective sampling rate. For instance, in the laboratory experiments conducted in [26] using 200 Hz with the digital platform, an effective sampling rate higher than 10 Hz was calculated. In both cases, the sampling rate is higher or in the range of 1–5 Hz, which is the conventional rate of DVLS [32], [33].

The motivation behind the analog configuration was to check the possibility of obtaining similar results with a more robust rapid platform. As shown, both sensor configurations are able to correctly estimate the velocity; however, both have their advantages and disadvantages. Digital sensors have a higher resolution ($0.03 \text{ Pa} < 0.0695 \text{ Pa}$) due to the lower measuring range ($\pm 1244 \text{ Pa} < \pm 2000 \text{ Pa}$) and an unknown internal process of average filtering. Additionally, the internal analogue-to-digital converter (ADC) and temperature sensors reduce the number of necessary components in the hardware. On the other side, due to the I2C connection, and because we use sensors with the same address, it is necessary to implement a multiplexer, which slows down the possible sampling frequency ($200 \text{ Hz} < 400 \text{ Hz}$). Also, the measuring range of the digital sensors can be limiting for some applications and they are more expensive (due to their resolution, on-board compensation, and stability). The connectors in the digital sensors require a more complex design and are more difficult to install. In addition, it is not possible to control the calibration process, which generates a black box effect and makes it impossible to apply customized workflows.

C. Time Series and Acceleration Analysis

In Fig. 7, the results of the acceleration tests are shown for three of the experiments (low = $0.02 \text{ m}^2/\text{s}$, medium =

$0.20 \text{ m}^2/\text{s}$, and high = $2.00 \text{ m}^2/\text{s}$) with both sensor types. In this figure, considering the results of the previous sections, the velocities have been calculated after average filtering the signals and downsampling them to 10 Hz.

As can be seen in Fig. 7, the quadratic relation between the v and Δp holds for all accelerations, which allows us to apply (4) instantly. In Fig. 7(a)–(d), decelerations are shown as an example, demonstrating similar behavior and, thus, the possibility of using (4).

The good performance of the correction algorithm (5) becomes apparent when raw and corrected signals from the beginning of each series are compared [cf., details in Fig. 7(a)–(e)]. Using (4) would produce an overestimation in the low-range velocities, which could only be compensated if the average value of the long-time data series of Δp was considered for v calculation. This overestimation may have been caused by the observed stepping error of the carriage; nevertheless, it can happen with other natural pressure sources, too. In view of the results, using (5) seems to provide a solution to achieve a better result and a higher sampling frequency during low velocities. Likewise, the algorithm can be applied online due to its simplicity.

After applying the correction algorithm, the C_e between measured velocity signal and estimated velocity is in all cases higher than 0.999. Furthermore, the estimated velocity signals are able to reproduce the small velocity oscillation produced by the control system of the tow tank [see Fig. 7(d)–(b)], this accuracy could be essential to correct deviations during AUV navigation.

Contrary to absolute pressure sensors, differential sensors mechanically filter the static water pressure contribution. This provides increased sensitivity and allows for direct mechanical filtering of disturbances such as waves. The positive effect of this performance was observed during the conducted experiments. The carriage generated surface waves, which were undetected in the pressure sensor time series data. This can be a potential issue that should be further considered in systems where the distance between pressure taps is larger, for passage through standing waves, or for wavelengths smaller than the offset between taps.

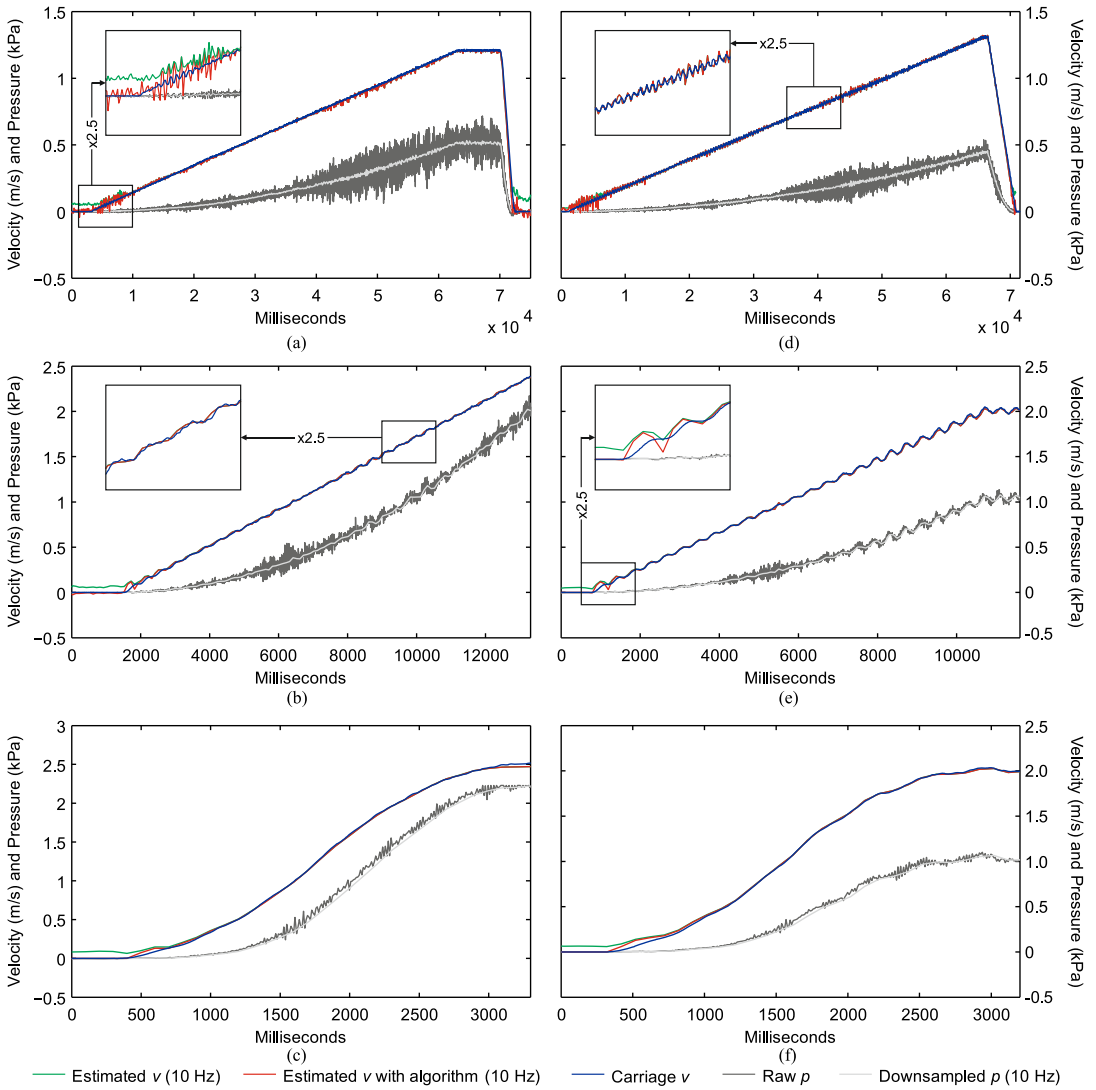


Fig. 7. Time series analysis of the velocity estimation for three scenarios (low acceleration, medium acceleration, and high acceleration) for both electronic types. Analog sensor: (a) acceleration of 0.02 m/s^2 , deceleration of 0.5 m/s^2 , and detail of the correction algorithm performance; (b) acceleration of 0.20 m/s^2 and detail of velocity oscillation tracking; (c) acceleration of 2.00 m/s^2 . Digital sensor: (d) acceleration of 0.02 m/s^2 , deceleration of 0.3 m/s^2 , and detail of velocity oscillation tracking; (e) acceleration of 0.20 m/s^2 and detail of the correction algorithm performance; (f) acceleration of 2.00 m/s^2 .

IV. SUMMARY AND CONCLUSION

In this paper, underwater differential pressure sensor speedometry is introduced and studied. Building on our previous results, a full-scale prototype using analog and digital sensors was tested in a marine tow tank. The speed calculation is based on a simple formulation built upon the conservation of energy. It shows the ability to calculate the speed in moving platforms as well as correct angular deviations, which may be useful to correct sensor misalignment.

The comparison of analog and digital sensors revealed similar results. Considering the tested prototype, the analog sensors

offer the more promising alternative as they provide a higher sampling rate and have a lower price and the possibility of implementing customized calibration processes.

Analysis showed that differential pressure speedometry correctly estimated the velocity, and was able to detect the rapid fluctuations caused by the belt drive. A basic derivation using the conservation of energy was developed and applied to accurately estimate the velocity. The mean absolute errors were 0.0087 m/s for analog and 0.0107 m/s and digital sensors.

The effective sampling frequency in the velocity range of $0\text{--}2 \text{ m/s}$ was found to be higher than other available technolo-

gies, which makes differential pressure sensor speedometry a valuable complement to existing solutions. Likewise, it seems to be a viable alternative for those AUVs outside the application range of DVLs or ADCPs, such as small, low cost, or low energy requirement vehicles.

V. FUTURE WORK

Future work will concentrate on the implementation of the prototype into a real AUV and subsequent prototype testing in laboratory and field conditions. Direct comparison with existing key technologies for speedometry such as DVL could provide more information about the performance of our sensor technology. In addition, we plan to develop sensor-fusion algorithms using differential pressure sensors, inertial measurements, and DVLs to access the complementary potential of our sensors for navigation and control. The extension of the sensor system into two or three dimensions is another promising research topic which could provide new methods for underwater speedometry and navigation.

ACKNOWLEDGMENT

The authors would like to thank the staff of the Small Craft Competence Centre. In addition, they would like to thank the staff at the Centre for Biorobotics for their advice and active participation during the development and testing of the prototype.

REFERENCES

- [1] L. Paull, S. S. Saedi, M. Seto, and H. H. Li, "AUV navigation and localization: A review," *IEEE J. Ocean. Eng.*, vol. 39, no. 1, pp. 131–149, Jan. 2014.
- [2] D. Loebis, R. Sutton, and J. Chudley, "Review of multisensor data fusion techniques and their application to autonomous underwater vehicle navigation," *J. Mar. Eng. Technol.*, vol. 1, no. 1, pp. 3–14, 2002.
- [3] L. Stutters, H. Liu, C. Tiltman, and D. J. Brown, "Navigation technologies for autonomous underwater vehicles," *IEEE Trans. Syst. Man, Cybern. C*, vol. 38, no. 4, pp. 581–589, Jul. 2008.
- [4] J. C. Kinsey and L. L. Whitcomb, "Towards in-situ calibration of gyro and Doppler navigation sensors for precision underwater vehicle navigation," in *Proc. IEEE Int. Conf. Robot. Autom.*, 2002, vol. 4, pp. 4016–4023.
- [5] G. Grenon, P. E. An, S. M. Smith, and A. J. Healey, "Enhancement of the inertial navigation system for the Morpheus autonomous underwater vehicles," *IEEE J. Ocean. Eng.*, vol. 26, no. 4, pp. 548–560, Oct. 2001.
- [6] L. Whitcomb and D. Yoerger, "Towards precision robotic maneuvering, survey, and manipulation in unstructured undersea environments I introduction," *Dana*, vol. 8, pp. 45–54, 1998.
- [7] B. Jalving, K. Gade, K. Svartveit, A. Willumsen, and R. Sørhagen, "DVL Velocity Aiding in the HUGIN 1000 integrated inertial navigation system," *Model. Identif. Control*, vol. 25, no. 4, pp. 223–235, 2004.
- [8] D. A. Fong and N. L. Jones, "Evaluation of AUV-based ADCP measurements," *Limnol. Oceanogr. Methods*, vol. 4, no. 3, pp. 58–67, 2006.
- [9] A. Kenny and G. Lopez, "Advances in and extended application areas for Doppler sonar," in *Proc. MTS/IEEE OCEANS*, 2012, pp. 1–9.
- [10] T. Salumäe *et al.*, "Design principle of a biomimetic underwater robot U-CAT," in *Proc. MTS/IEEE OCEANS*, 2014, pp. 1–5.
- [11] D. L. Rudnick, R. E. Davis, C. C. Eriksen, D. M. Fratantoni, and M. J. Perry, "Underwater gliders for ocean research," *Mar. Technol. Soc. J.*, vol. 38, no. 2, pp. 73–84, 2004.
- [12] O. A. Viquez, E. M. Fischell, N. R. Rypkema, and H. Schmidt, "Design of a general autonomy payload for low-cost AUV R & D," in *Proc. IEEE/OES Auton. Underwater Veh.*, 2016, pp. 151–155.
- [13] B. Hartmann, N. Link, and G. F. Trommer, "Indoor 3D position estimation using low-cost inertial sensors and marker-based video-tracking," in *Proc. IEEE/ION Position Location Navig. Symp.*, 2010, pp. 319–326.
- [14] 2017. [Online]. Available: <https://www.openrov.com/products/trident/>
- [15] E. Ower and R. C. Pankhurst, *The Measurement of Air Flow*. Amsterdam, The Netherlands: Elsevier, 2014.
- [16] J. D. Anderson, Jr., *Fundamentals of Aerodynamics*. New York, NY, USA: McGraw-Hill, 2010.
- [17] K. H. Beij, *Aircraft Speed Instruments*, 1933.
- [18] K. E. Garman *et al.*, "An airborne and wind tunnel evaluation of a wind turbulence measurement system for aircraft-based flux measurements," *J. Atmos. Ocean. Technol.*, vol. 23, no. 12, pp. 1696–1708, 2006.
- [19] E. N. Brown, C. A. Friehe, and D. H. Lenschow, "The use of pressure fluctuations on the nose of an aircraft for measuring air motion," *J. Appl. Meteorol. Climatol.*, vol. 22, no. 1, pp. 171–180, 1983.
- [20] J. Hacker and T. Crawford, "The BAT-probe: The ultimate tool to measure turbulence from any kind of aircraft (or sailplane)," *Tech. Soaring*, vol. 23, no. 2, pp. 43–46, 1999.
- [21] T. Salumäe and M. Kruusmaa, "Flow-relative control of an underwater robot," *Proc. Roy. Soc. A, Math. Phys. Eng. Sci.*, vol. 469, no. 2153, 2013, Art. no. 20120671.
- [22] J. F. Fuentes-Pérez *et al.*, "Current velocity estimation using a lateral line probe," *Ecol. Eng.*, vol. 85, pp. 296–300, 2015.
- [23] C. Wang, W. Wang, and G. Xie, "Speed estimation for robotic fish using onboard artificial lateral line and inertial measurement unit," in *Proc. IEEE ROBOT. 2015*, pp. 285–290.
- [24] W. Wang, Y. Li, X. Zhang, C. Wang, S. Chen, and G. Xie, "Speed evaluation of a freely swimming robotic fish with an artificial lateral line," in *Proc. IEEE Int. Conf. Robot. Autom.*, 2016, pp. 4737–4742.
- [25] S. Dijkgraaf, "The functioning and significance of the lateral-line organs," *Biol. Rev.*, vol. 38, no. 1, pp. 51–105, 1963.
- [26] J. F. Fuentes-Pérez, K. Kalev, J. A. Tuhtan, and M. Kruusmaa, "Underwater vehicle speedometry using differential pressure sensors: Preliminary results," in *Proc. IEEE/OES Auton. Underwater Veh.*, 2016, pp. 156–160.
- [27] Y. Xu and K. Mohseni, "A pressure sensory system inspired by the fish lateral line: Hydrodynamic force estimation and wall detection," *IEEE J. Ocean. Eng.*, vol. 42, no. 3, pp. 532–543, Jul. 2017.
- [28] M. Kabaciński and J. Pospolita, "Numerical and experimental research on new cross-sections of averaging Pitot tubes," *Flow Meas. Instrum.*, vol. 19, no. 1, pp. 17–27, 2008.
- [29] A. Travin, M. Shur, M. Strelets, and P. Spalart, "Detached-eddy simulations past a circular cylinder," *Flow Turbul. Combust.*, vol. 63, pp. 293–313, 1999.
- [30] M. Carreras *et al.*, "Sparus II, design of a lightweight hovering AUV," in *Proc. Int. Workshop Marine Technol.*, 2013, pp. 152–155.
- [31] A. Cho, J. Kim, S. Lee, and C. Kee, "Wind estimation and airspeed calibration using a UAV with a single-antenna GPS receiver and pitot tube," *IEEE Trans. Aerosp. Electron. Syst.*, vol. 47, no. 1, pp. 109–117, Jan. 2011.
- [32] Ø. Hegrenæs, A. Ramstad, T. Pedersen, and D. Velasco, "Validation of a new generation DVL for underwater vehicle navigation," in *Proc. IEEE/OES Auton. Underwater Veh.*, 2016, pp. 342–348.
- [33] J. C. Kinsey, R. M. Eustice, and L. L. Whitcomb, "A survey of underwater vehicle navigation: Recent advances and new challenges," in *Proc. IFAC Conf. Manoeuv. Control Mar. Craft*, 2006, pp. 1–12.



Juan Francisco Fuentes-Pérez received the B.Eng. degree in forestry engineering, specialized in hydraulics, and the M.Sc. degree in engineering for agroforestry development from the University of Valladolid, Valladolid, Spain.

He has been collaborating in several research projects focused on the design, simulation, and evaluation of fishways, and he has been involved in artificial lateral line technology and its applications for the evaluation of aquatic ecosystems and its use in underwater robotics since 2014. He is currently working

toward the Ph.D. degree and is a Junior Researcher at the Centre for Biorobotics, School of Computer Systems, Tallinn University of Technology, Tallinn, Estonia.

His current research interests include underwater sensing, underwater robotics, fluid mechanics, ecohydraulics, and fishways.



Christian Meurer received the B.Eng. degree in biotechnology from the Ernst-Abbe Hochschule, Jena, Germany, in 2012 and the M.Sc. degree in bionics/biomimetics from the Hochschule Rhein-Waal, Kleve, Germany, in 2015. He is currently working toward the Ph.D. degree within the framework of the Estonian Centre of Excellence in ICT Research (EX-CITE), Centre for Biorobotics, School of Computer Systems, Tallinn University of Technology, Tallinn, Estonia

He is currently a Junior Researcher with the Centre for Biorobotics, School of Computer Systems, Tallinn University of Technology. His current research interests include bioinspired actuation and sensing for underwater robots, as well as control of autonomous underwater vehicles.



Maarja Kruusmaa received the B.Eng. degree in computer engineering from Tallinn University of Technology, Tallinn, Estonia and the Ph.D. degree in computer engineering from Chalmers University of Technology, Gothenburg, Sweden.

She is currently the Head of the Centre for Biorobotics, Tallinn University of Technology. Her research mainly focuses on bio-inspired underwater robotics. During the past years she has worked on flow sensing underwater robots, bio-inspired robot locomotion, experimental fluid dynamics and robot

learning.



Jeffrey Andrew Tuhtan received the B.Sc. degree in civil engineering from California Polytechnic University, San Luis Obispo, CA, USA, in 2004 and the M.Sc. degree in water resources engineering and management and the Dr. Eng. degree in hydraulics from the University of Stuttgart, Stuttgart, Germany, in 2007 and 2011, respectively.

He is currently with the Centre for Biorobotics, Department of Computer Systems, Tallinn University of Technology, Tallinn, Estonia, where he leads the Environmental Sensing and Intelligence Group.

His current research interests include environmental intelligence, applied fluid mechanics, and remote sensing.

Appendix 4 - Publication 2

II

C. Meurer, J. Francisco Fuentes-Perez, N. Palomeras, M. Carreras, and M. Krusmaa, "Differential Pressure Sensor Speedometer for Autonomous Underwater Vehicle Velocity Estimation," IEEE Journal of Oceanic Engineering, pp. 1-33, 2019

Differential Pressure Sensor Speedometer for Autonomous Underwater Vehicle Velocity Estimation

Christian Meurer^{1b}, Juan Francisco Fuentes-Pérez^{2b}, Narcís Palomeras^{2b}, Marc Carreras^{2b}, and Maarja Kruusmaa^{1b}

Abstract—Velocity estimation is central for the reliable navigation of autonomous underwater vehicles (AUVs). Doppler velocity logs (DVLs), currently the leading technology for underwater velocity estimation, can be too big, expensive, and energy consuming to be used on low-cost and small AUVs or for long missions. In our previous work, a system based on differential pressure sensors was developed for estimating surge velocity. In this paper, we combine this system with an inertial measurement unit to compensate for orientation errors and create a differential pressure sensor speedometer (DPSS). We propose and demonstrate the DPSS prototype as an important step toward a small, inexpensive, and energy-efficient alternative or complement to a DVL in certain applications. This paper presents the first underwater field tests of a sensor using differential pressure for velocity estimation. Tests were conducted with a SPARUS II AUV (IQUA Robotics, Girona, Spain). To demonstrate the efficacy of our proposed solution, we compare the surge velocity estimation of the DPSS and the vehicle's DVL in bottom and water locks. Trials were conducted by varying the trajectory and velocity of the vehicle in three different environments. We show that the DPSS displayed a superior performance with respect to the DVL water lock for velocities above 0.6 m/s. The differences in the velocity estimations of the DVL in bottom lock for high velocities were as small as 0.013 m/s. These results encourage further development of the presented technology.

Index Terms—Autonomous underwater vehicle (AUV), differential pressure sensors, Doppler velocity log (DVL), dead reckoning, flow sensing.

I. INTRODUCTION

FOR THE successful operation and recovery of autonomous underwater vehicles (AUVs), robust navigation and localization are crucial [1], [2]. However, the availability of sophisticated sensor systems for navigation and localization is restricted by the size, energy requirements, budget, and operation conditions of the particular vehicle. Especially with the increasing

use of low-cost and small vehicles, there is a need for alternative sensor solutions. This paper describes field tests to validate a small, low-cost, and energy-efficient sensor system for surge velocity estimation that uses differential pressure sensors.

Unlike terrestrial or aerial environments, autonomous underwater navigation is impeded by the rapid high-frequency attenuation of sensor signals or by the lack of salient features in mostly unstructured environments. Common navigation methods, such as satellite-based global positioning units, are not directly implementable. Existing underwater navigation solutions can be divided into three main categories [3]: acoustic navigation, geophysical navigation, and inertial navigation.

Acoustic navigation requires additional hardware to be deployed, which creates a local coordinate system. Therefore, this solution is limited to environments where hardware deployment is feasible. Though geophysical navigation uses the features near the AUV to track location within an environment, it is not extensible to unstructured or open water environments. Inertial navigation, the most basic navigation method, uses dead reckoning techniques to estimate the position of the vehicle. Inertial navigation is insensitive to environmental characteristics, making it suitable for operations in either featureless or complex environments. Further, this method removes the need for a costly and complex infrastructure, decreasing the expenses for AUV missions. Though current inertial navigation systems (INS) provide increasingly accurate heading and acceleration measurements that can improve overall position estimates [1], this method suffers from unbounded errors [4]. In best practice, the methods mentioned above are combined using sensor fusion and state estimation [4], [5] to increase the overall robustness and accuracy of the navigation system. Methods for sensor fusion and state estimation include Kalman filters, particle filters, and simultaneous localization and mapping [5]. The most commonly adopted method for state estimation is the extended Kalman filter (EKF) that can handle nonlinear processes with Gaussian error distributions at a moderate computational load.

Due to its global applicability, inertial navigation is the core technique for most navigation solutions. Measuring velocity directly is a particularly compelling way to complement measurements from INSs. Doppler velocity logs (DVLs) are the most widely applied class of velocity sensors used to aid the INS [6]–[9], providing velocity estimation with a sufficiently narrow error margin [4]. DVLs are preferably used in bottom lock (BL) mode that relies on a smooth surface where the scattering of

Manuscript received September 15, 2018; revised February 10, 2019; accepted March 21, 2019. Date of publication May 2, 2019; date of current version July 14, 2020. This work was supported in part by the EU FP7 project ROBOCADEMY under Grant 608096, in part by the European Regional Development Fund, in part by the Estonian Centre of Excellence in ICT Research project EXCITE (TAR16013), and in part by the Estonian Research Council grant (IUT-339). (Corresponding author: Christian Meurer.)

Associate Editor: B. Bingham.

C. Meurer, J. Francisco Fuentes-Pérez, and M. Kruusmaa are with the Centre for Biorobotics, Tallinn University of Technology, Tallinn 12616, Estonia (e-mail: christian.meurer@taltech.ee; juan.fuentes@taltech.ee; maarja.kruusmaa@taltech.ee).

N. Palomeras and M. Carreras are with the Computer Vision and Robotics Institute, Universitat de Girona, Girona 17003, Spain (e-mail: npalomer@eia.udg.edu; marc.carreras@udg.edu).

Digital Object Identifier 10.1109/JOE.2019.2907822

hydroacoustic signals can be avoided. In regions with uneven or absent surfaces, DVLs can employ a water lock (WL) mode to estimate velocity. However, DVL WL has certain limitations as it cannot provide the same accuracy as the BL and relies on the presence of particles that can reflect the hydroacoustic signals in water. As recent work suggests, using acoustic Doppler current profilers (ADCP) can solve some of these problems [10], [11].

However, despite recent efforts to reduce their size [12]–[14], DVLs and ADCPs are difficult to integrate in small vehicles with a limited payload capacity [15]. Further, as active sensing devices, DVLs have a high energy consumption, which impedes their application in vehicles on long-term missions [16]. Additionally, low-cost vehicles used in areas such as high-risk applications [17], swarm operations [18], or consumer robots [19] could benefit from an inexpensive alternative for velocity estimation.

In this paper, we propose a low-cost, small-sized, and energy-efficient technology for estimating surge velocity based on differential pressure sensors. The proposed solution builds upon our previous work, which was originally bioinspired by fish lateral line sensing [20]. Several artificial lateral line systems have been proposed earlier [21], [22], but none of them has been combined with a fully autonomous AUV and, to the best of the authors' knowledge, none have been tested outside of the carefully controlled laboratory environment. The artificial lateral line systems proposed earlier have been based on various technological approaches, such as micromachined piezoresistive cantilevered beams [23], [24], optical flow sensors [25], or commercially available absolute or gauge pressure sensors [26]–[32]. In contrast, our system is built with commercially available, inexpensive and robust pressure sensors, which are most suitable for field conditions.

Flow estimation based on pressure sensors can be achieved by applying Bernoulli's law, which establishes a quadratic relation between flow velocity and pressure [33], [34]. However, the quadratic relation implies that a high sensitivity for pressure is required for low velocity estimations. Absolute and gauge pressure sensors measure pressure relative to a fixed reference, which increases the pressure ranges and reduces the pressure sensitivity proportionally to the operation depth. To overcome this problem, differential pressure sensors can be used.

These sensors can measure a pressure difference across two points in the same plane. Thus, the static component of the pressure is mechanically filtered out, which decreases the necessary pressure range to be measured, increasing the sensitivity of the sensor [22], [35]. In our previous publication, we described a prototype to estimate the surge velocity for torpedo-shaped AUVs based on differential pressure sensors [36]. The prototype was calibrated and tested in laboratory conditions and able to estimate velocity with an accuracy of 0.012 m/s. Given the envisioned applications where it may be difficult to use DVLs in BL or where no velocity aiding is available at present, this accuracy is sufficiently close to those achieved by DVLs [37], which motivated the field tests presented in this paper. By testing in field, self-motion effects induced by environmental dynamics had to be considered. In this paper, we enhance the proposed

prototype with an inertial measurement unit (IMU) to compensate for such self-motion effects.

We will refer to the resulting sensor system as differential pressure sensor speedometer (DPSS) and present its performance in field tests. The DPSS was integrated into a commercial AUV (SPARUS II, IQUA Robotics) and tested in different environmental conditions including several depths in protected and open waters. SPARUS II followed three types of trajectories (linear, lawn mower, and loop) at surge velocities ranging between 0.1 and 1.5 m/s. For tests in the protected environment with target velocities greater than 1 m/s, the differences in the velocity estimations of DPSS and DVL, expressed as root-mean-square error (RMSE), did not exceed 0.032 m/s. Furthermore, minimum errors of 0.013 m/s could be achieved, which were very close to the ideal accuracy of the DPSS.

This paper is organized as follows: In Section II, we provide the theoretical background and design of the DPSS. Section III describes the experimental platform, the SPARUS II AUV, used for field tests. The experimental setup and data analysis for the field tests are explained in Section IV. In Section V, we present the results from our field tests and discuss them. Finally, we conclude this paper in Section VI and provide some remarks about lessons learned during the field trials and potential for future work.

II. DIFFERENTIAL PRESSURE SENSOR SPEEDOMETER

In this section, we present the theoretical background and the physical implementation of the DPSS. We start by deriving the velocity model relating the pressure measurements of the DPSS with the surge velocity. We then describe the design and physical setup of the DPSS, which ensures accurate and stable measurements.

A. Velocity Model

Based on the conservation of energy within a fixed fluid volume assuming an inviscid and incompressible flow and neglecting elevation effects, Bernoulli's law describes the fundamental relation between pressure p and velocity v as

$$p + \frac{1}{2}\rho v^2 = \text{const} \quad (1)$$

where ρ is the density of the fluid.

Bernoulli's law can be used to estimate flow velocity around an immersed rigid body. The fluid motion over spherical shapes has been especially used for flow speed estimation in aeronautics [38], [39]. As explained in Fig. 1, a spherical body with two specific measurement points for pressure on its surface can be utilized to estimate the flow speed.

In Fig. 1(a), point A is defined as the stagnation point, where the velocity v_A equals zero, whereas point B represents a static point, where the velocity v_B is equal to the free stream velocity v_∞ . Under the assumption of an irrotational and steady flow, points A and B can be used together with (1) to derive a general equation for flow velocity, which is commonly known as the

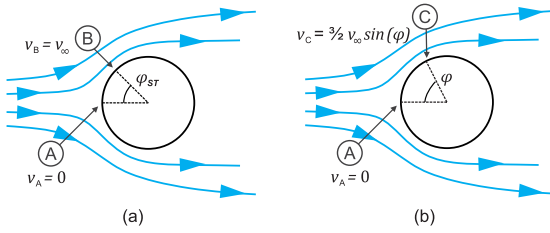


Fig. 1. Irrotational inviscid and incompressible flow over a sphere. The stagnation point on the spheres surface is indicated by A. (a) We introduce the static point B, respective velocities v_A and v_B and the enclosing angle φ_{ST} . (b) We introduce an arbitrary surface point C, respective velocities v_A and v_C and the enclosing angle φ . In both cases, v_∞ denotes the free stream velocity.

Pitot equation

$$p_B + \frac{1}{2}\rho v_B^2 = p_A \tag{2}$$

$$v_\infty = v_B = \sqrt{\frac{2(p_A - p_B)}{\rho}} = \sqrt{\frac{2\Delta p}{\rho}}. \tag{3}$$

Equation (3) assumes that the measurement point B is a static point of a specific body. To relax this constraint, the relation between the velocity v_c at an arbitrary position C on the spherical body and the free stream velocity needs to be established. For a high Reynolds number flow regime past a sphere, this relation can be described with [33]

$$v_c = \frac{3}{2} v_\infty \sin(\varphi) \tag{4}$$

where φ is defined as the angle between stagnation point A and measurement point C [see Fig. 1(b)]. Equation (3) can be rewritten for arbitrary locations of measurement points by replacing v_B with (4) as follows:

$$v_\infty = \sqrt{\frac{2}{\rho} \frac{4\Delta p}{9\sin^2(\varphi)}}. \tag{5}$$

Equation (3) and subsequently (5) only allow accurate flow velocity estimation if the stagnation point faces the flow, which cannot always be guaranteed in dynamic applications underwater. This problem can be solved by introducing a second measurement point C* at a mirrored position from point C. Equation (5) can be used to utilize two pressure differences $\Delta p_1 = p_A - p_C$ and $\Delta p_2 = p_A - p_{C^*}$ between the stagnation point and the two additional measurement points. First, we take the quadratic average of the pressure differences and express them in terms of free stream velocity using (2) and (4) as follows:

$$\begin{aligned} & \sqrt{\frac{\Delta p_1^2 + \Delta p_2^2}{2}} \\ &= \sqrt{\frac{\left(\frac{1}{2}\rho\left(\frac{3}{2}v_\infty \sin(\varphi_1)\right)^2\right)^2 + \left(\frac{1}{2}\rho\left(\frac{3}{2}v_\infty \sin(\varphi_2)\right)^2\right)^2}{2}} \tag{6} \end{aligned}$$

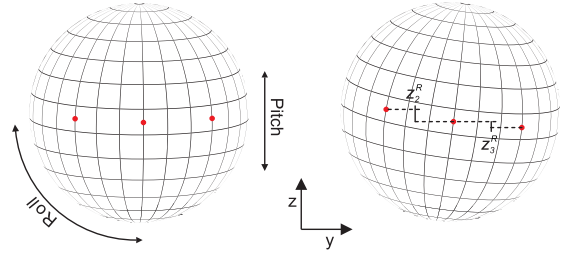


Fig. 2. Effect of roll and pitch distortions on the position of the pressure measurement points in the yz plane. z_2^R and z_3^R represent the z components of the two measurement points with an angular distortion.

with φ_1 and φ_2 describing the angles between stagnation point A and the additional measurement points C and C*. In our case, point C* is mirrored from C and thus $\varphi_1 = \varphi_2 = \varphi$. We can then further simplify (6) and calculate v_∞ as follows:

$$v_\infty = \sqrt[4]{\frac{2\alpha(\varphi)}{\rho^2} (\Delta p_1^2 + \Delta p_2^2)} \tag{7}$$

with

$$\alpha(\varphi) = \left(\frac{4}{9\sin^2(\varphi)}\right)^2. \tag{8}$$

Equation (7) agrees well with the relation found through computational fluid dynamics (CFD) analysis and laboratory experiments in [35], which provided satisfactory performance for deviations from the yaw axis of up to 45° with an accuracy of 0.009 m/s [36]. Additionally, the derivation in this paper provides an explanation, based on first principles, for the empirical coefficient $\alpha(\varphi)$ used in [35] and [36].

In real-world conditions, disturbances induced by the dynamic environment are not restricted to a single dimension. The motion of a vehicle may cause movements in roll and pitch directions, which invalidate the no-elevation assumption of the above derivation. To compensate for those effects, additional hydrostatic pressure components need to be introduced. Fig. 2 shows a simplified example of the expected effects.

A correction algorithm based on measurements of roll (ϕ) and pitch (θ) motions is applied. We define the initial Cartesian coordinates of the pressure measurement points relative to the center of the sphere with $r_i = [x_i \ y_i \ z_i]^T \ i \leq 3$ and calculate the new coordinates caused by roll and pitch disturbances r_i^R with

$$r_i^R = r_i * R(\phi, \theta) = [x_i^R \ y_i^R \ z_i^R]^T \tag{9}$$

where $R(\phi, \theta)$ is a direction cosine matrix based on roll and pitch measurements while yaw is neglected, which is given as follows:

$$R(\phi, \theta) = \begin{bmatrix} \cos(\theta) & 0 & -\sin(\theta) \\ \sin(\phi)\sin(\theta) & \cos(\phi) & \sin(\phi)\cos(\theta) \\ \cos(\phi)\sin(\theta) & -\sin(\phi) & \cos(\phi)\cos(\theta) \end{bmatrix}.$$

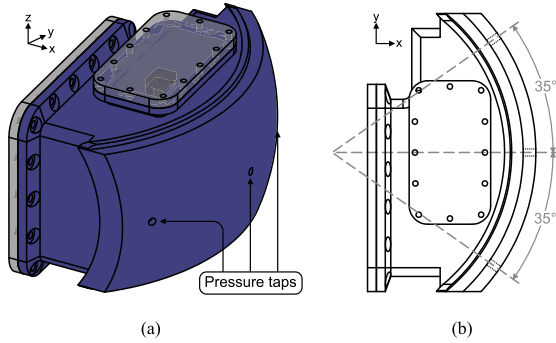


Fig. 3. DPSS housing shown in (a) isometric view and (b) top view. Both views indicate the location of the pressure taps at the stagnation point (0°) and the additional measurement points ($\pm 35^\circ$).

The additional hydrostatic components are then calculated based on the vertical distance between the stagnation and the two additional measurement points (see Fig. 2). The corrected pressure differences are as follows:

$$\begin{aligned}\Delta p_{hc_1} &= \Delta p_1 - (z_2^R - z_1^R) \rho g \\ \Delta p_{hc_2} &= \Delta p_2 - (z_3^R - z_1^R) \rho g\end{aligned}\quad (10)$$

with ρ representing the density of water and g defined as the gravitational constant. This results in a compensated equation (6) given as follows:

$$v_\infty = \sqrt[4]{\frac{2\alpha(\varphi)}{\rho^2} (\Delta p_{hc_1}^2 + \Delta p_{hc_2}^2)}. \quad (11)$$

Throughout the above derivation, an idealized flow field is assumed and, thus, the velocity estimation based on (11) will be sensitive to disturbances. Such disturbances can include near surface, near bottom, and near structure effects. In laboratory conditions, it was shown that the velocity estimation was insensitive toward wall effects at a distance of 0.25 m [35] and water surface at a distance of 0.5 m [36]. The experiments described in this paper were well within those limits. A more extensive characterization of those boundaries including objects with complex geometries and dynamic water surfaces in field conditions may be part of future research.

B. DPSS Design

The DPSS utilizes two differential pressure sensors to measure pressure across three points on its surface, and an IMU is used to detect angular disturbances. A microcontroller embedded in the DPSS uses the velocity model (11) to relate the pressure measurements of the differential pressure sensors with the surge velocity.

The pressure on the surface of the DPSS is measured using three flush holes normal to its surface, which we call pressure taps. Fig. 3 illustrates the location of the pressure taps on the surface of the DPSS at 0° (stagnation point) and $\pm 35^\circ$. The pressure differences are measured using two analog differential pressure

sensors (NXP Semiconductors MPXV7002). As already mentioned in Section I, differential pressure sensors are not sensitive to depth changes, contrary to absolute pressure sensors, which enables the DPSS to measure with a higher sensitivity. The analog signal is converted using a 16-b analog-to-digital converter (Linear Technology, Milpitas, CA, USA, LTC1867), and the temperature is monitored with a 13-b sensor (Analog Devices, Norwood, MA, USA, ADT7301). Furthermore, a six-degree-of-freedom IMU (InvenSense, San Jose, CA, USA, MPU-6050) provides input for the correction algorithm. An Arduino Micro is used as the processing unit for the sensor information. Finally, the information from the DPSS is transmitted to the AUV using a serial connection with a transmission rate of 100 Hz. All electronic components have a total power consumption of 243.5 mW and are integrated into a three-dimensional printed water-tight housing (see Fig. 3). Table I compares the DPSS with three small-scale DVLs regarding size, weight, and energy consumption. The DPSS is smaller and more energy efficient in comparison to all the three DVLs, whereas there is still potential to decrease the dimensions and weight of our sensor system. A one-to-one price comparison is difficult because the DVLs are fully developed products, whereas the DPSS is still in a prototype stage. However, based on a rough comparison, the price range for the DPSS should be around one order of magnitude lower.

In underwater applications, stiff membranes are used to ensure water tightness of pressure sensors, which limits the sensitivity for low-pressure ranges. However, due to the quadratic relation of pressure and velocity, high sensitivities and a small pressure range ($< \pm 2000$ Pa) are necessary to measure low velocities. To overcome those limitations, we selected an air pressure sensor able to operate in high humidity environments and included an internal tubing system within the housing of the DPSS, which always maintains a layer of air between the sensors and the environment (see Fig. 4). The geometry of the tubing enables to trap a single volume of air and is designed to prevent the formation of several air pockets, which would increase measurement noise. However, the volume of the trapped air is variable and is expected to depend on environmental conditions, such as angle of deployment of the sensor into the water, depth, and temperature. This variability affects the sensor readings and must be accounted for.

The DPSS prototype used during this study was specifically designed to be integrated with a SPARUS II AUV, which has an interchangeable head section [40]. Fig. 5 shows the computer-aided design (CAD) drawing of the prototype, with the DPSS as its main component, a supporting frame, and covers forming the payload area of SPARUS II. When assembled, the covers of SPARUS II and the exposed face of the DPSS form a hemisphere, which allows the use of (11).

C. DPSS Performance Characterization

DPSS performance for surge velocity estimation was characterized by experiments in a tow tank, which are described in [36]. As discussed before, the relation between pressure and velocity (3) is quadratic; therefore, similar pressure deviations

TABLE I
COMPARISON OF DPSS WITH THREE SMALL-SCALE DVLS REGARDING SIZE, WEIGHT, AND POWER CONSUMPTION

Sensor	Size	Weight (air/water)	Power consumption
	L x W x H [cm]	[kg]	[W]
Teledyne Pathfinder [12]	22 x 10.16 x 7.11	1.9 / 0.7	2.6
Nortek DVL1000 [13]	15.8 x Ø 11.4	1.3 / 0.15	1.3
NavQuest 600 Micro [14]	17.4 x Ø 12.6	2.9 / 1.2	2 - 5
DPSS	9 x 15.7 x 8.9	0.7 / 0.44	0.244

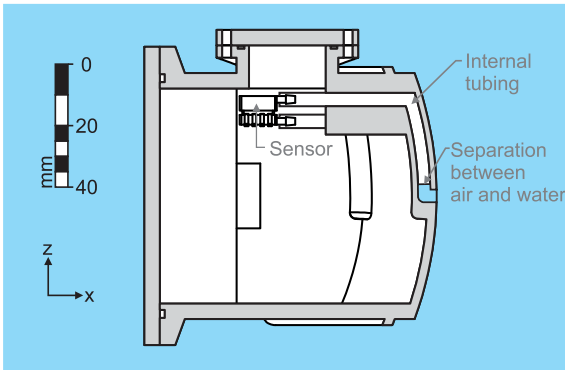


Fig. 4. Cross-sectional view of the DPSS showing the internal tubing and the air–water interface.

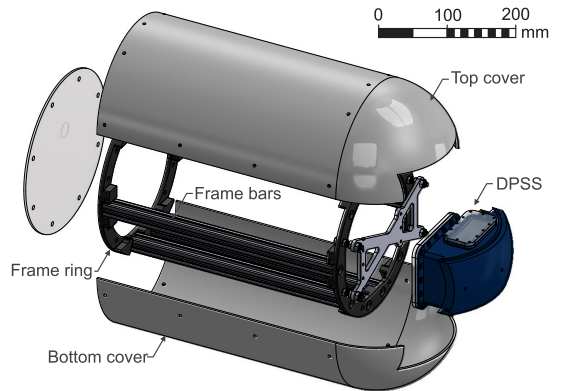


Fig. 5. Exploded view of the DPSS together with a frame and covers reproducing a payload section for a torpedo-shaped robot.

cause higher velocity variations for lower velocities. We thus expected higher errors of the DPSS for low velocities in a dynamic environment. In addition, the number of pressure samples considered in calculating velocity influenced the accuracy of the DPSS. It was shown in [36] that a stable optimum accuracy was obtained for sampling rates from 5 to 13 Hz.

To establish an error model for the DPSS, it would be possible to propagate the nominal error of the commercial pressure sensors through (11). However, the error estimates provided by the manufacturer are conservative, which makes it difficult to establish an accurate error model. Instead, we developed the error model based on empirical data and lumped possible errors together in a probabilistic error term “err” assuming a normal distribution where the mean μ represents the sensor accuracy

$$v_\infty = \sqrt[4]{\frac{2\alpha(\varphi)}{\rho^2} (\Delta p_{hc_1}^2 + \Delta p_{hc_2}^2) + \text{err}} \quad \text{err} \sim N(\mu, \sigma^2). \quad (12)$$

Fig. 6 shows the PDF of the velocity errors from the performance experiments described in [36]. The velocity error follows a Gaussian distribution $N(\mu, \sigma^2)$, resulting in an accuracy of the DPSS of $\mu = 0.012$ m/s and a standard deviation of $\sigma = 0.009$ m/s. However, the accuracy of the tow tank used in [36] was limited to 0.01 m/s. Therefore, we assumed a standard

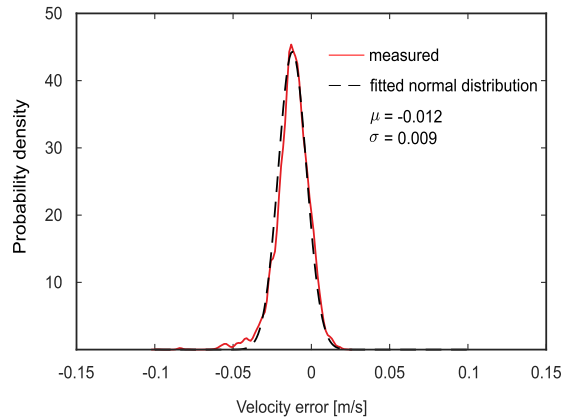
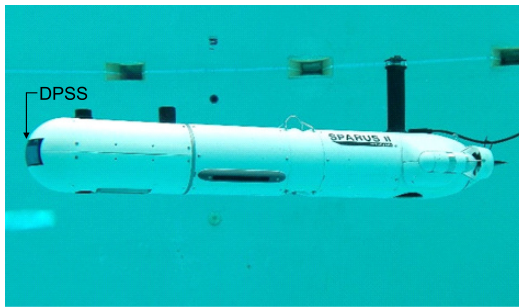


Fig. 6. Probability density function (PDF) of the DPSS velocity error obtained during tow tank experiments [36] (red) and fitted Gaussian distribution (dashed) with estimated mean μ and standard deviation σ .

deviation of $\sigma = 0.01$ m/s. Under field conditions, other possible pressure sources or flow field distortions may modify the described performance; for instance, the influence of waves or currents and attitude dynamics of the AUV.

**General specifications:**

Length: 1.6 m
Hull diameter: 0.23 m
Max. width: 0.46 m
Weight in air: 52 kg
Max. depth: 200 m
Li-Ion batteries: 1.4 kWh
Endurance: 8-10 h
Max. surge velocity: 1.5-2.0 m/s

Installed sensors:

IMU: Analog Devices ADIS
DVL: Teledyne RDI Explorer 600
GPS: OEM Fastrax IT 500
Pressures sensor: Keller

Fig. 7. SPARUS II AUV in an indoor pool at Underwater Robotics Research Centre (CIRS), University of Girona, Girona, Spain, with the integrated DPSS. General specifications (adapted from [40]) and sensor suite specifications used during the experiments can be seen on the right.

III. EXPERIMENTAL PLATFORM—SPARUS II

A. SPARUS II System Overview

SPARUS II is a lightweight surveillance AUV for long-term missions with a classical torpedo-shaped hull. The general specifications and the specific test configuration of the robot are presented in Fig. 7.

The vehicle has two horizontal thrusters, a vertical thruster, and fins at the stern that enable actuation in surge, heave, pitch, and yaw direction. The bow of the robot is a customizable payload area with a volume of 8 L supporting a maximum weight of 7 kg. The DPSS was integrated into the front part of the payload area. For this work, the covers of the payload area were changed to create a spherical head (see Figs. 5 and 7).

The software architecture of SPARUS II is based on the open source Robot Operating System (ROS) [41]. The basic sensor suite of SPARUS II used during the experiments consists of a pressure sensor, IMU, DVL, and a GPS (see Fig. 7). The information of all sensors was forwarded to an EKF for sensor fusion and state estimation [42]. The data provided by the sensors, including the DPSS and the EKF state estimation, were stored in separate datalog files.

The DVL (Teledyne RD Instruments, Inc., Poway, CA, USA, Explorer 600), integrated at the rear conical part of SPARUS II, was used in this study as the reference for velocity estimation. Using the frequency shift of backscattered acoustic signals, it estimates the velocity of SPARUS II in three degrees of freedom with an accuracy of 1.15% of distance traveled [37]. Velocity can be measured relative to a solid surface (BL) or particles in the water (WL). The navigation framework of SPARUS II favored velocity information from BL, if available, because it usually is more accurate. Subsequently, the BL mode was used to create the reference velocity estimation for the WL and the DPSS.

IV. EXPERIMENTAL CONFIGURATION

Field trials were conducted in the harbor area of Sant Feliu de Guíxols, Catalonia, Spain (see Fig. 8). SPARUS II was in autonomous mode throughout each trial. However, for safety reasons and monitoring and recording real-time telemetry data, the vehicle was connected to a wireless access point buoy.

A. Test Conditions and Trajectories

The DPSS was tested in three different sets of conditions, which we will define as test settings A, B, and C. As can be seen in Fig. 8, the tests in setting A and B were conducted in the same area protected by harbor walls, whereas the tests in setting C were conducted in open water with larger environmental disturbances. Based upon observable conditions at the time of testing, setting A was assumed to represent the most stable environment, with settings B and C representing higher and highest waves, respectively (see Table II). The potential effect of surface waves on the recorded pressure data [43] was further decreased for setting A by using a target depth of 4 m, as opposed to the target depth of 3 m for settings B and C. Table II summarizes the experimental conditions of the three test settings.

For each of these settings, three types of trajectories were executed: linear, lawn mower, and loop (see Fig. 9). We will refer to a single successful trial of a trajectory as a “run.” Every run was conducted twice for each velocity in each setting, and we subsequently divided such a pair of runs in repetition 1 and repetition 2. Due to the dynamics of the testing environment, a one-to-one comparison between those repetitions was not feasible. However, it is possible to infer some information about reproducibility by comparing the distributions of the whole data set of the repetition 1 runs versus the repetition 2 runs.

The linear trajectory [see Fig. 9(a)] was designed to verify the laboratory calibration in [36] for field conditions. The vehicle initially dived to target depth and then performed the first of two linear “tracks.” At a predefined length, the vehicle surfaced, performed a maneuver to reorient back toward the initial starting direction, dived, and performed the second of the linear tracks. Only the parts of the trajectory that were at the target depth were used in the data set. On each linear track, SPARUS II was moving with a different target velocity. In total, four pairs of different target velocities were tested (see Table III). Due to an error in setting the target depth, the second repetitions for the target velocity pairs of 0.4–0.5 m/s and 0.75–1.0 m/s in setting B were conducted at a target depth of 4 m.

The lawn mower [see Fig. 9(b)] and loop [see Fig. 9(c)] trajectories were used to assess the robustness of the DPSS during turns and check its performance for standard trajectories commonly used in underwater robotics. For those trajectories, we



Fig. 8. Location of the test site for field trials: harbor area of Sant Feliu de Guíxols (Catalonia, Spain). WGS84 (km)—41.7775° N, 3.0325° E.

TABLE II
TEST SETTINGS FOR FIELD TRIALS INCLUDING WEATHER CONDITIONS, DEPTH, AND TEST SITE

Setting	Date	Local time [hh:mm]	Wave height [m]	Temperature [°C]	Depth (m)	Test site
A	03.05.17	10:18 - 12:28	0.7	16	4	Harbor
B	25.04.17	10:39 - 12:57	0.82 - 0.94	16.3	3	Harbor
C	25.04.17	13:22 - 15:10	0.94	16.2 - 16.3	3	Open water

Note: Wave heights for settings A and B were expected to be lower than stated, due to the shielding effect of the harbor walls (temperature and wave heights according to environmental monitoring of the Spanish Government—<http://www.puertos.es/es-es/oceanografia/Paginas/portus.aspx>).

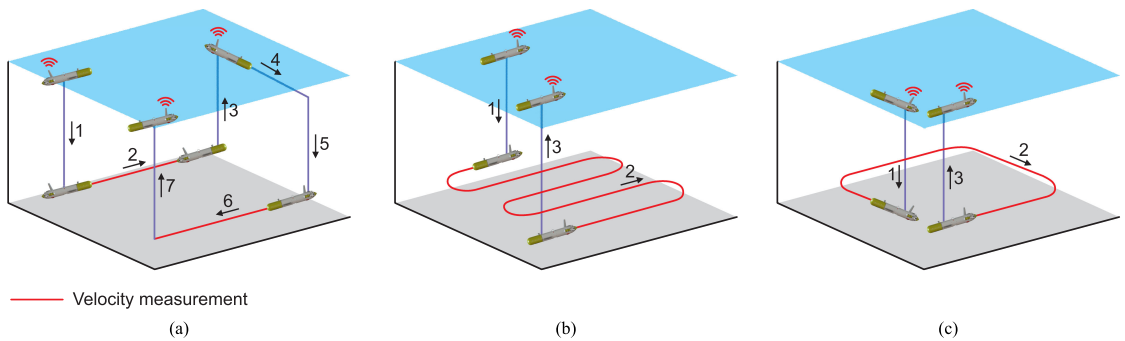


Fig. 9. Trajectories used during field trials (the segments at which the velocities were measured are colored in red). (a) Linear—After receiving a stable GPS signal at the starting point, the robot dived to its target depth (1) and started moving forward along the first linear track with the first target velocity (2). Once the first endpoint was reached, the robot stopped and surfaced (3). After the robot received a stable GPS signal and the dead reckoning position estimation was corrected, the AUV moved to the second starting point (4) and dived to target depth (5). Once target depth was reached the robot moved forward on the second linear track with the second target velocity (6), the robot stopped upon reaching the second endpoint and surfaced (7). The run was completed once the robot got a stable GPS signal at the final endpoint. (b) Lawn mower and (c) loop—After receiving a stable GPS signal at the starting point, the robot dived to its target depth (1) and started to follow a lawn mower or loop trajectory and maintained a constant velocity (2). When the endpoint was reached, the robot surfaced and got the final GPS signal (3).

TABLE III
PAIRS OF TARGET VELOCITIES FOR THE LINEAR TRAJECTORY AND THEIR TARGET DEPTH DEPENDING ON REPETITION (“REP”) AND SETTING

Linear trajectory	First target velocity [m/s]	Second target velocity [m/s]	Target depth (rep1/ rep2) [m]		
			Setting A	Setting B	Setting C
1	0.2	0.3	4/4	3/3	3/3
2	0.4	0.5	4/4	3/4	3/3
3	0.75	1.0	4/4	3/4	3/3
4	1.5	2.0	4/4	3/3	3/3

Note: Two deviations in target depth for setting B are marked in bold font.

chose two target velocities, 0.5 m/s and 1.0 m/s, which are on the lower bound of the operational speeds for torpedo-shaped AUVs [44]. These velocities were chosen to test the lower limits of the DPSS since the quality of the velocity estimation was expected to increase with velocity. After getting a stable GPS signal at its starting position, SPARUS II executed a vertical dive to the target depth and then performed either a lawn mower or loop trajectory with constant velocity. After SPARUS II reached the final location, it surfaced and waited for a stable GPS signal. A complete description of the test parameters for all trajectories can be found in Appendix A.

B. Data Analysis

The current design of the DPSS estimates velocity in surge direction up to a minimum depth of 0.5 m in the absence of significant deviations in depth. Additionally, waves had distorting effects on the velocity estimation close to the surface. We thus restricted the performance comparison of DVL and DPSS to velocity estimation in surge direction at target depth (red segments in Fig. 9). For the work described in this paper, the surge velocity estimation was sufficient, because the sway velocity was close to 0 m/s for all tests (see Appendix B).

During the trials, the raw data from all sensors, in addition to the state estimates produced by the EKF, were recorded automatically within the ROS framework. The raw pressure measurements of the differential pressure sensors were sampled at a rate of 100 Hz and averaged over 20 samples to achieve optimum accuracy. Thus, the DPSS provided velocity estimations with an effective sampling rate of 5 Hz, which was comparable to the sampling rate of the DVL (6 Hz).

An important factor regarding the DPSS velocity calculation is the volume of air inside the internal tubes of the housing. This volume was expected to depend on the angle at which the sensor is deployed in the water, the depth of the sensor, and the temperature of the surrounding environment. Therefore, for each deployment, different reference offsets Θ_1 and Θ_2 were created for each pressure differential (Δp_{hc}). Thus, (11) must be corrected for those offsets and becomes

$$v_{\infty} = \sqrt[4]{\frac{2\alpha(\varphi)}{\rho^2} \left((\Delta p_{hc1} - \Theta_1)^2 + (\Delta p_{hc2} - \Theta_2)^2 \right)} + \text{err} \quad \text{err} \sim N(\mu, \sigma^2). \quad (13)$$

TABLE IV
OFFSETS USED TO COMPENSATE THE VOLUME CHANGE OF AIR IN THE DPSS TUBING FOR DIFFERENT DEPLOYMENTS

Date	Depth [m]	Θ_1 [Pa]	Θ_2 [Pa]
25.04.17	3	8.2195	-12.7527
25.04.17	4	75.3163	46.1951
03.05.17	4	60.0390	23.6200

A single pair of offsets was computed offline for each day of deployment. As the air in the tubing is compressible, the offsets are depth dependent and an additional pair of offsets had to be computed for the two trials in test setting B, which were conducted at a target depth of 4 m. The offsets were calculated by three independent regression fits taking the respective DVL BL velocities at target depth as a reference and are shown in Table IV.

As it is very difficult to establish a reliable ground truth for velocity estimation under field conditions, we restricted the analysis of the DPSS velocity estimation to a comparison between DPSS and DVL. It is important to note that DVL in BL and DPSS do not measure the same type of velocity. The DVL measures the velocity of the vehicle relative to the ground, whereas the DPSS measures the vehicle’s velocity with respect to the fluid stream. Thus, waves, currents, and other related disturbances were expected to have a stronger effect on the DPSS velocity estimation. The DVL velocity estimation in WL provided a comparison with a similar sensing principle. Therefore, both the DPSS velocity estimation and the DVL estimation in WL in reference to the DVL BL are presented. For the following comparisons, it is further important to consider that all tests were conducted in conditions where environmental disturbances could not be neglected. Those disturbances introduced attitude dynamics to the AUV that affected both velocity sensors. In the case of the DPSS, the hydrostatic correction algorithm (9) was used to partially compensate for those dynamics. For the velocity estimation of the DVL, a compensation of attitude dynamics as suggested by Liu *et al.* [45] was not considered. We thus did expect a decrease in accuracy for both sensors compared to their nominal values of 0.3% of measured velocity and 0.012 m/s.

The general performances of velocity estimations were compared using the correlation between the DPSS and DVL data.

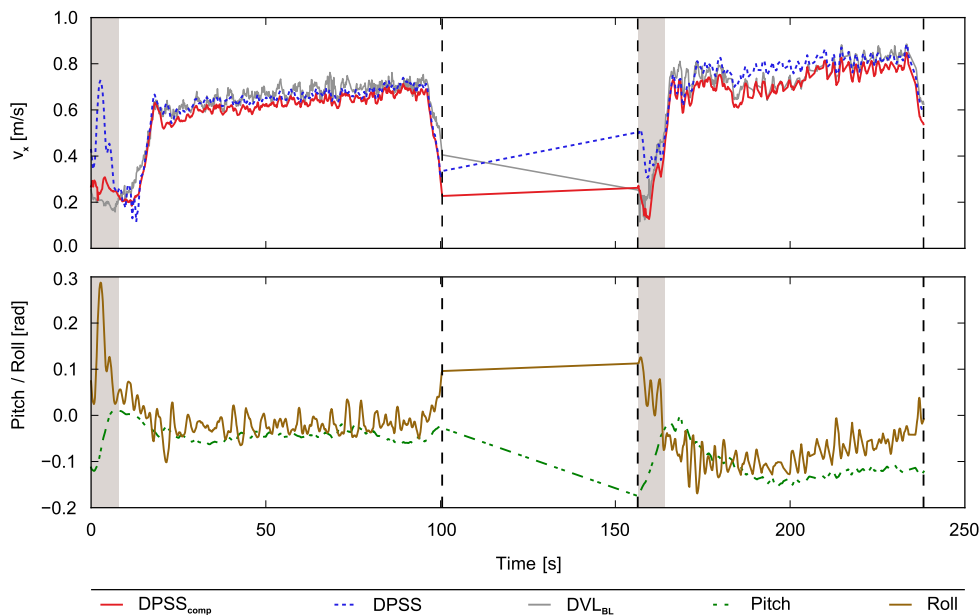


Fig. 10. DPSS velocity estimation with (red) and without (blue) hydrostatic compensation. Further shown are pitch and roll estimates of the AUV (lower part). The DVL BL velocity estimation is given in gray for comparison. The dashed lines mark the beginning and end of the movement of SPARUS II at target depth. The movements of the vehicle toward/on the surface are irrelevant for the analysis and are not shown. The light shaded regions highlight intervals where the hydrostatic compensation had a high impact.

Assuming the velocity estimations of DPSS and DVL to be equal, we defined a fit of $v_{DVL_x} = v_{DPSS_x}$ and evaluated it with the coefficient of determination R^2 . Furthermore, the RMSE between DPSS and DVL was used to compare both velocity estimations. In the context of this paper, and due to the environmental disturbances, the RMSE should be considered as a difference between the two devices rather than an absolute error from a device to a ground truth. To reduce the effect of those influences, the RMSEs are computed based on the filtered velocity estimations produced by the EKF of SPARUS II [42]. The dynamic environment affecting DVL and DPSS, the early development stage of a “field-ready” DPSS, opposed to the well-established DVL, and the DPSS’s intended application as a supplement to existing technologies or as a solution in situations where the use of other velocity sensors is not feasible, will be considered during the performance evaluation.

To assess the repeatability of the experiments, we divided the RMSEs of DPSS and DVL velocity estimates for all trials into two groups based on repetitions. We used the Student’s t -test to check the null hypothesis stating that there is no significant difference of RMSEs between the two groups, based on a cutoff value for statistical significance of 0.05. A direct comparison of the DPSS time series of two runs with identical parameters was not feasible due to the highly dynamic environment. However, since DPSS and DVL were affected by the same environmental disturbances, the RMSEs between their velocity estimations were expected to be comparable. The RMSEs between DPSS and DVL were further used in the linear trajectory trials to

validate the laboratory calibration of [36] for field conditions and to check the performance of the DPSS across a wide range of velocities (from 0.2 to 2 m/s). It is important to note that those velocities represented the target velocities which were, if at all, only reached at the end of a run. The deviations from the desired velocities were caused by the limited space for the linear trajectory trials and by inherent mechanisms of the controller provided by the AUV. The RMSEs in the results section are therefore presented in relation to the velocity range the AUV achieved during each test.

The RMSEs were further computed for the lawn mower and loop trajectories to assess the velocity estimation for common AUV trajectories with a special focus on turns.

V. RESULTS AND DISCUSSION

A. General Performance of DPSS Velocity Estimation

The effect of the hydrostatic correction algorithm [see Fig. 2 and (10)] in relation to the pitch and roll of the robot is shown in Fig. 10. The shaded regions indicate intervals where the correction had the highest impact on the velocity estimation.

The hydrostatic compensation effectively reduced the peaks, caused by pitch and roll deviations due to a simultaneous heave and surge motion, at the start of the trials. This could be especially beneficial for the accuracy of DPSS-aided position estimation. Fig. 10 also illustrates the presence of permanent pitch and roll deviations during some of the trials, which could have been

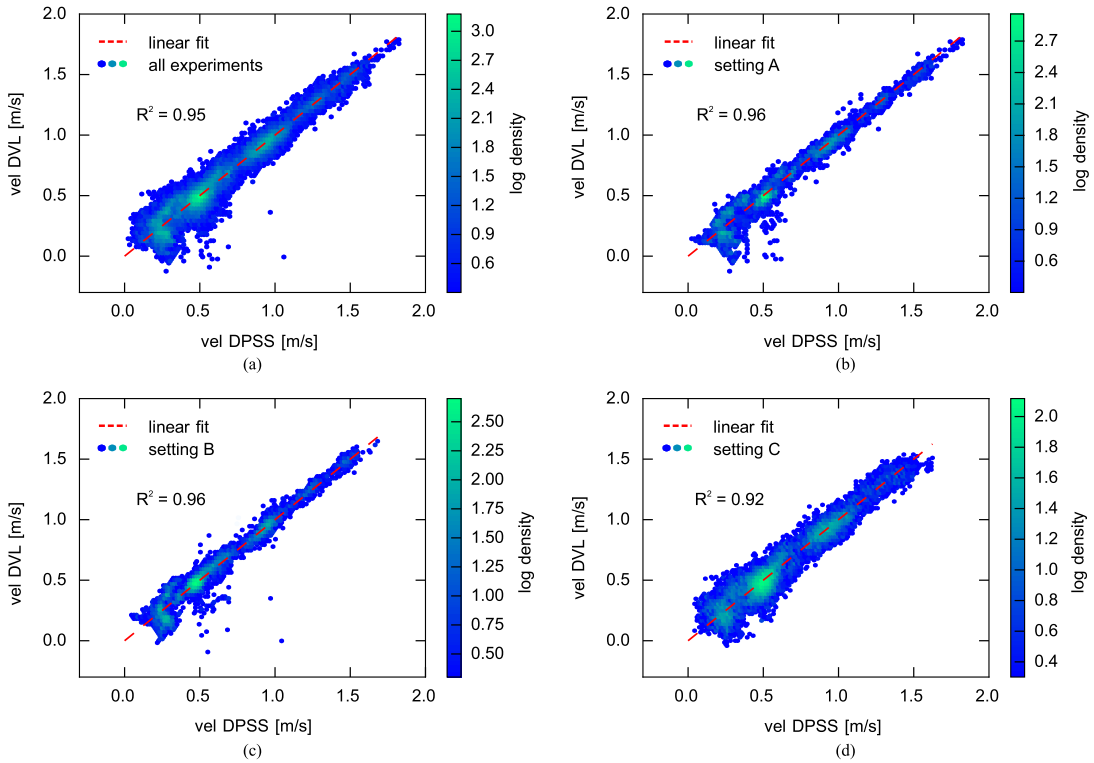


Fig. 11. Logarithmic density plot showing the correlation of surge velocity estimates of the DVL in BL and DPSS. (a) Correlation plot for all experiments. (b)–(d) Correlation plots for settings A–C. For all plots, R^2 value, based on an assumed fit of $v_{DVL} = v_{DPSS}$ (red dotted line), is provided to assess the quality of the correlation.

caused by the surface buoy attached to SPARUS II or small inaccuracies of the robot's trim. The compensation of these permanent deviations caused the DPSS estimates to differ more from the DVL reference for the first linear track, but for the second linear track, the difference between the estimates decreased. As the DVL was also susceptible to roll and pitch disturbances [45], a definitive conclusion regarding the performance of the correction algorithm, beyond the peak reduction, cannot be drawn. This highlights the need for further investigation on the effects of roll and pitch deviations on the DPSS velocity estimation to improve the correction algorithm and expand it beyond hydrostatic effects.

Fig. 11 shows a logarithmic density plot of the correlation between velocity estimations of DPSS and DVL with associated R^2 values. While Fig. 11(a) shows the correlation for all runs, Fig. 11(b)–(d) visualizes the individual velocity correlations for the three test settings.

R^2 value of 0.95 for the data set of all runs shows a high correlation between velocity estimations of DVL and DPSS. Therefore, it is possible to assume that the DPSS had comparable average performance. The variation in correlation is dependent on the target velocity, which can be seen in the higher variability of the correlation for smaller target velocities in all plots. This

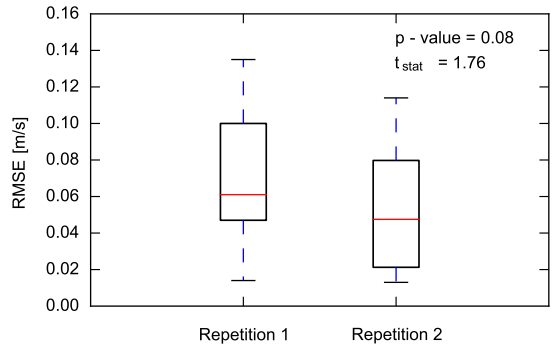


Fig. 12. Distribution of RMSEs between velocity estimations of the DPSS and the DVL in BL for all experiments grouped by repetitions. Further shown are the p -value and t -statistic for the Student's t -test assuming the null hypothesis that no significant difference exists between the two groups.

was expected due to the quadratic relationship between pressure and velocity. Pressure sensors need to have high sensitivities to accurately measure at low velocities. At the same time, the sensitivity to environmental disturbances is concurrently increased,

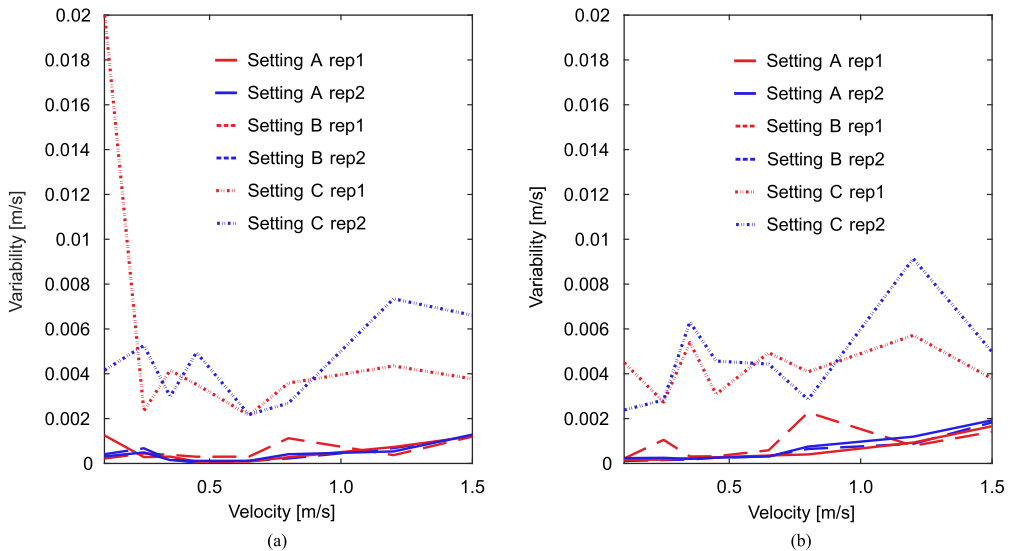


Fig. 13. Variability plot of velocity estimations in three different environmental settings for (a) DPSS and (b) DVL in BL.

causing a higher variability in the estimations of the DPSS for low velocities.

Fig. 11 further shows the general effect of the environmental conditions for different settings. The density distributions for settings A and B [see Fig. 11(b) and (c)] are equally narrow, whereas the distribution for setting C [see Fig. 11(d)] is wider. This is also reflected in R^2 values, which is 0.96 for settings A and B and 0.92 for setting C. First, this suggests that the environmental influences between settings A and B (difference in depth of 1 m and smaller surface waves) were negligible regarding the correlation between velocity estimations. Second, it shows that there were stronger environmental influences in the open sea. In setting C, both sensors have a higher variance in their velocity estimation, possibly due to stronger sea currents and wave actions affecting the movement of the robot. However, R^2 value remains above 0.9, showing that the DPSS mean velocity estimation is robust enough to be used in dynamic field conditions.

Fig. 12 shows the mean and distribution of RMSEs grouped by repetitions. The test statistic and p -value of the Student's t -test are shown as well. The p -value of 0.08 supports the null hypothesis that no significant difference exists between the RMSEs for both repetition groups. This indicates that a certain repeatability of the results exists for comparable test conditions.

B. Linear Trajectories

The dynamic nature of the testing environment required an analysis of the variability of the velocity estimations of DVL and DPSS to provide a better basis for the comparison of both sensors and the evaluation of the DPSS's performance. Fig. 13 shows the variability of both velocity sensors for the range of tested velocities and indicates that the variability was similar for

both sensors. It is also clearly shown that the increased environmental dynamics in setting C caused a higher variability in the velocity estimation of both sensors. The observed variability indicated, while being only a rough estimate of the true variance, that the dynamic environment decreased the ideal accuracies of both DVL [37] and DPSS [36]. This was considered during the performance evaluation of the DPSS velocity estimation.

Fig. 14(a) visualizes the RMSEs between DPSS and DVL BL velocity estimations for the linear trajectories grouped by setting and repetition. The RMSEs are generally higher for low velocities and decrease with increasing velocity in all settings.

For velocities greater than 1 m/s, a reasonable operation range for torpedo-shaped AUVs, the RMSEs for settings A and B lie below 0.04 m/s and decrease toward 0.02 m/s for higher velocities, approaching the nominal DPSS accuracy of 0.012 m/s. The RMSEs for setting C lie below 0.06 m/s for velocities greater than 0.8 m/s. Given the dynamic environment, the early development stage of the DPSS and envisioned applications for vehicles are unable to equip other velocity aiding technologies; those results do encourage further development of the technology. The difference between repetitions was generally low, but a significant deviation can be observed for velocities between 0.6 and 1 m/s in setting A. A possible explanation for those differences could be the calculation of the offsets. Only one pair of offsets for each day of deployment was calculated. Therefore, changes in the air volume inside the DPSS's connection tubes due to repeated surfacing and submerging between runs could not be fully corrected. This hypothesis is supported by the big difference of the RMSEs for both replicates of setting B at velocities between 0.3 and 0.6 m/s. As explained in Section IV-B, a new pair of offsets was calculated for the second replicate. Those

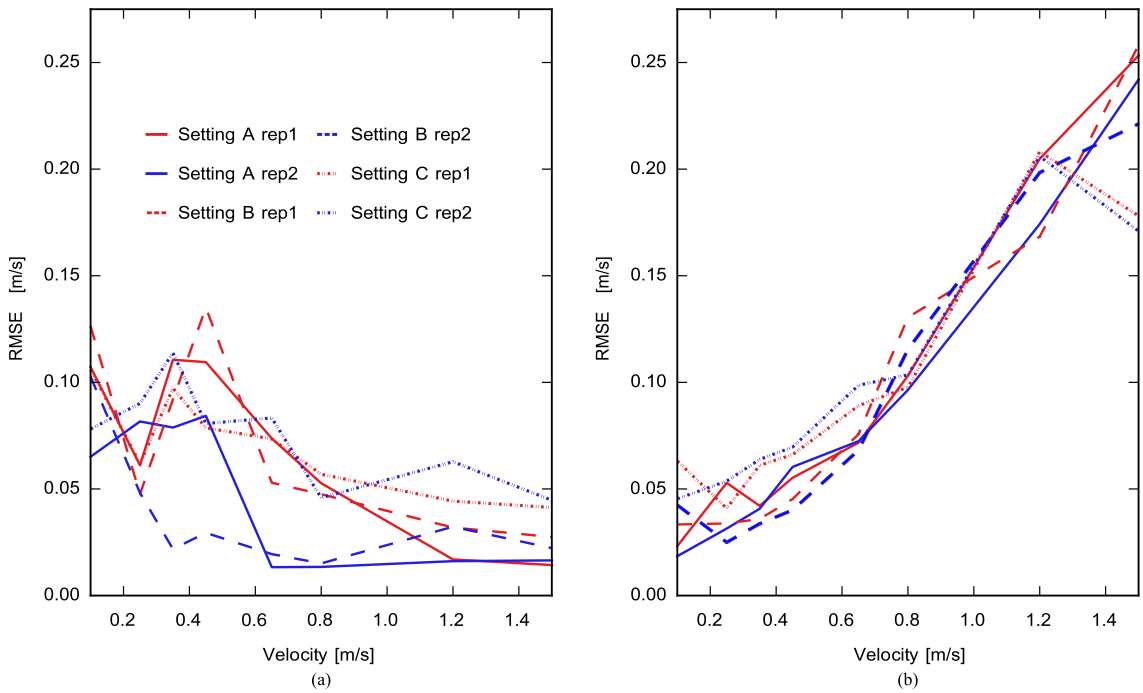


Fig. 14. RMSEs of velocity estimations for (a) DPSS versus DVL in BL and (b) DVL in BL versus DVL in WL at different target velocities. Repetitions are distinguished by color and settings are distinguished by line type.

new offsets corrected for most of the mentioned variability significantly improved the velocity estimation. This supports the suggestion in [36] that computing new offsets by an autocalibration process before the start of each run could enhance the DPSS velocity estimation, especially for low velocities. Such an autocalibration could be achieved by commanding the vehicle to wait at its starting position at target depth and letting the DPSS sample for a specified amount of time at zero velocity. Aside from the expected improvement in accuracy, the autocalibration procedure would make the offset calculation fully independent from any external sensors. Future tests utilizing this autocalibration procedure are necessary to fully verify the positive effect on the accuracy of the velocity estimation. However, such a procedure necessitates a vehicle capable of hovering, which limits the applicability of the calibration. In the future, we will try to establish a model relating external factors, such as depth and temperature, to the offset based on first principles and experimental data. With such a model, the autocalibration would be only necessary at the start of a new deployment on the surface.

Furthermore, Fig. 14(a) illustrates that the differences in velocity estimation decreased with increasing target velocity. This indicates that environmental disturbances, such as turbulence and currents, had a larger effect on the pressure signals for lower velocities, which can be explained by the quadratic relationship between pressure and velocity (12). Ocean current disturbances,

for instance, could be compensated by using an ocean current observer or a complementary velocity sensor with different error characteristics [46], [47]. Fig. 14(b) shows the RMSEs between the DVL velocity estimates in BL and WL. The error increases with increasing velocity from below 0.05 to around 0.25 m/s. There is no clear distinction between settings. Compared to the DPSS, the DVL WL estimation seems to show better performance for low velocities up to 0.6 m/s. However, for velocities greater than 0.6 m/s, the WL error steadily increases, whereas the DPSS error decreases, resulting in a significant difference for the highest velocities. This shows the potential advantage of DPSS velocity estimation in situations where the DVL cannot utilize the BL mode.

C. Lawn Mower and Loop Trajectories

The comparison between DVL in BL and DPSS for the lawn mower and loop trajectories across all settings (see Fig. 15) shows satisfying results as the RMSEs are well below or equal to their counterparts in the linear experiments. The RMSEs are similar for settings A and B, mostly in a range between 0.03 and 0.02 m/s, whereas the RMSEs for setting C are between 0.058 and 0.04 m/s. The improvement compared to the linear experiments could be caused by a longer period of constant velocity. The error between DVL in BL and WL shown in the same figure

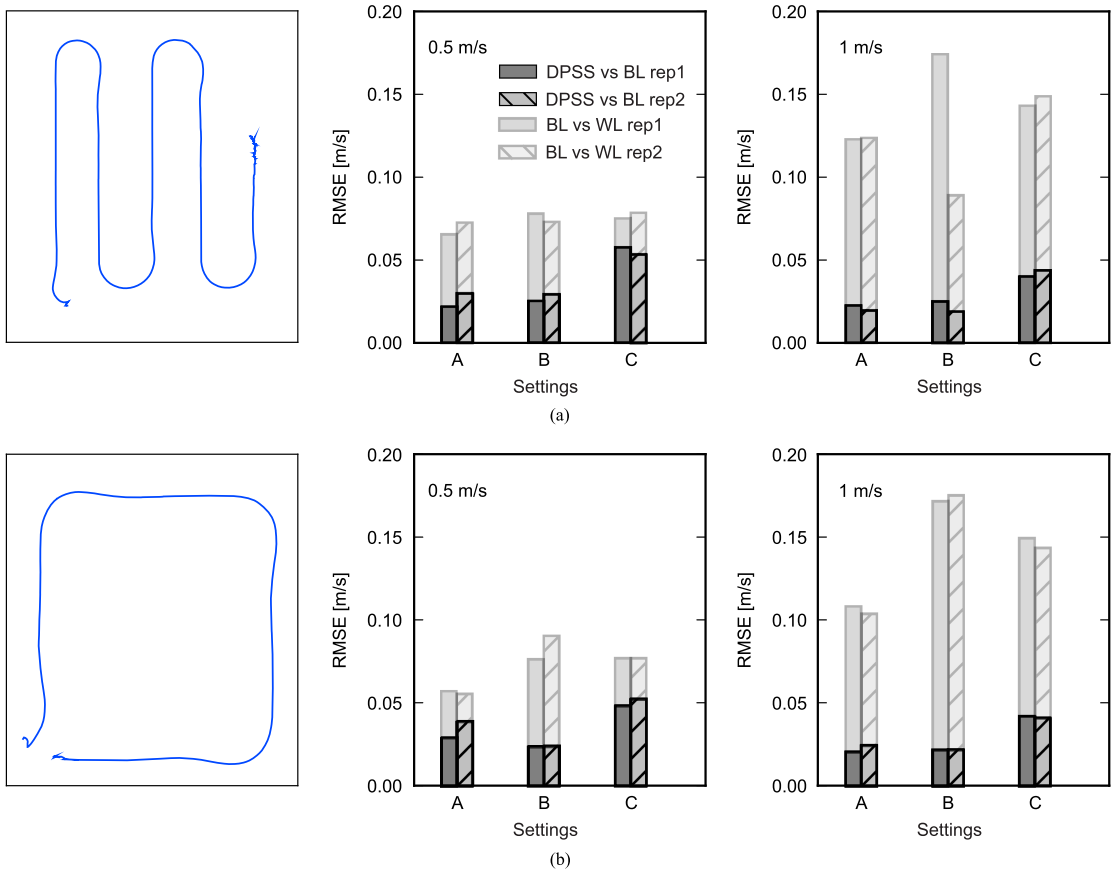


Fig. 15. RMSEs for velocity estimations of DPSS versus DVL in BL and BL versus DVL in WL for (a) lawn mower and (b) loop trajectories at target velocities of 0.5 and 1.0 m/s in settings A, B, and C.

exceeds the error for the DPSS in all cases. The difference is especially apparent for the target velocity of 1 m/s, which indicates that the DPSS velocity estimation in the tested conditions seems to be superior to the DVL in WL. Furthermore, the results show that the quality of DPSS velocity estimation does not degrade for longer distances. However, experiments on bigger scales will be necessary to characterize the long-term performance of the DPSS. The results further indicate that the DPSS is capable of reliable surge velocity estimation for common mission trajectories of AUVs at the lower end of typical target velocities. The estimation for the higher target velocity of 1 m/s seems to be generally better. This suggests, together with the results of the linear trajectory experiments, that a further increase in accuracy and robustness can be expected for typical cruising speeds of AUVs around 2 m/s.

A second incentive for the lawn mower and loop trajectory experiments was to test the robustness of the velocity estimation during turns. Fig. 16 shows one example for each tested trajectory and indicates the regions of turning. The DPSS velocity

estimations closely follow the DVL estimations in both cases and no significant deviations during the turning events could be observed.

Furthermore, peaks toward a lower velocity in the DVL velocity estimation during the second turn and after the third turn in Fig. 16(a) highlight a general limitation of the DVL velocity estimation in BL. To produce reliable velocity estimates, the DVL requires a smooth reference surface. Fig. 17 illustrates this by showing that the readings of the DVL are severely corrupted when SPARUS II is moving close to the harbor wall (at approximately 90 s) where the bottom gets rougher. The DPSS does not have such problems and exhibits a superior accuracy compared to the velocity measurements of the DVL in WL. The DPSS could, therefore, be used as a complementary sensor for AUVs equipped with a DVL, which need to move through highly unstructured or featureless areas. A combination of DVL and DPSS could be further used to increase the robustness of autonomous navigation against ocean currents. As navigation based on DVL or DPSS input relies on dead reckoning,

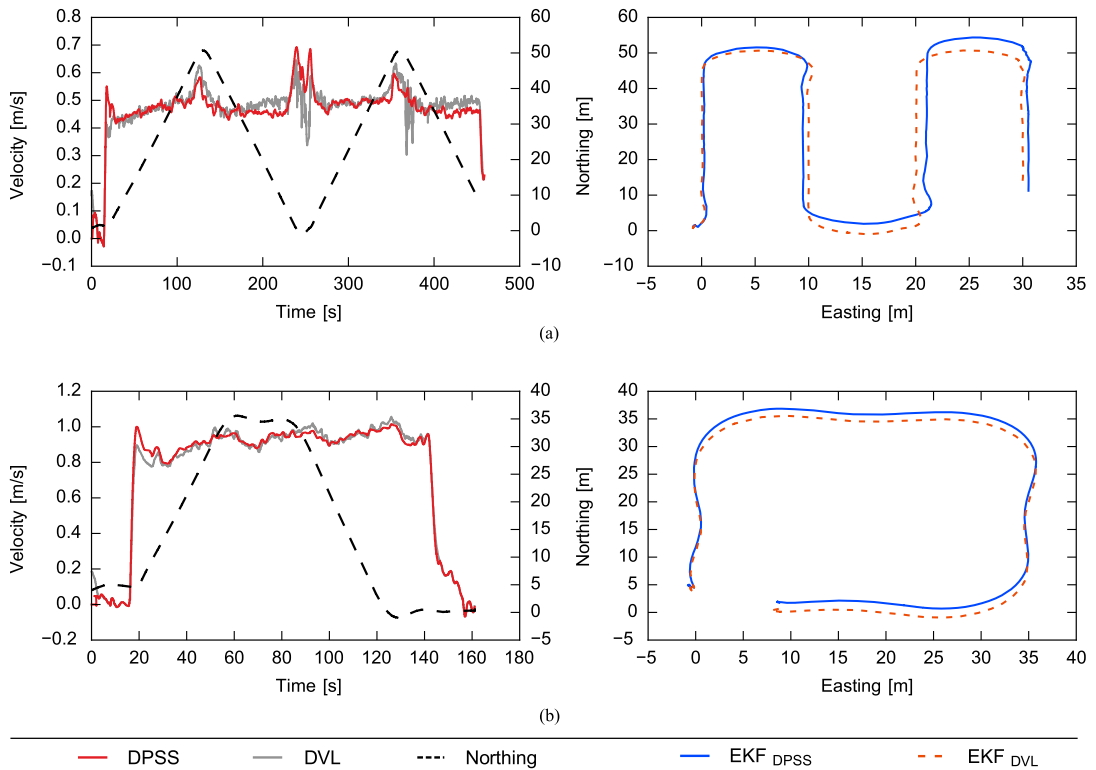


Fig. 16. Two examples of EKF velocity estimates (left) and EKF position estimates (right) based on BL DVL and DPSS data, respectively, for (a) lawn mower trajectory and (b) loop trajectory. The black dashed line indicating the northing position of the AUV illustrates the turning points of the curved trajectories.

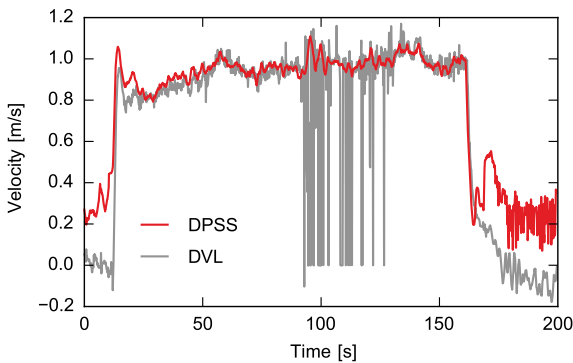


Fig. 17. Example of the raw velocity readings for DPSS and DVL in BL for a lawn mower trajectory. The robot got close to the harbor wall and thus moved over an unstructured and nonsmooth ground at around 90 s.

estimation errors are unbounded in both cases. Low-cost and small-package navigation solutions with bounded error estimates are the subject of recent work [48], [49]. A combination

of the DPSS with such solutions could lead to an accurate self-sustainable navigation suite completely independent from large and costly sensors.

VI. SUMMARY AND CONCLUSION

In this paper, we present the DPSS for underwater vehicle velocity estimation as an extension of previous work [36] by combining velocity estimation based on differential pressure with IMU-based orientation corrections. We integrated the DPSS into the SPARUS II AUV and conducted the first field tests of a sensor using differential pressure for velocity estimation on an autonomous underwater robot. The field tests validated the surge velocity estimation of the DPSS against the state-of-the-art technology (DVL). For a range of target velocities between 0.2 and 2 m/s, SPARUS II followed three different trajectories in three different test settings, and the surge velocity estimations of the DPSS and a DVL in BL and WL were compared. The quality of the DPSS velocity estimations increased with increasing velocity and subsequently decreasing impact of environmental influences the pressure readings, whereas the quality of the DVL WL estimation decreased with increasing velocity. The difference

between DPSS and DVL in BL was further dependent on the strength of the environmental dynamics. For linear trajectories at higher velocities (>1 m/s), the differences between the velocity estimates did not exceed 0.032 m/s in less dynamic environments and 0.063 m/s in highly dynamic environments. Results for lawn mower and loop trajectories were even more encouraging. Here, the differences for the target velocity of 0.5 m/s did not exceed 0.039 m/s in less dynamic environments and 0.058 m/s in highly dynamic environments. This contrasts the results of the linear trajectory experiments and indicates the potential of the DPSS to reliably estimate lower velocities down to 0.5 m/s as well. Furthermore, the difference between DVLs in BL and WL always exceeded the differences between DVLs in BL and DPSS, indicating that the DPSS surge velocity estimation was superior for the DVL WL measurements for the given test conditions. Deviations within the linear trajectory experiments and the differences to the lawn mower and loop trajectories highlight the need for an improved offset calculation. Identification and quantitative analysis of the influencing factors on the offset will be a future research topic. This research could lead to an auto-calibration procedure for the DPSS, utilizing measurements at zero velocity and a model relating the volume of air inside the tubing to external conditions, such as pressure and temperature. Such a procedure combined with further disturbance correction methods, such as a hydrodynamic correction of the pressure readings, will be implemented and tested in the future work to increase the accuracy of the DPSS, especially for lower velocities. A comparison of the DPSS performance with a propeller turns to speed model will be another possible focus of the future research.

Aside from the validation of the DPSS in field conditions, several additional lessons have been learned during the field tests.

- 1) Both DPSS and DVL were similarly affected by environmental disturbances, illustrated by the differences of test settings A and B compared to setting C. This highlights the need for a reliable test setup with a suitable ground truth for velocity estimation in field conditions.
- 2) The DPSS showed a robust performance even in the open sea setting with higher environmental disturbances. However, for low velocities, the impact of disturbances was higher for the DPSS compared to that of the DVL. Future investigations in those low velocity regions are necessary.
- 3) The hydrostatic correction algorithm successfully contributed to a more accurate velocity estimation of the DPSS, especially at the beginning of trials. However, further investigations regarding the hydrodynamic effects of roll and pitch distortions are necessary.
- 4) The results with the two trials conducted at a different target depth suggest that an auto-calibration procedure to compute individual offsets before each trial would significantly enhance the velocity estimation of the DPSS.
- 5) The DPSS has an improved performance over the DVL in BL in terrains with rough or unstructured surfaces.

TABLE V
PARAMETER SETUP FOR LINEAR TRACK EXPERIMENTS

Run	Velocities (m/s)		Distance (m)	Depth (m)	
				Setting B & C	Setting A
1	0.2	0.3	22		
2	0.4	0.5	35		
3	0.75	1	60	3*	4
4	1.5	2	70**		

Note: *Depth in setting A second repetition for 0.4 and 0.5 m/s and 0.75 and 1 m/s was 4 m instead of 3 m.

**Distance in setting A second repetition for 1.5 and 2 m/s was 60 m instead of 70 m.

TABLE VI
PARAMETER SETUP FOR LAWN MOWER EXPERIMENTS

Setting	Run	Velocities (m/s)	Distance traveled (m)		Depth (m)
			First repetition	Second repetition	
A	1	0.5	230		4
	2	1.0	70		
B	1	0.5	290	270	3
	2	1.0	180	170	
C	1	0.5	350	230	3
	2	1.0	260		

TABLE VII
PARAMETER SETUP FOR LOOP EXPERIMENTS

Setting	Run	Velocities (m/s)	Distance traveled (m)		Depth (m)
			First repetition	Second repetition	
A	1	0.5	115	135	4
	2	1.0	150	125	
B	1	0.5	120	112	3
	2	1.0	110	114	
C	1	0.5	200		3
	2	1.0	195		

Considering all this, we conclude that the successful field tests of the DPSS prototype mark an important step in developing a useful sensor for a variety of underwater vehicles. Due to its low energy requirements, a power consumption of 243.5 mW, the DPSS could be used for vehicles on long-term deployments, such as underwater gliders or long-range AUVs. Further, low-cost and/or small AUVs, which do not have the budget or space to carry sophisticated sensor systems, could also benefit from a small and inexpensive velocity sensor to improve the accuracy of their navigation. The DPSS has further potential as a viable complement for DVL-aided navigation systems by increasing redundancy and enabling more precise navigation during mid-water column travels or missions with highly unstructured environments. In addition to the suggested topics in the learned lessons, the velocity estimation for sway and heave and the influence of both on the surge velocity estimation is a topic for the future research.

APPENDIX A
EXPERIMENTAL SETUP

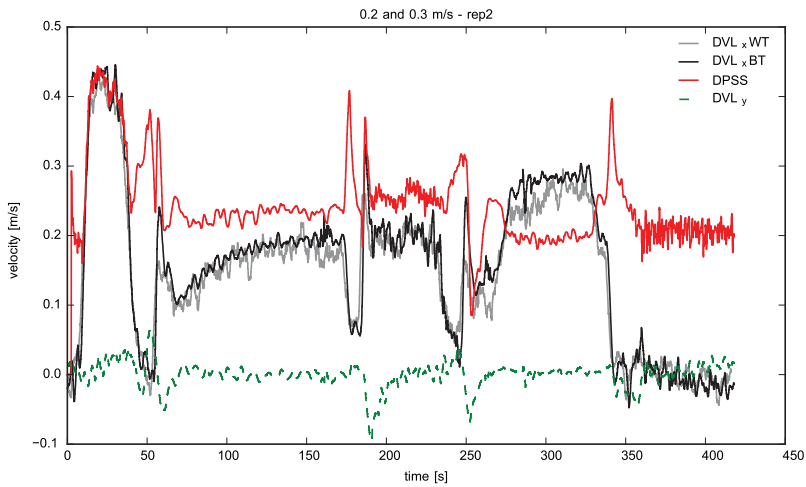
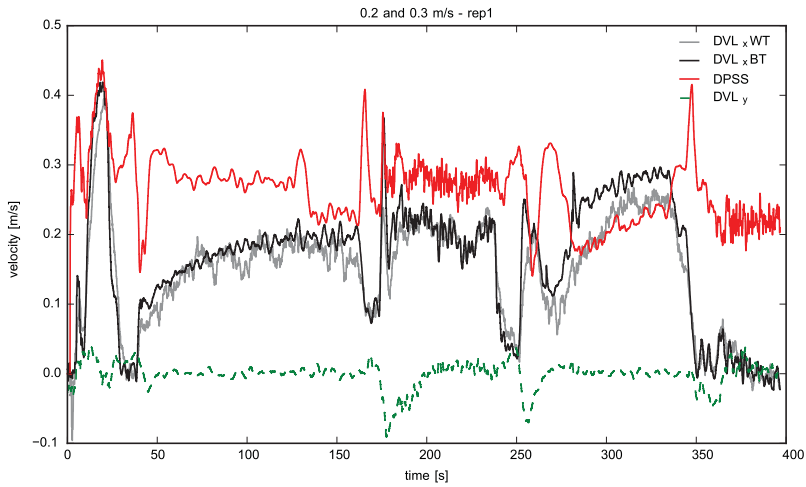
See Tables V–VII.

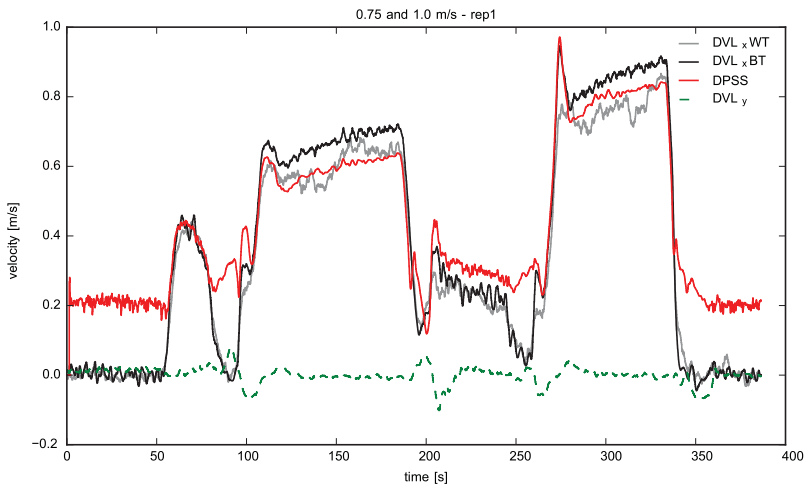
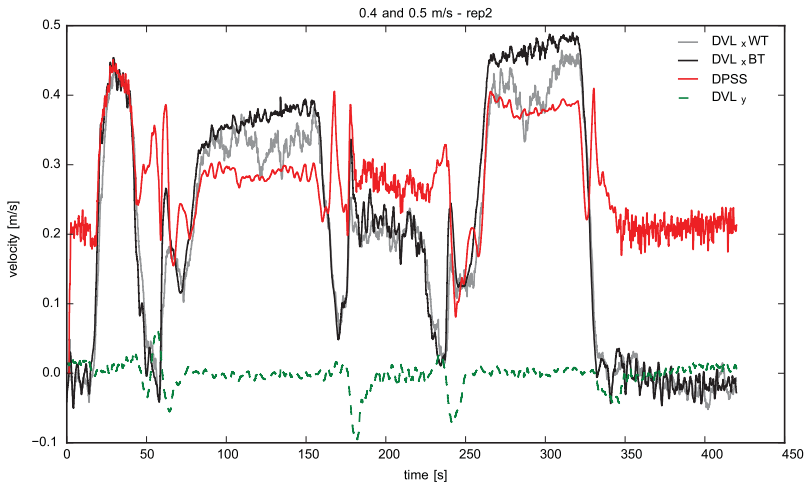
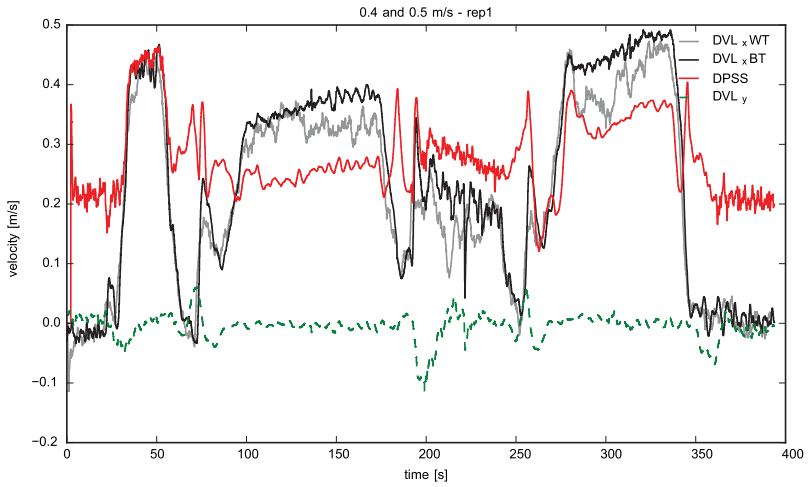
APPENDIX B
EKF VELOCITIES

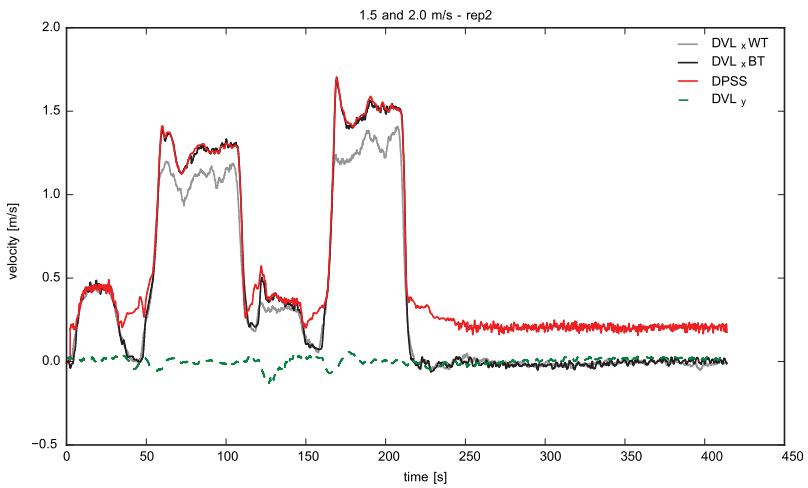
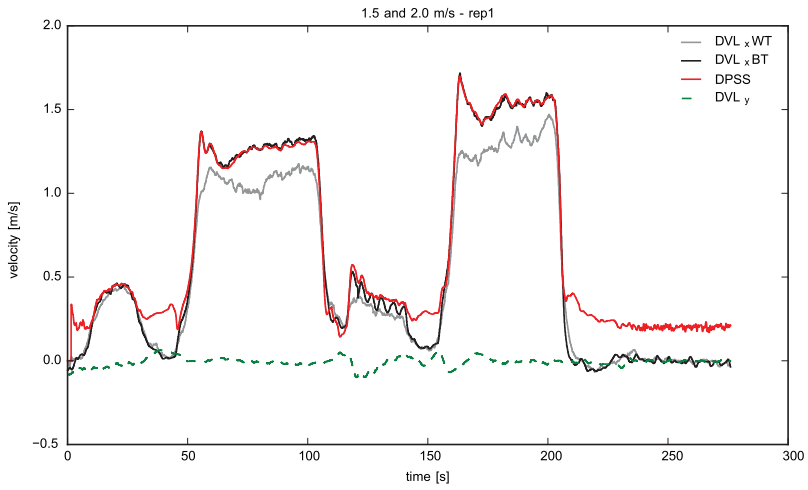
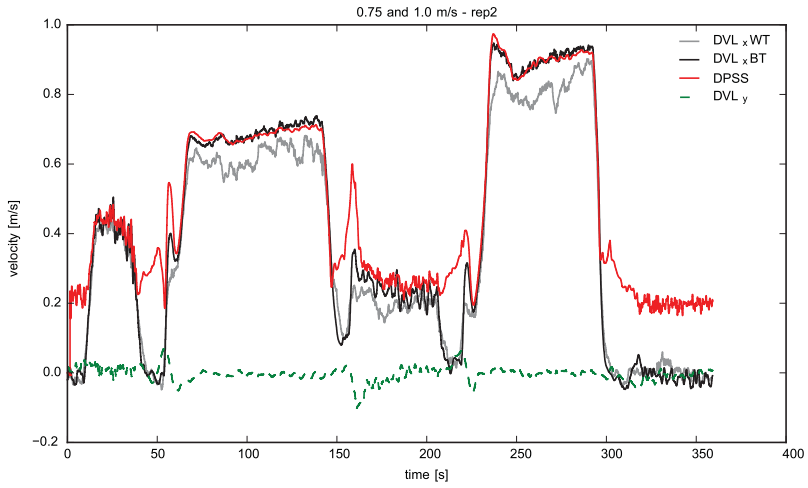
The following figures show EKF estimates for surge velocity from the DVL in BL (DVL_x BL) and DVL in WL (DVL_x WL) and the DPSS. Additionally, the EKF estimates for sway velocity from the DVL in BL (DVL_y) are shown

Setting A

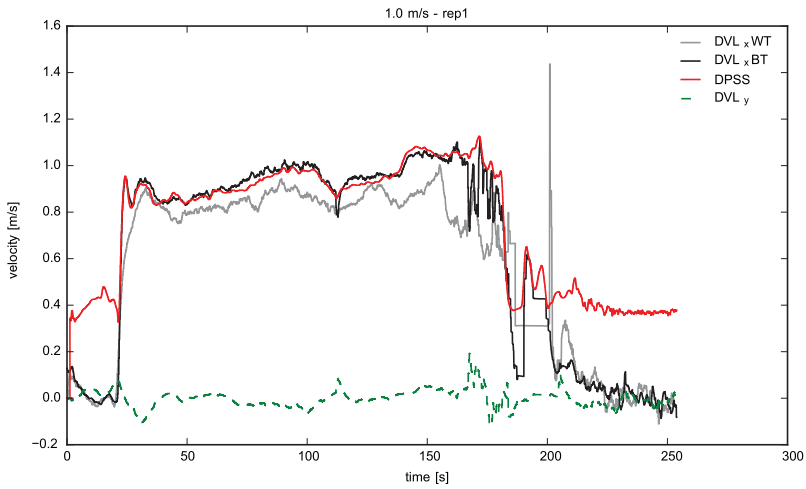
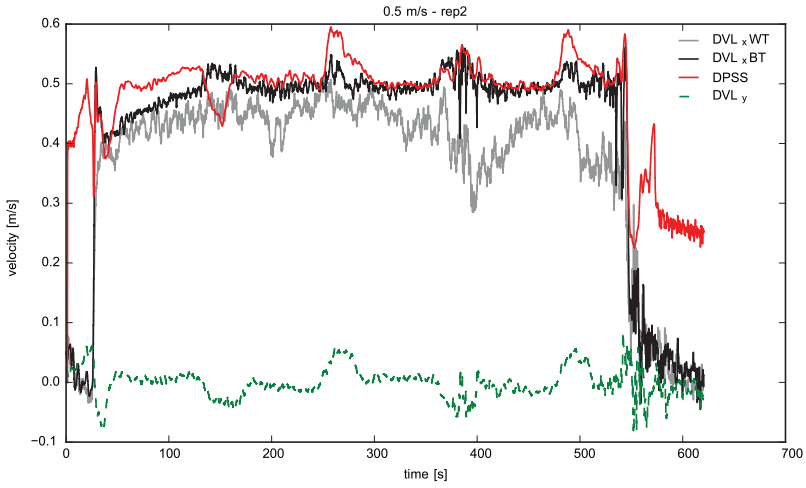
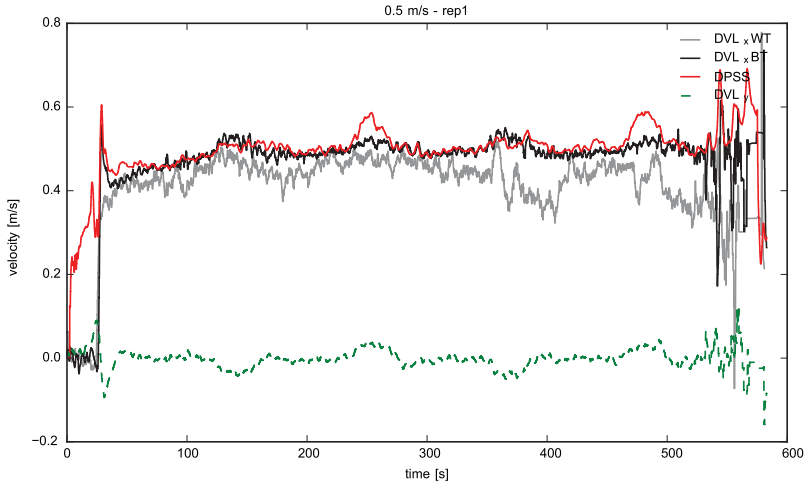
Linear Trajectories

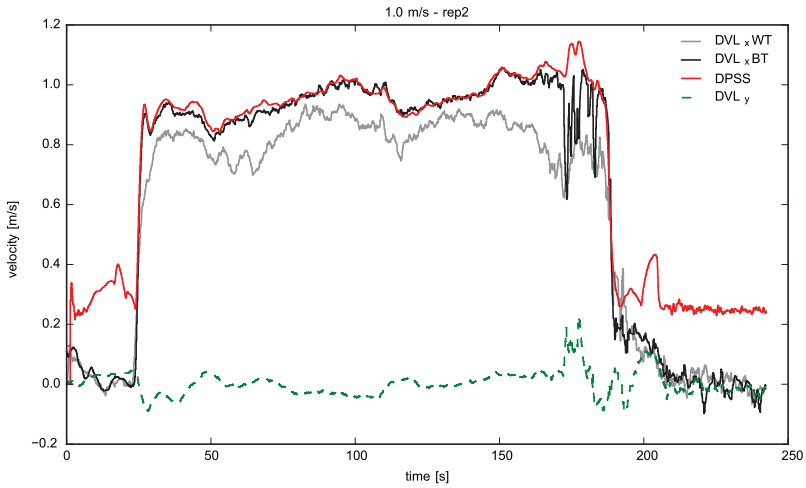




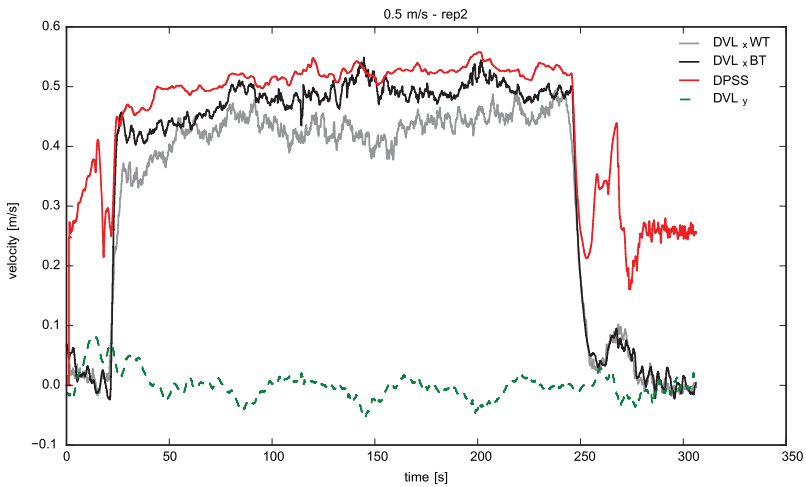
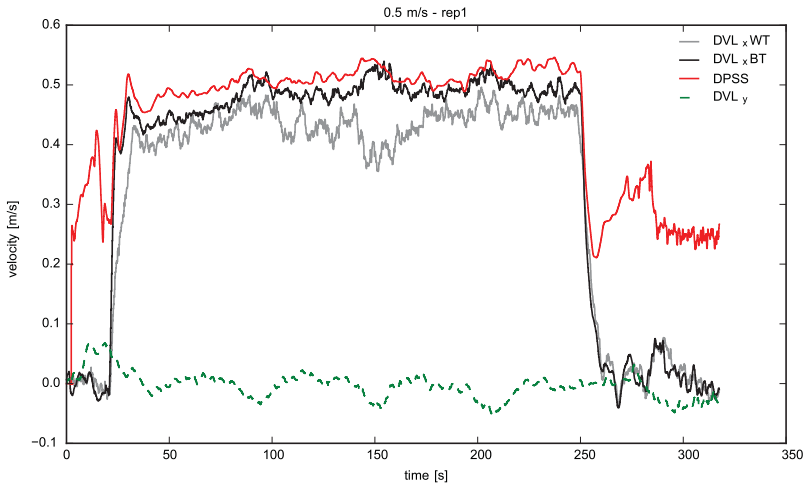


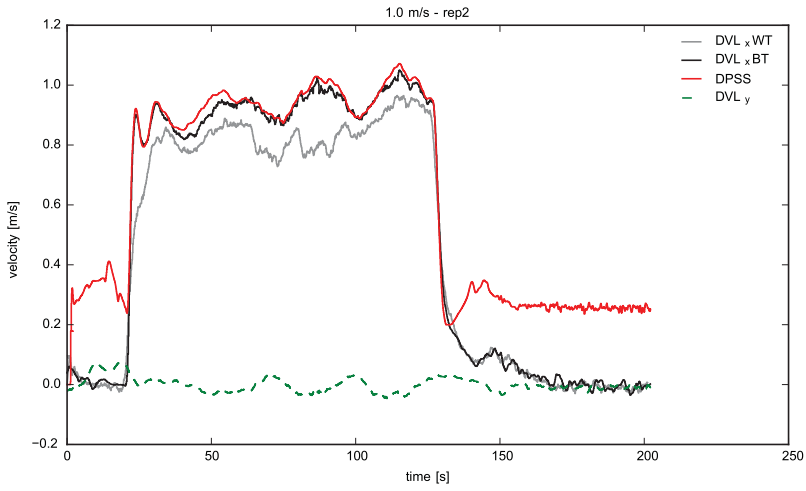
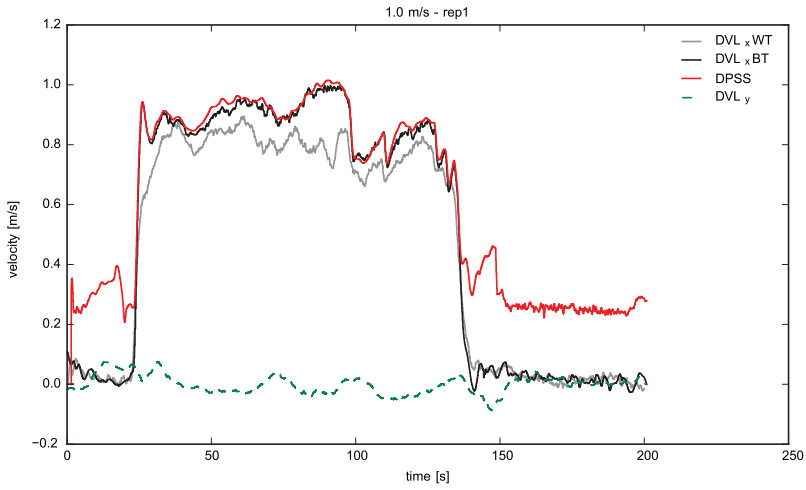
Lawn Mower Trajectories



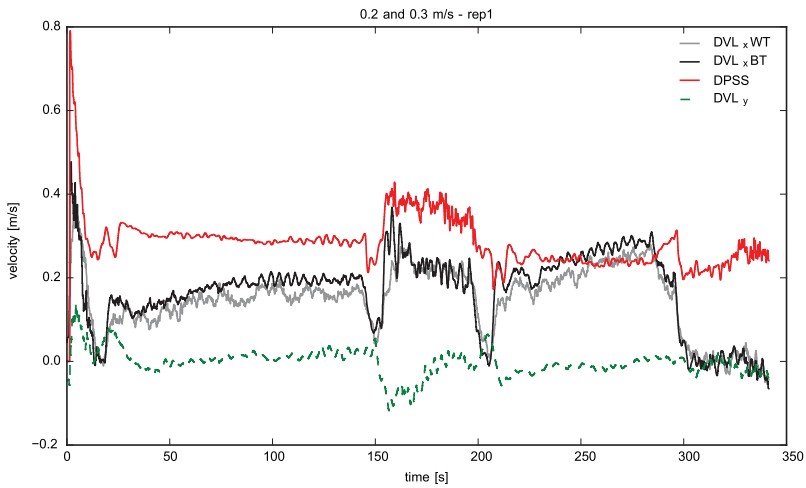


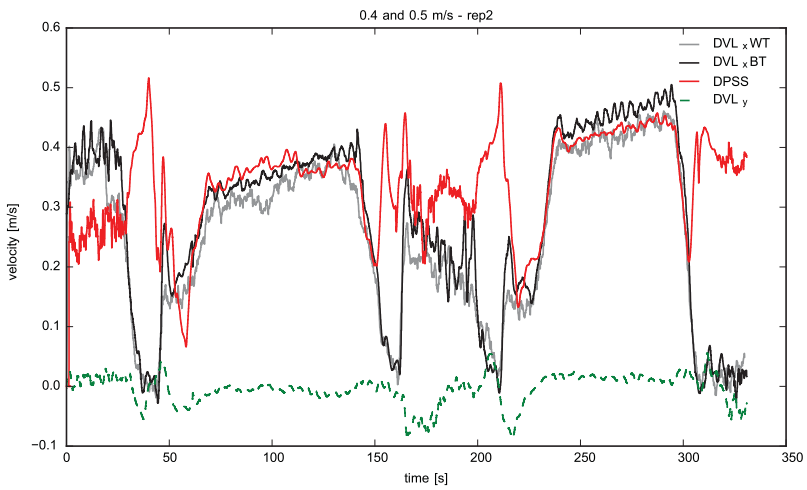
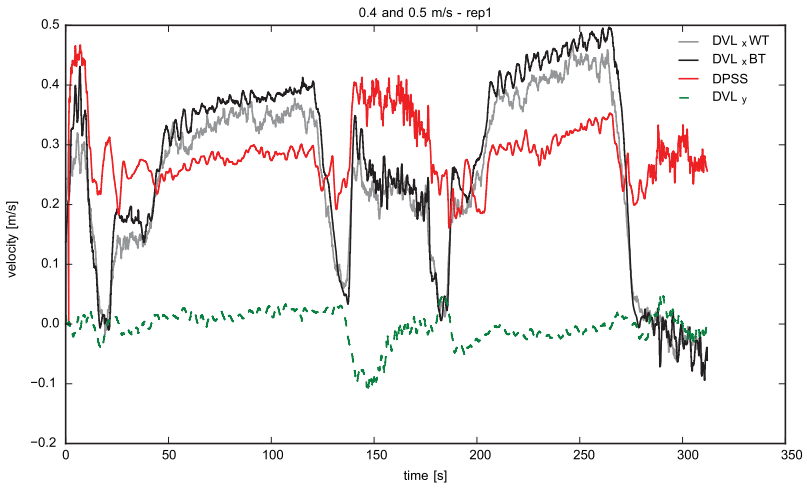
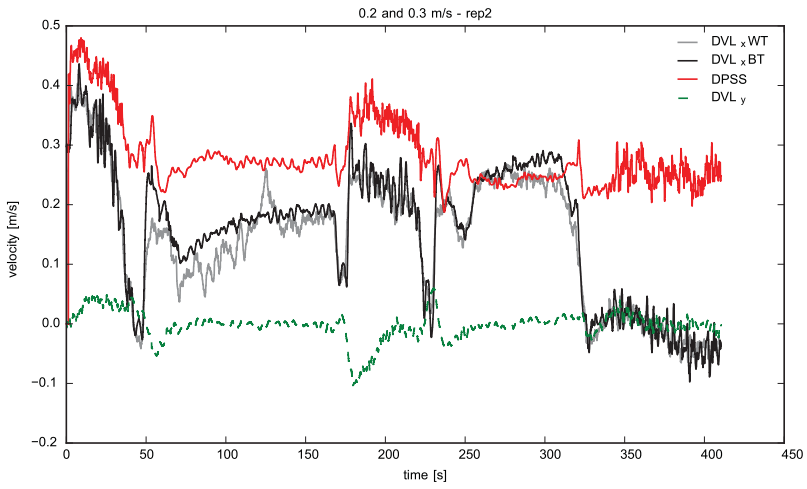
Loop Trajectories

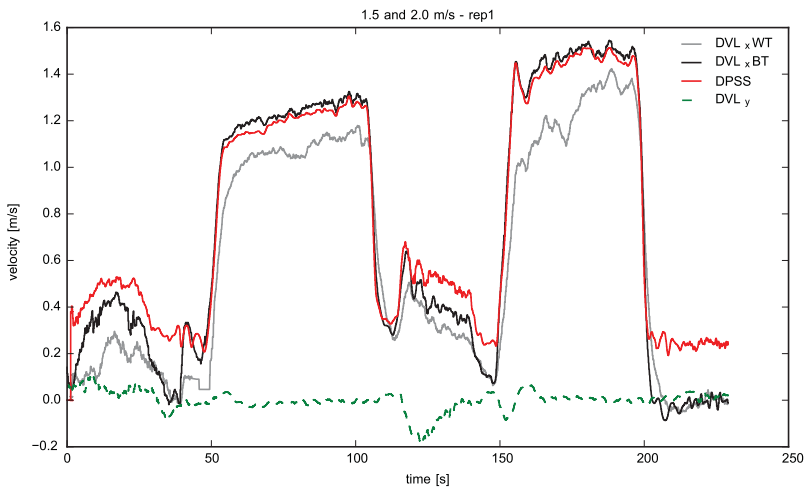
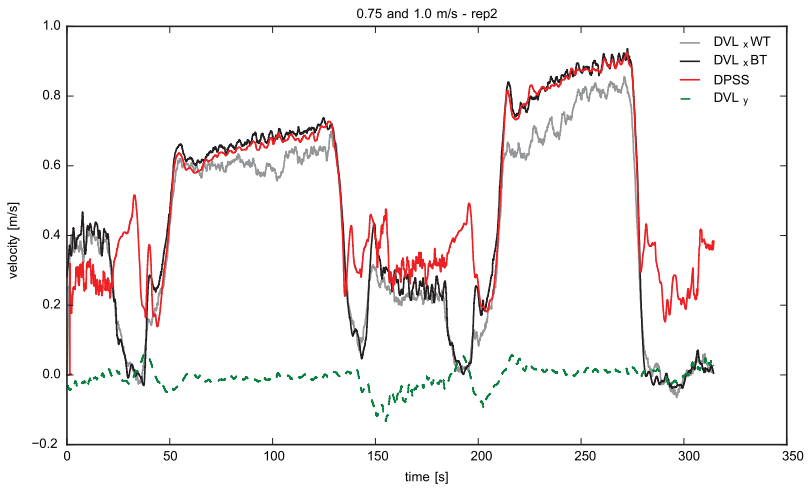
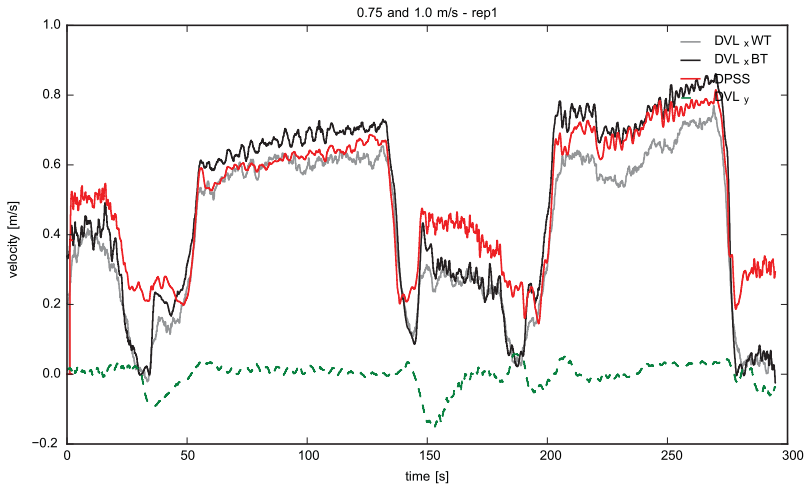


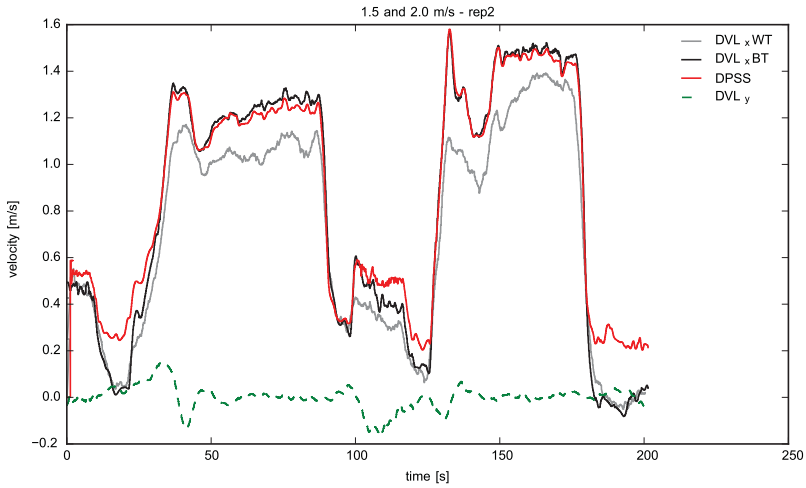


Setting B
Linear Trajectories

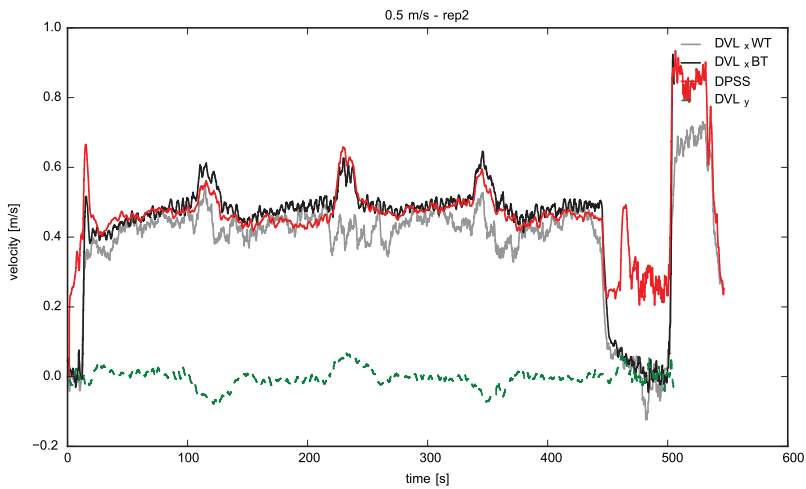
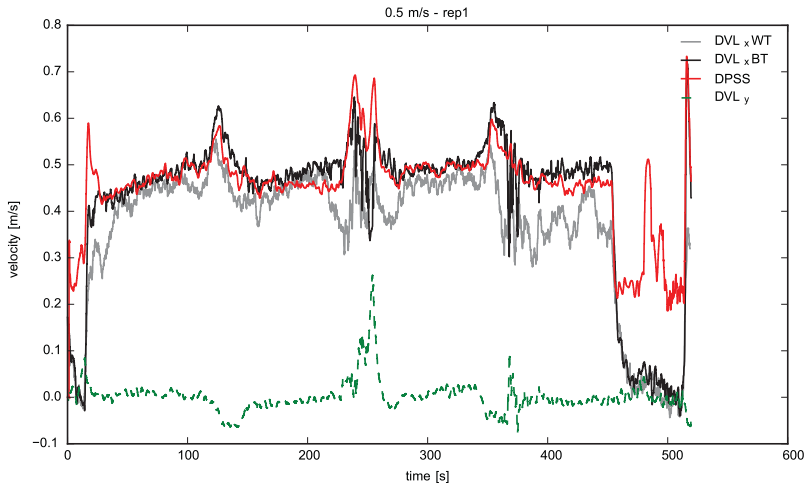


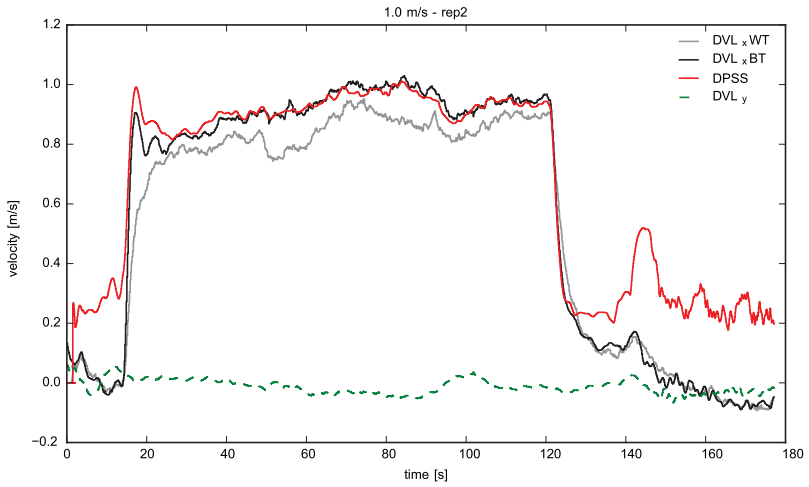
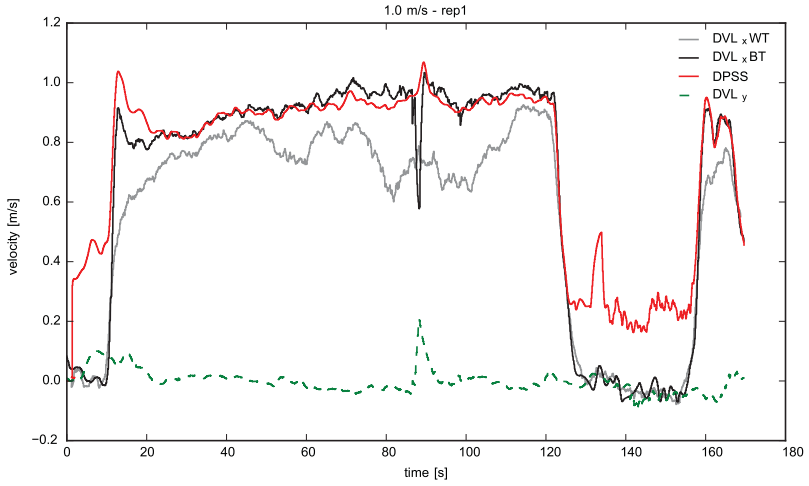




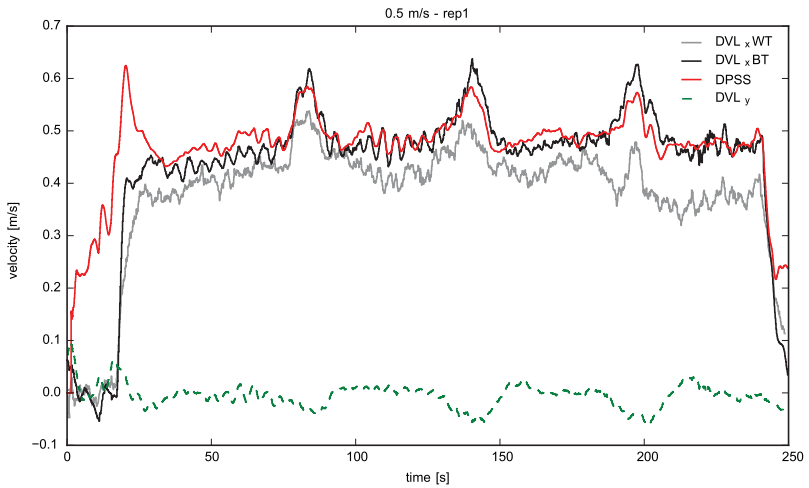


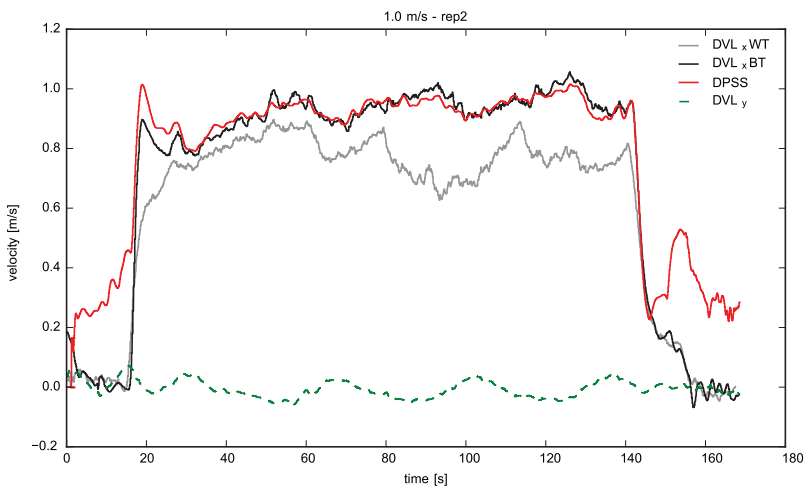
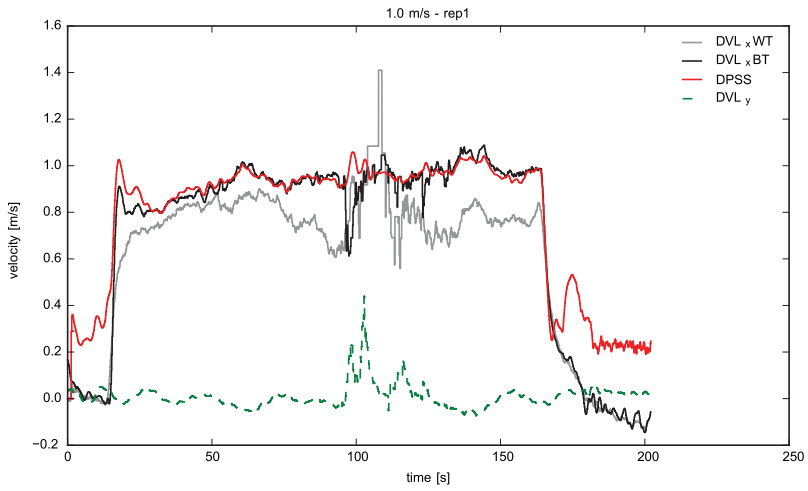
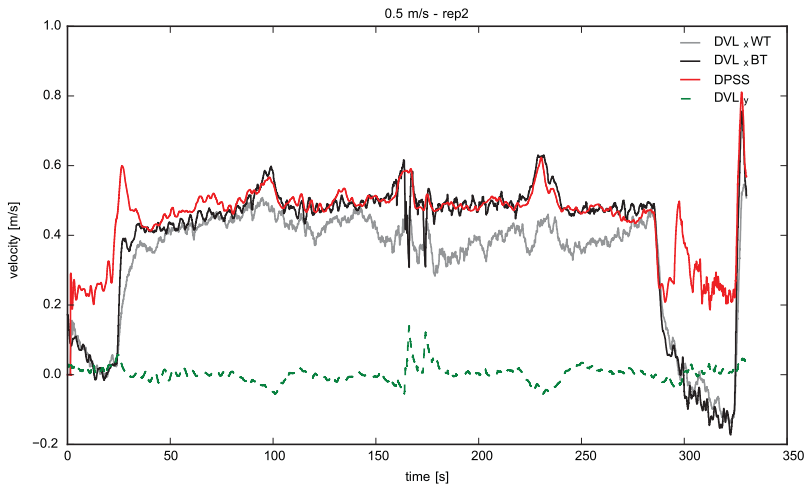
Lawn Mower Trajectories



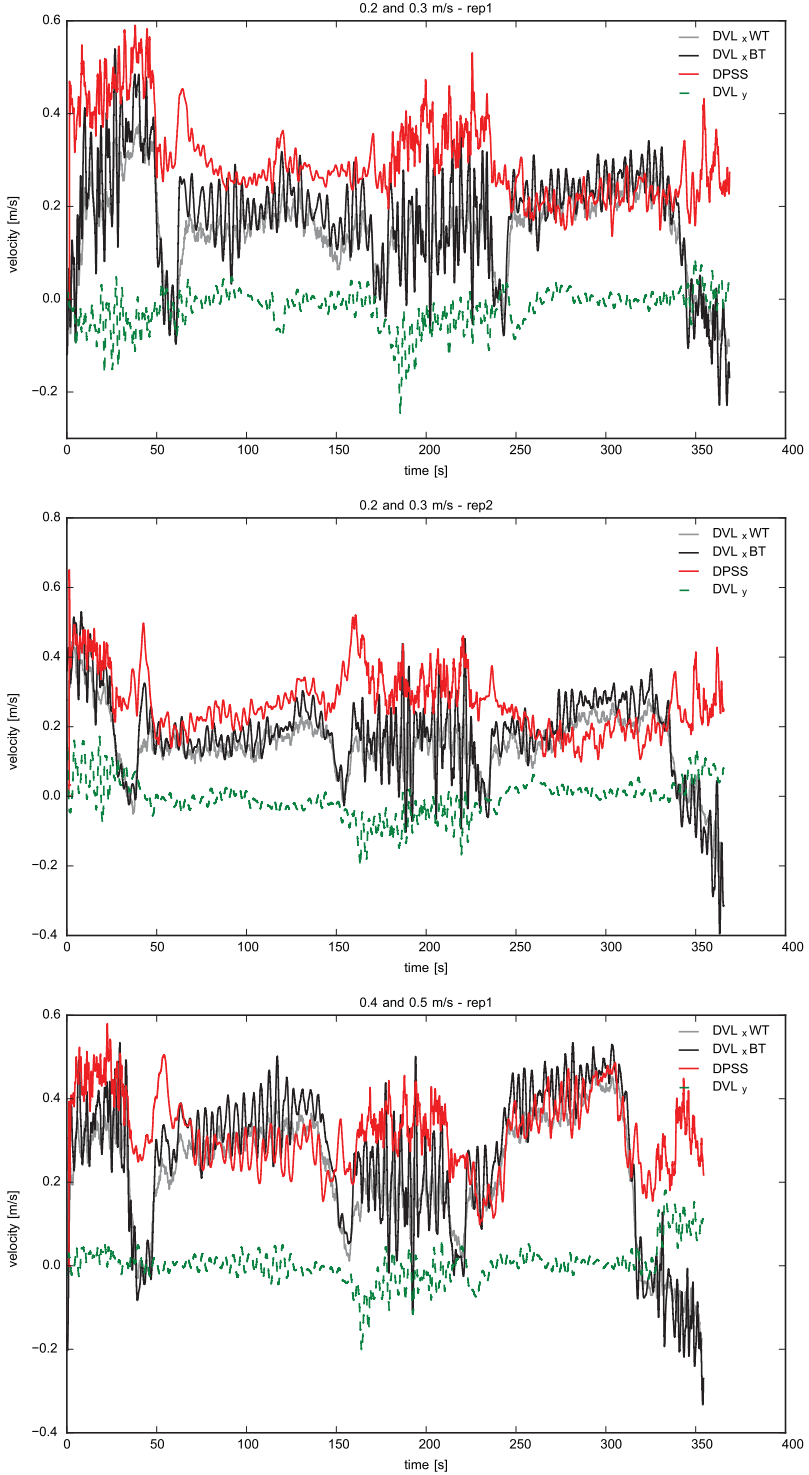


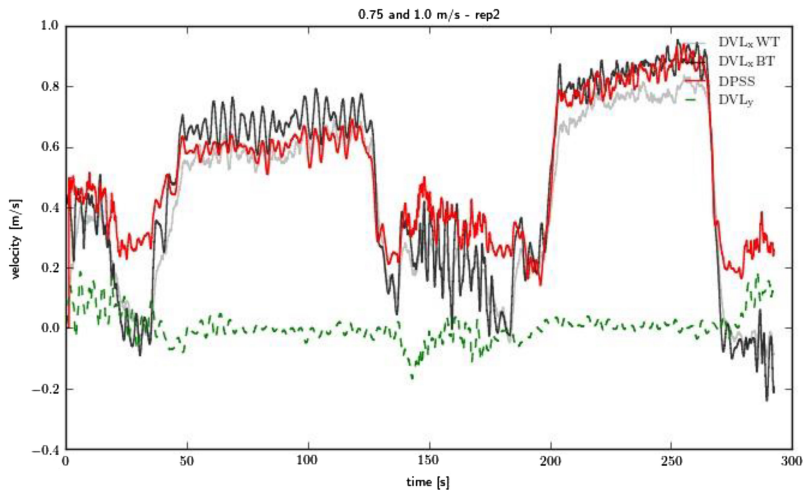
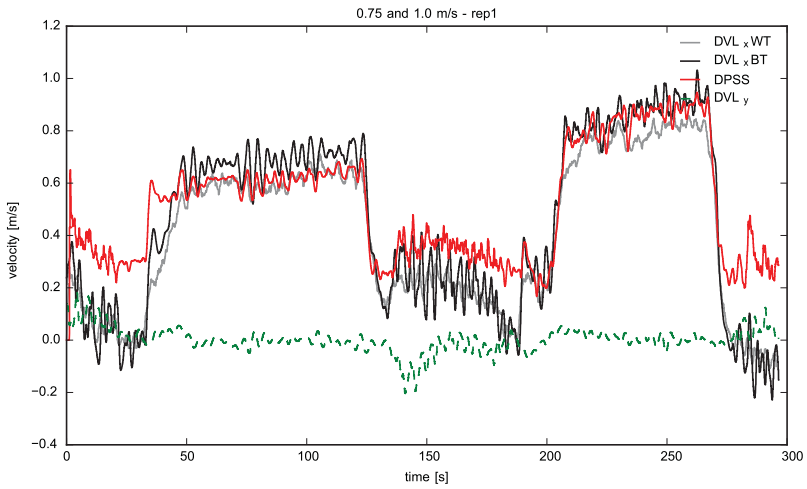
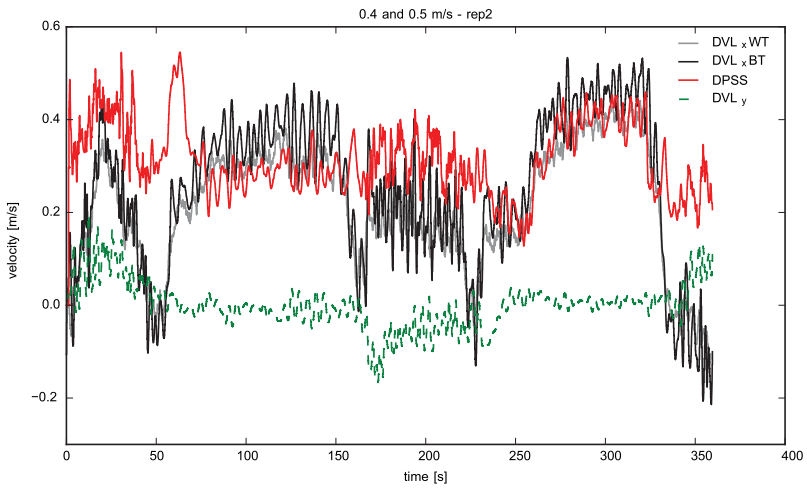
Loop Trajectories

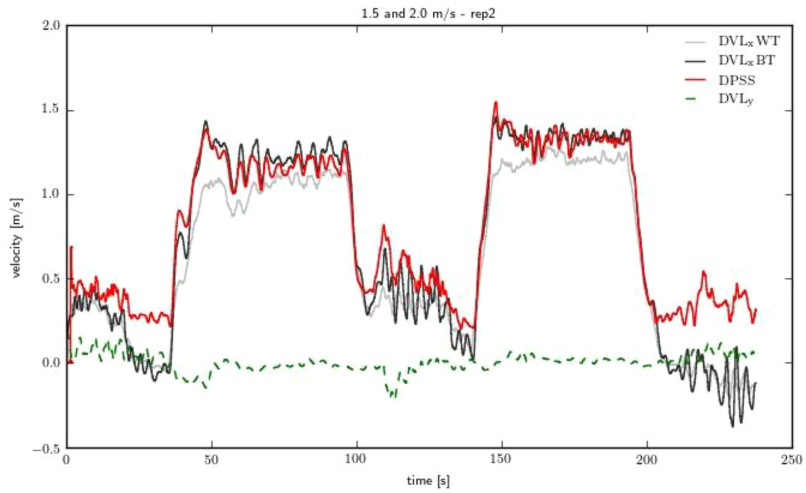
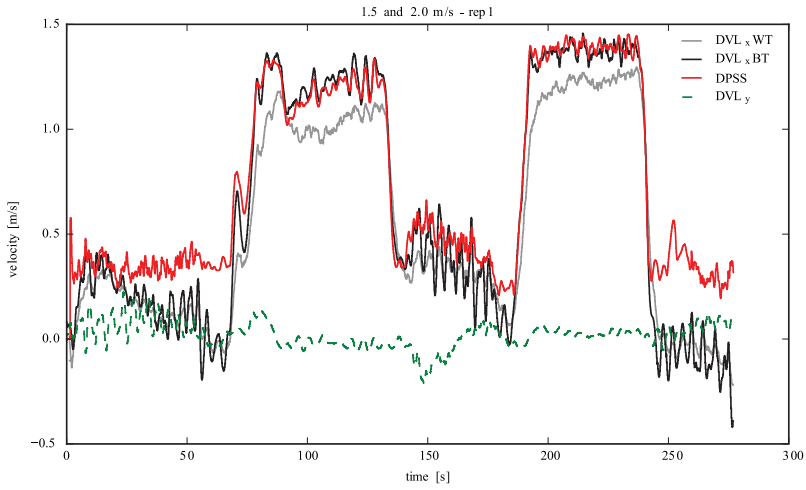




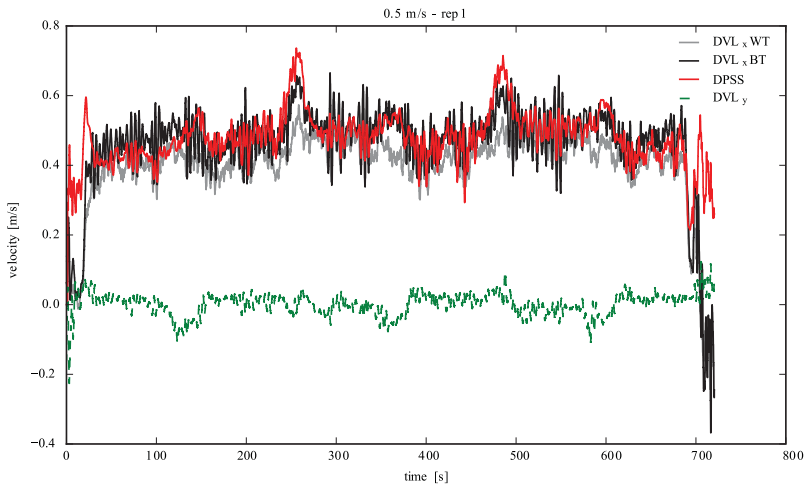
Setting C
Linear Trajectories

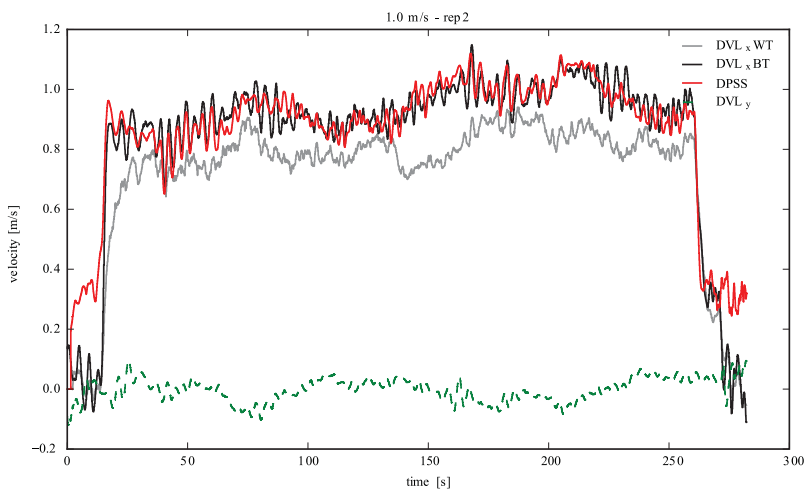
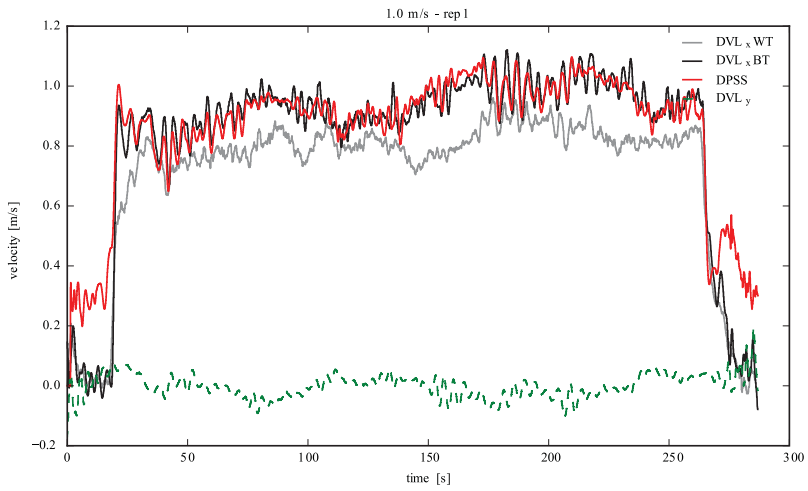
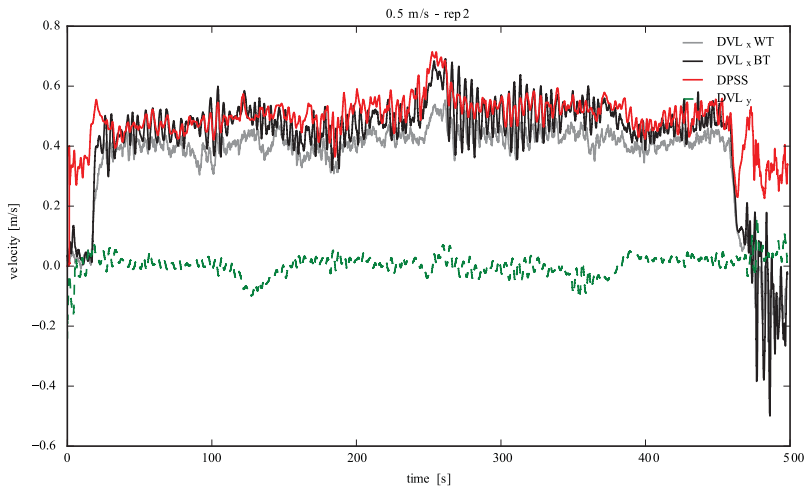




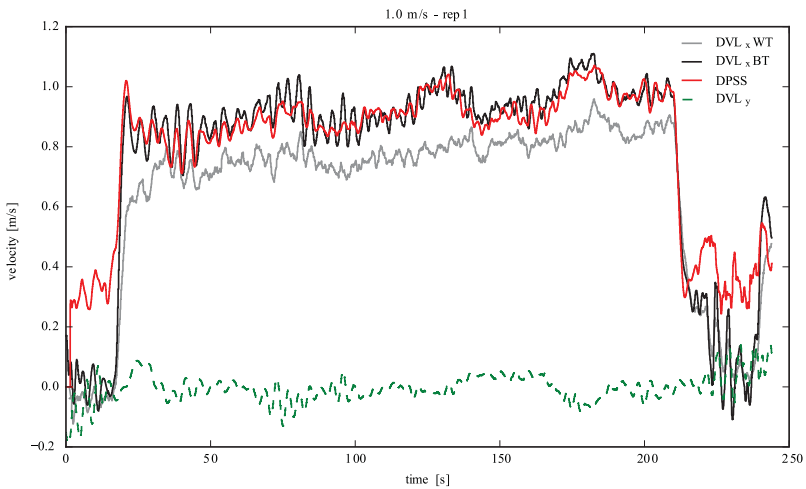
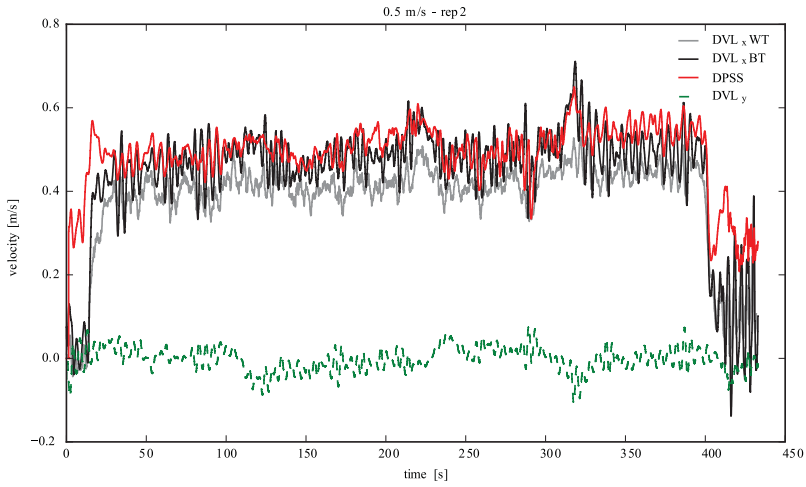
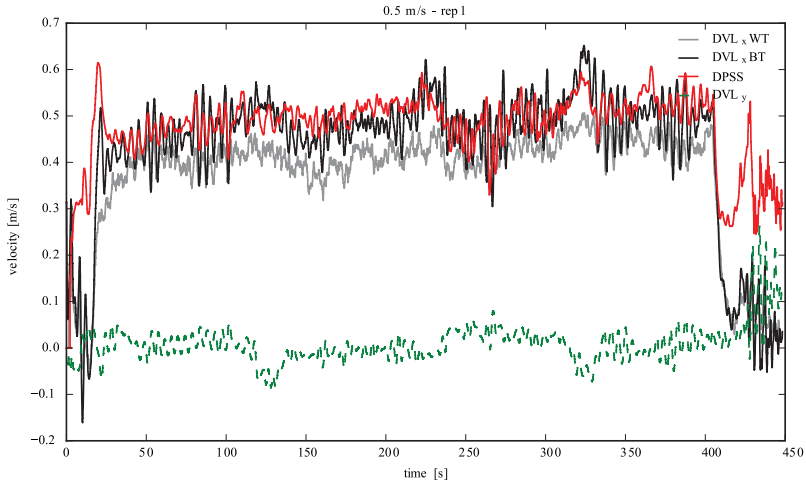


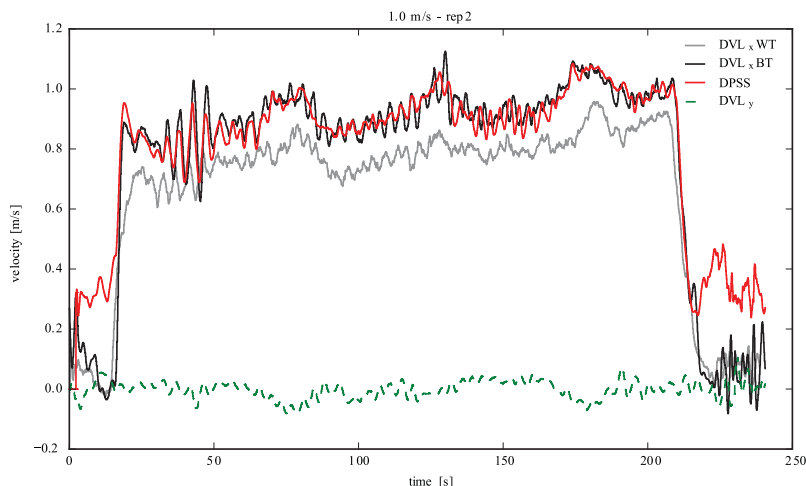
Lawn Mower Trajectories





Loop Trajectories





ACKNOWLEDGMENT

The authors would like to thank C. Candela, L. Magí, J. D. Hernández, and È. Pairet for their valuable help during field trials. Furthermore, the authors would also like to their colleagues at the Centre for Biorobotics for fruitful and inspiring discussions throughout the creation of this paper.

REFERENCES

- [1] L. Paull, S. Saeedi, M. Seto, and H. Li, "AUV navigation and localization: A review," *IEEE J. Ocean. Eng.*, vol. 39, no. 1, pp. 131–149, Jan. 2014.
- [2] P. E. Hagen, O. Midtgaard, and O. Hasvold, "Making AUVs truly autonomous," in *Proc. OCEANS Conf.*, 2007, pp. 1–4.
- [3] J. Melo and A. Matos, "Survey on advances on terrain based navigation for autonomous underwater vehicles," *Ocean Eng.*, vol. 139, pp. 250–264, 2017.
- [4] J. C. Kinsey, R. M. Eustice, and L. L. Whitcomb, "A survey of underwater vehicle navigation: Recent advances and new challenges," *IFAC Conf. Maneuvering Control Mar. Craft*, vol. 88, pp. 1–12, Apr. 2006.
- [5] L. Stutters, H. Liu, C. Tiltman, and D. J. Brown, "Navigation technologies for autonomous underwater vehicles," *IEEE Trans. Syst. Man, Cybern. C, Appl. Rev.*, vol. 38, no. 4, pp. 581–589, Jul. 2008.
- [6] L. Whitcomb, D. Yoerger, H. Singh, and D. Mindell, "Towards precision robotic maneuvering, survey, and manipulation in unstructured undersea environments—1. Introduction," in *Robotics Research: The Eighth International Symposium*, vol. 8. London, U.K.: Springer-Verlag, 1998, pp. 45–54.
- [7] G. Grenon, P. E. An, S. M. Smith, and A. J. Healey, "Enhancement of the inertial navigation system for the Morphus autonomous underwater vehicles," *IEEE J. Ocean. Eng.*, vol. 26, no. 4, pp. 548–560, Oct. 2001.
- [8] B. Jalving, K. Gade, K. Svartveit, A. Willumsen, and R. Sørhagen, "DVL velocity aiding in the HUGIN 1000 integrated inertial navigation system," *Model. Identification Control*, vol. 25, no. 4, pp. 223–235, 2004.
- [9] Ø. Hegrenæs, A. Ramstad, T. Pedersen, and D. Velasco, "Validation of a new generation DVL for underwater vehicle navigation," in *Proc. IEEE/OES Auton. Underwater Vehicles*, 2016, pp. 342–348.
- [10] L. Medagoda, J. C. Kinsey, and M. Eilders, "Autonomous underwater vehicle localization in a spatiotemporally varying water current field," in *Proc. IEEE Int. Conf. Robot. Autom.*, 2015, pp. 565–572.
- [11] M. J. Stanway, "Water profile navigation with an Acoustic Doppler Current Profiler," in *Proc. Ocean. IEEE Sydney*, 2010, pp. 1–5.
- [12] Teledyne RD Instrum., Inc., "Datasheet pathfinder DVL," Teledyne RD Instrum. Inc, Poway, CA, USA, 2017. [Online]. Available: http://www.teledynemarine.com/Pathfinder_DVL
- [13] Nortek, AS, "Datasheet Nortek DVL1000/DVL500," Nortek AS, Rud, Norway, 2017. [Online]. Available: <http://www.nortek-com/lib/datasheets/nortek-dv>
- [14] LinkQuest, Inc., "Datasheet NavQuest 600 Micro," LinkQuest, Inc., San Diego, CA, USA, 2009. [Online]. Available: <http://www.linkquest.com/html/NavQuest600M.pdf>
- [15] T. Salumäe *et al.*, "Design principle of a biomimetic underwater robot U-CAT," in *Proc. Oceans St. John's*, 2014, pp. 1–5.
- [16] D. L. Rudnick, R. E. Davis, C. C. Eriksen, D. M. Fratantoni, and M. J. Perry, "Underwater gliders for ocean research," *Mar. Technol. Soc. J.*, vol. 38, no. 2, pp. 73–84, 2004.
- [17] B. Allotta *et al.*, "The ARROWS project: Adapting and developing robotics technologies for underwater archaeology," *IFAC-PapersOnLine*, vol. 48, no. 2, pp. 194–199, 2015.
- [18] C. Osterloh, T. Pionteck, and E. Machle, "MONSUN II: A small and inexpensive AUV for underwater swarms," in *Proc. 7th German Conf. Robot.*, 2012, pp. 1–6.
- [19] OpenROV, "OpenROV/products/trident," OpenROV, Berkeley, CA, USA, [Online]. Available: <https://www.openrov.com/products/trident/>, Accessed on: Feb. 16, 2017.
- [20] M. Kruusmaa, G. Toming, T. Salumäe, J. Ježov, and A. Ernits, "Swimming speed control and on-board flow sensing of an artificial trout," in *Proc. IEEE Int. Conf. Robot. Autom.*, 2011, pp. 1791–1796.
- [21] J. Mogdans and H. Bleckmann, "Coping with flow: Behavior, neurophysiology and modeling of the fish lateral line system," *Biol. Cybern.*, vol. 106, no. 11/12, pp. 627–642, 2012.
- [22] Y. Xu and K. Mohseni, "A pressure sensory system inspired by the fish lateral line: Hydrodynamic force estimation and wall detection," *IEEE J. Ocean. Eng.*, vol. 42, no. 3, pp. 532–543, Jul. 2017.
- [23] C. Abels, A. Quattieri, M. De Vittorio, W. M. Megill, and F. Rizzi, "A bio-inspired real-time capable artificial lateral line system for freestream flow measurements," *Bioinspiration Biomimetics*, vol. 11, no. 3, 2016, Art. no. 035006.
- [24] M. Asadnia *et al.*, "MEMS sensors for assessing flow-related control of an underwater biomimetic robotic stingray," *Bioinspiration Biomimetics*, vol. 10, no. 3, pp. 1–15, 2015.
- [25] A. Klein and H. Bleckmann, "Determination of object position, vortex shedding frequency and flow velocity using artificial lateral line canals," *Beilstein J. Nanotechnol.*, vol. 2, no. 1, pp. 276–283, 2011.
- [26] V. I. Fernandez, "Performance analysis for lateral-line-inspired sensor arrays," Ph.D. dissertation, Dept. Mech. Eng., Massachusetts Inst. Technol., Cambridge, MA, USA, 2011.
- [27] A. Gao and M. Triantafyllou, "Bio-inspired pressure sensing for active yaw control of underwater vehicles," in *Proc. OCEANS Conf.*, 2012, pp. 1–7.
- [28] R. Venturelli *et al.*, "Hydrodynamic pressure sensing with an artificial lateral line in steady and unsteady flows," *Bioinspiration Biomimetics*, vol. 7, no. 3, 2012, Art. no. 36004.

- [29] T. Salumäe and M. Kruusmaa, "Flow-relative control of an underwater robot," *Proc. Roy. Soc. A Math. Phys. Eng. Sci.*, vol. 469, no. 2153, 2013, Art. no. 20120671.
- [30] F. Zhang, F. D. Lagor, D. Yeo, P. Washington, and D. A. Paley, "Distributed flow sensing for closed-loop speed control of a flexible fish robot," *Bioinspiration Biomimetics*, vol. 10, no. 6, 2015, Art. no. 65001.
- [31] C. Wang, W. Wang, and G. Xie, "Speed estimation for robotic fish using onboard artificial lateral line and inertial measurement unit," in *Proc. IEEE Int. Conf. Robot. Biomimetics*, 2015, pp. 285–290.
- [32] W. Wang, Y. Li, X. Zhang, C. Wang, S. Chen, and G. Xie, "Speed evaluation of a freely swimming robotic fish with an artificial lateral line," in *Proc. IEEE Int. Conf. Robot. Autom.*, 2016, pp. 4737–4742.
- [33] J. Anderson, Jr., *Fundamentals of Aerodynamics*, 3rd ed. New York, NY, USA: McGraw-Hill, 1985.
- [34] J. F. Fuentes-Pérez *et al.*, "Current velocity estimation using a lateral line probe," *Ecol. Eng.*, vol. 85, pp. 296–300, 2015.
- [35] J. F. Fuentes-Pérez, K. Kalev, J. A. Tuhtan, and M. Kruusmaa, "Underwater vehicle speedometry using differential pressure sensors: Preliminary results," in *Proc. IEEE/OES Autom. Underwater Vehicles*, 2016, pp. 156–160.
- [36] J. F. Fuentes-Pérez, C. Meurer, J. A. Tuhtan, and M. Kruusmaa, "Differential pressure sensors for underwater speedometry in variable velocity and acceleration conditions," *IEEE J. Ocean. Eng.*, vol. 43, no. 2, pp. 418–426, Apr. 2018.
- [37] Teledyne RD Instrum., Inc., "Datasheet Teledyne explorer DVL," Poway, CA, USA, 2017. [Online]. Available: <http://www.teledynemarine.com/explorer-doppler-vel>
- [38] E. Ower and R. C. Pankhurst, *The Measurement of Air Flow*. Amsterdam, The Netherlands: Elsevier, 2014.
- [39] K. H. Bejj, "Aircraft speed instruments," NACA Rep. 420, 1932.
- [40] M. Carreras *et al.*, "Sparus II, design of a lightweight hovering AUV," in *Proc. 5th MARTECH Int. Workshop Mar. Technol.*, 2013, pp. 152–155.
- [41] M. Quigley *et al.*, "ROS: An open-source Robot Operating System," in *Proc. ICRA Workshop Open Source Softw.*, vol. 3, no. 3.2, 2009, pp. 5–11.
- [42] N. Palomerias, S. Nagappa, D. Ribas, N. Gracias, and M. Carreras, "Vision-based localization and mapping system for AUV intervention," in *Proc. MTS/IEEE OCEANS Conf.*, Bergen, Norway, 2013, pp. 1–7.
- [43] R. M. Sorensen, *Basic Coastal Engineering*, 3rd ed. Boston, MA, USA: Springer, 2006.
- [44] M. R. Dhanak and N. I. Xiros, *Springer Handbook of Ocean Engineering*. New York, NY, USA: Springer, 2016.
- [45] P. Liu, B. Wang, Z. Deng, and M. Fu, "A correction method for DVL measurement errors by attitude dynamics," *IEEE Sens. J.*, vol. 17, no. 14, pp. 4628–4638, Jul. 2017.
- [46] O. Hegrehaes, E. Berglund, Ø. Hegrenæs, and E. Berglund, "Doppler water-track aided inertial navigation for autonomous underwater vehicle," in *Proc. OCEANS Conf. Eur.*, 2009, pp. 1–10.
- [47] D. Chang, W. Wu, C. R. Edwards, and F. Zhang, "Motion tomography: Mapping flow fields using autonomous underwater vehicles," *Int. J. Robot. Res.*, vol. 36, no. 3, pp. 320–336, Mar. 2017.
- [48] B. Claus, J. H. Kepper, S. Suman, and J. C. Kinsey, "Closed-loop one-way-travel-time navigation using low-grade odometry for autonomous underwater vehicles," *J. Field Robot.*, vol. 35, no. 4, pp. 421–434, Jun. 2018.
- [49] Y. T. Tan, M. Chitre, and F. S. Hover, "Cooperative bathymetry-based localization using low-cost autonomous underwater vehicles," *Auton. Robots*, vol. 40, no. 7, pp. 1187–1205, Oct. 2016.



Christian Meurer received the B.Eng. degree in biotechnology from the Ernst-Abbe Hochschule, Jena, Germany, in 2012, and the M.Sc. degree in bionics/biomimetics from the Hochschule Rhein-Waal, Kleve, Germany, in 2015.

He is currently a Junior Researcher with the Centre for Biorobotics, School of Computer Systems, Tallinn University of Technology, Tallinn, Estonia, working toward the Ph.D. degree within the framework of the Estonian Centre of Excellence in ICT Research (EXCITE). His work in this paper includes defining the

research problems, producing and calibrating the DPSS prototype and attachment for SPARUS II, planning and conducting the experiments, processing the data and writing the paper. His current research interests include bioinspired actuation and sensing for underwater robots, as well as flow relative control of autonomous underwater vehicles.



Juan Francisco Fuentes-Pérez received the M.Sc. degree in engineering for agroforestry development from the University of Valladolid, Spain. He is currently working toward the Ph.D. degree in flow sensing artificial lateral lines at the Centre for Biorobotics, School of Computer Systems, Tallinn University of Technology, Estonia.

He has been collaborating in several research projects focused on the design, simulation, and evaluation of fishways, and involved in artificial lateral line technology and its applications for the evaluation of aquatic ecosystems and its use in underwater robotics since 2014. He is currently a Junior Researcher with the Centre for Biorobotics, School of Computer Systems, Tallinn University of Technology, Tallinn, Estonia. His work in this paper includes defining the research problems, producing and calibrating the differential pressure sensor speedometer prototype and attachment for SPARUS II, planning and conducting the experiments, processing the data, and writing the paper. His current research interests include underwater and flow sensing, underwater robotics, fluid mechanics, ecohydraulics, and fishways.



Narcís Palomerias received the M.Sc. degree in computer science and the Ph.D. degree in information technologies from the University of Girona, Girona, Spain, in 2004 and 2011, respectively.

He is currently a Postdoctoral Fellow with the University of Girona, Girona, Spain, and also a member of the Underwater Robotics Laboratory, Computer Vision and Robotics Group (VICOROB). He has participated in several research projects, both national and European, all of them are related to underwater robotics (TRIDENT, PANDORA, MORPH, MERBOTS, LOONDOCK, TWINBOT, etc.), as well as in several European networks, such as EXCELLABUST and STRONGMAR among others. He has also participated in several European autonomous underwater vehicle (AUV) competitions such as SAUC-E'06, SAUC-E'10, SAUC-E'11, and ERL'17. He is currently working with the IP of the Spanish 3DAUV project focused on autonomous exploration in complex environments using AUVs and one of the leaders of the COLA2 project: an open source generic control architecture for marine vehicles. His work in this paper includes support regarding the software setup for the experiments as well as aiding in the handling of SPARUS II. His research activity mainly focuses on underwater robotics in research topics, such as planning and exploration, intelligent control architectures, and mission control.



Marc Carreras received the B.Sc. degree in industrial engineering in 1998 and the Ph.D. degree in computer engineering in 2003 from the University of Girona, Girona, Spain.

He is currently an Associate Professor with the Computer Vision and Robotics Institute, University of Girona. From 1999 to 2019, he has participated in 24 research projects (European and national projects). He is an author of about 150 publications. He has supervised five Ph.D. dissertations and participated in several European autonomous underwater vehicle (AUV) competitions (five times winner). His work in this paper includes defining the research problem, providing the hardware for the experimental setup, and planning and revising the experiments. His research activity mainly focuses on underwater robotics in research topics, such as intelligent control architectures, robot learning, path planning, and AUV design, modeling, and identification.



Maarja Kruusmaa received the Ph.D. degree in computer engineering from the Chalmers University of Technology, Gothenburg, Sweden, in 2002.

She is currently the Head of the Centre for Biorobotics, Tallinn University of Technology, Tallinn, Estonia. She worked on flow sensing underwater robots, bioinspired robot locomotion, experimental fluid dynamics, and robot learning. Her work in this paper includes defining the research problems, planning and revising the technical approach, and writing the paper. Her research mainly focuses on

bioinspired underwater robotics

Appendix 5 - Publication 3

III

C. Meurer, A. Simha, Ü. Kotta, and M. Kruusmaa, "Nonlinear orientation controller for a compliant robotic fish based on asymmetric actuation," in Proceedings - IEEE International Conference on Robotics and Automation (ICRA), vol. 2019-May, pp. 4688–4694, Institute of Electrical and Electronics Engineers Inc., may 2019

Nonlinear Orientation Controller for a Compliant Robotic Fish Based on Asymmetric Actuation

Christian Meurer¹, Ashutosh Simha², Ülle Kotta² and Maarja Kruusmaa¹

Abstract—Compliant fish-like robots are being developed as efficient and dependable underwater observation platforms with low impact on the observed environment. Orientation control is an essential building block to achieve autonomy for those vehicles. So far, the major focus has been on rigid tails or on flexible tails with a high degree of actuation. We present a novel control strategy for an underactuated robotic fish with a flexible tail optimized for cruising. The basis for our approach is the generation of asymmetric velocity profiles of the robot's tail beats. To achieve such velocity profiles, the usual sinusoidal tail actuation is replaced with skewed triangle waves. We provide a simple formulation for such waves, where their skew is dependent on only one variable which we define as skew factor. Furthermore, a nonlinear control law is derived to achieve the desired turning motions. We implement the controller on a compliant fish-like robot with a simple actuation mechanism. The control scheme is experimentally validated, and its robustness is tested in field trials.

I. INTRODUCTION

Honed by millions of years of evolution, fish are very well adapted to underwater locomotion. They show superior maneuverability and efficiency compared to conventional engineered systems [1]. Exploiting those characteristics has the potential to lead to better propulsion mechanisms for underwater vehicles used for applications such as oceanographic surveys or monitoring of underwater facilities. Furthermore, fish inspired robots can be used to study fish locomotion in a controlled environment [2], provide platforms to study robot-animal interaction [3], [4] and enable observations of marine life with minimal disturbance [5].

These reasons have led to the development of an increasing number of fish robots [6], [7], [8], [9], [10]. A wide variety of propulsion mechanisms has been studied and adapted. Presently, most of the fish-like robots are based on body and/or caudal fin (BCF) locomotion, due to its superiority regarding thrust production and acceleration [11]. The kinematics of the compliant tail of real fish are mostly mimicked by utilizing discrete and rigid mechanism [12], [13], [14], [15]. While it is easier to formulate the kinematics and dynamics of those mechanisms, they add to the mechanical complexity, size and energy consumption of the robotic system. To circumvent those limitations, fish robots with compliant tails have been suggested and designed [16], [17], [18], [19]. Compliant structures show the potential

¹Centre for Biorobotics, Department of Computer Systems, Tallinn University of Technology, 12616 Tallinn, Estonia christian.meurer, maarja.kruusmaa@taltech.ee

²Department of Software Science, Tallinn University of Technology, 12616 Tallinn, Estonia ashutosh.iisc@gmail.com; kotta@cc.ioc.ee

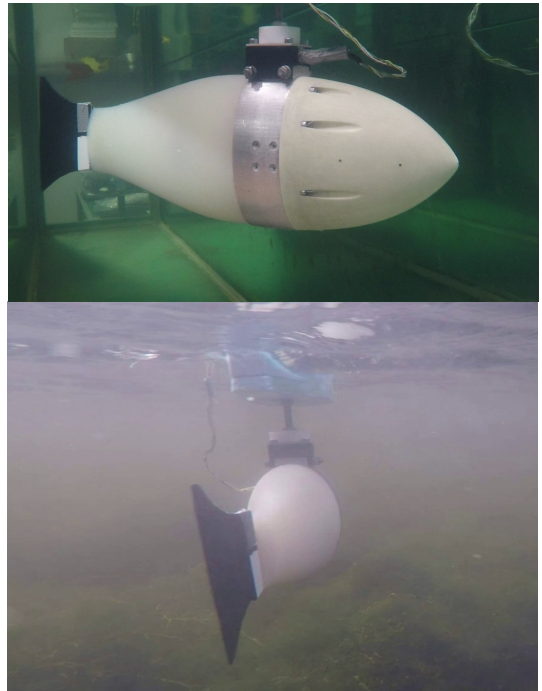


Fig. 1. **Fish-like robot with compliant tail:** The FILOSE robot represents a class of underactuated fish-like robots with compliant tails. If such robots are optimized for mechanical simplicity and cruising, orientation control becomes a challenging problem.

to increase the locomotion efficiency of fish-like robots [20]. One of the first robots to use a compliant structure was developed within the FILOSE project [21] and is shown in Fig. 1. The compliant tail of the FILOSE robot was designed to mimic the kinematics of a rainbow trout by exploiting passive material and shape properties. This led to a simple and very robust mechanical actuation mechanism. Only a minimal set of control parameters is necessary to facilitate complex kinematics. Furthermore, it has been shown that a compliant tail design can increase motion efficiency by interacting with the ambient flow [22].

For most of their envisioned applications fish-like robot would benefit from autonomous capabilities. An essential part of every autonomy framework is the orientation control of the robot. The main focus of biologists [23], [24] and

roboticists alike has been centered on rapid maneuvers, which are facilitated by large tail bending angles [25], [26], [27], [10]. Hirata et al. [28] present three distinct turning modes which either use a tail offset for steady turns or frozen tail deflections for rapid turns. Yu et al. [29] generate turning maneuvers based on step functions which influence the lateral excursion of the robotic tail. However, little attention has been given to more economic steady turns, which could play an important role during inspection and observation tasks of fish robots. Hu et al. [30] and Tan et al. [31] focus on steady turns by adding an offset to the tail oscillation. All presented orientation control strategies require rather large bending angles of the tails and/or refined control of distinct tail sections. For robots with simple and robust actuation mechanisms optimized for cruising, such orientation control strategies are difficult to implement. The FILOSE robot is an example of such a class of vehicles. It was optimized for simplicity and straight cruising and is not capable of producing large tail deflections. Furthermore, the compliant passive tail does not allow on-line manipulation of specific parts. The FILOSE robot's capability to sense flow enabled the successful implementation of flow relative control strategies [32], [33], [34]. A problem remains for applications in conditions where flow is absent and new control strategies need to be developed within the boundaries of the specific actuation of this robot type.

Gray [35] and Webb et al. [36] suggest that some fish use asymmetric tail motions for turning maneuvers, where the tail beat in the direction of turning seems to be accelerated. In this paper we show that this strategy can be utilized to implement steady turning maneuvers for underactuated compliant fish robots. We define and implement a novel skewed waveform as actuator input to produce asymmetric tail motions. Furthermore, we use a nonlinear PD controller to control the orientation of the fish-like robot. We will use the FILOSE robot as a platform to validate this new approach of orientation control in field tests. However, the proposed approach extends to other fish-like robot platforms discussed.

II. THE FILOSE ROBOT

The robot consists of a rigid head and a compliant silicon tail with a rigid fin emulating the morphology of a rainbow trout (*Oncorhynchus mykiss*). The tail is actuated by a single servo motor (Futaba BLS152 brushless servo) which is connected to an actuation plate embedded in the silicon tail. Two steel wires transform the rotation of the motor into a bending motion of the tail (Fig. 2b) The rigid head contains all on-board electronics including an Arduino Mini micro-controller and an BNO055 9-axis absolute orientation sensor (Bosch Sensortec). The overall size of the robot amounts to 500 mm x 8.5 mm x 15.6 mm (L x H x W) with a mass of 3.04 kg. The FILOSE robot is connected to a float which carries a battery pack and a bluetooth module (HC-05 Guangzhou HC Information Technology) for wireless communication. The disturbance on the robot's motion caused by the cable in the previous configuration is thus removed. Fig. 2a shows the robot with the attached float. Data processing and higher

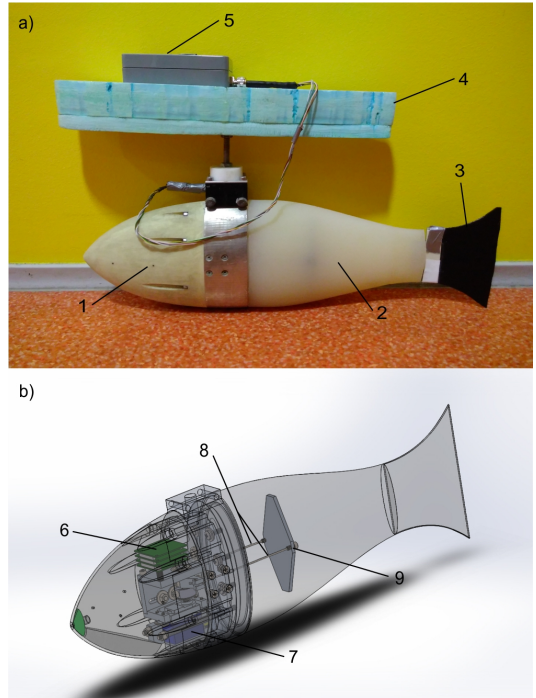


Fig. 2. **Specifics of the FILOSE robot:** a) Side view: 1 - rigid head of the robot; 2 - compliant silicon tail; 3 - rigid fin; 4 - Styrofoam float; 5 - splash proof box containing battery pack and bluetooth module. b) CAD drawing of electronics and actuation mechanism: 6 - microcontroller and orientation sensor; 7 - servomotor; 8 - steel cables; 9 - actuation plate

level control are implemented in LabView on an external computer.

The motor actuates the compliant tail based on a sinusoidal input φ of the form:

$$\varphi(t, f, A, \varphi_0) = A * \sin(2\pi ft) + \varphi_0 \quad (1)$$

where A is the amplitude of the motor's oscillation, f is the oscillation frequency, t is time and φ_0 is the oscillation offset. The surge velocity of the robot can be controlled by altering either amplitude or frequency. Salumäe et al. [34] identified that the FILOSE robot is most efficient with an actuation frequency of 2 Hz, which was subsequently used for all experiments. In conditions with high flow speeds, a non-zero oscillation offset is sufficient to induce turning. However, in conditions lacking high flow speeds such an actuation scheme produces very small turning rates and is therefore ineffective.

III. CONTROL FRAMEWORK

We propose an asymmetric periodic actuation signal for the motor torque which controls the tail motion, such that the rise and fall times are distinct. Such a waveform is motivated by two factors:

- Faster motion of the tail in one lateral direction over the other creates an imbalance in the drag-induced torque acting on the tail in each wave period, therefore generating a non-zero net average torque.
- The tail motion can also be regarded as *internal torque actuation* and therefore the anterior rigid head exhibits a recoil motion due to momentum conservation. This recoil is also asymmetric due to the asymmetric internal actuation.

The net effect is that the FILOSE robot turns in the direction of the faster tailbeat while traveling forward. To create the asymmetric tail actuation, the existing sinusoidal motor input (1) had to be replaced by an asymmetric waveform. In this section we will describe the generation of this waveform and its effect on the turning behavior of the FILOSE robot. Furthermore, we will derive a nonlinear feedback controller which changes the input waveform based on input from the robot's orientation sensor.

A. Waveform Generation

The required waveform is derived from a standard triangle wave. We introduce a skew factor which tilts the triangle wave either clockwise or counterclockwise. This skew causes the slope of one side of the triangle wave to increase while the counterpart decreases, which is proportional to the actuation velocity of the motor during both halves of the tail beat. We define a piecewise continuous function $\varphi(t, f, A, \tau)$ as new input waveform and we introduce the skew parameter $\tau \in \mathbb{R}, 0.1 \leq \tau \leq 0.9$.

$$\varphi(t, f, A, \tau) = \begin{cases} 0 & t = 0 \\ \frac{2Af\Phi(t)}{\tau} & 0 \leq \Phi(t) < \frac{\tau}{2}T \\ \frac{A(1-2f\Phi(t))}{1-\tau} & \frac{\tau}{2}T \leq \Phi(t) < (1-\frac{\tau}{2})T \\ \frac{A(2f\Phi(t)-2)}{\tau} & (1-\frac{\tau}{2})T \leq \Phi(t) \leq T \end{cases} \quad (2)$$

$T = f^{-1}$ is the wave period of the function and we define $\Phi(t) = t \bmod T$ as modulo operator for time. For a τ of 0.5 a triangle wave is generated without skew, which should induce no turning action. The upper and lower limits of τ also define the limits of the corresponding turning rate. Two 8th order Savitzky-Golay filters are used to smooth the output signal. Fig. 3 compares the two limit cases for skew with a standard sine wave to illustrate the difference in the actuation patterns.

B. Orientation Controller

The dynamics of the planar orientation Ψ of the robot is given by:

$$J\ddot{\Psi} = -k_d\dot{\Psi} + \mathcal{C}(\Psi, \dot{\Psi}, t) + U, \quad (3)$$

where J is the inertia about the vertical axis, U is a control torque, k_d is a damping factor for the drag which is assumed to be linear and $\mathcal{C}(\Psi, \dot{\Psi}, t)$ is a lumped quantity denoting the *Coriolis* force and other external disturbances and unmodeled dynamics, and is assumed to be a small or

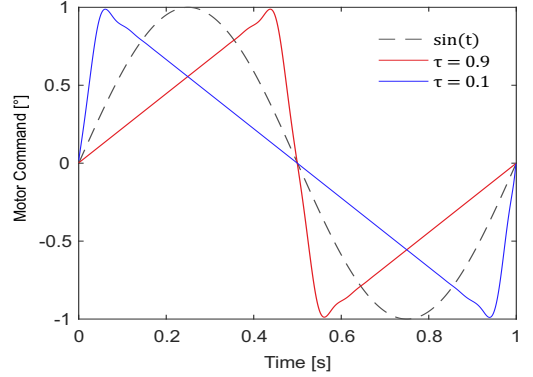


Fig. 3. **Input waveforms for the motor of the FILOSE robot:** All functions are normalized and have a wave period $T = 1$ s. The skewed triangle waves are represented by the limit cases $\tau = 0.9$ and $\tau = 0.1$, all other waveforms lie between these two cases. The standard sine wave commonly used for actuation is shown as reference

negligible quantity (and is therefore ignored for the stability analysis). The preceding two assumptions are valid at low angular velocities. However, for a more accurate description of the dynamics at different regimes, one needs to employ the nonlinear models given in [37].

A feedback control law is designed for the skew factor τ based on the empirically validated assumption that it is related to the torque U as

$$\tau = 0.5 + \alpha U \quad (4)$$

where α is an experimentally determined constant. The control law is derived based on the nonlinear proportional-derivative control strategy as described in [38]. A heading angle error function is chosen (as in [39]) as

$$\Theta(\theta) = 2 - \sqrt{2(1 + \cos(a\theta))} \quad (5)$$

where $\theta = \Psi - \Psi_d$ and a is a factor that determines the *tightness* of the error. Its differential is obtained as

$$d\Theta(\theta) = \frac{a \sin(a\theta)}{2\sqrt{2(1 + \cos(a\theta))}} \quad (6)$$

which is smooth and well defined as long as $a\theta \neq \pm\pi$. Now consider the Lyapunov function

$$V = \frac{2}{a}\Theta(\theta) + \frac{\alpha}{2}(J\dot{\theta})^2 \quad (7)$$

Its derivative along the controlled trajectories of (3) with $\mathcal{C}(\theta, \dot{\theta}, t) = 0$, for Ψ_d fixed is obtained as

$$\dot{V} = \frac{2}{a}d\Theta\dot{\theta} + \dot{\theta}(U - k_d\dot{\theta}) \quad (8)$$

A control law for U is designed as

$$U = -\frac{1}{\alpha} \frac{\sin(a\theta)}{\sqrt{2(1 + \cos(a\theta))}} \quad (9)$$

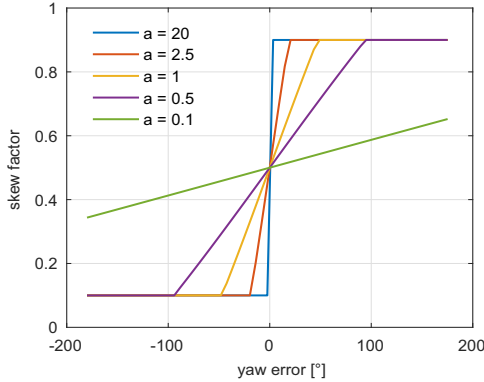


Fig. 4. **Skew factor τ vs. heading error:** The choice of the tightness factor a determines the error bandwidth for which the derived controller operates between the two maximum skew factors of 0.9 and 0.1. A bigger tightness factor leads to an increased tracking rate, but also to a higher risk of overshoot. For very high tightness factors the controller approximates a bang bang control.

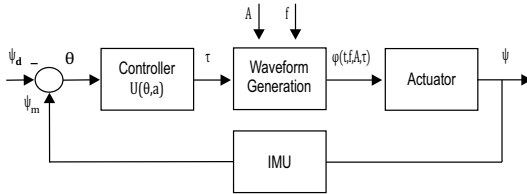


Fig. 5. **The proposed control scheme:** The shown parameters are: ψ - yaw, ψ_m - measured yaw, ψ_d - desired yaw, θ - heading error ($\psi - \psi_d$), τ - skew factor, φ^* - motor input, A - actuation amplitude and f - actuation frequency

The dynamics of V with the above control law is now obtained as

$$\dot{V} = -k_d \dot{\theta}^2 \quad (10)$$

We now use the *LaSalle* theorem [40] in the region $a\theta \neq \pm\pi$ to conclude that Θ asymptotically vanishes. The control law for the skew factor τ is now designed after substituting (9) in (4) after taking into account saturation effects as the skew factor is limited within the region $(\tau_{max}, \tau_{min}) = (0.9, 0.1)$. We set:

$$\tau = \begin{cases} 0.4 * \text{sign}(\theta) + 0.5 & |a\theta| \geq \pi/4 \\ \frac{\sin(a\theta)}{\sqrt{2(1 + \cos(a\theta))}} + 0.5 & |a\theta| < \pi/4 \end{cases} \quad (11)$$

Note that the above PD control law differs from the standard one considered in [38], in order to avoid sluggish tracking when $a\theta$ is close to $\pm\pi$. Increasing the tightness factor a increases the tracking rate (Fig. 4), at the cost of an overshoot after reaching the desired orientation. Fig. 5 shows the complete orientation control scheme.

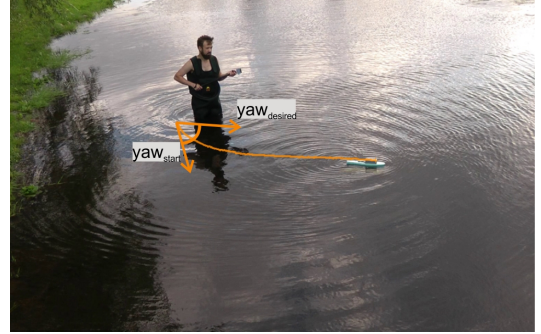


Fig. 6. **Field trials:** The FILOSE robot was manually turned towards its initial orientation (yaw_{start}) and then released to reach its desired orientation ($yaw_{desired}$). A trial was finished when the orientation error settled within a 2% error band or when the robot approach the edges of the pond.

IV. EXPERIMENTAL SETUP

To validate the proposed asymmetric motor input and nonlinear controller a series of experiments were conducted. After initial tests in a small laboratory tank a sufficiently large pond was chosen as a test site to evaluate the robustness of the control scheme under field conditions (Fig. 6). Due to interference between motor and magnetometer, the orientation sensor was operated in "IMU mode", which uses only accelerometer and gyroscope. To account for sensor drift, the desired yaw was redefined for each trial and the starting orientation was chosen such that the initial error was comparable across trials. The setpoint for the controller was defined around 110° away from the starting orientation. The robot was manually kept at the starting position and released upon the start of the actuation. The trials were stopped when the orientation error had settled within the 2% bound or the robot ran out of space for movement. The frequency of the tail actuation was held constant at 2 Hz and the actuation amplitude was set to $A = 30^\circ$. This experimental setup allowed to study the effectiveness of the controller and to determine its step response for different tightness factors. We use the standard metrics of rise time (10%), overshoot and settling time (2%) to quantify the controller performance. Due to time and resource constraints only a limited number of trials was feasible. Ten trials were conducted for a tightness factor of $a = 20$ and four trials for $a = 5$. Where possible we provide the means and standard deviations of the metrics introduced above.

V. RESULTS AND DISCUSSION

A distinct oscillation is superimposed on the general trend of the yaw signal in all trials. This oscillation is caused by the recoil of the anterior part of the robot due to the tail motion. The yaw is subsequently time averaged over one tail beat cycle to smooth the output signal. The default orientation control based on an offset fails to approach the desired yaw setpoint in a reasonable amount of time (Fig. 7a). The trial with an offset $\varphi_0 = 10^\circ$ had to be aborted after 19s

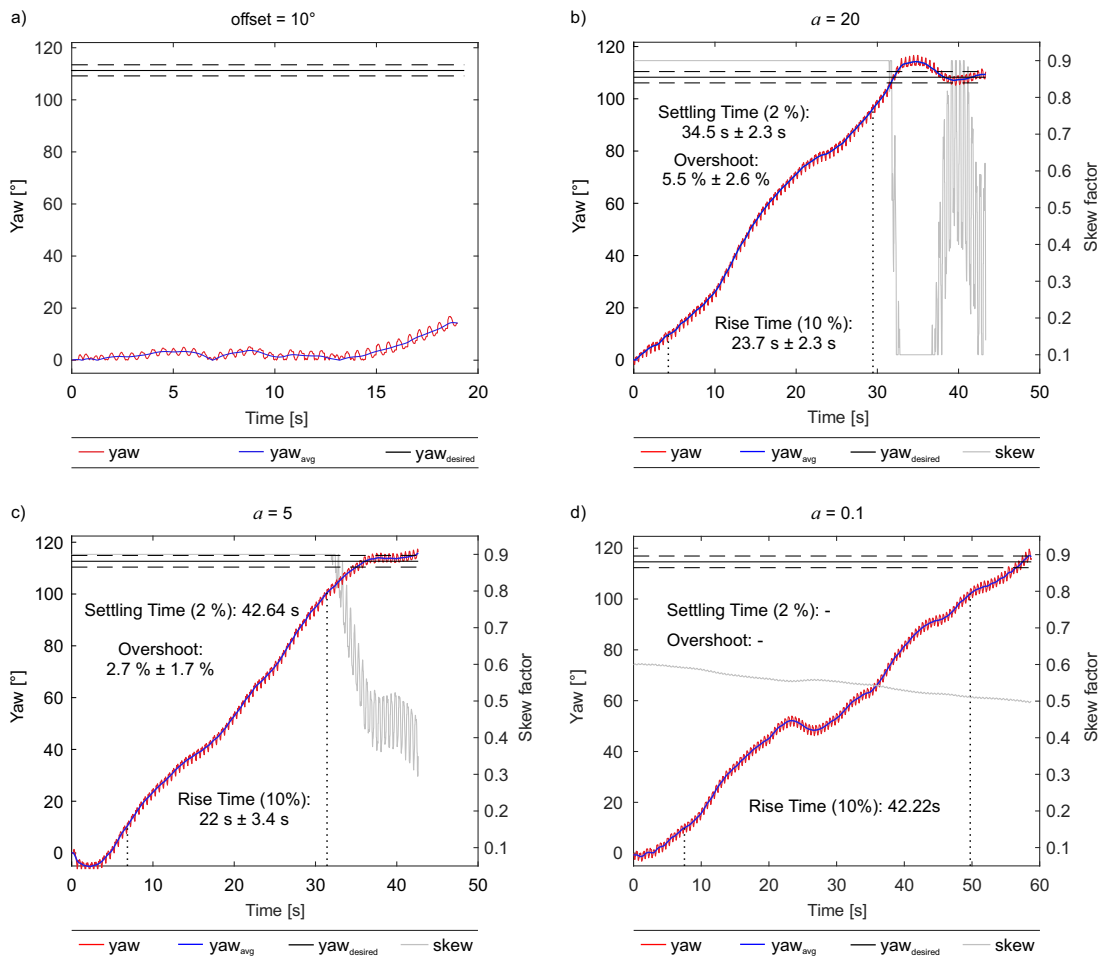


Fig. 7. **Results of the field trials:** Shown are the time series of instantaneous (red) and averaged over one tail beat cycle (blue), yaw angle during field tests for different parameter settings. For figures b) - d) the time series of the skew factor (grey) is shown to visualize the control action. In a) the default orientation control with an oscillation offset of $\varphi_0 = 10^\circ$ was used. In b) - d) the novel orientation control was applied with tightening factors of $a = 20, 5, 0.1$ respectively. The controller performance is characterized by the rise time from 10% to 90% of the desired yaw, the overshoot in % of the desired yaw and the settling time where the actual yaw stays within a 2% error band of the desired yaw.

because the robot was approaching the edge of the pond. This result supports our assumption that the offset based control is not effective for the FILOSE robot in the absence of significant flow. In contrast to that, with our proposed control scheme, the robot could reach the setpoint in all tested configurations (Fig. 7b-d). While the setpoint was always reached, the results clearly show the dependency of the controller performance on the tightness factor. For $a = 20$ the desired setpoint is reached with a mean overshoot of $5.5\% \pm 2.6\%$ (Fig. 7b). The time series of the skew factor illustrates the control action during the experiment. For a tightness factor of twenty the controller approaches a bang-bang control which is reflected in the overshoot. With a smaller tightness factor the approach towards the setpoint

was expected to be less steep, reducing the amount of overshoot. This is illustrated in Fig. 7c showing the controller performance for $a = 5$. For a heading error smaller than 15° , the skew factor decreases from its maximum at 0.9 towards 0.5. This causes the turning rate of the robot to decrease, which results in a smoother approach towards the setpoint with very little overshoot. However, this achieved at the expense of a larger settling time, because for $a = 5$ the skew factor and subsequently the turning rate are small when the heading approaches the setpoint. Furthermore, a bigger steady state error is present which in several cases kept the orientation error outside of the 2% error bound. We therefore, do not show any summarized values for settling time with this parameter setting. A further decrease of the

tightness factor causes the controller to deviate earlier from the maximum skew which results in a slower turning motion. Fig. 7d shows the extreme case for a skew factor of 0.1. Here the controller has a very narrow operational range between a skew factor of 0.6 and 0.5, which causes a significantly slower turning motion. This is reflected by a much higher rise time and the absence of any stabilization of the yaw around the setpoint. Furthermore, the controller was more susceptible to disturbances because the heading error increases again after 24 s, possibly due to local currents in the pond or wind induced disturbances acting on the float. However, the robot was able to recover and continued to turn towards the setpoint. Environmental influences also seem to be reflected in the controller performances for larger gain factors (Fig. 7b and c), because the turning rates are varying for constant skew factors. The results suggest that the controller is robust against such influences. Another limiting factor for the turning rate was the necessary attachment of the FILOSE robot to a float. Its NACA profile reduces drag in surge direction but produces a large drag in lateral direction which opposes the turning motion. It can be thus expected that the control performance would be improved on a free swimming robot.

VI. CONCLUSION AND FUTURE WORK

In this paper we present a novel approach to control turning manoeuvres specifically suited, but not limited to, compliant fish-like robots with tight constraints on tail bending. We modulated the velocity of single tail beats during a tail beat cycle by replacing the conventional sinusoidal motor input with skewed triangle waves. We control the steepness of the skew with a single parameter, which we define as skew factor. We further introduced a nonlinear PD controller to adjust the skew factor based on information from an orientation sensor. The controller showed convergence towards the setpoint and robustness against disturbances in field conditions. The results suggest that a gain factor of around five provides a good controller performance with very little overshoot and an acceptable rise time. The control scheme is generic and can be applied to any fish-like robot using BCF locomotion mechanism. With this new control approach we enable the FILOSE robot to conduct reliable and steady turns in conditions without flow. Additionally, the authors see this work as a starting point to establish an asymmetric velocity profile of tail beats as an additional and complementary tool to existing turning manoeuvres. Future work will focus on improving the proposed turning controller by optimizing the waveforms used as motor input. The optimization should be driven by an in-depth analysis of the fluid-body interactions causing the turning moment, specifically taking into account recent findings which suggest an increased importance of local hydrodynamic drag for undulations [41]. Another optimization could be the combination of sinusoidal inputs for straight swimming with asymmetric inputs for turning. Additionally, the presented controller could be part of a path following or trajectory tracking controller for the FILOSE robot.

ACKNOWLEDGEMENTS

The authors would like to thank Juan Francisco Fuentes-Perez for his help during field tests and Jaan Rebane for invaluable assistance with the hardware of the robot. This work was supported in parts by the Estonian Centre of Excellence in ICT Research project EXCITE (No. TAR16013) and the Estonian Research Council grant (No. IUT-339)

REFERENCES

- [1] D. Scaradozzi, G. Palmieri, D. Costa, and A. Pinelli, "BCF swimming locomotion for autonomous underwater robots: a review and a novel solution to improve control and efficiency," *Ocean Engineering*, vol. 130, pp. 437–453, 2017.
- [2] G. V. Lauder and P. G. Madsen, "Fish locomotion: Kinematics and hydrodynamics of flexible foil-like fins," *Experiments in Fluids*, vol. 43, no. 5, pp. 641–653, 2007.
- [3] S. Marras and M. Porfiri, "Fish and robots swimming together: attraction towards the robot demands biomimetic locomotion," *Journal of The Royal Society Interface*, vol. 9, no. 73, pp. 1856–1868, 2012.
- [4] M. Kruusmaa, G. Rieucan, J. C. C. Montoya, R. Markna, and N. O. Handegard, "Collective responses of a large mackerel school depend on the size and speed of a robotic fish but not on tail motion," *Bioinspiration and Biomimetics*, vol. 11, no. 5, p. 056020, oct 2016.
- [5] R. K. Katzschmann, J. DelPreto, R. MacCurdy, and D. Rus, "Exploration of underwater life with an acoustically controlled soft robotic fish," *Science Robotics*, vol. 3, no. 16, p. eaar3449, mar 2018.
- [6] M. S. Triantafyllou and G. G. Triantafyllou, "An efficient swimming machine," *Scientific American*, vol. 272, no. 3, pp. 64–71, 1995.
- [7] R. J. Mason and J. W. Burdick, "Construction and Modelling of a Carangiform Robotic Fish," in *Experimental Robotics VI*. London: Springer London, 2000, pp. 235–242.
- [8] X. Tan, D. Kim, N. Usher, D. Laboy, J. Jackson, A. Kapetanovic, J. Rapai, B. Sabadus, and X. Zhou, "An autonomous robotic fish for mobile sensing," in *IEEE International Conference on Intelligent Robots and Systems*. IEEE, oct 2006, pp. 5424–5429.
- [9] V. Kopman and M. Porfiri, "Design, modeling, and characterization of a miniature robotic-fish for research and education in biomimetics and bioinspiration," *IEEE/ASME Transactions on Mechatronics*, vol. 18, no. 2, pp. 471–483, 2012.
- [10] J. Yu, C. Zhang, and L. Liu, "Design and control of a single-motor-actuated robotic fish capable of fast swimming and maneuverability," *IEEE/ASME Transactions on Mechatronics*, vol. 21, no. 3, pp. 1711–1719, 2016.
- [11] J. E. Colgate and K. M. Lynch, "Mechanics and control of swimming: A review," *IEEE Journal of Oceanic Engineering*, vol. 29, no. 3, pp. 660–673, 2004.
- [12] J. Yu, M. Tan, S. Wang, and E. Chen, "Development of a biomimetic robotic fish and its control algorithm," *IEEE Transactions on Systems, Man, and Cybernetics, Part B: Cybernetics*, vol. 34, no. 4, pp. 1798–1810, 2004.
- [13] J. Liu and H. Hu, "Biological Inspiration: From Carangiform Fish to Multi-Joint Robotic Fish," *Journal of Bionic Engineering*, vol. 7, no. 1, pp. 35–48, 2010.
- [14] R. J. Clapham and H. Hu, "ISplash-I: High performance swimming motion of a carangiform robotic fish with full-body coordination," in *Proceedings - IEEE International Conference on Robotics and Automation*. IEEE, may 2014, pp. 322–327.
- [15] L. Li, C. Wang, and G. Xie, "Modeling of a carangiform-like robotic fish for both forward and backward swimming: Based on the fixed point," in *Proceedings - IEEE International Conference on Robotics and Automation*. IEEE, may 2014, pp. 800–805.
- [16] P. Valdivia y Alvarado, "Design of biomimetic compliant devices for locomotion in liquid environments," Ph.D. dissertation, Massachusetts Institute of Technology, 2007.
- [17] B. P. Epps, P. Valdivia Y Alvarado, K. Youcef-Toumi, and A. H. Tchet, "Swimming performance of a biomimetic compliant fish-like robot," *Experiments in Fluids*, vol. 47, no. 6, pp. 927–939, 2009.
- [18] C. Fiazza, T. Salumäe, M. Listak, G. Kulikovskis, R. Templeton, O. Akanyeti, W. Megill, P. Fiorini, and M. Kruusmaa, "Biomimetic mechanical design for soft-bodied underwater vehicles," in *OCEANS 2010 IEEE - Sydney*. Sydney, NSW: IEEE, 2010, pp. 1–7.

- [19] R. K. Katzschmann, A. D. Marchese, and D. Rus, "Hydraulic Autonomous Soft Robotic Fish for 3D Swimming," in *Experimental Robotics*. Springer International Publishing, 2016, pp. 405–420.
- [20] M. S. Triantafyllou, G. S. Triantafyllou, and D. K. P. Yue, "Hydrodynamics of Fishlike Swimming," *Annual Review of Fluid Mechanics*, vol. 32, no. 1, pp. 33–53, jan 2000.
- [21] M. Kruusmaa, P. Fiorini, W. Megill, M. De Vittorio, O. Akanyeti, F. Visentin, L. Chambers, H. El Daou, M. C. Fiazza, J. Jezov, M. Listak, L. Rossi, T. Salumae, G. Toming, R. Venturelli, D. S. Jung, J. Brown, F. Rizzi, A. Qualtieri, J. L. Maud, and A. Liszewski, "FILOSE for svenning: A flow sensing bioinspired robot," *IEEE Robotics and Automation Magazine*, vol. 21, no. 3, pp. 51–62, 2014.
- [22] J. Ježov, O. Akanyeti, L. D. Chambers, and M. Kruusmaa, "Sensing oscillations in unsteady flow for better robotic swimming efficiency," in *2012 IEEE International Conference on Systems, Man and Cybernetics (SMC)*. Seoul: IEEE, 2012, pp. 91–96.
- [23] D. Weihs, "A Hydrodynamical Analysis of Fish Turning Manoeuvres," *Proceedings of the Royal Society B: Biological Sciences*, vol. 182, no. 1066, pp. 59–72, jul 1972.
- [24] G. Wu, Y. Yang, and L. Zeng, "Routine turning maneuvers of koi carp *Cyprinus carpio* koi: effects of turning rate on kinematics and hydrodynamics." *The Journal of experimental biology*, vol. 210, no. Pt 24, pp. 4379–89, dec 2007. [Online]. Available: <http://www.ncbi.nlm.nih.gov/pubmed/18055627>
- [25] J. M. Anderson and N. K. Chhabra, "Maneuvering and stability performance of a robotic tuna." *Integrative and comparative biology*, vol. 42, no. 1, pp. 118–126, 2002.
- [26] C. Rossi, W. Coral, J. Colorado, and A. Barrientos, "A motor-less and gear-less bio-mimetic robotic fish design," in *Proceedings - IEEE International Conference on Robotics and Automation*. IEEE, may 2011, pp. 3646–3651.
- [27] A. D. Marchese, C. D. Onal, and D. Rus, "Autonomous Soft Robotic Fish Capable of Escape Maneuvers Using Fluidic Elastomer Actuators," *Soft Robotics*, vol. 1, no. 1, pp. 75–87, mar 2014.
- [28] K. Hirata, T. Takimoto, and K. Tamura, "STUDY ON TURNING PERFORMANCE OF A FISH ROBOT," in *First International Symposium on Aqua Bio-Mechanisms*, 2000, pp. 287–292.
- [29] J. Yu, M. Wang, M. Tan, and Y. F. Li, "Step function based turning maneuvers in biomimetic robotic fish," in *Proceedings - IEEE International Conference on Robotics and Automation*. IEEE, may 2009, pp. 3431–3436.
- [30] Q. Hu, D. R. Hedgepeth, L. Xu, and X. Tan, "A framework for modeling steady turning of robotic fish," in *Proceedings - IEEE International Conference on Robotics and Automation*. IEEE, may 2009, pp. 2669–2674.
- [31] X. Tan, M. Carpenter, J. Thon, and F. Alequin-Ramos, "Analytical modeling and experimental studies of robotic fish turning," in *2010 IEEE International Conference on Robotics and Automation*. IEEE, may 2010, pp. 102–108.
- [32] T. Salumäe, I. Rañó, O. Akanyeti, and M. Kruusmaa, "Against the flow: A Braitenberg controller for a fish robot," in *2012 IEEE International Conference on Robotics and Automation (ICRA)*. Saint Paul, MN: IEEE, 2012, pp. 4210–4215.
- [33] D. S. Jung, P. P. Pott, T. Salumae, and M. Kruusmaa, "Flow-aided path following of an underwater robot," in *Proceedings - IEEE International Conference on Robotics and Automation*, 2013, pp. 4602–4607.
- [34] T. Salumäe and M. Kruusmaa, "Flow-relative control of an underwater robot," *Proceedings of the Royal Society A: Mathematical, Physical and Engineering Science*, vol. 469, no. 2153, p. 20120671, 2013.
- [35] J. Gray, "Directional Control of Fish Movement," *Proceedings of the Royal Society B: Biological Sciences*, vol. 113, no. 781, pp. 115–125, jun 1933.
- [36] P. W. Webb and A. G. Fairchild, "Performance and maneuverability of three species of teleostean fishes," *Canadian Journal of Zoology*, vol. 79, no. 10, pp. 1866–1877, oct 2001.
- [37] T. I. Fossen, *Nonlinear modelling and control of underwater vehicles*. Fakultet for informasjonsteknologi, matematikk og elektroteknikk, 1991.
- [38] F. Bullo and A. D. Lewis, *Geometric control of mechanical systems: modeling, analysis, and design for simple mechanical control systems*. Springer Science & Business Media, 2004, vol. 49.
- [39] A. Simha, S. Vadgama, and S. Raha, "Almost-global exponential tracking of a variable pitch quadrotor on se (3)," *IFAC-PapersOnLine*, vol. 50, no. 1, pp. 10268–10273, 2017.
- [40] M. Krstic, I. Kanellakopoulos, P. V. Kokotovic *et al.*, *Nonlinear and adaptive control design*. Wiley New York, 1995, vol. 222.
- [41] R. Godoy-Diana and B. Thiria, "On the diverse roles of fluid dynamic drag in animal swimming and flying," *Journal of the Royal Society Interface*, vol. 15, no. 139, p. 20170715, feb 2018.

Appendix 6 - Publication 4

IV

A. Kaldmäe, Ü. Kotta, C. Meurer, and A. Simha, "Event-based control for differentially flat systems: Application to autonomous underwater vehicle," in IFAC-PapersOnLine, vol. 52, pp. 180–185, Elsevier B.V., sep 2019

Event-Based Control for Differentially Flat Systems: Application to Autonomous Underwater Vehicle[★]

Arvo Kaldmäe^{*} Ülle Kotta^{*} Christian Meurer^{**}
Ashutosh Simha^{*}

^{*} Department of Software Science, Tallinn University of Technology,
Akadeemia tee 21, 12618 Tallinn, Estonia (e-mail:
{arvo,kotta}@cc.ioc.ee;ashutosh.simha@taltech.ee).

^{**} Department of Computer Systems, Tallinn University of Technology,
Akadeemia tee 15a, 12618 Tallinn, Estonia (e-mail:
christian.meurer@taltech.ee)

Abstract: The problem of trajectory tracking for nonlinear differentially flat systems is addressed in the paper. A novel event-based control methodology is developed for systems depending on unmeasurable disturbances. A standard flatness-based feedforward control is applied when the flat outputs are close to their desired values. If the error becomes too large, the feedforward controller parameters are updated based on the measurements of the flat outputs and on the estimates of their time-derivatives. The developed control strategy is applied to an autonomous underwater vehicle. Simulations show that the vehicle tracks the pre-defined reference trajectory both in healthy situation as well as in the case of certain mechanical faults.

© 2019, IFAC (International Federation of Automatic Control) Hosting by Elsevier Ltd. All rights reserved.

Keywords: Feedforward control, events, fault tolerance, robotics.

1. INTRODUCTION

Flatness property provides a natural way of controlling dynamical systems, since a feedforward controller can be easily constructed based on the reference trajectory of the flat output. However, in general, one must assume that the system does not depend on unknown inputs (disturbances) and is described by an exact model. These are very restrictive assumptions for practical applications. Most papers (see, for example, Chung et al. (2007); Al-louache et al. (2011); Menhour et al. (2014); Bröcker and Herrmann (2017)) combine the feedforward controller with other approaches, such as PID control or pole placement, to guarantee stability or tracking. In this paper a different, novel approach is described for flatness-based control.

Event-based control is a control method that closes the feedback loop only if an event indicates that it is necessary (see Lunze (2015) for an introduction and survey). This event can be, for example, that the output trajectory deviates from the desired trajectory too much. The main advantages of the event-based control are irregular sampling and reduced communication between system components, which can save energy. The event-triggered approach has received increased research interest due to rapid development of network and communication technology. The basic configuration of event-based control consists of the event generator, the controller and the control input generator. The event generator continuously compares the current system behavior and the desired behavior and generates

events, when the differences become too large. The controller determines the control input at the event times, based on the information sent to it at these times. The control input generator (usually it is a simple zero-order hold) uses the values of the control input received from the controller to generate continuous-time input for the plant until the next event appears.

In this paper a new approach for flatness-based control is developed following the ideas of the event-based control. More precisely, the flatness-based feedforward controller works as the controller and the control input generator in the event-based control setting. The feedforward controller is designed such that system output, which is also assumed to be the flat output, converges to its desired reference trajectory. However, unmodelled dynamics and external disturbances affect the system. An event generator detects when the actual output value is too far from the desired one. At that time instance the measurements of the system outputs and the estimates of their time-derivatives are used to redefine the feedforward controller parameters. As the developed control approach is an event-based strategy, it has all the benefits of an event-based control approach compared to traditional methods. However, unlike standard event-based approaches, here a feedforward control instead of zero-order hold is applied between the events. Then, at event times the feedforward control is updated according to the measurements and estimates of the state variables.

The proposed control strategy is tested on a bioinspired autonomous underwater vehicle, called U-CAT (Salumäe et al. (2014)). The vehicle was developed to assist in the

[★] The work of A. Kaldmäe and C. Meurer was supported by the Estonian Center of Excellence in IT (EXCITE), funded by the European Regional Development Fund.

exploration of archaeological sites, see Allotta et al. (2015). Due to the low cost of U-CAT it is specifically suited for high risk explorations in shipwrecks or other confined areas such as caves or submerged buildings. Four fin actuation configuration of U-CAT (see Fig. 1 and 2) enables it to translate along and rotate around all of its principle axes. Various schemes have been proposed to control depth and yaw of the vehicle, see Salumäe et al. (2017) and Preston et al. (2018). The latter showed the capability of U-CAT to autonomously move in confined spaces. An area of control which has not been explored so far is fault tolerance control, which is especially significant considering the envisioned high risk applications of the vehicle. Due to its 4-fin configuration U-CAT exhibits redundancies in actuation which can be explored for fault tolerant control. Accurate state estimation is one of the major difficulties of underwater robotics and necessitates control schemes which are robust against measurement noise. An event based control scheme provides the opportunity for longer sampling periods and thus could mitigate some of the difficulties in state estimation. Underwater vehicles are further subjected to dynamic disturbances which can not be modelled accurately, such as ocean currents or eddies. Furthermore, often the identification of parameters for the model can not be done analytically and relies on experiments, which introduce some uncertainty. A controller which is robust against disturbances and model parameter uncertainties would thus be beneficial. A situation where two of the four fins fail to operate is simulated. Since both the fault free and the faulty models are flat one is able to test the proposed control scheme on these models. Simulations show that the U-CAT tracks the predefined trajectory and that the controller is robust against disturbances and unmodelled forces.

2. EVENT-BASED CONTROL

Consider a nonlinear control system of the general form

$$\dot{x} = f(x, u), \quad (1)$$

where $x(t) \in X \subseteq \mathbb{R}^n$ is the system state and $u(t) \in U \subseteq \mathbb{R}^m$ is the system input. It is assumed that the function f is analytic and satisfies on some open and dense subset of $X \times U$ the condition $\text{rank}[\partial f / \partial u] = m$.

The most common way of defining flatness property of system (1) is the following.

Definition 1. System (1) is said to be flat if there exists an output function

$$y = h(x, u, \dots, u^{(l)}) \quad l \geq 0 \quad (2)$$

($y \in \mathbb{R}^m$), called flat output, such that

$$x = \varphi_x(y, \dots, y^{(k)}) \quad (3)$$

$$u = \varphi_u(y, \dots, y^{(k+1)}) \quad (4)$$

for some $k \in \mathbb{N}$ and functions φ_x, φ_u .

A more formal definition of flatness and more thorough discussion can be found, for example, from Fliess et al. (1995, 1999); Lévine (2009). The flat output is not unique and one can always find infinitely many flat outputs for any flat system. Note that under the assumption $\text{rank}[\partial f / \partial u] = m$ the dimension of the flat output is equal to $m = \dim u$. Finding a flat output is, in general, a

very difficult problem (see Aranda-Bricaire et al. (1995); Chetverikov (2001); Lévine (2009, 2011); Schlacher and Schöberl (2013); Schöberl and Schlacher (2014)), though, often it has a practical meaning and can be guessed from the configuration of the physical object. For example, in robotics, often the position of some moving part is the flat output.

First we describe how to track a predefined trajectory for a flat system (1). An *event-based* controller is defined such that the system output trajectory follows the reference trajectory. We make the following assumption.

Assumption 1. The elements of controlled output of system (1) are also the elements of flat output of system (1).

Though the assumption seems to be rather restrictive, in many practical examples it is satisfied, see Sira-Ramirez and Agrawal (2004); Lévine (2009) and references therein. Also, Assumption 1 is, in general, not necessary, but helps to simplify the controller design. If it is not satisfied, then one has to find the reference trajectory of the flat output y from the relation (2), based on the reference trajectories of the system states and inputs. In other words, one has to guarantee that if the flat output converges to its reference trajectory, then the controlled output of the system also converges to its reference trajectory.

Let $y = (y_1, \dots, y_m)^T$ be the flat output of system (1) for which we want to construct a tracking controller. We choose a trajectory for every $y_i(t)$ such that it converges to the reference trajectory $r_i(t)$ of $y_i(t)$, and substitute them for y in (4) to define a feedforward controller. Define, for $i = 1, \dots, m$,

$$y_{ir}(t) = p_i(t)e^{-K_i t} + r_i(t), \quad (5)$$

where $r_i(t)$ is the trajectory we want the variable y_i to follow, $K_i > 0$ is a constant parameter and $p_i(t) \in \mathbb{R}[t]$ is a polynomial in t , which is chosen such that the initial state and input satisfy the relations (3) and (4), i.e.,

$$\begin{aligned} x(0) &= \varphi_x(y_r(0), \dots, y_r^{(k)}(0)) \\ u(0) &= \varphi_u(y_r(0), \dots, y_r^{(k+1)}(0)), \end{aligned} \quad (6)$$

where $y_r = (y_{1r}, \dots, y_{mr})^T$. Thus, the coefficients of the polynomials $p_i(t)$ depend on the initial conditions of x and u . The degree ρ_i of the polynomial $p_i(t)$ is equal to the highest time-derivative of y_i which appears in the relations (3) and (4). Moreover, the desired trajectories $r_i(t)$ have to be $k+1$ times differentiable, so that one could find the time-derivatives of (5) up to the order $k+1$.

Note that usually one takes simply $y_{ir}(t) = r_i(t)$ in (5). However, first, in this case the reference trajectory $r_i(t)$ must satisfy $r_i(0) = y_i(0)$, which means that the trajectory planning becomes much more difficult. Second, choosing $y_{ir}(t)$ as in (5) allows us to easily define the event-based control strategy without solving the trajectory planning problem whenever an event happens.

The coefficients of the polynomials $p_i(t)$, $i = 1, \dots, m$, in (5) can be calculated as follows. The time-derivatives of y_{ir} in (5) are

$$y_{ir}^{(j)}(t) = \sum_{\mu=0}^j \binom{j}{\mu} (-K_i)^\mu p_i^{(j-\mu)}(t) e^{-K_i t} + r_i^{(j)}(t) \quad (7)$$

for $j \geq 0$. Assuming that $p_i(t) = \sum_{\lambda=0}^{\rho_i} p_{i,\lambda} t^\lambda$ one has $p_i^{(j)}(0) = j! p_{i,j}$. By substituting $y_{ir}^{(j)}$ from (7) to (3) and (4) for $y_i^{(j)}$ one gets

$$\begin{aligned} p_{i,0} &= e_i(0) \\ p_{i,j} &= \frac{e_i^{(j)}(0)}{j!} - \sum_{\mu=1}^j \binom{j}{\mu} (-K_i)^\mu \frac{(j-\mu)!}{j!} p_{i,j-\mu}, \quad j > 0 \end{aligned} \quad (8)$$

where $e_i(0) = y_i(0) - r_i(0)$. Then the coefficients $p_{i,j}$, $j = 0, \dots, \rho_i$, can be computed by solving the equations (8). Note that the coefficients will depend on the initial conditions of the error e_i and its time-derivatives. These can be computed, for example, from the initial conditions of system states and inputs.

By substituting y_{ir} in (5) and its time-derivatives to (4) for y_i and its derivatives, one gets a feedforward controller, which, by the definition of flatness, yields the trajectories (5) for the elements of flat output y , which we want to control. Note that the polynomials $p_i(t)$ are chosen such that the trajectories (5) pass the initial conditions.

Lemma 2. The error $\bar{e}_i(t) = y_{ir}(t) - r_i(t)$, $i = 1, \dots, m$, satisfies $\lim_{t \rightarrow \infty} \bar{e}_i(t) = 0$.

Proof. Since the proof is valid for every $i = 1, \dots, m$, we leave out the indices i everywhere. Let $p(t) = \sum_{j=0}^{\rho} p_j t^j$. Then from (5) one gets

$$\bar{e}(t) = \sum_{j=0}^{\rho} p_j t^j e^{-Kt}. \quad (9)$$

After using the L'Hospital's rule repetitively, one gets for any $j \geq 0$

$$\begin{aligned} \lim_{t \rightarrow \infty} (p_j t^j e^{-Kt}) &= \lim_{t \rightarrow \infty} \frac{p_j t^j}{e^{Kt}} = \lim_{t \rightarrow \infty} \frac{p_j j t^{j-1}}{K e^{Kt}} = \dots \\ &= \lim_{t \rightarrow \infty} \frac{p_j j!}{K^j e^{Kt}} = 0. \end{aligned}$$

Thus, $\lim_{t \rightarrow \infty} \bar{e}(t) = 0$. \square

Lemma 2 says that the feedforward controller

$$u = \varphi_u(y_r, \dots, y_r^{(k+1)}), \quad (10)$$

ensures that the output trajectories converge to the desired trajectories $r_i(t)$ as $t \rightarrow \infty$. Larger $K_i > 0$ results in faster convergence.

Remark 3. In principle, instead of constants K_i in (5) the time-functions $K_i(t)$ can be taken, that satisfy the condition $K_i(t) > 0$ for $t \in (0, \infty)$.

So far, the constructed feedforward controller (10) assumes that the system model (1) is exact and there are no external disturbances. When the disturbances affect the system, i.e., when instead of (1) we have

$$\dot{x} = f(x, u, w), \quad (11)$$

where $w(t) \in W \subseteq \mathbb{R}^\sigma$ is the (unmeasurable) disturbance, then the computed control (10) will not yield exactly the desired trajectory y_r , since the relation (4) is not exact anymore. Instead, when applied to system (11), the real trajectory of y_i starts to deviate from the desired trajectory y_{ir} . To compensate this error, we introduce a feedback loop, based on the ideas of event-based control. First, we apply the feedforward control (10) as if there

are no external or internal disturbances. Since the system (11) is actually affected by the disturbances, there will be a non-zero error between $y_i(t)$ and $y_{ir}(t)$. Assume that at the time instant t_1 the error between the measured output and the one in (5) exceeds a pre-defined threshold ϵ . Then this time instant is set to be a new initial time instant and the coefficients of polynomials $p_i(t)$ in (5) are *recomputed* based on the actual measurements of the system outputs, estimations of their time-derivatives and inputs at time instant t_1 . Also the reference trajectories have to be redefined, since they are now shifted, i.e., a new reference trajectory is $\tilde{r}_i(t) = r_i(t_1 + t)$. By doing so, at the time instant t_1 we define a new trajectory (5) for the output y_i , which will converge to the desired trajectory \tilde{r}_i . To conclude, at the time instant t_1 the *error* between the measured output and the desired trajectory (5) *is set to zero again*. The idea of the method can be summarized in the following algorithm:

0. Specify the threshold value ϵ and parameters K_i , $i = 1, \dots, m$.
1. Compute y_{ir} , $i = 1, \dots, m$, from (5).
2. Compute the feedforward control (10).
3. At all time, monitor the error $\hat{e}_i(t) := y_i(t) - y_{ir}(t)$. If at the time instant t_1 the error $|\hat{e}_i(t_1)| > \epsilon$, at least for one i , then follow the steps:
 - a. Set the new reference trajectory as $\tilde{r}_i(t) := r_i(t + t_1)$.
 - b. Recompute the coefficients of polynomials $p_i(t)$ in (5) such that the trajectories $y_{ir} = p_i(t)e^{-K_i t} + \tilde{r}_i(t)$ satisfy $x(t_1) = \varphi_x(y_r(0), \dots, y_r^{(k)}(0))$ and $u(t_1) = \varphi_u(y_r(0), \dots, y_r^{(k+1)}(0))$. Note that the coefficients $p_{i,j}$ of $p_i(t)$ depend on the values of the system states and inputs at the time instant t_1 . This requires that the state is measurable or, at least, can be estimated.
 - c. Let $y_{ir} = p_i(t)e^{-K_i t} + \tilde{r}_i(t)$ and go to step 2.

Remark 4. Note that the proposed method works only if the disturbances affect the system in such way that the flatness property is not lost. That is, when y is a vector of flat outputs for the nominal model, then it is also for the model with disturbances. This must be true generically.

3. U-CAT MODEL

The full six degree of freedom (6 DOF) model of U-CAT can be described by the equations (see Fossen (2011)):

$$M\dot{\nu} + C(\nu)\nu + D(\nu)\nu + g(\eta) = \tau \quad (12)$$

$$\dot{\eta} = J(\eta)\nu, \quad (13)$$

where $\eta = [x, y, z, \varphi, \theta, \psi]^T$ describes the position and orientation of the robot in the earth-fixed frame, $\nu = [u, v, w, p, q, r]^T$ represents the linear and angular velocities in the body-fixed frame, and $J(\eta) \in \mathbb{R}^{6 \times 6}$ maps the body-fixed frame to the earth fixed frame (see Fig. 1). The inertia matrix of the vehicle is denoted by M , while C and D represent Coriolis-centripetal and damping effects respectively and $g(\eta)$ is the vector of gravitational / buoyancy forces and moments. Finally, $\tau = [X, Y, Z, K, M, N]^T$ is the vector of control inputs. See Salumäe et al. (2017) for more details about the model. The development of the controller in this paper will be restricted to two dimensional movement of the vehicle with no change along the

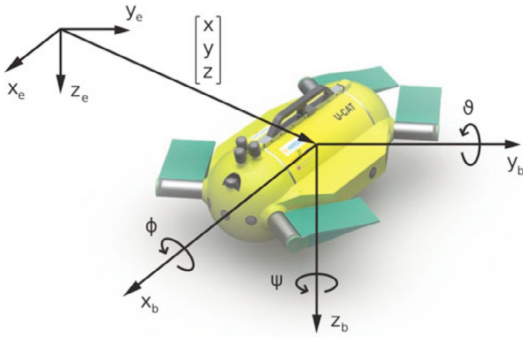


Fig. 1. Autonomous underwater vehicle U-CAT and its coordinate frames. x_b, y_b, z_b represent the position of the robot in body frame and x_e, y_e, z_e denote the earth fixed reference frame. The position vector of the vehicle is defined in the earth fixed reference frame $\eta = [x, y, z, \varphi, \theta, \psi]^T$. / figure adapted from Salumäe et al. (2017)

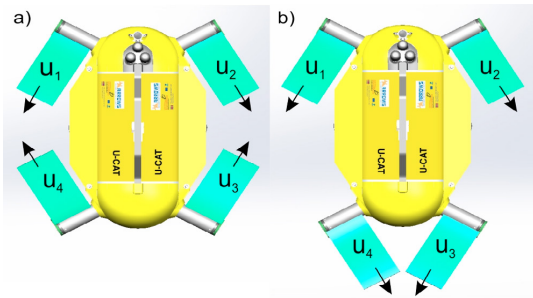


Fig. 2. Top view of U-CAT with depicting control inputs for each fin $[u_1, u_2, u_3, u_4]$. a) fin configuration for SLOW mode, b) fin configuration for FAST mode.

z axis. The rationale behind this is that the fins of U-CAT have to be oriented vertically for movement along the z -axis which essentially decouples this movement from the motions along the two other axes. Thus, the control scheme can be cascaded as well.

U-CAT has two motion modes, denoted by SLOW and FAST, which depend on the fin configuration (see Fig. 2). In SLOW mode all fins are rotated inward and fins 1 and 2 are the main contributors to the locomotion and fins 3 and 4 act as stabilizers. By reducing the states of U-CAT to $[x, u, y, v, \psi, r]^T =: [x_1, x_2, x_3, x_4, x_5, x_6]^T$ we define the state space model for SLOW mode:

$$\begin{aligned} \dot{x}_1 &= x_2 \cos(x_5) - x_4 \sin(x_5) \\ \dot{x}_2 &= -\frac{C_1}{C_2} x_4 x_6 - \frac{X_{uu}}{C_2} x_2 |x_2| + X + w_1 \\ \dot{x}_3 &= x_2 \sin(x_5) + x_4 \cos(x_5) \\ \dot{x}_4 &= -\frac{C_3}{C_4} x_2 x_6 - \frac{Y_{vv}}{C_4} x_4 |x_4| + Y + w_2 \\ \dot{x}_5 &= x_6 \\ \dot{x}_6 &= -\frac{C_5}{C_6} x_2 x_4 - \frac{N_{rr}}{C_6} x_6 |x_6| + N + w_3, \end{aligned} \quad (14)$$

where $w = [w_1, w_2, w_3]^T$ represents the unknown disturbance vector.

In FAST mode all fins face in one direction and have an equal contribution to the locomotion. A fault in fins 3 and 4 will not have a significant effect on the motion performance in SLOW mode and FAST mode would degenerate to SLOW mode in this case. The robot is thus already fault tolerant by design for this case of fault. Therefore, we concentrate on faults of fins 1 and 2. In SLOW mode the fins would have to reorient themselves in FAST mode configuration. We thus limit our control design to FAST mode configuration of U-CAT and consider the case where fins 1 and 2 are faulty. In particular, we assume that both fin 1 and fin 2 have stopped working. The model for direct FAST mode setting will be written in terms of the faulty control inputs to the third and fourth fins (u_3, u_4) instead of the generalized control inputs X, Y and N in (14) and is described by the equations:

$$\begin{aligned} \dot{x}_1 &= x_2 \cos(x_5) - x_4 \sin(x_5) \\ \dot{x}_2 &= -\frac{C_1}{C_2} x_4 x_6 - \frac{X_{uu}}{C_2} x_2 |x_2| + \alpha_1 (u_3 + u_4) + w_1 \\ \dot{x}_3 &= x_2 \sin(x_5) + x_4 \cos(x_5) \\ \dot{x}_4 &= -\frac{C_3}{C_4} x_2 x_6 - \frac{Y_{vv}}{C_4} x_4 |x_4| + w_2 \\ \dot{x}_5 &= x_6 \\ \dot{x}_6 &= -\frac{C_5}{C_6} x_2 x_4 - \frac{N_{rr}}{C_6} x_6 |x_6| + \alpha_3 (u_3 - u_4) + w_3. \end{aligned} \quad (15)$$

where α_1 is a parameter which accounts for the angle of the fins on the horizontal plane of the vehicle and α_3 is a parameter for the moment arm from the fin to the center of mass of U-CAT.

The vector of flat output of system (14) is composed of $y_1 = x_1, y_2 = x_3, y_3 = x_5$. Note that the controlled variables x_1, x_3 and x_5 are elements of the flat output, meaning that Assumption 1 is satisfied. However, the model (15) is not flat. For control purposes we make additional assumptions to simplify the equations (15) to get a flat system. First, body symmetry is assumed which leads to equal added mass terms, i.e., $-C_1 = C_2 = C_3 = C_4$ and $C_5 = 0$. Second, we assume that the drag terms in second and fourth equations of (15) are linear due to piecewise linearization at nominal velocities. This gives us simplified model equations

$$\begin{aligned} \dot{x}_1 &= x_2 \cos(x_5) - x_4 \sin(x_5) \\ \dot{x}_2 &= x_4 x_6 - L x_2 + \alpha_1 (u_3 + u_4) + w_1 \\ \dot{x}_3 &= x_2 \sin(x_5) + x_4 \cos(x_5) \\ \dot{x}_4 &= -x_2 x_6 - L x_4 + w_2 \\ \dot{x}_5 &= x_6 \\ \dot{x}_6 &= -\frac{N_{rr}}{C_6} x_6 |x_6| + \alpha_3 (u_3 - u_4) + w_3 \end{aligned} \quad (16)$$

for some constant L . Then the flat outputs of system (16) are $y_1 = x_1$ and $y_2 = x_3$.

Table 1. Values of the parameters

Parameter	Value	Parameter	Value
C_1	-40	C_2	59
C_3	59	C_4	40
C_5	-19	C_6	2.8179
X_{uu}	56	Y_{vv}	551
N_{rr}	0.7226	α_1	0.0147
α_3	-1.77437	L	0.1673

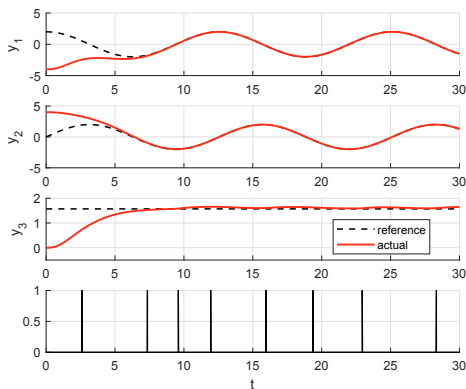


Fig. 3. Trajectories of flat outputs for $K_1 = K_2 = K_3 = 1$ and $\epsilon = 0.02$ (healthy model (14)). The bottom graph shows event times.

4. SIMULATION RESULTS

The simulation studies demonstrate the effectiveness and applicability of the proposed method. The healthy U-CAT is simulated in SLOW mode, i.e., using the model (14). For the faulty U-CAT the model (16) is used.

4.1 Healthy situation

Here we test the developed trajectory tracking strategy on a healthy U-Cat model (14). The situation, where the underwater vehicle starts from the point $(-4; 4)$ on a (x_1, x_3) -plane with $x_5 = x_2 = x_4 = x_6 = 0$ and does circles around 0 with radius 2, is simulated. At the same time, the angle x_5 will go from 0 to the new set point $\pi/2$. The parameters K_i , $i = 1, 2, 3$, are all taken equal to 1. The error threshold $\epsilon = 0.02$. All three disturbances w_i , $i = 1, 2, 3$, have randomly changing values between -1 and 1. The trajectories for the flat outputs and the event times are displayed in Fig. 3.

The simulations presented in Fig. 3 were done under the assumption that exact measurements are available. Next, measurement noise is added to describe a more realistic situation. All three outputs are assumed to have a measurement noise between -0.1 and 0.1. Note that the error threshold ϵ cannot be much smaller than the measurement noise. Otherwise continuous sampling is achieved and the system will be most probably unstable. Thus, now we take $\epsilon = 0.2$. Also, one can change the parameters to get better tracking. However, this results in higher values for the inputs. The trajectories for the flat outputs are displayed in Fig. 4 together with the event times.

4.2 Faulty situation

Next we consider a situation where the first two fins of U-CAT are not working. That is, we use the faulty U-CAT model (16) to compute the values for the control inputs. However, the model (15) is used to simulate the faulty U-CAT behavior. The system is driven from the initial starting position $x = 0$ towards a pick up point

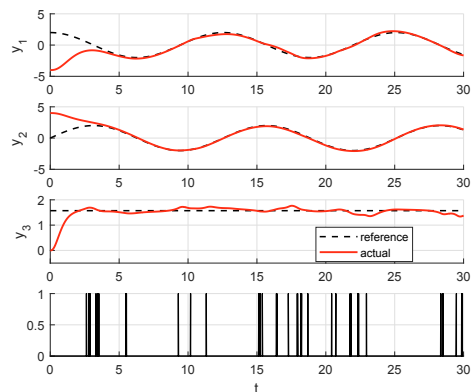


Fig. 4. Trajectories of flat outputs for $K_1 = K_2 = 1.5$, $K_3 = 3.5$ and $\epsilon = 0.2$, under the measurement noise (healthy model (14)). The bottom graph shows event times.

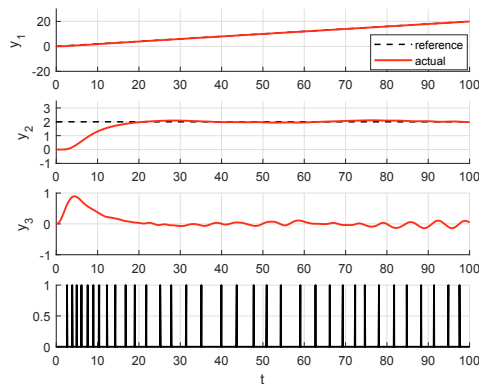


Fig. 5. Trajectories of outputs $y_1 = x_1$, $y_2 = x_3$ and $y_3 = x_5$ for $K_1 = K_2 = 0.6$ and $\epsilon = 0.02$ (faulty model (15)). The bottom graph shows event times.

with constant speed. The parameters K_i , $i = 1, 2$, are all taken equal to 0.6. The error threshold $\epsilon = 0.02$. All three disturbances w_i , $i = 1, 2, 3$, have randomly changing values between -1 and 1. The trajectories for the outputs $y_1 = x_1$, $y_2 = x_3$ and $y_3 = x_5$ are displayed in Fig. 5 together with the event times. Note that only y_1 and y_2 are the flat outputs, so we can define a reference trajectory only for these variables. Fig. 6 presents the same situation when the measurement noise is added to the simulations. As before, all three outputs are assumed to have a random measurement noise between -0.1 and 0.1. Note that despite the simplified model (16) was used for controller design, satisfactory performance of the faulty U-CAT is achieved.

5. CONCLUSION

A novel event-based control approach was presented for differentially flat systems. The idea is to apply the basic flatness-based feedforward control when the system

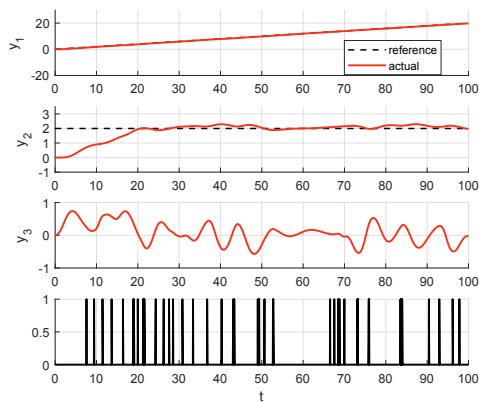


Fig. 6. Trajectories of outputs $y_1 = x_1$, $y_2 = x_3$ and $y_3 = x_5$ for $K_1 = K_2 = 0.55$ and $\epsilon = 0.2$ under the measurement noise (faulty model (15)). The bottom graph shows event times.

performance is good enough and update (based on the measurements of the outputs and the estimates of their time-derivatives) the feedforward control at event times, which indicate deviation from the desired output values. The approach was tested on simulations for an underwater vehicle U-CAT. Two cases were simulated. First, the healthy case and then the case, when two of the vehicles fins were stopped working.

The paper presents preliminary work on the subject. There is a lot of space for improvement. In particular, a formal proof of stability of the closed-loop system is missing. Many questions, for instance, how to deal with the system constraints, and whether the approach be extended to non-flat systems, need an answer. From application point of view the future goal is to test the approach experimentally on U-CAT. Also, we would like to add a fault detection scheme so that the U-CAT can be made fault tolerant against failure of some of the vehicles fins.

REFERENCES

- Allotta, B., Costanzi, R., Ridolfi, A., Colombo, C., Bellavia, F., Fanfani, M., Pazzaglia, F., Salvetti, O., Moroni, D., Pascali, M.A., Reggiannini, M., Kruusmaa, M., Salumäe, T., Frost, G., Tsiogkas, N., Lane, D.M., Cocco, M., Gualdesi, L., Roig, D., Gündogdu, H.T., Tekdemir, E.I., Dede, M.I.C., Baines, S., Agneto, F., Selvaggio, P., Tusa, S., Zangara, S., Dresen, U., Latti, P., Saar, T., and Daviddi, W. (2015). The ARROWS project: Adapting and developing robotics technologies for underwater archaeology. *IFAC-PapersOnLine*, 48(2), 194–199. doi:10.1016/j.ifacol.2015.06.032.
- Allouache, M., Lowenberg, M., and Wagg, D. (2011). Synthesis of flatness control for a multi-axis robot manipulator: an experimental approach. In *IEEE International Symposium on Robotic and Sensors Environments*, 1–6. Montreal, Canada. doi:10.1109/ROSE.2011.6058539.
- Aranda-Bricaire, E., Moog, C.H., and Pomet, J.B. (1995). A linear algebraic framework for dynamic feedback

- linearization. *IEEE Trans. on Automatic Control*, 40(1), 127–132.
- Bröcker, M. and Herrmann, L. (2017). Flatness based control and tracking control based on nonlinearity measures. *IFAC PapersOnLine*, 50(1), 8250–8255. doi:10.1016/j.ifacol.2017.08.1394.
- Chetverikov, V.N. (2001). New flatness conditions for control systems. In *Proceedings of the 5th IFAC Symposium on Nonlinear Control Systems*, 168–173. St. Petersburg, Russia.
- Chung, S.K., Koch, C.R., and Lynch, A.F. (2007). Flatness-based feedback control of an automotive solenoid valve. *IEEE Transactions on Control Systems Technology*, 15(2), 394–401. doi:10.1109/TCST.2006.886440.
- Fliess, M., Lévine, J., Martin, P., and Rouchon, P. (1995). Flatness and defect of nonlinear systems: introductory theory and examples. *Int. J. of Control*, 61(6), 1327–1361.
- Fliess, M., Lévine, J., Martin, P., and Rouchon, P. (1999). A Lie-Bäcklund approach to equivalence and flatness of nonlinear systems. *IEEE Trans. on Automatic Control*, 44(5), 922–937.
- Fossen, T.I. (2011). *Handbook of Marine Craft Hydrodynamics and Motion Control [Bookshelf]*. John Wiley & Sons. doi:10.1109/MCS.2015.2495095.
- Lévine, J. (2009). *Analysis and control of nonlinear systems: a flatness-based approach*. Springer, Berlin.
- Lévine, J. (2011). On necessary and sufficient conditions for differential flatness. *Applicable Algebra in Engineering, Communication and Computing*, 22(1), 47–90.
- Lunze, J. (2015). Event-based control: Introduction and survey. In *Event-Based Control and Signal Processing*, 3–20. CRC Press, Boca Raton.
- Menhour, L., d'Andrea Novel, B., Fliess, M., and Mounier, H. (2014). Coupled nonlinear vehicle control: flatness-based setting with algebraic estimation techniques. *Control Engineering Practice*, 22, 135–146. doi:10.1016/j.conengprac.2013.09.013.
- Preston, V., Salumäe, T., and Kruusmaa, M. (2018). Underwater confined space mapping by resource-constrained autonomous vehicle. *Journal of Field Robotics*, 35(7), 1122–1148. doi:10.1002/rob.21806.
- Salumäe, T., Chemori, A., and Kruusmaa, M. (2017). Motion Control of a Hovering Biomimetic Four-Fin Underwater Robot. *IEEE Journal of Oceanic Engineering*, 1–18. doi:10.1109/JOE.2017.2774318.
- Salumäe, T., Raag, R., Rebane, J., Ernits, A., Toming, G., Ratas, M., and Kruusmaa, M. (2014). Design principle of a biomimetic underwater robot U-CAT. In *2014 Oceans - St. John's*, 1–5. IEEE, St. John's, NL. doi:10.1109/OCEANS.2014.7003126.
- Schlacher, K. and Schöberl, M. (2013). A jet space approach to check pfaffian systems for flatness. In *Proceedings of the 52nd Conference on Decision and Control*, 2576–2581. Florence, Italy.
- Schöberl, M. and Schlacher, K. (2014). On an implicit triangular decomposition of nonlinear control systems that are 1-flat - a constructive approach. *Automatica*, 50(6), 1649–1655.
- Sira-Ramirez, H. and Agrawal, S.K. (2004). *Differentially flat systems*. CRC Press, New York.

Appendix 7 - Publication 5

V

C. Meurer, J. F. Fuentes-Perez, K. Schwarzwald, M. Ludvigsen, A. J. Sorensen, and M. Kruusmaa, "2D estimation of velocity relative to water and tidal currents based on differential pressure for autonomous underwater vehicles," IEEE Robotics and Automation Letters, vol. 5, pp. 3444–3451, apr 2020

2D Estimation of Velocity Relative to Water and Tidal Currents Based on Differential Pressure for Autonomous Underwater Vehicles

Christian Meurer ¹, Juan Francisco Fuentes-Pérez ¹, Kordula Schwarzwälder, Martin Ludvigsen ²,
Asgeir Johan Sørensen ², and Maarja Kruusmaa ¹

Abstract—Reliable navigation of autonomous underwater vehicles (AUVs) depends on the quality of their state estimation. Providing robust velocity estimation thus plays an important role. While water currents are main contributors to the navigational uncertainty of AUVs, they are also an important variable for oceanographic research. For both reasons, water current estimation is desirable during AUV operations. State of the art velocity estimation relies on expensive acoustic sensors with considerable energy requirements and a large form factor such as Doppler Velocity Logs (DVL) and Acoustic Doppler Current Profilers (ADCP), while water currents are either estimated with the same sensors, or with algorithms that require accurate position feedback. In this letter, we introduce a low-cost, lightweight and energy efficient sensor (DPSSv2) to estimate fluid relative velocity in 2D based on differential pressure. The sensor is validated in field trials on-board an AUV in the presence of tidal currents. We further show that, while moving against the currents, our device is capable of estimating tidal currents in situ with comparable accuracy to a DVL, given a source for absolute vehicle velocity. Additionally, we establish the limitations of the current design of DPSSv2 while moving with the currents.

Index Terms—Marine robotics, autonomous vehicle navigation, sensor fusion.

Manuscript received September 10, 2019; accepted February 10, 2020. Date of publication February 26, 2020; date of current version March 10, 2020. This letter was recommended for publication by Associate Editor Prof. M. Dunbabin and Prof. J. Roberts upon evaluation of the reviewers' comments. This work was supported in part by the Estonian Centre of Excellence in ICT Research Project EXCITE under Grant TAR16013, in part by the Estonian Research Council under Grant IUT-339 and in part by the Research Council of Norway through the Centres of Excellence funding scheme, Project 223254 - NTNU AMOS. (Corresponding author: Christian Meurer.)

Christian Meurer and Juan Francisco Fuentes-Pérez are with the Centre for Biorobotics, Department of Computer Systems, Tallinn University of Technology, 12616 Tallinn, Estonia (e-mail: christian.meurer@taltech.ee; juan.fuentes@ttu.ee).

Kordula Schwarzwälder is with the Department of Civil and Environmental Engineering, Norwegian University of Science and Technology, 7491 Trondheim, Norway (e-mail: kordula.v.a.schwarzwalder@ntnu.no).

Martin Ludvigsen and Asgeir Johan Sørensen are with the Centre for Autonomous Marine Operations and Systems, Norwegian University of Science and Technology, 7491 Trondheim, Norway (e-mail: martin.ludvigsen@ntnu.no; asgeir.sorensen@ntnu.no).

Maarja Kruusmaa is with the Centre for Biorobotics, Department of Computer Systems, Tallinn University of Technology 12616, Tallinn, Estonia, and also with the Centre for Autonomous Marine Operations and Systems, Norwegian University of Science and Technology, 7491 Trondheim, Norway (e-mail: maarja.kruusmaa@ttu.ee).

Digital Object Identifier 10.1109/LRA.2020.2976318

I. INTRODUCTION

VELOCITY estimation for AUVs is essential for successful underwater navigation and allows the use of such vehicles for long term autonomous missions, such as in situ monitoring and sampling in marine environments [1]–[3]. The rapid high frequency attenuation of electromagnetic signals underwater impedes the use of navigation methods such as satellite global positioning. A local positioning system can be established with acoustic devices [4], but this increases the cost and complexity of missions and restricts use cases to areas where deployment of acoustic infrastructure is feasible. Inertial navigation systems (INS) rely on heading and acceleration measurements and use dead reckoning techniques to estimate velocity and position of a vehicle [4]. They do not require additional infrastructure and are at the core of most standard navigation solutions. Though state of the art INS provide increasingly accurate measurements, they usually need to be complemented by aiding sensors to prevent a rapidly growing error drift.

The most common way to complement INS is the use of sensors that directly provide velocity estimates. The velocity can be measured relative to a static reference, which directly provides the velocity of a vehicle. In cases where such a reference does not exist, the vehicle velocity can be estimated relative to the surrounding fluid. However, the marine environment is inherently dynamic and the fluid surrounding a submerged vehicle is seldom at rest. Water currents can affect both the motion of an AUV and velocity readings relative to the fluid flow. A combination of sensors and/or techniques to estimate absolute and relative velocity can help to increase the robustness of a navigation system.

Beyond the capabilities for navigation, such a sensor suite can also enable the estimation of hydraulic influences such as water currents, which can be used to inform controllers for dynamic positioning or trajectory tracking. Estimates of water currents can also help to update and improve oceanographic models [5], or can be used as information for adaptive sampling decisions [6]. If a source of vehicle velocity relative to a static reference and a source of vehicle velocity relative to the surrounding fluid are simultaneously available, the water current velocity can be calculated as their difference.

The most widely applied sensor class for velocity aiding are Doppler Velocity Logs (DVLs) [7], which use the reflection of an

acoustic signal to estimate velocity. DVLs can be used in bottom lock (BL) relative to the smooth surface of a structure such as the sea bottom, or in water lock (WL) relative to particles suspended in the surrounding water. Depending on the mode, the vehicle velocity is measured as a total velocity over ground (DVL-BL), or as velocity relative to the surrounding fluid flow (DVL-WL). While the DVL-BL is generally the more accurate and preferred mode, its use is restricted to areas where a smooth surface can be used to reflect the signals. This cannot be guaranteed for mid-water column travels during deep sea applications or in highly unstructured environments. The quality of DVL-WL velocity estimates is restricted by the presence of a sufficient number of reflecting particles in the water and it has a smaller signal to noise ratio.

For long term deployments in complex and potentially unknown environments sensor redundancy and cost efficiency are key factors. Furthermore, a reduction in size and energy consumption is essential for such missions, as well as for the improvement of navigation capabilities of low cost and low energy vehicles. These objectives have motivated our previous work, where we introduced a sensor for surge velocity based on differential pressure [8] referred to as Differential Pressure Sensor Speedometer (DPSS) and verified its utility as a low cost and energy efficient system for speed estimation in surge [9].

In this work we present a new enhanced and smaller version of the DPSS (DPSSv2), building upon our previous work. Based on geometric principles and potential flow theory, we expand the velocity estimation from 1D to 2D, and estimate velocity relative to water in the horizontal plane. While the previous sensor was tightly integrated and tailored for a specific AUV, we now present a standalone system which can be employed in a wide variety of vehicles. Furthermore, we characterize the performance of the DPSSv2 in field conditions under the influence of tidal currents. We show that the DPSSv2 can be used in conjunction with another sensor providing total vehicle velocity to estimate water currents in situ.

II. RELATED WORK

A common approach to estimate water currents uses the concept of observers from control theory. Given an observable model describing the movement of a vehicle, a second model can be developed based on inputs and weighted outputs of the real system. The observer can then be used to estimate states which are not directly measurable. Assuming a steady, incompressible and irrotational current, Encarnação *et al.* [10] proposed a nonlinear Luenberger type observer based on the horizontal kinematics of an AUV, which has been frequently used afterwards [11]–[13]. Refsnes *et al.* [14] used a nonlinear Luenberger type observer based on the dynamics of the vehicle, specifically capturing the effect of water currents on the modelled Coriolis and centripetal forces for an underactuated AUV. Recently, high gain observers have been proposed to estimate water currents based on a dynamic vehicle model [15], [16]. While the proposed observers have been shown to be accurate in simulation and have been partially verified with field data, they all assume accurate state feedback for position. For surface vehicles this

is not a restrictive assumption, whereas underwater vehicles can not densely sample position data. They either operate outside of any acoustic network and do not get any direct position measurements at all or they get sparse updates from GPS fixes after surfacing.

Building upon sparse but periodical GPS fixes, several approaches with varying levels of complexity and accuracy have been used to estimate water currents. Those approaches are limited to missions where periodical resurfacing of the vehicle is inherent in the mission or, at least, feasible. A class of AUVs which periodically surfaces and utilizes GPS fixes are water gliders. A solution to estimate currents for robust navigation of ocean gliders is the use of a motion integration error [17]. This approach assumes that no vertical currents are present due to stratification and calculates a depth averaged horizontal current based on the difference between dead reckoning position estimates and sparse GPS fixes. The method does not account for dynamics of the flow field. The motion tomography introduced by Chang *et al.* [18] expands on the previous approach and computes the most likely flow field, based on the motion integration error. Additionally, predictive ocean models have been used to estimate currents and to assist with the guidance of gliders [19], [20]. However, those models are computationally complex and only provide a coarse resolution for a given position. Lee *et al.* [21] combine a model of the region of interest with a Gaussian Process Expectation Minimization algorithm, using sparse GPS data to predict the ocean current field surrounding a glider. While the proposed solutions do work for gliders, they can not be used for long term AUV missions in the deep sea or under ice where surfacing is not an option.

Several solutions for water current estimation that do not require direct measurements of global vehicle position have been proposed. Randeni *et al.* [22] used motion responses of the AUV in turbulent environments together with a model of the vehicle's dynamics to estimate water currents. However, this approach requires a calibration of the algorithm in still water which might be not feasible for certain deployments. Medagoda *et al.* [23] employ an ADCP mounted on a Sentry AUV to facilitate velocity estimation during midwater column travels. While this is a viable approach for heavyweight vehicles such as the Sentry AUV, the size and energy consumption of an ADCP and the computational costs of the proposed algorithm might be restrictive for smaller classes of AUVs. Hegreaneas *et al.* showed that an INS aided either by a dynamic model [24], [25] of the vehicle, or a DVL-WL in combination with a DVL-BL can be used for water current estimation. We propose the DPSSv2 as an alternative source to estimate velocity relative to water, which can be used as a replacement of a DVL-WL, or as a complement providing in situ estimates of velocity relative to water for the approaches previously mentioned in this section.

III. METHODOLOGY

In this section we first describe the mathematical derivations for surge and sway velocity estimation. Then we present the design of the DPSSv2 and explain the experimental setup used

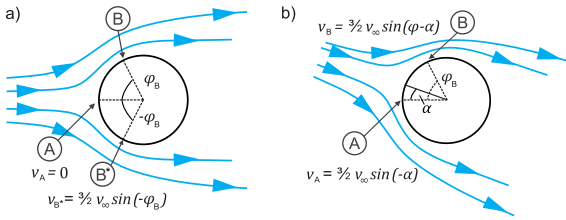


Fig. 1. **Irrotational, inviscid and incompressible flow over a sphere:** (a) Point A marks the stagnation point on the spheres' surface where the local velocity is zero. Points B and B* describe mirrored and arbitrary positions at the spheres' surface for an angle $0^\circ \leq \varphi_C \leq 90^\circ$. (b) Point A is angled towards the flow by α and the local velocity is nonzero. Given the same configuration as in (a) both measurement points A and B are shifted by the angle of incoming flow.

to verify its performance. Finally, we describe the analysis of the experimental data.

A. 2D Velocity Estimation

1) *Surge Velocity Model:* Assuming a planar, inviscid, irrotational and incompressible flow and the conservation of energy within a fixed fluid volume, the relation between pressure p and velocity v can be described by Bernoulli's law:

$$p + \frac{1}{2}\rho v^2 = \text{const} \quad (1)$$

Where p describes the fluid pressure, ρ the fluid density and v the flow velocity. Equation (1) can be used to estimate flow velocity around an immersed rigid body and has been extensively employed for flow speed estimation in aeronautics [26]. By assuming a steady flow over a spherical body and utilizing the directional finding Pitot-static concept [27], we can define a stagnation point A and two mirrored points B and B* on the spheres' surface as can be seen Fig. 1(a). Based on the pressure measurements at those three points we can infer the free stream velocity v_∞ . The necessary relation between pressure and velocity was derived based on geometric principles in [9] and was verified under laboratory conditions [8] with an accuracy of 0.012 m/s for surge speed estimation. To accurately estimate surge speed in field conditions, self motion effects of the vehicle carrying the sensor have to be taken into account. The final relation including hydrostatic correction terms for pitch θ and roll ϕ motions of an AUV is given by:

$$v_\infty = \sqrt[4]{\frac{2\alpha(\varphi)}{\rho^2}((\Delta p_1 - \Delta h_1 \rho g)^2 + (\Delta p_2 - \Delta h_2 \rho g)^2)} \quad (2)$$

with

$$\alpha(\varphi) = \left(\frac{4}{9 \sin^2(\varphi)}\right)^2 \quad (3)$$

and

$$\begin{aligned} \Delta h_1 &= (x_B - x_A) \cos(\phi) \sin(\theta) - (y_B + y_A) \sin(\phi) \\ \Delta h_2 &= (x_{B^*} - x_A) \cos(\phi) \sin(\theta) - (y_{B^*} + y_A) \sin(\phi) \end{aligned} \quad (4)$$

where Δp_1 and Δp_2 represent the pressure differences between the stagnation point and the arbitrary mirrored points B / B* and $\varphi = \varphi_B = -\varphi_{B^*}$ is the planar angle between the

stagnation point and points B / B*. Additionally, g represents the gravitational constant and $x_{(\cdot)}$ and $y_{(\cdot)}$ are Cartesian coordinates of the respective measurement points relative to the center of the sphere. Equation (2) has been validated under field conditions and showed a comparable performance to a DVL-BL for operational velocities above 1 m/s. Refer to [9] for more details.

2) *Sway Velocity Model:* The model for sway velocity is based on the assumption, that the location of the stagnation point on the spherical object will change in the presence of a non zero flow in sway direction (see Fig. 1(b)). We furthermore assume that Eq. (2) is invariant to changes in flow direction of up to 45° [28] and captures the true velocity component in surge direction. The velocity estimation for a single differential pressure sensor for the general case can be written as:

$$\Delta p_1 = p_A - p_B = \frac{1}{2}\rho(v_B^2 - v_A^2 + 2g\Delta h_1) \quad (5)$$

Note that with h_1 the elevation compensation presented in Eq. (4) is also utilized for the estimation of the velocity component in sway direction. Based on potential flow theory, the relationship between free stream velocity v_∞ and the velocity at a specified point (\cdot) on the surface of a sphere in a steady flow can be defined as [29]:

$$v_{(\cdot)} = \frac{3}{2}v_\infty \sin(\varphi_{(\cdot)}). \quad (6)$$

Inserting Eq. (6) in Eq. (5) and accounting for a change in flow direction by the angle α results in the following relation:

$$\Delta p_1 = \frac{1}{2}\rho \left[\frac{9}{4}v_\infty^2 (\sin^2(\varphi_B - \alpha) - \sin^2(-\alpha)) + 2g\Delta h_1 \right] \quad (7)$$

Using trigonometric identities and solving for α we get:

$$\alpha = \frac{\varphi_B - \arcsin\left(\frac{8(\Delta p_1 - \rho g \Delta h_1)}{9\rho v_\infty^2 \sin(\varphi_B)}\right)}{2} \quad (8)$$

Based on the assumption that $v_\infty = v_x$ as given by Eq. (2), the sway velocity component can be estimated by:

$$v_y = v_x \tan(\alpha) \quad (9)$$

3) *Planar Water Current Estimation:* The planar velocity vector estimated by the DPSSv2 is relative to the fluid flow surrounding the sensor. The total velocity vector $v_{total} \in \mathbb{R}^2$ of a vehicle moving through a moving fluid in its body frame can be defined as:

$$v_{total}^B = v_{rel}^B + v_c^B \quad (10)$$

where $v_{rel}^B \in \mathbb{R}^2$ describes the velocity relative to water vector estimated by the DPSSv2 and $v_c^B \in \mathbb{R}^2$ is the vector of water current velocity in body frame. Given a source for v_{total}^B such as a DVL-BL, the water current velocity in the global frame v_c^G can be calculated as:

$$v_c^G = R(\psi)(v_{total}^B - v_{rel}^B) \quad (11)$$

where $R(\psi) \in \mathbb{R}^2$ is the standard planar rotation matrix, which transforms the velocities from the local body frame into the global frame and ψ is the heading angle of the vehicle relative to the true north provided by the IMU.

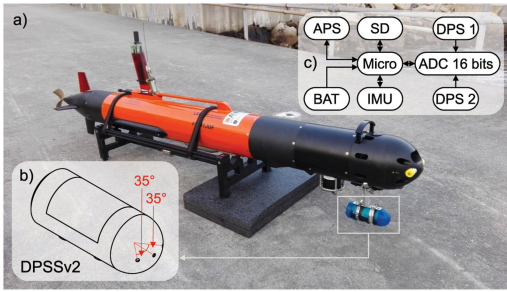


Fig. 2. LAUV Fridtjof and integrated DPSSv2 for Field trials: (a) DPSSv2 attached to the LAUV. (b) Sketch of the DPSSv2 with the distribution of the pressure taps. (c) Architecture of the DPSSv2. DPS - differential pressure sensor, APS - absolute pressure sensor, BAT - battery and ADC - analog to digital converter.

B. DPSSv2

The new sensor system developed in this letter (DPSSv2) provides a stand alone system to use in any AUV. To achieve this, our previous DPSS design (DPSSv1, [8]) is scaled down to a bullet shaped cylinder 14.1cm long, 5 cm in diameter and with a weight of 0.27kg (volume reduction of 28% and weight reduction of 39%). As pictured in Fig. 2, the DPSSv2 is equipped with: 1) two differential pressure sensors (MPXV7002DP from NXP semiconductors / range: ± 2 kPa, accuracy: 5Pa) to measure pressure across three different points, subsequently called pressure taps, on the sensor surface at the stagnation point and at $\pm 35^\circ$ from the stagnation point on each side, 2) an absolute pressure sensor (MS583730BA from TE Connectivity/ range: 0 to 30bar, accuracy: 30mbar) for depth estimation, 3) an IMU (BNO005 from Bosch) that provides information about sensor orientation (used in Eq. (4)) and 4) a micro-controller based data-logger (Feather M0 Adalogger from Adafruit) with integrated battery charger and SD card reader for data acquisition and preliminary computations.

The performance of the DPSSv2 was verified with a series of controlled experiments in a tow tank (for test description see [8]). Under such conditions, the differential pressure based velocity estimation was shown to be insensitive to structural effects at a distance greater than 0.25 m for walls and 0.5 m for the water surface [8]. Both conditions are well met in the experimental setup in this letter. The tow tank experiments were conducted for surge velocities in still water ranging from 0.1 m/s to 2 m/s. The surge velocity error followed a Gaussian distribution resulting in an accuracy of $\mu = 0.01$ m/s with a standard deviation of $\sigma = 0.046$ m/s. The DPSSv2 was not tested for deviations in yaw, but based on tests with a comparable prototype described in [28] and using Eq. (8), an angular accuracy of $\mu = 6.1^\circ$ with a standard deviation of $\sigma = 3.5^\circ$ was determined.

C. Experimental Setup

Field trials were conducted in the Trondheim Fjord, close to the island of Tautra, Norway (see Fig. 3(a) and 3(b)). The current dynamics in the Trondheim Fjord are mostly driven by a semi-diurnal tide, making the expected flow field time

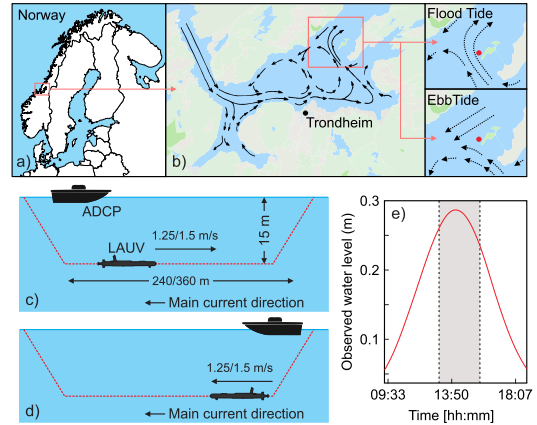


Fig. 3. Test site and experimental setup: (a) and (b) Test site (red dot) with mean tidal current patterns for the upper fluid layer reproduced from [30]. (c) and (d) Experimental setup to test the estimation of tidal currents with the DPSSv2. (e) Tidal cycle for the day of the experiments 2019/05/20. The grey area in the tidal graph represents the time slot of the experiments.

varying with a reversal in flow direction between ebb and flood tide conditions [30] three times a day. The experiments were conducted before and after the maximum tide was reached as shown in Fig. 3(e). Therefore, we expected the tidal current measurements to reflect the change in flow direction between flood and ebb flows.

The experimental setup consisted of a light AUV (LAUV) [31], equipped with an IMU (Microstrain 3DM-GX4-25) and a DVL (Nortek DVL 1 MHz) providing WL and BL velocity estimates simultaneously. Additionally, the DPSSv2 was mounted on the LAUV (see Fig. 2). A boat employing an ADCP (Sontek River Surveyor M9) gathered global current measurements for comparison. During the experiments, the DPSSv2 sampled data autonomously, which were then analysed in post processing. To estimate the tidal current velocity components in surge and sway, the velocity estimates of DPSSv2 and DVL-WL were referenced to the total velocity estimates given in our case by the DVL-BL.

The velocity estimation was tested in 14 trials, while the vehicle followed a straight line trajectory at constant depth (15 m, Fig. 3(c) and 3(d)). Six trials were conducted with the minimum velocity the vehicle was able to reliably maintain (1.25 m/s) in the given conditions and for eight trials the target velocity was set to 1.5 m/s. In both cases, half of the trials were conducted against the main direction of the anticipated current and the other half in the opposite direction. Four trials at the beginning of the experiments with a target velocity of 1m/s were excluded from the analysis, because the LAUV could not ensure a stable movement in those conditions.

D. Data Analysis

The raw differential pressure measurements from the DPSSv2, sampled at a rate of 100 Hz, were averaged to 5 Hz, using a rolling mean to achieve maximum accuracy [8]. The

resulting sampling rate was equal to the sampling rate of the employed DVL. A constant offset in the differential pressure sensors was compensated for by subtracting the pressure measured for zero velocity in air. The surge and sway velocity components were then calculated with Eq. (2) and Eq. (9), respectively. For the DVL velocities raw sensor values were used, with outliers removed, based on validity information provided by the sensor. Furthermore, we restricted the data-analysis to the part of each trial where the LAUV had reached its target depth and moved in a straight line.

The main focus of the data analysis was to evaluate the ability of the DPSSv2 to estimate tidal currents in conjunction with a source for total vehicle velocity, provided by the DVL-BL in our experiments. We compared the results with the tidal current velocity estimation from the DVL-BL - DVL-WL pair. This evaluation implicitly includes a performance characterization for the DPSSv2's capability to estimate velocity relative to water. The DVL-WL and the DPSSv2 body frame velocities in surge and sway were subtracted from the respective DVL-BL total vehicle velocities. The resulting planar current velocity vector was then rotated into a global reference frame using Eq. (11), based on the heading provided the LAUV's attitude and heading reference system. Magnitude and angle relative to true north of the estimated tidal currents were then compared to characterize the performance of the DPSSv2 - DVL-BL current estimation in relation to the DVL-WL - DVL-BL estimation. Additionally, the tidal current estimates from the ADCP were used for comparison. The median (IQR) for each time series per trial was used as evaluation metric.

Furthermore, we investigated how the tidal current estimates from the DPSSv2 - DVL-BL pairing were impacted by changes in the motion direction of the LAUV (with and against anticipated current direction) and different vehicle velocities. For this purpose we concentrated on tidal current estimates in the body fixed frame, because the interpretation of the effects is more intuitive here. For brevity we subsequently refer to DPSSv2 and DVL-WL tidal current estimations, with the implicit indication that all results for tidal current estimations have been augmented with DVL-BL velocity readings. We took the median and IQR of the absolute differences between DVL-WL and DPSSv2 current velocity estimates for each trial as evaluation metrics and divided the trials into sub-classes based on target velocity and direction of movement.

IV. RESULTS AND DISCUSSION

We first present results for DVL-WL, ADCP and DPSSv2 tidal current estimates, represented by their magnitude and heading angle relative to true north in a global reference frame. We use those results to motivate our subsequent choice to concentrate on a comparison between DVL-WL and DPSSv2 and show the influences of the tidal conditions on the estimation performance. We then compare the DVL-WL and DPSSv2 tidal current estimates for the different sub-classes shown in Table I. For this comparison the planar tidal current vectors are split up into their respective surge and sway components in a body referenced frame, to get a more intuitive understanding of the estimation performance of the DPSSv2.

TABLE I
TRIALS DIVIDED INTO SUB-CLASSES BASED ON DIFFERENT TEST CONDITIONS

Direction	Velocity [m/s]	Trial Number
against current	1.25	5, 9, 13
	1.5	1, 3, 7, 11
with current	1.25	6, 10, 14
	1.5	2, 4, 8, 12

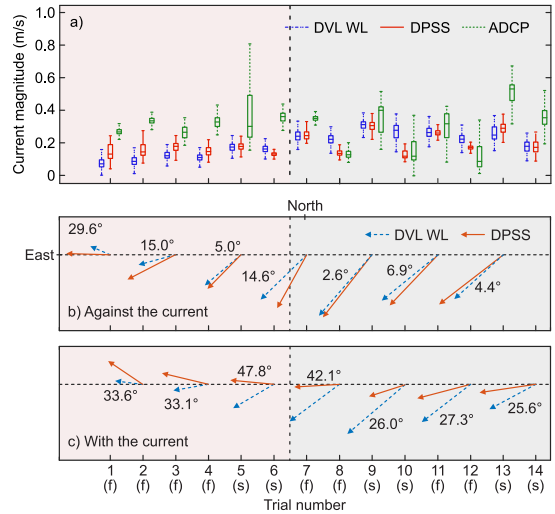


Fig. 4. Estimation of tidal current velocity vector for DVL, DPSSv2 and ADCP: Tidal current estimates for the DVL and DPSSv2 are both augmented by DVL-BL readings. (a) Magnitude estimates of the tidal current in the global reference frame represented by median, IQR and extreme values for each trial. (b) and (c) Median magnitude and heading estimates of the tidal current relative to true north for DVL and DPSSv2 (ADCP estimates are not used in the performance comparison and thus omitted to improve the readability of the figures). The difference between the two median heading estimates in degrees is annotated for each trial. Instances where the LAUV was moving with the currents (c) are distinguished from instances where the LAUV was moving against the currents (d). The trial numbers are further augmented with either (s) for trials with the slower velocity of 1.25 m/s or (f) for the faster velocity of 1.5 m/s. The light beige patch (trials 1–6) represents slack water conditions close to high tide where the currents are less strong, more turbulent and change direction eventually. The light grey patch (trials 7 to 14) shows the tidal conditions for ebb flow after the maximum tidal water level.

A. Tidal Current Magnitude and Heading in Global Frame

Fig. 4(a) shows that DVL-WL and DPSSv2 estimate, in most cases, a lower current velocity with less variance than the ADCP. Due to the tidal influence the flow direction and flow velocity were changing over the course of the experiments. Surface waves were affecting the stability of the boat where the ADCP was installed. Furthermore, resulting from the signal to noise ratio, the depth of interest was, even though the values were sufficient at that level, close to the limit. Additionally, salinity levels and salinity stratification were changing throughout the trials, which affected the ADCP data.

In general, the data shows that it is difficult to select a reliable reference for current estimation under highly dynamic field conditions. We evaluated predictions from a publicly available current model of the Norwegian Meteorological Institute [32], which indicated small current velocities during the first trials

TABLE II

MEDIAN (IQR) IN M/S FOR ABSOLUTE DIFFERENCE IN CURRENT VELOCITY ESTIMATION IN BODY FRAME BETWEEN DVL WL AND DPSS. THE FOLLOWING SUB-CLASSES ARE PRESENTED: AGAINST - AGAINST THE CURRENT, WITH - WITH THE CURRENT, HIGH - HIGHER VELOCITY (1.5 M/S) AND LOW - LOWER VELOCITY (1.25 M/S)

		against	with	total
high	surge	0.05 (0.06)	0.05 (0.06)	0.05 (0.06)
	sway	0.04 (0.04)	0.09 (0.06)	0.07 (0.06)
low	surge	0.03 (0.04)	0.07 (0.08)	0.04 (0.06)
	sway	0.02 (0.03)	0.1 (0.05)	0.05 (0.07)
total	surge	0.04 (0.05)	0.06 (0.06)	
	sway	0.03 (0.04)	0.09 (0.05)	

and a reversal in flow direction shortly before high tide. Those predictions were best matched by DPSSv2 and DVL-WL tidal current estimates. Based on this information and due to the lower variance in the DPSSv2 and DVL-WL estimates we decided to base the subsequent evaluation of the DPSSv2 performance on a comparison with the DVL-WL. We refrain from defining a ground truth and treat both sensors as data sources with uncertainties and evaluate the similarity of the provided tidal current estimates.

Fig. 4(b) and 4(c) show magnitude and direction of the estimated currents for DVL-WL and DPSS. The reversal of flow direction can be seen from estimates of both sensors. The results for trials conducted at a later point in time (towards the right of the figure) indicate that the flow conditions were more stable as the water level was moving away from its maximum. The figure also shows that the DVL and DPSSv2 estimates have good agreement for trials where the vehicle went against the current. However, for trials in the direction of the current the estimates differ especially regarding the heading angle.

B. Influence of Direction of Movement and Vehicle Velocity

To better understand the underlying cause of the observed contrast regarding the direction of movement, we evaluate the differences between DVL-WL and DPSS current estimation in the vehicle's body frame for sway and surge direction separately. Additionally, we investigate the effect of the two target velocities on the differences between the current estimates. Table II presents summary statistics (median absolute difference with IQR) for the following four scenarios: 1) higher velocity - against currents (high - against), 2) higher velocity - with currents (high - with), 3) lower velocity - against currents (low - against), 4) lower velocity - with currents (low - with).

The statistics show, that the main contribution to a bigger difference for trials along the current direction is coming from the sway velocity estimation. This is an expected result, because the assumption of potential flow around the DPSSv2 with a stagnation point on the spherical head section, which was used to derive equations (2) and (8), does not hold with the movement of the sensor along the ambient flow. The surge velocity estimation is to some degree affected by the same problem. This is detailed in Fig. 5 which shows velocity estimates for DVL-BL, DVL-WL

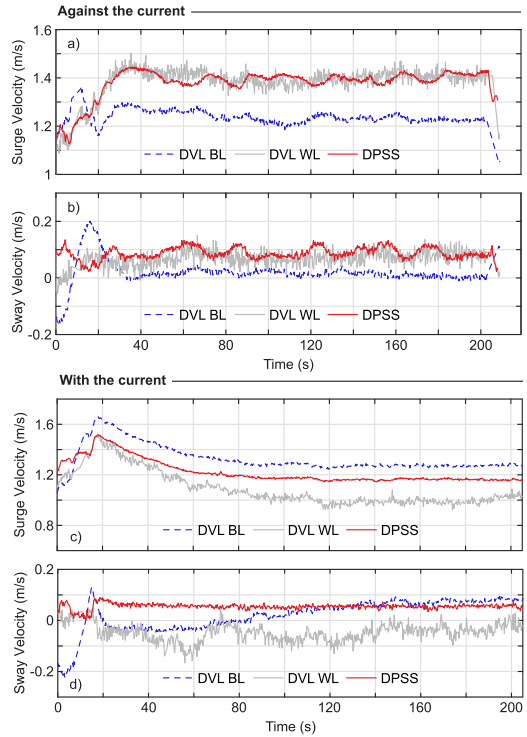


Fig. 5. Velocity estimation for DVL (BL and WL) and DPSSv2: surge (a) and sway (b) against the main current direction for trial number 5. Surge (c) and (d) sway along the main current direction for trial number 10.

and DPSSv2 for a trial against the tidal currents and along the tidal currents respectively.

Fig. 5(a) and 5(b) show the surge and sway velocity estimations for trial number 5, when the vehicle is moving against the tidal current. In this case the relative velocity is the sum of total vehicle and water current velocity and DVL-WL and DPSSv2 should overestimate the velocity components. This can be seen for both surge and sway directions. Additionally, it can be seen that the DPSSv2 velocity estimation tracks the DVL-WL velocity estimations very closely for surge and sway components, as the potential flow assumption holds in this case. The DPSSv2 further estimates velocity with less variance compared to the DVL-WL estimations at the same effective sampling rate.

In contrast, Fig. 5(c) and 5(d) show the velocity estimates for trial number 10, where the movement of the LAUV is along the tidal current. The DVL-WL underestimates the total velocity component in surge direction Fig. 5(c) due to the superimposed velocity component of the current. For the sway component in Fig. 5(d) a change in direction can be seen for the total velocity, which is not reflected in the DVL-BL readings due to the superimposed current flowing with an angle of attack relative to the LAUV. The DPSSv2 velocity estimation for the surge component is also underestimating the surge speed but by a smaller margin compared to the DVL-WL. Regarding the sway component of the velocity the DPSSv2 fails to resolve

the direction of the velocity component relative to the flow and does not follow changes due to the lack of potential flow. This lack of accurate relative velocity estimation, specifically in sway direction, causes the great deviations for the heading angles of the tidal current estimates in the global reference frame shown in Fig. 4(b).

This inherent limitation of the DPSSv2 for situations, in which it is not facing the flow, could be resolved through the design of trajectories, which guarantee changes in the direction of movement such as lawn mower patterns. It has been shown in [33] and [34] that a few changes in heading can make water relative velocities and water currents observable. Furthermore, combining the DPSSv2 estimates with sparse GPS fixes, or a model aided INS could provide those methods with in situ velocity updates and subsequently help to correct the DPSSv2 errors for movements along the ambient flow. To that end, a combination with many approaches presented in Section II is conceivable.

The summary statistics in Table II also show a difference between higher and lower target vehicle velocities, with the median absolute differences being smaller for the lower target velocity. At first glance this is a surprising result, because the DPSSv2 velocity estimation should be more robust against disturbances at higher vehicle velocities, due to the quadratic relationship between pressure and velocity. However, the actual tidal current velocity needs to be considered, which was smaller during slack water. Due to the omission of the first four trials at low target velocity, almost all lower target velocity trials were conducted during ebb flow after slack water, which provided more stable environmental conditions with higher tidal current velocities (see Fig. 4). Another reason for the increased differences at higher target velocities could be a performance degradation of the DVL-WL for higher vehicle velocities as shown in [9].

However, in all cases where the potential flow assumption was valid, the DPSSv2 tidal current estimation was close to the DVL-WL with a median absolute (IQR) difference in global tidal current magnitude of 0.03 m/s (0.043 m/s) and heading of 8.13° (11.0°). Those differences are close to the accuracy bound, defined for the DPSS under field conditions reported in [9] and at the same scale as estimation errors reported by other approaches [16], [35]. The results show that the DPSSv2 can be a viable option to improve velocity estimation for vehicles that can not equip state of the art sensors such as DVL or ADCP.

Another important factor for successful and reliable navigation for AUVs, specifically in long term and/or deep sea missions, is redundancy. Fig. 6 shows a case where the DVL readings are corrupted by an unknown disturbance, whereas the DPSSv2 readings are not affected. The addition of the DPSSv2 to the sensor suite of a vehicle already equipped with the state of the art velocity aiding technology could thus provide additional reliability and stability for the velocity estimation.

V. CONCLUSION AND FUTURE WORK

In this study we presented a flow-relative velocity sensor for marine vehicles, using differential pressure. We expanded the

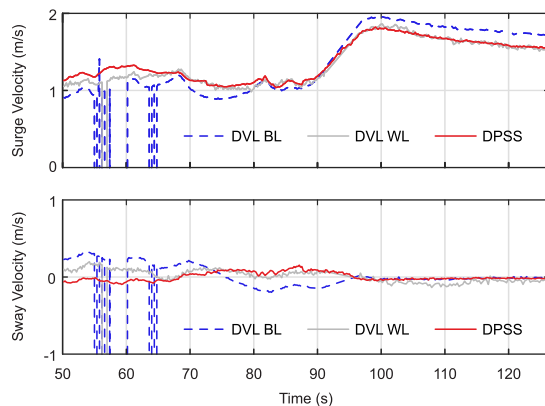


Fig. 6. Extract of the time series for velocity estimation of DVL and DPSSv2 for a trial: From 55 s to 65 s the DVL returns false readings due to unknown disturbances

capabilities of the sensor developed in our previous works [8], [9] to measure velocity components in two dimensions (surge and sway) and provided a design reducing size and weight compared to the previous version. We validated the new prototype under field conditions on an AUV. The presented DPSSv2 can be used as a complementary sensor for existing sensor suites to increase robustness and redundancy. The sensor can also provide water-relative velocity information for navigation in conditions where GPS and DVL-BL are not available such as mid-water column operations. This has the potential to simplify the logistics of long term experiments by decreasing the need for external infrastructure such as support vessels or acoustic networks. With a small form factor and low power requirements, 0.244 W versus 1.3 W for the deployed DVL, the device has the potential to provide in situ velocity estimation to vehicles, which can not equip state of the art velocity sensors due to size, budget or energy restrictions. This work has shown that a robust planar velocity estimation is already possible in operation conditions that do not violate the potential flow assumptions. A combination with other proposed methods and algorithms that quantify water currents or fluid relative velocity has the potential to expand the robustness of the DPSSv2 in situ velocity estimation to more general conditions. While it is difficult to compare production costs of fully developed products versus lab prototypes, we estimate that the costs for the DPSSv2 are roughly one order of magnitude smaller than the DVL used in this study.

We characterized the velocity estimation performance of DPSSv2 under the influence of tidal currents and evaluated its capability to estimate those tidal currents when combined with a sensor providing total vehicle velocity estimates. The results showed that in combination with a DVL-BL the DPSSv2 could estimate tidal currents with a similar accuracy as the DVL-WL when the sensor was facing the currents. The acquired tidal current estimates can in turn be used to increase the precision of navigation or to inform and update oceanographic models. Future work will continue on three fronts: (1) expanding sensor to 3D velocity estimation, (2) exploring the use of aiding sensors

such as GPS or INS, and algorithms such as water current observers to resolve problems when the sensor moves in line with the current, and (3) producing a standalone navigation system independent of other sources for vehicle velocity estimation.

ACKNOWLEDGMENT

The authors would like to thank Tore Mo-Bjørkelund and Øystein Sture from the NTNU Applied Underwater Robotics Laboratory for their help during field trials and Jeffrey A. Tuhtan and Margit Egerer from the Centre for Biorobotics for fruitful discussions and insights during the writing process.

REFERENCES

- [1] N. E. Leonard, D. A. Paley, R. E. Davis, D. M. Fratantoni, F. Lekien, and F. Zhang, "Coordinated control of an underwater glider fleet in an adaptive ocean sampling field experiment in Monterey Bay," *J. Field Robot.*, vol. 27, no. 6, pp. 718–740, Nov. 2010.
- [2] A. Branch *et al.*, "Front delineation and tracking with multiple underwater vehicles," *J. Field Robot.*, vol. 36, no. 3, pp. 568–586, May 2019.
- [3] T. O. Fossum *et al.*, "Toward adaptive robotic sampling of phytoplankton in the coastal ocean," *Sci. Robot.*, vol. 4, no. 27, Feb. 2019, Art. no. eaav3041.
- [4] L. Paull, S. Saeedi, M. Seto, and H. Li, "AUV navigation and localization: A review," *IEEE J. Ocean. Eng.*, vol. 39, no. 1, pp. 131–149, Jan. 2014.
- [5] E. Kalnay, *Atmospheric Modeling, Data Assimilation and Predictability*. Cambridge, U.K.: Cambridge University Press, 2003.
- [6] T. O. Fossum *et al.*, "Information-driven robotic sampling in the coastal ocean," *J. Field Robot.*, vol. 35, no. 7, pp. 1101–1121, Oct. 2018.
- [7] B. Jalving, K. Gade, K. Svartveit, A. Willumsen, and R. Sørhagen, "DVL velocity aiding in the HUGIN 1000 integrated inertial navigation system," *Model., Identification Control*, vol. 25, no. 4, pp. 223–235, 2004.
- [8] J. F. Fuentes-Pérez, C. Meurer, J. A. Tuhtan, and M. Kruusmaa, "Differential pressure sensors for underwater speedometry in variable velocity and acceleration conditions," *IEEE J. Ocean. Eng.*, vol. 43, no. 2, pp. 418–426, Apr. 2018.
- [9] C. Meurer, J. Francisco Fuentes-Perez, N. Palomeras, M. Carreras, and M. Kruusmaa, "Differential pressure sensor speedometer for autonomous underwater vehicle velocity estimation," *IEEE J. Ocean. Eng.* to be published.
- [10] P. Encarnação, A. Pascoal, and M. Arcaç, "Path following for marine vehicles in the presence of unknown currents," *IFAC Proc. Vol.*, vol. 33, no. 27, pp. 507–512, Sep. 2000.
- [11] A. P. Aguiar and A. M. Pascoal, "Dynamic positioning and way-point tracking of underactuated AUVs in the presence of ocean currents," in *Proc. 41st IEEE Conf. Decis. Control*, 2002, pp. 2105–2110, vol. 2.
- [12] S. Moe, W. Caharija, K. Y. Pettersen, and I. Schjøberg, "Path following of underactuated marine surface vessels in the presence of unknown ocean currents," in *Proc IEEE. Amer. Control Conf.*, Jun 2014, pp. 3856–3861.
- [13] C. Paliotta and K. Y. Pettersen, "Geometric path following with ocean current estimation for ASVs and AUVs," in *Proc IEEE. Amer. Control Conf.*, Jul. 2016, pp. 7261–7268.
- [14] J. E. Refsnes, K. Y. Pettersen, and A. J. Sørensen, "Control of slender body underactuated AUVs with current estimation," in *Proc. IEEE Conf. Decis. Control*, 2006, pp. 43–50.
- [15] S. Fan, W. Xu, Z. Chen, and F. Zhang, "Nonlinear observer design for current estimation based on underwater vehicle dynamic model," in *Proc. IEEE OCEANS Shanghai*, Apr. 2016, pp. 1–5.
- [16] E. Kim, S. Fan, and N. Bose, "Autonomous underwater vehicle Model-Based High-Gain observer for ocean current estimation," in *Proc. IEEE AUV IEEE/OES Auton. Underwater Vehicle Workshop, Proc.*, Nov. 2018, pp. 1–6.
- [17] L. M. Merckelbach, R. D. Briggs, D. A. Smeed, and G. Griffiths, "Current measurements from autonomous underwater gliders," in *Proc. IEEE Working Conf. Current Meas. Technol.*, 2008, pp. 61–67.
- [18] D. Chang, W. Wu, C. R. Edwards, and F. Zhang, "Motion tomography: Mapping flow fields using autonomous underwater vehicles," *Int. J. Robot. Res.*, vol. 36, no. 3, pp. 320–336, Mar. 2017.
- [19] R. N. Smith, J. Kelly, Y. Chao, B. H. Jones, and G. S. Sukhatme, "Towards the improvement of autonomous glider navigational accuracy through the use of regional ocean models," in *Proc. ASME 29th Int. Conf. Ocean, Offshore Arctic Eng.*, 2010, pp. 597–606.
- [20] D. Chang, F. Zhang, and C. R. Edwards, "Real-time guidance of underwater gliders assisted by predictive ocean models," *J. Atmospheric Ocean. Technol.*, vol. 32, no. 3, pp. 562–578, Mar. 2015.
- [21] K. M. B. Lee, C. Yoo, B. Hollings, S. Anstee, S. Huang, and R. Fitch, "Online estimation of ocean current from sparse GPS data for underwater vehicles," in *Proc. IEEE Int. Conf. Robot. Autom.* Montreal, 2019, pp. 3443–3449.
- [22] S. A. Randeni P. A. L. Forrest, R. Cossu, Z. Q. Leong, and D. Ranmuthugala, "Determining the horizontal and vertical water velocity components of a turbulent water column using the motion response of an autonomous underwater vehicle," *J. Mar. Sci. Eng.*, vol. 5, no. 3, Jul. 2017, Art. no. 25.
- [23] L. Medagoda, J. C. Kinsey, and M. Eilders, "Autonomous Underwater Vehicle localization in a spatiotemporally varying water current field," in *Proc. IEEE Int. Conf. Robot. Autom.*, May 2015, no. June, pp. 565–572.
- [24] Ø. Hegrenæs and O. Hallingstad, "Model-aided INS with sea current estimation for robust underwater navigation," *IEEE J. Ocean. Eng.*, vol. 36, no. 2, pp. 316–337, Apr. 2011.
- [25] Ø. Hegrenæs and E. Berglund, "Doppler water-track aided inertial navigation for autonomous underwater vehicle," in *Proc. IEEE OCEANS 'Bremen: Balancing Technol. Future Needs.*, May 2009, pp. 1–10.
- [26] E. Ower and R. C. Pankhurst, *The Measurement of Air Flow*. New York, NY, USA: Elsevier, 2014.
- [27] C. J. Fechheimer, "Measuring Device," U.S. Patent 1 834 392A, 1931.
- [28] J. F. Fuentes-Pérez, K. Kalev, J. A. Tuhtan, and M. Kruusmaa, "Underwater vehicle speedometry using differential pressure sensors: Preliminary results," in *Proc. IEEE/OES Auton. Underwater Vehicles*, 2016, pp. 156–160.
- [29] J. Anderson Jr, *Fundamentals of Aerodynamics*. New York, NY, USA: Tata McGraw-Hill Education, 1985, vol. Third Edit.
- [30] P. Jacobson, "Physical oceanography of the trondheimsfjord," *Geophysical Astrophysical Fluid Dyn.*, vol. 26, no. 1-2, pp. 3–26, Oct. 1983.
- [31] A. Sousa *et al.*, "LAUV: The Man-Portable autonomous underwater vehicle," *IFAC Proc. Vol.*, vol. 45, no. 5, pp. 268–274, Jan. 2012.
- [32] Yr, "YR - Coastal Forecast," 2019. [Online]. Available: https://www.yr.no/place/Ocean/63.44180_10.36698/hour_by_hour.html. Accessed on: May 20, 2019.
- [33] Ø. Hegrenæs, O. Hallingstad, and B. Jalving, "A framework for obtaining steady-state maneuvering characteristics of underwater vehicles using seatrial data," in *Proc. IEEE Mediterranean Conf. Control Autom.*, Jun. 2007, pp. 1–6.
- [34] Ø. Hegrenæs, O. Hallingstad, and B. Jalving, "Comparison of mathematical models for the HUGIN 4500 AUV based on experimental data," in *Proc. IEEE Int. Symp. Underwater Technol., UT Int. Workshop Scientific Use Submarine Cables Related Technol.*, Apr. 2007, pp. 558–567.
- [35] D. Chang, C. R. Edwards, F. Zhang, and J. Sun, "A data assimilation framework for data-driven flow models enabled by motion tomography," *Int. J. Intell. Robot. Appl.*, vol. 3, no. 2, pp. 158–177, Jun. 2019.

Curriculum Vitae

1. Personal data

Name Christian Meurer
Date and place of birth 06.08.1990 Suhl, Germany
Nationality German

2. Contact information

E-mail christian.meurer@taltech.ee

3. Education

2016–... Tallinn University of Technology, School of Information Technologies
Information and Communication Technology, PhD studies
2012–2015 Rhine-Waal University of Applied Sciences, Faculty of Technology and Bionics,
Bionics, Biomimetics, MSc
2009–2012 Ernst-Abbe-Hochschule Jena, Faculty of Medical Engineering and Biotechnology,
Biotechnology, BSc

4. Language competence

German native
English fluent

5. Professional employment

2016–... Centre for Biorobotics, Tallinn University of Technology - Junior Researcher
2014–2015 EvoLogics GmbH, Berlin, Germany - Intern for Master Thesis
2013–2014 Ocean Tech-Lab, Rhine-Waal University of Applied Sciences - Student Employee

6. Voluntary work

2013–2014 2nd European International Subrace, Team-Leader of the HSRW-Submarine Team
2013–2014 Founding member and 1st chairman of the HSRW-Ocean Tech e.V.
2013–2014 Student representative on the Examination Board of the Faculty of Technology
and Bionics of the Rhine-Waal University of Applied Sciences
2012–2013 12th International Submarine Races, Team-Member of the HSRW-Submarine Team

7. Computer skills

- Operating systems: MS, Linux
- Document preparation: MS Word, LaTeX
- Programming languages: Python, C++
- Scientific packages: Matlab, Mathematica, ROS, Gazebo
- Other: SolidWorks, DaVinci Resolve, CorelDraw

8. Honours and awards

- 2020, Outstanding Reviewer Award winner, IOP Publishing
- 2015, Award for the best Graduation (MSc.) at the faculty of Technology and Bionics of the Rhine-Waal University of Applied Sciences
- 2014, BMT Award for Innovation with the HSRW-Submarine Team during the 2nd European International Submarine Races, Gosport, Uk

9. Defended theses

- 2015, "Launch and Recovery Mechanism for a Bionic AUV: A Mechatronic Gripper Module with Thermo-Hydraulic Actuation", MSc, supervisor Prof. Dr. William Megill, Rhine-Waal University of applied Sciences, Faculty of Technology and Bionics
- 2011, "Alternative Splicing in the Donor-Array at Intron 15 of the Human Cystathionine Beta Synthase Gene", BSc, supervisor Prof. Dr. Waldemar Künkel, Ernst-Abbe-Hochschule Jenay, Faculty of Medical Engineering and Biotechnology

10. Field of research

- motion control for autonomous underwater vehicles
- state estimation for autonomous underwater vehicles

11. Scientific work

Papers

1. J. F. Fuentes-Pérez, C. Meurer, J. A. Tuhtan, and M. Kruusmaa, "Differential Pressure Sensors for Underwater Speedometry in Variable Velocity and Acceleration Conditions," IEEE Journal of Oceanic Engineering, vol. 43, no. 2, pp. 418–426, 2018
2. C. Meurer, J. Francisco Fuentes-Perez, N. Palomeras, M. Carreras, and M. Kruusmaa, "Differential Pressure Sensor Speedometer for Autonomous Underwater Vehicle Velocity Estimation," IEEE Journal of Oceanic Engineering, pp. 1–33, 2019
3. C. Meurer, A. Simha, Ü. Kotta, and M. Kruusmaa, "Nonlinear orientation controller for a compliant robotic fish based on asymmetric actuation," in Proceedings - IEEE International Conference on Robotics and Automation (ICRA), vol. 2019-May, pp. 4688–4694, Institute of Electrical and Electronics Engineers Inc., may 2019
4. A. Kaldmäe, Ü. Kotta, C. Meurer, and A. Simha, "Event-based control for differentially flat systems: Application to autonomous underwater vehicle," in IFAC-PapersOnLine, vol. 52, pp. 180–185, Elsevier B.V., sep 2019
5. C. Meurer, J. F. Fuentes-Perez, K. Schwarzwaldner, M. Ludvigsen, A. J. Sorensen, and M. Kruusmaa, "2D estimation of velocity relative to water and tidal currents based on differential pressure for autonomous underwater vehicles," IEEE Robotics and Automation Letters, vol. 5, pp. 3444–3451, apr 2020

Elulookirjeldus

1. Isikuandmed

Nimi Christian Meurer
Sünniaeg ja -koht 06.08.1990, Suhl, Germany
Kodakondsus Saksamaa

2. Kontaktandmed

E-post christian.meurer@taltech.ee

3. Haridus

2016–... Tallinna Tehnikaülikool, Infotehnoloogia teaduskond,
2012–2015 Rhine-Waal University of Applied Sciences, Faculty of Technology and Bionics,
Bionics, Biomimetics, MSc
2009–2012 Ernst-Abbe-Hochschule Jena, Faculty of Medical Engineering and Biotechnology,
Biotechnology, BSc

4. Keelteoskus

saksa keel emakeel
inglise keel kõrgtase

5. Teenistuskäik

2016–... Centre for Biorobotics, Tallinn University of Technology - Junior Researcher
2014–2015 EvoLogics GmbH, Berlin, Germany - Intern for Master Thesis
2013–2014 Ocean Tech-Lab, Rhine-Waal University of Applied Sciences - Student Employee

6. Vabatahtlik töö

2013–2014 2nd European International Subrace, Team-Leader of the HSRW-Submarine Team
2013–2014 Founding member and 1st chairman of the HSRW-Ocean Tech e.V.
2013–2014 Student representative on the Examination Board of the Faculty of Technology
and Bionics of the Rhine-Waal University of Applied Sciences
2012–2013 12th International Submarine Races, Team-Member of the HSRW-Submarine Team

7. Computer skills

- Operatsioonisüsteemid: MS, Linux
- Kontoritarkvara: MS Word, LaTeX
- Programmeerimiskeeled: Python, C++
- Teadustarkvara paketid: Matlab, Mathematica, ROS, Gazebo

8. Autasud

- 2020, Outstanding Reviewer Award winner, IOP Publishing
- 2015, Award for the best Graduation (MSc.) at the faculty of Technology and Bionics of the Rhine-Waal University of Applied Sciences
- 2014, BMT Award for Innovation with the HSRW-Submarine Team during the 2nd European International Submarine Races, Gosport, UK

9. Kaitstud lõputööd

- 2015, "Launch and Recovery Mechanism for a Bionic AUV: A Mechatronic Gripper Module with Thermo-Hydraulic Actuation", MSc, supervisor Prof. Dr. William Megill, Rhine-Waal University of applied Sciences, Faculty of Technology and Bionics
- 2011, "Alternative Splicing in the Donor-Array at Intron 15 of the Human Cystathionine Beta Synthase Gene", BSc, supervisor Prof. Dr. Waldemar Künkel, Ernst-Abbe-Hochschule Jenay, Faculty of Medical Engineering and Biotechnology

10. Teadustöö põhisuunad

- autonoomsete allveeliikurite juhtimine
- autonoomsete allveeliikurite olekuhindamine

11. Teadustegevus

Teadusartiklite, konverentsiteeside ja konverentsiettekannete loetelu on toodud ingliskeelse elulookirjelduse juures.

ISSN 2585-6901 (PDF)
ISBN 978-9949-83-710-6 (PDF)